PIEZOELECTRIC NANOSTRUCTURES OF ZINC OXIDE: SYNTHESIS, CHARACTERIZATION AND DEVICES

A Thesis

Presented to

the Academic Faculty

by

Puxian Gao

In Partial Fulfillment

of the Requirements for the Degree

Doctor of Philosophy in Materials Science and Engineering

Georgia Institute of Technology

December, 2005

PIEZOELECTRIC NANOSTRUCTURES OF ZINC OXIDE:

SYNTHESIS, CHARACTERIZATION AND DEVICES

Approved by:

Dr. Zhong L. Wang, Advisor
School of Materials Science and Engineering
Georgia Institute of Technology

Dr. C. P. Wong
School of Materials Science and Engineering
Georgia Institute of Technology

Dr. Christopher J. Summers
School of Materials Science and Engineering
Georgia Institute of Technology

Dr. W. Jack Lackey
School of Mechanical Engineering
Georgia Institute of Technology

Dr. David N. Ku
School of Mechanical Engineering
Georgia Institute of Technology

Date Approved: November 22, 2005

ACKNOWLEDGEMENTS

Firstly, I would like to express my great appreciation to Dr. Zhong Lin Wang, for his instantly inspiring guidance, constant support, valuable advices, and hearty encouragement through the entire course of this study. I would also like to thank Dr. C. P. Wong, Dr. Christopher J. Summers, Dr. W. Jack Lackey and Dr. David N. Ku for serving as my committee members.

Special thanks are given to the members in our nanoscience research group, who have helped me throughout my research and study at Georgia Tech. The names specially need to be mentioned here are: Dr. Xuedong Bai, Dr. Yong Ding, Dr. Jing Li, Dr. Carsten Ronning, Ms. Yolande Berta, Dr. Christopher Ma, Xudong Wang, William Hughes, Daniel Moore, Changshi Lao, Jun Zhou, Wenjie Mai, and Jin Liu.

Thanks also go to Dr. Yiyi Zhang from Department of Biomedical Engineering at Georgia Tech/Emory University, and Dr. Xingming Gao from Department of Chemistry at Georgia State University for their collaboration and help.

I gratefully acknowledge the financial support from NSF, the NASA Vehicle Systems Program and Department of Defense Research and Engineering (DDR&E), and the Defense Advanced Research Projects Agency.

Finally, I am heavily indebted to my parents, who have taught me to be a strong person physically and mentally regardless of time and location, and my lovely wife who has been firmly supporting me, encouraging me from the behind.

Puxian Gao

Georgia Tech, December 2005

TABLE OF CONTENTS

LIST OF TABLES

LIST OF FIGURES

SUMMARY

In this thesis, a systematic study has been carried out on the synthesis, characterization and device fabrication of piezoelectric ZnO nanstructures. The following goals have been achieved: a). Rational design and growth control over versatile nanostructures of ZnO; b). Improved chemical and physical understanding about the growth of ZnO nanostructures; c). Initial device applications based on as-grown nanostructures with biosensing as the main objective.

Firstly, through a systematic investigation on the Sn-catalyzed ZnO nanostructure, an improved understanding of the chemical and physical process occurring during the growth of hierarchical nanostructures has been achieved. Decomposed Sn from SnO_2 has been successfully demonstrated and proved to be an effective catalyst guiding the growth of not only aligned ZnO nanowires, but also the hierarchical nanowire-nanoribbon junction arrays and nanopropeller arrays. During the vapor-liquid-solid (VLS) catalyzing growth process at high temperature, Sn in the liquid state has been proved to be able to guide the growth of nanowires and nanoribbons in terms of growth directions, side facets, and crystallographic interfaces between Sn and ZnO nanostructures.

Secondly, using pure ZnO as the only source material, by precisely tuning and controlling the growth kinetics, a variety of hierarchical polar surface dominated nanostructures have been achieved, such as single crystal nanorings, nanobows, nanosprings and superlattice nanohelices. High yield synthesis of ZnO nanosprings over 50% has been successfully obtained by mainly controlling the pre-pumping level associated with the partial pressure of residual oxygen during the vapor-solid growth process. The rigid superlattice nanohelices of ZnO has been discovered, which is a result

of minimization of the electrostatic energy induced by polar surfaces. The formation process of the nanohelix has been systematically characterized.

Thirdly, two new strategies have been successfully developed for fabricating ZnO quantum dots and synthesis of ZnO nanodiskettes and nanotubes. The formation process is based on a common concept of self-assembly.

Finally, a series of devices and applications based on several piezoelectric ZnO nanostructures, such as nanobelts, nanopropellers and nanohelices, have been carried out utilizing the electro-mechanical resonance, bio-surface functionalization, device fabrication and electrical characterization. Individual nanobelt and nanohelix based nanodevices have been successfully fabricated for applications in chemical and biological sensing. The study opens a few new areas in oxide nanostructures and applications.

CHAPTER 1

INTRODUCTION

1.1 One-dimensional Metal Oxide Nanostructures

As for the definition of nanostructures, a widely accepted one is that "nanostructure" represents a system or object with at least one dimension on the order of one-hundred nanometer or less. Typical oxide nanostructures are of three types of dimensional categories: 0-dimension, 1-dimension and 2-dimension. 0-dimensional nanostructures such as nanoparticles (quantum dots) and 2-dimensional thin films have been extensively explored and utilized in many applications. In the late 1960s, "whiskers" of the metal oxide nanostructures represented a morphology category with a wire-like shape, and the emergence of the nanoscale science and technology in the last few years brought them into an emerging category of "one-dimensional oxide nanostructures".

Generally, a one dimensional (1D) nanostructure is a material with two physical dimensions in the nano range (1~100 nanometer), while the third one can be very large. Typically four types of 1D nanostructure configurations are reported in literature, including nanotubes[1], nanowires[2,3,4,5], nanorods[6,7,8] and nanobelts (nanoribbon)[9,10,11,12,13]. These nanostructures have potential applications in nanoelectronics, nano-optoelectronics and nanoelectromechanical systems.[3,4,14,15,16,17,18,19,20,21,22,23] Figure 1.1 is a set of four figures representing the four different typical morphologies made by ZnO. Amongst them, nanobelt (nanoribbon) is the newest one being recognized and investigated extensively since its discovery in

2001.[10] By utilizing a dramatically increased surface-to-volume ratio and the novel physical properties brought by the nano-scale structure, nano-scale sensors and transducers with superior performance could be achieved. [24]

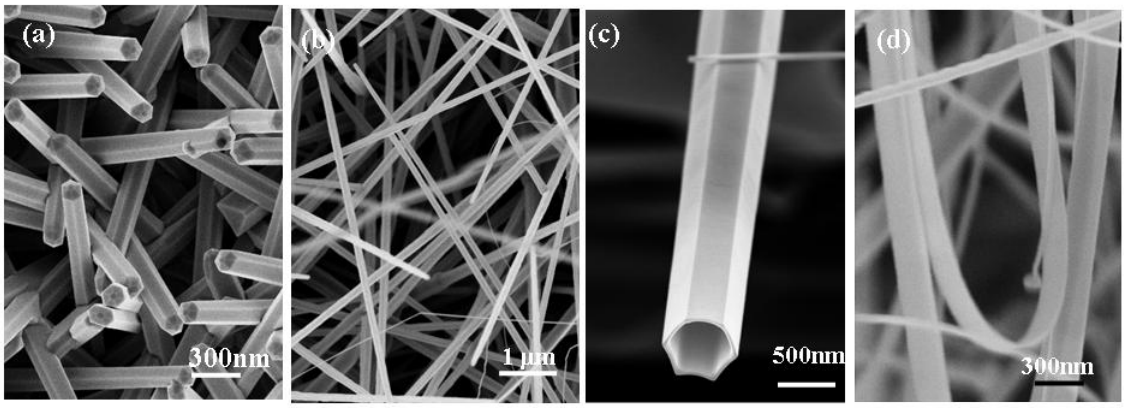

Figure 1.1 Four types of 1D nanostructure configurations made by ZnO: a) nanorods; b) nanowires; c) nanotube; d) nanobelts.

1.1.1 Synthesis Techniques

During the last decade, one-dimensional metal oxide nanostructures have been extensively investigated. Most of the studies have been focused on the synthesis and fabrication of the nanostructures. Typically, two categories of synthesis and fabrication techniques are generally used. One is the so called “bottom-up” techniques using vapor phase deposition, chemical synthesis, self-assembly and location manipulations. The other is the “top-down” approach utilizing the lithography and precision engineered tools like cutting, etching, grinding etc. to fabricate nanoscale objects out of bulk materials. In the bottom-up category, several approaches have been well-established, which include an extensively explored vapor phase deposition method, including chemical vapor deposition (CVD) and physical vapor deposition (PVD), and liquid phase deposition (solution synthesis approach).

1.1.1.1 Vapor Phase Deposition Method

Vapor phase deposition method is the most versatile method for 1D nanostructures synthesis and fabrication in the past few years. Chemical vapor deposition (CVD) and physical vapor deposition (PVD) are two typical vapor phase deposition methods. Both methods can be sub-classified based on the source of energy used, as summarized in Table 1.1.[25]

Table 1.1 Vapor phase deposition techniques for nanostructure fabrication

Vapor phase deposition techniques	Thin film and coatings	One dimensional nanostructures
Physical vapor deposition processes (PVD) (1) Thermal evaporation (2) Electron beam-PVD (3)Sputtering Magnetron sputtering Direct current diode sputtering Radio frequency sputtering (4)Cathodic arc discharge (5) Pulse laser deposition	All fiit	(1) is the most popular method, low cost, pure products, but operation temperature could be very high; (2) Very few use (3) Nanorods synthesis (4) Carbon nanofibres synthesis (5) is used for complex and high melting point compound.
Chemical vapor deposition processes (CVD) (1) Thermal CVD (2) Low pressure CVD (LPCVD) (3) Plasma enhanced CVD (PECVD) (4) Photochemical and laser-CVD (LCVD) (5) Metal-organic CVD (MOCVD) (6) Molecule Beam Epitaxy (MBE) (7) Atomic Layer Deposition (ALD)	All fit	(1)-(3) (4)-(7) are are very suitable for superlattice and core-shell nanostructures fabrications.

1.1.1.1a Physical Vapor Deposition Method

The traditional physical vapor deposition method is dedicated to the thin film and coating technology, which generally rely on the physical vaporization and condensation processes of materials. Based on the source of energy, five typical methods have been developed (Table 1.1[25]). The first one is the “thermal evaporation” process, which generally uses resistor heater in a furnace to heat and facilitate the vaporization of source materials and nanostructure deposition process. This method has been fully developed as

one of the most versatile methods for 1D nanostructure fabrication[4,9-13]. Examples of 1D nanostructures grown by thermal evaporations are rather diverse, including the elemental group such as Si and Ge, the II-VI group (ZnS, CdS, ZnSe, CdSe etc.), III-V group (GaAs, InAs, InP, GaP, GaN, etc.) and semiconducting oxides (ZnO, CdO, PbO, In_2O_3, Ga_2O_3, SnO_2, SnO, etc.). The second type of PVD is the Electron-beam PVD, which has been extensively used for fabrications of ceramic thin film and coatings, but so far no reports has been found for application in 1D nanostructure synthesis.

The third type of method is so called "sputtering processes". Sputtering is the removal of surface atoms due to bombardment from a flux of impinging energetic particles. The consequences of the interaction between an incident particle and a solid surface are mostly dictated by the kinetic energy of the projectile particle, although its internal energy may also play a significant role. Surface diffusion is usually used for explanation of the nanoscale islands or rods growth during the sputtering process. Sputter methods have been utilized for some nanorods synthesis such as W[26], Si[27], B[28,29],CNx[30], etc.

Cathodic arc discharge is another important physical vapor deposition method. It is famous for synthesis of the first batch of carbon nanotubes back to 1993[1,31]. It has been very popular as a method for fabrication of carbon related nanostructures, but there are very few applications in growth of oxide nanostructures.

Pulse laser deposition (PLD)[32] is a developed method for creation of nanostructures back to the seminal work on $YBa_2Cu_3O_{7-x}$ thin film growth by Venkatesan and co-workers in 1987[33]. The process is that the source material is rapidly evaporated from a bulk target in a vacuum chamber by focusing a high power laser pulse on its

surface. A large number of material types have been deposited as thin films using PLD. For some complex and high T_m (melting point) compounds, there is no doubt that using the PLD could be simpler and easier to receive better quality of nanostructures. PLD has been used for synthesis of 1D nanostructures since early 90s in the last century. It has been successfully used in carbon nanotube synthesis[34] with high yield instead of using cathode arc discharge despite of a large amount of impurity. In the past decade, using PLD method, a variety of 1D complex compound and core-shell structured nanostructures have been synthesized [35,36,37]. Outside the auspices of high-performance semiconductor applications, PLD is as promising research tool for investigating new growth phenomena and systems as any other technique, and can offer some unique features.

1.1.1.1b Chemical Vapor Deposition

Chemical vapor deposition (CVD) can be classified into six or more categories regarding the difference of the vacuum control level, heating source and reactants gas types etc., as shown in Table I. Thermal CVD, LPCVD, LCVD, and MOCVD have been used to synthesize several types of nanowires. Using a similar set-up as the thermal evaporation method in PVD approach, thermal CVD just involves chemical reaction during the deposition process rather than a physical evaporation and deposition process. It has produced high quality carbon nanotube[38] and nanowires including GaN[39,40], GaAs etc. Like thermal evaporation in PVD, in thermal CVD, a solid source could be placed upstream. The solid is vaporized through heating, which is transported by a carrier gas that feeds the catalyst and source material for nanowire growth.

LPCVD is a technique for fabrication of thermal oxide layer on semiconductor wafers in electronic industry. This approach uses commercial oven or furnace as a main reaction chamber, which are generally composed of the reactant gas control and supply system and temperature/pressure control system. The pressure control is normally under 0.1 torr. Despite of an old technique for oxide film growth in electronic industry, recently the LPCVD is a successful method for synthesis of various nanostructures such as carbon nanotube[41,42], and Si nanowire[43,44,45], etc.

In Laser CVD, the CVD setup has been modified for laser ablation with controlled doses, leading to a control over nanowire lengths and diameters. Such a precision control made it possible to form superlattices[46] or core-shell[47] structures with doping. MBE has been used to grow 1D nanostructure of III-V group semiconductor compounds such as GaN[48], GaAs[49], InGaAs[42] and AlGaAs[50] etc. ALD seemly has been used for fabrication of templates and ordered core-shell nanostructures[51, 52, 53, 54] due to its precise control on atomic layer-by-layer deposition.

1.1.1.2 Solution-based chemical synthesis methods

As a generic method for synthesis of nanostructures, chemical synthesis has been a powerful method for producing raw nanomaterials. Since the emergence of one-dimensional nanomaterials, solution based chemical synthesis methods have been extensively explored for fabrication of one-dimensional nanostructures. Many materials such as elemental noble metals Au, Pt, Ag[4], etc., tri- or multi-elemental compounds like $Ba(Sr)TiO_3$[55,56], $LaPO_4$[57], $CePO_4$[58], BaH_2SiO_4[59] etc., in nanowire-like shape have been successfully synthesized via solution based chemical synthesis methods, which can not be

easily fabricated by using vapor phase methods. The 1D nanostructures synthesized by chemical synthesis can be easily achieved in a large yield, but the large amount of impurities usually contained in the products always dramatically hinder its application, although complex post filtering and purification is useful for increasing its purity. From the cost point of view, a low-cost chemical synthesis with high yield undoubtedly is ideal for future commercialization of 1D nanostructure.

1.1.1.3 Conjunctional methods involving lithography patterning

As described above, almost all of the techniques associated with the traditional thin film and coating processing have somehow successfully found applications in fabrication of 1D nanostructure. Lithography is a key technology in semiconductor industry for processing devices and circuits at wafer level in a designed sequence. It involves the feature patterning on a surface through exposure to a variety of sources such as light, ions or electrons, and then a subsequent etching and/or deposition of materials to produce the desired devices. The ability to pattern features in the nanometer range is a key to the future nanoelectronics.

Figure 1.2 is a diagram showing the convergence of the top-down and bottom-up production techniques. It is worth noting that there is an overlapping area between top-down and bottom-up approach since late 1990s in the extrapolated area. Then hybrid methods combining both approaches should be desired techniques in the future. To date, more and more effort have been put together for using the conjunctional synthesis methods to fabricate hierarchical or ordered building blocks of nanomaterials. An impact example can go to the development of soft-lithography technique, which has taken the

advantage of both the improved understanding of self-assembly and nanolithography process.

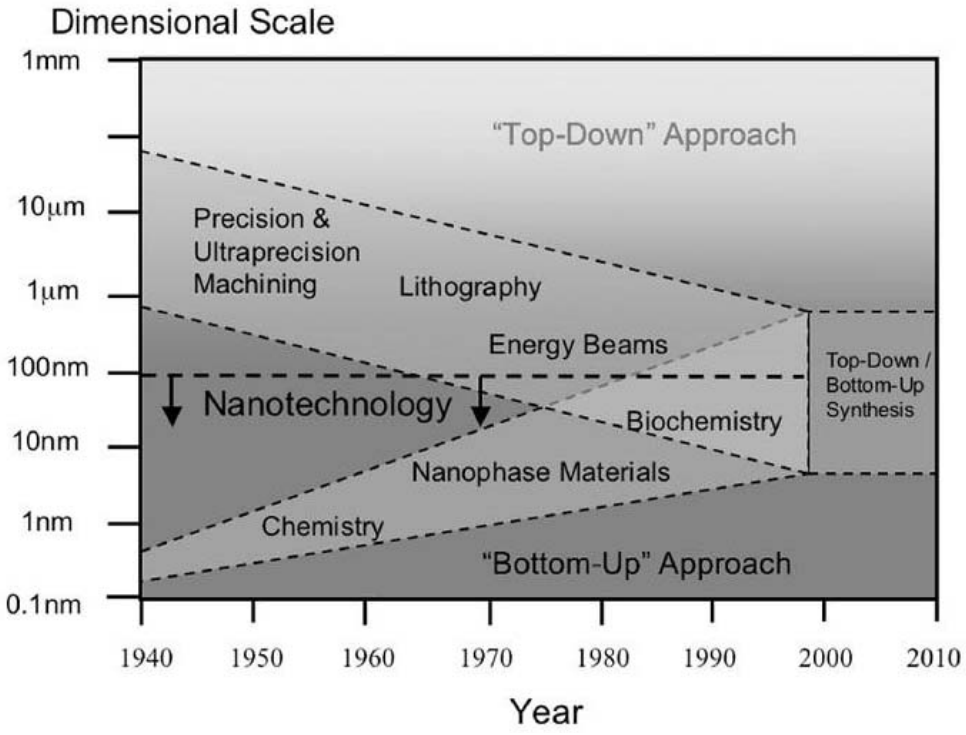

Figure 1.2 A schematic diagram showing the convergence of the top-down and bottom-up approaches.

Currently most of conjunctional synthesis methods utilize the lithography patterned substrate for catalysts patterning or selective modification purpose. It has been reported that by taking advantage of self assembled gold or Ni patterning, patterned growth of carbon nanotubes[60], arrays of ZnO nanowire, GaN, AlGaN etc. for 2D photonic crystal applications have been successfully achieved. By utilizing the brownian motion of nanowires in fluids and also the lithographical microfluidic channels on the deposition substrate, the positional aligned nanwires arrays along the microfluidic channels can be obtained at a large scale. Using the same strategy, a large scale cross-bar

arrays[61] of nanowires with a certain robustness and repeatability for nanocomputing have been successfully achieved for nanocomputing test and measurement.

The growth of patterned and aligned one-dimensional nanostructures is important for applications in sensing, optoelectronics, and field emission. Several groups have successfully achieved the aligned growth of ZnO nanorods and nanowires on a sapphire substrate via the VLS process with the use of Au as catalysts, which initiate and guide the growth. The epitaxial orientation relationship between the nanorods and the substrate leads to aligned growth.

Ren et al. and Wang et al. have reported the conjunction of the self-assembly-based mask technique with the surface epitaxial approach to grow large-area hexagonal arrays of aligned carbon nanotubes and ZnO nanorods. As shown in figure 1.3 is a series of SEM images illustrating the synthesis process for ZnO nanorod arrays. Three main steps are involved. The hexagonally patterned ZnO nanorod arrays are grown on a single-crystal Al_2O_3 substrate on which patterned Au catalyst particles have been dispersed. First, a two-dimensional, large area, self-assembled and ordered monolayer of submicron polystyrene spheres is introduced onto the single-crystal Al_2O_3 substrate (figure 1.3a). Second, a thin layer of Au particles is deposited onto the self-assembled monolayer; the spheres are then etched away, leaving a patterned Au catalyst array (figure 1.3b). Finally, nanowires are grown on the substrate using the VLS process (figure 1.3c). The spatial distribution of the catalyst particles determines the pattern of the nanowires. This step can

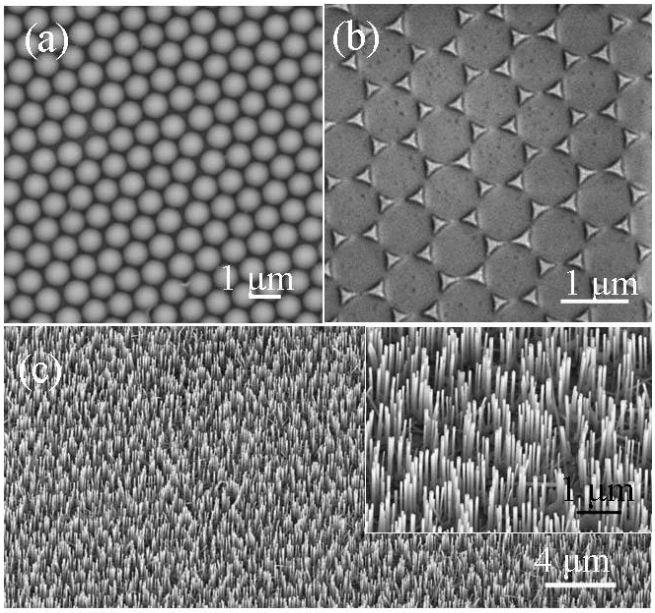

Figure 1.3 A series of SEM images illustrating the synthesis process for ZnO nanorods array involves three main steps.

be achieved using a variety of mask technologies for producing complex configurations. The key is to choose the optimum match between the substrate lattice and the nanowires, for which the epitaxial orientation relationship between the nanowire and the substrate results in the aligned growth of nanowires normal to the substrate. The distribution of the catalyst particles defines the location of the nanowires, and the epitaxial growth on the substrate results in the vertical alignment.

In the mean time, some researchers have been working on the conjunction of vapor phase deposition, chemical synthesis and lithography techniques for synthesis of hierarchical building blocks of functional materials for nanodevice applications.

1.1.2 One-dimensional Metal Oxide Nanostructures

Metal oxide is one of the most important functional material candidates for chemical and biological sensing and transduction. Its unique and tunable physical properties have made itself an excellent candidate for electronic and optoelectronic

applications. As a result, nanostructures of metal oxides have emerged as a frontier field in advanced science and technology since the microelectronics revolution in 1970s; as the thin film technology has been comprehensively developed and pushed to commercialization for ultra-large scale integrated circuits (ULSI).

Now in the early 21st century, one-dimensional metal oxide nanostructures have become a major research topic in the current nanoscience and nanotechnology. As described in the introduction, three typical morphological configurations have been clearly defined: wire-like, tube-like and belt (ribbon)-like nanostructures. Metal oxide nanowires, nanotubes and nanobelts are fascinating groups of materials that have enormous potential for novel applications. Electronic applications include transistors[62,63,64,65], chemical sensors[66,67,68], biological sensors[69], integrated circuits[70,71] and logic devices. NEMS, or nanoelectromechanical systems, and optical devices such as photonics, LEDs, and lasers are also possible. For these purpose, one-dimensional metal oxide nanostructures will function as the most important category of building blocks. The rational control and hierarchical fabrication of these building blocks so far are still challenging. In this section, a brief review is given about the rational control and hierarchical synthesis of one-dimensional metal oxides nanostructures involving the bottom-up self-assembly and top-down physical assembly processes.

1.1.2.1 Oxide Nanowires

For synthesis of nanowires, the bottom-up synthesis is the most cost-effective means for producing nanowires in large quantities. Nevertheless, randomly oriented assemblies of nanowires have been a hindrance for massively parallel device applications. To meet the requirement of massive production and integration, hierarchical

and ordered nanostructure consisting of a large number of individual nanowires is an optimum choice. To date, the invention and development of techniques such as microfluidics, field driven self-assembly, and template-confined growth have led to successful creations of alignment and architecture assembly of various nanowires.

Quite a lot reports on the metal oxide nanowires such as ZnO, In_2O_3[72], SnO_2[73], SiO_2[74] etc., have been seeking the rational and controllable synthesis of these functional nanoscale materials. Generally, there are mainly two strategies for achieving the alignment of 1D nanostructures. One approach is to use patterned catalysts to grow oriented nanowires epitaxially on substrates with matched lattices. The other is to use arrays of nano-channels on substrates such as Porous Anode Alumina Membranes (PAAMs) as templates for growing metal oxide nanowire arrays[75]. The other strategy is to physically manipulate or assemble the randomly distributed nanowires into ordered and patterned forms using external fields such as electric, magnetic and hydro force.

A typical example of aligned growth is for ZnO, one of the most important metal oxides for electronic and optoelectronic applications. In 2001, aligned growth of ZnO nanowires on single crystal substrate has been achieved by using thermal CVD method[5]. In the report, the aligned ZnO nanowire arrays were grown on (11-20) sapphire substrates. A 1~3.5 nm thick layer of Au was coated on the substrate to function as catalysts. For, photonics applications, some new approaches have been implemented for growing patterned nanowire arrays with surface coating. As mentioned before, using self assembled gold or Ni patterning, patterned growth of carbon nanotubes[76] and ZnO nanowire arrays[77] for 2D photonic crystal applications also have been successfully demonstrated.

It is worth noting that most of nanowires synthesis and fabrication research have been on elemental and binary compound system, there are only a few reports on success of 1D nanostructures of tri-elemental or more complex compounds, even though ternary and complex metal oxides are an important class of oxides for structural and functional applications. For example, the perovskite oxides such as $BaTiO_3$ and $SrTiO_3$ [57, 58] are important ferroelectric materials. So far, it is a challenge to synthesize 1D nanostructures of these materials although $BaTiO_3$ nanowires have been synthesized using a solution based method. Recently, 1D nanostructures of Zn_2SnO_4 has been prepared via a reaction between element Sn, ZnS, and $Fe(NO)_3$ at 1350 °C in a high-temperature tube furnace[78]. $ZnGa_2O_4$ has been synthesized into nanowire shape using thermal CVD method[79].

1.1.2.2 Oxide nanotubes

The tubular structure is of a special and important morphological configuration in nature. Synthetic nanoscale tubular structures have caught great research attention since the discovery of carbon nanotube. In addition to the famous carbon nanotube, some important engineering and functional compounds such as MoS_2[80], MoS_3[81]and BN[82] have been synthesized into tubular structures. Using tungsten-comprised precursors, Al-rich mullite as an important engineering material has been fabricated in tubular shape[83]. GaN, an important blue light emission material, has been fabricated into nanotube arrays using a conjunctional of MOCVD and Thermal CVD, in which ZnO nanowire arrays were taken as the template for growing GaN nanotube arrays[84]. Via combustion assisted chemical vapor deposition method, nanotube arrays of SnO_2 have also been achieved[85], which could be of importance in nanosensing.

Using nanotube, nanobelt, and nanowires as templates, tubular structures can be synthesized for a wide range of materials. Most of these materials have to be inert to the environment, which can be removed later, or can be completely convertible by a chemical reaction. To date, ZnO has been one of the most extensively explored inorganic materials besides carbon in the nanoscale science and technology. Recently there have been quite a few reports about the successfully synthesis of ZnO microscale tubes[86,87], and also some nanotubes [88,89,90,91] with polycrystalline or textured crystal structures.

Chemically, solid ZnO is an ionic bonded crystal. The bonding between cation Zn^{2+} and O^{2-} is so strong that the melting point of ZnO is as high as 1975^{o}C. Zn metal is of a melting point as low as 411^{o}C and can be easily oxidized in air[92]. Both Zn and ZnO have a similar hexagonal crystal structure. A low melting point of Zn and the high melting point of ZnO as well as their hexagonal crystal structures could have given us a great advantage for designing and fabricating various metal-semiconductor core-shell nanostructures and tubular structures[93].

1.1.2.3 Oxide Nanobelts

As inspired by carbon nanotubes, research in 1D nanomaterials is the forefront in nanotechnology due to their unique electronic, optical, mechanical and chemical properties. For non-carbon based 1D nanostructures, devices have been fabricated utilizing semiconductor nanowires, such as Si and InP. Piezoelectric effect, an important phenomenon that couples electro-mechanical behaviors, appears to be forgotten in nanomaterials research. None of the well-known nanostructures, such as quantum dots and carbon nanotubes, exhibits an intrinsic piezoelectricity. This is an area that remains

to be explored because piezoelectric effect at nano-scale is critical in electromechanical sensors, actuators and resonators.

In 2001, semiconducting oxide nanobelts (nanoribbons) have been discovered, giving rise to a brand new configuration with respect to the nanowire configuration. The nanobelt is a 1D nanostructure that has a rectangular cross-section with well-defined crystal surfaces. As inspired by this discovery, research in functional oxide based 1D nanostructures is rapidly expanding and is becoming a forefront research in nanotechnology. In the past four years, synthesis of belt-like oxide, sulfides, and selenided based 1D nanostructures has drawn a lot of attention due to their unique geometrical structure and functional properties as well as their potential applications as building blocks for nanoscale electronic and optoelectronic devices. It is worth mentioning that a variety of functional nanodevices such as field effect transistors and ultra-sensitive nano-size gas sensors, nanoresonators and nanocantilevers have been fabricated based on individual nanobelts.

ZnO nanobelts, as shown in figure 1.4, are firstly synthesized by simply evaporating the pure commercial ZnO powders at high temperature. They are pure, structurally uniform, single crystalline, and mostly free from dislocations; they have a rectangular crosss-section with constant dimensions along the length. Up to now, the synthesized nanobelt dimension can be controlled with width of 5~500 nm, thickness of 3~400 nm, length of up to millimeter scale.

By adjusting the raw materials with the introduction of impurities, such as In and Ga, we have synthesized a nanoring structure of ZnO, which is of a perfect circular and uniform shape of the complete ring with flat surfaces (figure 1.5). Detailed microscopy

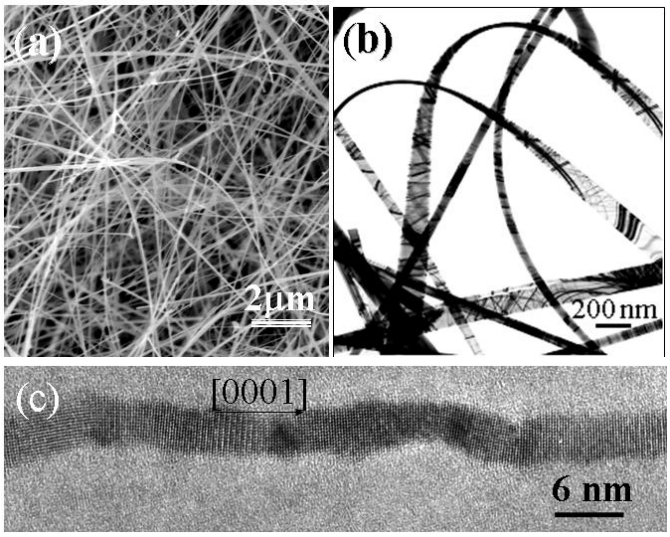

Figure 1.4 A series of SEM images illustrating the synthesis process for ZnO nanorods array involves three main steps.

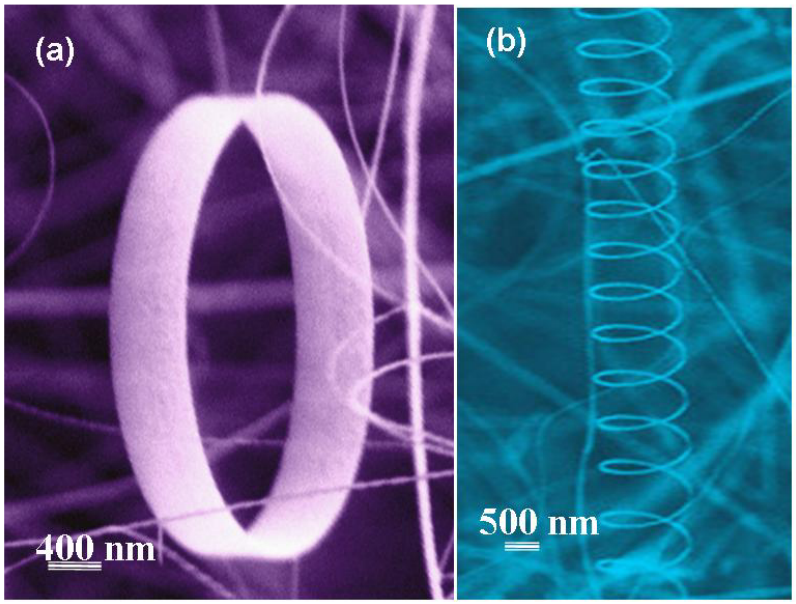

Figure 1.5 A perfect seamless single crystal nanoring structure (a) and nanospring structure (b).

study showed that the nanoring of ZnO is a single crystal polar nanobelt that is bent evenly at the curvature of the nanoring. The polar nanobelt is of a typical width of ~15 nm and thickness of ~10 nm, leading to a nanoring ~10 nm thick, 100 nm~1 μm high and with a radius around 2 μm. The forming of nanoring is resulted from the coaxial,

uniradius, epitaxial coiling of a polar nanobelt. The growth of nanoring structure is a process of self coiling of nanobelt with a spontaneous force balance in between elasticity, electrostaticity and surface tension. Calculations showed that the spontaneous self-coiling process is due to the small ratio of the thickness of nanoring to the curvature of the nanoring and the electrostatic interaction (inverse-charge sign identity of stacking polar surfaces (± (0001)) of nanobelt).

We have recently synthesized ZnO nanobelts that are dominated by the (0001) polar surface (figure 1.6). The nanobelt grows along [2110] (the a-axis), with its top/bottom

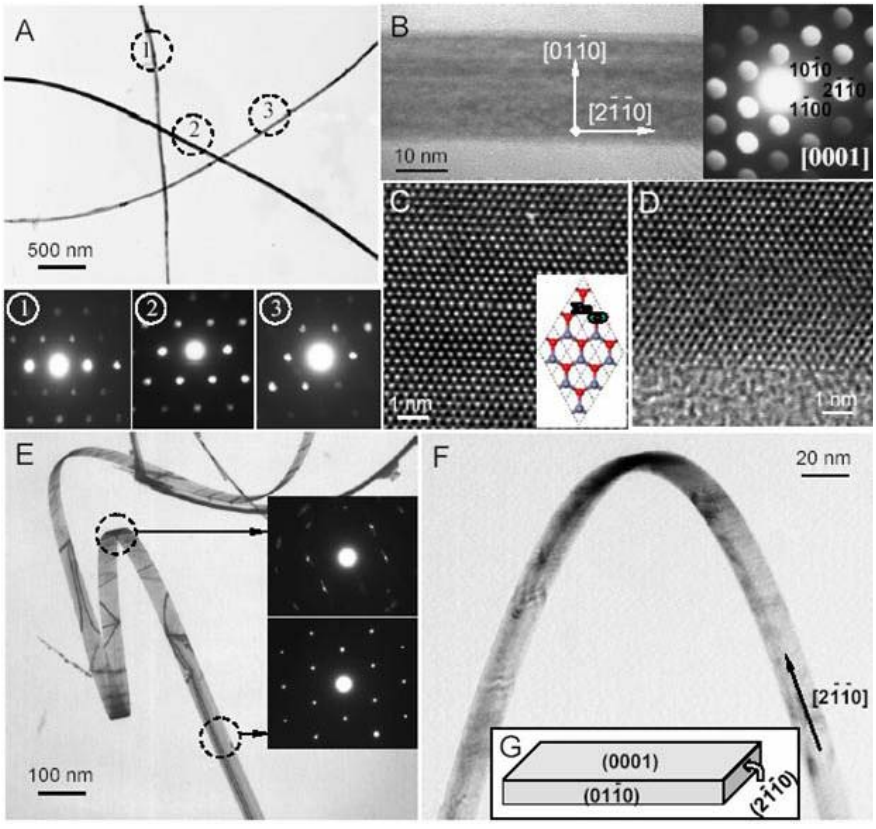

Figure 1.6 Structure characterization of polar surface dominated ZnO nanobelts.

surfaces ± (0001) and the side surfaces ± (0110). The dimensions are around 5-20 nm thick, with aspect ratio of ~1:4, leading to an extremely high flexibility and toughness. The formation of the nanorings and nanohelixes can be understood from the nature of the polar surfaces similar to the nanoring case. If the surface charges are uncompensated during the growth, the spontaneous polarization induces electrostatic energy as a result of the dipole moment. But rolling up to form a circular ring would minimize or neutralize the overall dipole moment, reducing the electrostatic energy. On the other hand, bending the nanobelt produces elastic energy. The stable shape of the nanobelt is determined by the minimization of the total energy contributed by spontaneous polarization and elasticity. If the nanobelt is rolled uniradially loop-by-loop, the repulsive force between the charged surfaces stretches the nanohelix, while the elastic deformation force pulls the loops together; the balance between the two forms the nanohelix/nanospring shown in figure 1.5. The nanohelix has a uniform shape with a radius of ~500-800 nm and evenly distributed pitches. Each is made of a uniformly deformed single-crystal ZnO nanobelt. In all, the nanorings and nanohelixes of single-crystalline ZnO nanobelts are spontaneous-polarization-induced structures, the result of a 90° rotation in polarization.

1.2 Piezoelectricity of Zinc Oxide

Zinc oxide is an important semiconductor compound with piezoelectricity. As a semiconductor, it has a typical wide band gap (3.37 eV) and a large excitation binding energy (60 meV), and exhibits near-UV emission and transparent conductivity. In this

section, a brief review will be focused on the origin of piezoelectricity and the piezoelectricity measurement of ZnO nanobelts using atomic force microscopy.

1.2.1 Orgin of Piezoelectricity of ZnO

ZnO could be of three types of crystal structures: wurtzite, zinc blende, or rocksalt (NaCl). The wurtzite structure is the natural form of ZnO. As shown in figure 1.7 is the crystal structure of wurzite structured ZnO, which has a hexagonal unit cell with two lattice parameters a, c respectively equal to 0.3249 and 0.52049 nm, belonging to space group $P6_3mc$. Wurtzite structured ZnO is composed of two alternating layers of atoms respectively corresponding to cation Zn^{2+} and anion O^{2-} , which are tetrahedrally bonded to each other. Inevitably it is of a non-central symmetry, resulting in the existence of spontaneous polarization along its c axis.

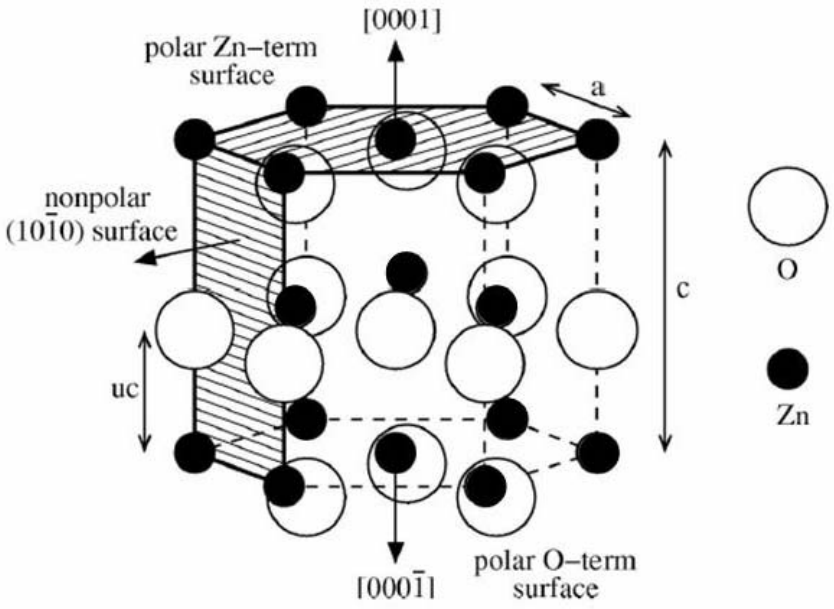

Figure 1.7 Crystal structure model of Wurzite ZnO.

To illustrate the piezoelectricity, one considers an atom with a positive charge that is surrounded tetrahedrally by anions (Figure 1.8a). The center of gravity of the negative

charges is at the center of the tetrahedron. By exerting a pressure on the crystal along the cornering direction of the tetrahedron, the tetrahedron will experience a distortion and the center of gravity of the negative charges will no longer coincide with the position of the positive central atom, an electric dipole is generated. If all of the tetrahedra in the crystal have the same orientation or some other mutual orientation that does not allow for a cancellation among the dipoles, the crystal will have a macroscopic dipole. The two opposite faces of the crystal have opposite electric charges.

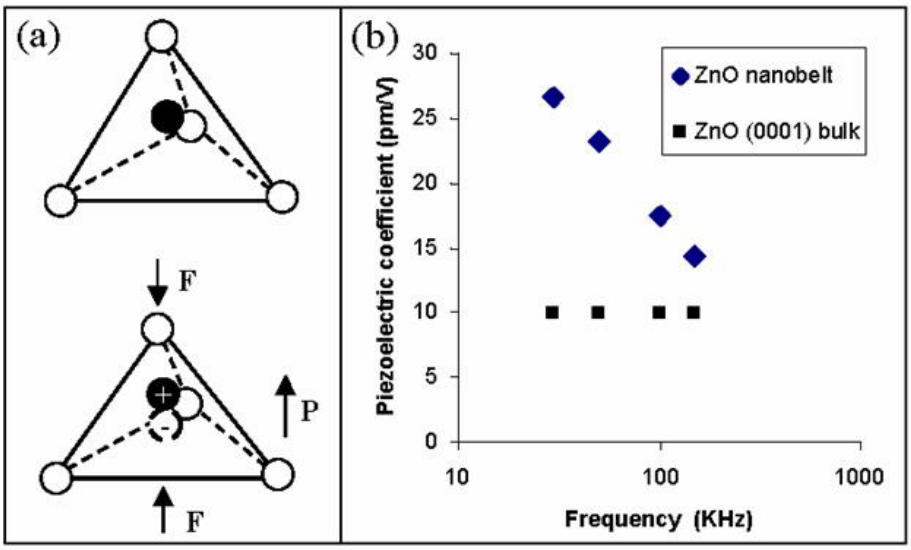

Figure 1.8 (a) Schematics showing piezoelectric effect in tetrahedrally coordinated cation-anion unit. (b) Experimentally measured piezoelectric coefficient d_{33} for ZnO and its comparison to that of the bulk.

Among the tetrahedrally bonded semiconductors, ZnO has the highest piezoelectric tensor or at least one comparable to that of GaN and AlN. This property makes it a technologically important material for many applications, which require a large electromechanical coupling. The piezoelectric tensor has three independent components in hexagonal wurtzite phase and one (e_{14}) in the cubic zinc-blende phase, which characterize the full piezoelectric tensors of such crystals. Two of these

components in wurtzite phase measure the polarization induced along the *c* axis, at zero electric field, by a uniform strain either along the *c* axis or in the basal plane. The relevant relationship is

$$P_z^{piezo} = e_{33}\varepsilon_z + e_{31}\varepsilon\_$$

where ε_z and ε_are the strain along the *c* axis and in the basal plane, respectively. e_{33} and e_{31} are the piezoelectric coefficients. The third independent component of the piezoelectric tensor, e_{15}, describes the polarization induced by a shear strain which is usually neglected for simplicity. The sign of the piezoelectric tensor is generally fixed assuming that the positive direction along the *c* axis goes from the cation to the anion.

Structurally, due to the three types of fastest growth directions: <0001>, <$01\bar{1}0$> and <$2\bar{1}\bar{1}0$> as well as the ±(0001) polar surfaces, ZnO nanostructures exhibit a long gallery of polar surface dominated morphologies including combs, springs, rings, bows and propellers etc. Therefore, the polar surface induced ZnO nanostructures could see potential applications in electro-mechanical coupled devices such as sensors, transducers and resonators.

1.2.2. Piezoelectricity of ZnO polar nanobelts

Piezoelectricity of ZnO is due to the atomic scale polarization. The piezoelectricity refers to a reverse process in which a contraction or elongation is created to the crystal once it is positioned in an electric field. Crystals can only be piezoelectric if they are non-central symmetric to ensure the non-compensation among the dipoles created by the tetrahedra. Piezoelectric effect can convert a mechanical vibration into an electric signal or vice versa.

It is widely used in resonators, controlling tip movement in scanning probe microscopy, sensors for vibration waves in air and under sea etc.

Piezoelectricity is different from ferroelectricity or ferromagnetism. Ferroelectricity is originated from electric dipole moment induced by the spontaneous polarization of the crystal, and ferromagnetism is based on atomic magnetic moment induced by electron spin. Ferroelectricity and ferromagnetism have many common characteristics, such as domains and hysteresis loops. If the dipoles can be canceled each other by the randomly oriented ferroelectric domains, the material does not exhibit a macroscopic dipole. It is called paraelectric. If these dipole domains cannot be canceled out with each other, the residual dipoles will add up, forming a macroscopic dipole, which is the ferroelectricity. Piezoelectricity, however, is originated from the polarization of the tetrahedral coordinated unit and it is a crystal structure determined effect. In nanometer scale, ferroelectricity and ferromagnetism may be greatly reduced or vanished, but piezoelectricity preserves with a possibility of enhanced performance due to the free boundary for volume expansion/contraction.

The piezoelectric coefficient of ZnO nanobelt has been measured by atomic force microscopy using a conductive tip.[94] After coating (100) Si wafer with a 100nm Pd, ZnO nanobelts were dispersed on the conductive surface. Then the whole surface was coated with another 5 nm Pd coating, which served as an electrode on ZnO nanobelt to get uniform electric field and avoid electrostatic effect. Extra care was taken to ensure that top and bottom surface of the nanobelt was not short circuited after Pd deposition. The ZnO nanobelt was located by a commercially available AFM under tapping mode. Piezoresponse force microscopy (PFM) is used to measure the effective piezoelectric

coefficient (d_{33}) of individual (0001) surface dominated zinc oxide nanobelt lying on conductive surface. Based on references of bulk (0001) ZnO and x-cut quartz, effective piezoelectric coefficient d_{33} of ZnO nanobelt is found to be frequency dependent and varies from 14.3pm/V to 26.7pm/V (Figure 1.8b), which is much larger than that of the bulk (0001) ZnO of 9.93pm/V. The results project the applications of ZnO nanobelts as nanosensors and nanoactuators.

1.3 Nanowires and Nanobelts for Sensing Application

Nanowires and nanobelts as the sensing probe for chemical and biological species detection are drawing more and more attention for their potential application not only in electronics and optoelectronics, aerospace engineering, but also in environment protection and biomedical healthcare. Nanowire and nanobelts sensors have several significant advantages over the other macroscopic counterparts. First they could be made potentially smaller, more sensitive, less-power consumptive with shorter response time. Secondly, for integration points of view, arrays or hierarchical organization of nanowire sensors could achieve nanoscale spatial resolution, which would provide accurate real-time information regarding not only the local species concentration, but also its spatial distribution.

Currently, nanowires and nanobelts sensors function based on three categories of signals. One is the reversible conductivity variation of the nanostructure upon absorption of the agent to be detected; the other two detection methods include mechanical mass sensing and optical detection. In terms of reversible conductivity change, the result-in

increased sensitivity and faster response time of nanowires and nanobelts are attributed to the large surface-to-volume ratio, and the small cross-section available for conduction channels. In the bulk, on the other hand, the abundance of charges can effectively shield external fields, and the abundance of material can afford many alternative conduction channels. Therefore a stronger chemical stimulus and longer response time is necessary to observe changes in the physical properties of a 3D sensor in comparison to a nanowire or nanobelt.

Mechanical mass sensor is based on the principle of mechanical resonance phenomena upon excitation of an alternating electric field, for which foreign molecules detection is due to a detectable small amount of frequency shift compared to the intrinsic mechanic beam resonance frequency after loading of a trivial amount of foreign chemical or biological species onto the mechanic beam, for which the frequency shift will be specifically different with respect to different foreign molecules. For this type of sensor, the geometry of nanowires and nanobelts will be a dominant fact for the sensitivity and working frequency range.

Generally, optical detection methods make use of the optical signal variation upon different exposure of foreign species to the sensing probe. The optical signal changes could be in terms of fluorescence properties, color change, and wavelength modulation. Some microwave range mass sensor in fact could be put in the category of optical sensor as well.

In chemical sensing regime, nanobelts have been demonstrated to be able to offer a substantially higher sensitivity than thin film metal oxide sensors. It has been experimentally observed that a SnO_2 nanobelt sensor can detect NO_2 at a concentration

level of 100 parts per billion (ppb)[95] (Figure 1.9). In traditional polycrystalline thin film metal oxide sensors, grain boundaries in the sensing thin films are responsible for degradation and poisoning of the sensor. And the lack of long-term stability has prevented the wide application of these sensors. On the other hand, the nanobelt sensor is highly stable because of its single crystalline structure.

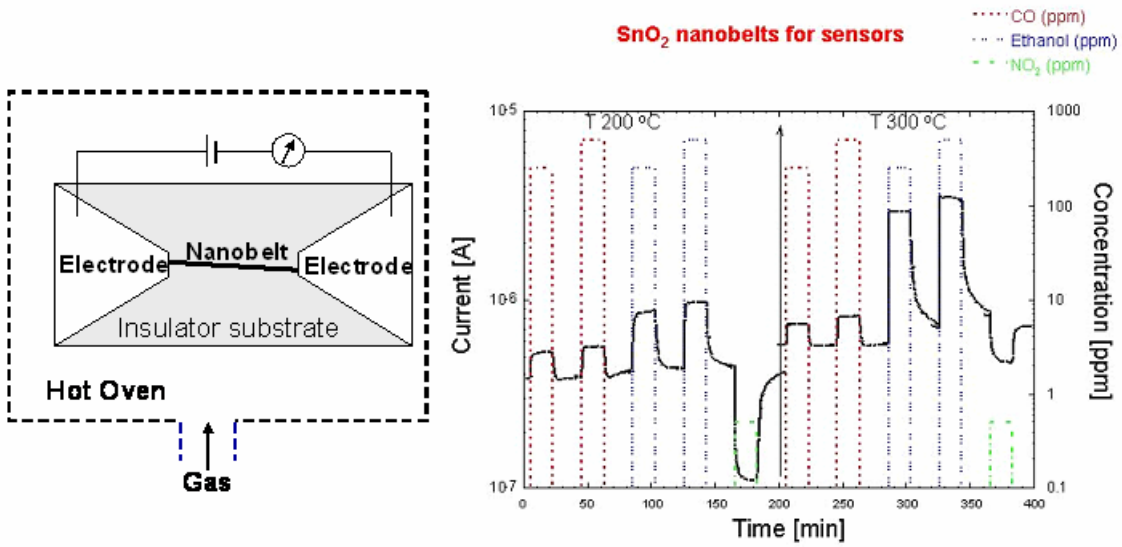

Figure 1.9 Response of a SnO_2 nanobelt sensor to different gases.

In the gas sensor, a flow-through technique is generally used for gas-sensing properties measurement. A constant flux of synthetic air mixed with desired amount (ppm) of test gases electrical conductance, and a proper measure will be taken to ensure the ohmic contact. The gaseous species CH_3OH or volatile sulfuric compounds will flow through a stabilized sealed chamber with controlled temperature, pressure and humidity.

Cantilever-based sensor is a prototype mechanical mass sensor, which has been used as an important approach in measuring nanoscale properties and phenomena. Microfabricated cantilevers are the most conventionally used cantivers with disadvantage

of size limitation. In 2003, using ZnO nanobelt as potential nanocantilver has been demonstrated in the atomic force microscope.[96] By integration between microelectromechanical system technology and self-assembled nanobelts, cost-effective cantilevers with much improved sensitivity could be achieved for a variety of applications such as biological and chemical sensors.

Semiconducting nanobelts are ideal candidates for cantilever applications. Structurally they are defect-free single crystals, providing excellent mechanical properties. The reduced dimensions of nanobelt cantilevers offer a significant increase in cantilever sensitivity. Combining the aforementioned techniques with micromanipulation has led to the horizontal alignment of individual ZnO nanobelts onto silicon chips. The aligned ZnO cantilevers shown in Figure 1.10 were manipulated to have a range of lengths. This exemplifies our ability to tune the resonance frequency of each cantilever and thus modify cantilevers for different applications such as contact, noncontact, and tapping mode atomic force microscopy. Periodic contrast of the ZnO cantilevers is observed as a result of electronic charge–induced vibrations during SEM operation. Such contrast is absent in regions where the nanobelts are in direct contact with the silicon substrate, suggesting adequate adhesion forces between the cantilevers and the silicon chip.

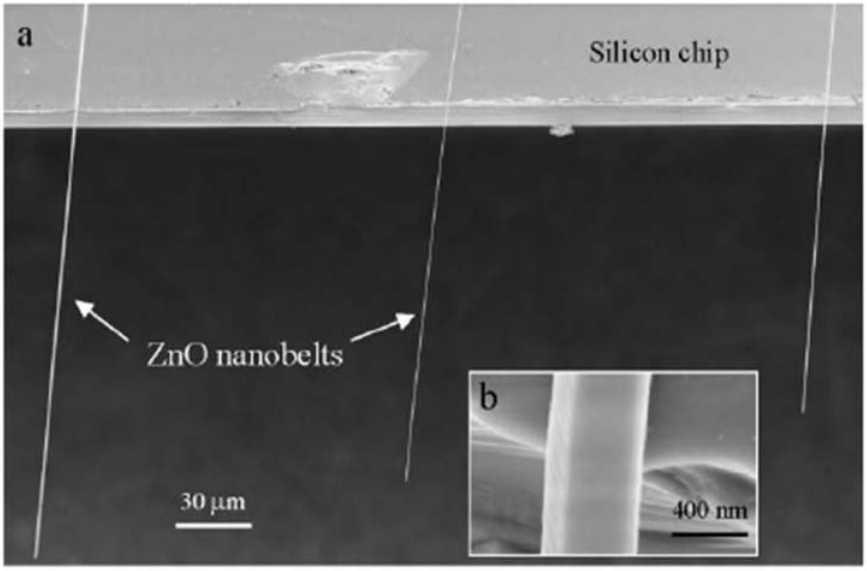

Figure 1.10 Manipulated aligned ZnO belts on Si chip as cantilevers array in atomic force microscope.

Since 1988, biosensors have been comprehended to be "an analytical device that incorporates a biological active material in intimate contact with an appropriate transduction element for the purpose of detecting—reversibly and selectively--- the concentration or activity of chemical species in any type of sample". Generally biological active material has to be survived in aqueous environment, such as specific ions buffered saline in human body, which means the operation of biosensors, has to be in aqueous environment. A fact is that, despite of the most intensively explored methodology developed for solid state sensing, the electrical transport detection in aqueous environment so far is still very challenging due to the high aqueous environment noise. Recently, there have been quite a few examples of using electrical detection methodology for biosensing, even though the life time issue of these devices is of a critical problem.

In 2001, Cui et al. built a two-terminal biosensor using Si nanowires, as shown in figure 1.11.[97] The silicon nanowires made by the VLS method were placed between two

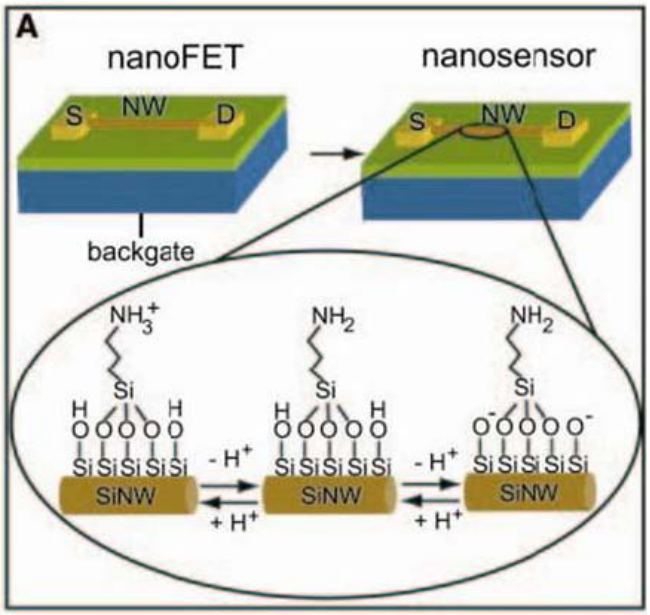

Figure 1.11 Si nanowire as chemical and biological sensor.

metal electrodes and modified the silicon oxide coating of the wire by the addition of molecules that are sensitive to the analyte to be detected. For example, a pH sensor was made by covalently linking an amine containing silane to the surface of the nanowire. The pH variation of the solution into which the nanowire was immersed caused protonation and deprotonation of the $-NH_2$ and the -SiOH groups on the surface of the nanowire. The variation in surface charge densities regulates the conductance of the nanowire. With the p-type characteristics of a silicon wire, the conductance increases with the addition of negative surface charge. The combined acid and base behavior of the surface groups results in an approximately linear dependence of conductance on pH in the pH range 2 to 9, thus leading to a direct readout pH meter. This same type of approach has been used for the detection of the binding of biomolecules, such as streptavidin using biotin-modified nanowires.

Recently, as a result of an instant exploration for nanowire biosensing, Si nanowires[98] and In_2O_3 nanowires/carbon nanotubes[99] have been demonstrated to be able to detect prostate cancer cell-related antigen with a high selectivity and sensitivity. In the Si nanowire case, the selective binding events between the antibody modified Si nanowires and the virus nanoparticles was detected via a distinct electrical conductivity variation happened in different biofluids, leading to a highly sensitive range of detection which might go to single cell or virus particle detection.[100] The biofluids transport pulse was realized by using microfluidic channels. As shown in figure 1.12 is the optical image of the device structure.

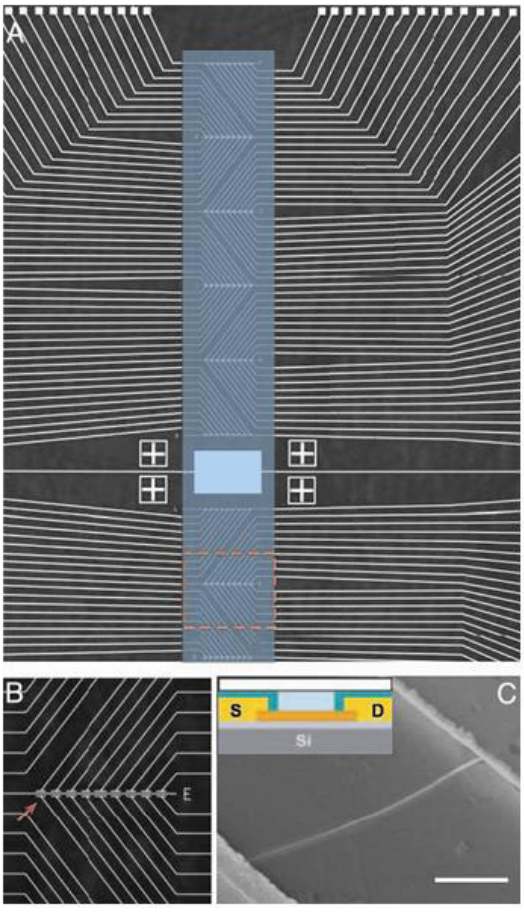

Figure 1.12 Si nanowire biosensor structure for single virus and prostate cancer cell-related antigen detection.

Microfluidics is now rapidly emerging as an enabling technology, having applications ranging from unmanned aerial vehicles to drug discovery and delivery. Given the importance of micro/nano mechanical and fluidic phenomena, it is necessary to understand the fluid mechanics, the heat and mass transfer, the chemistry, the biochemistry and engineering principles on which the design of devices is based. These subjects are essential in understanding the behavior of fluid flow through nano/micro channels.

Experimentally characterizing flow fields at length scales ranging from nanometers to micrometers is crucial in developing both modeling and design capabilities for microfluidics devices such as labs on a chip, microelectronic cooling devices and inkjets. Yet most classical diagnostic techniques for measuring velocity, temperature and concentration in incompressible flows cannot resolve flows at such scales. The leading techniques that are currently being used to characterize flows in channels with dimensions ranging from 10 μm to 100 μm are micro-particle image velocimetry (μPIV) for measuring time-averaged velocity fields and laser-induced fluorescence (LIF) for visualizing mixing. Alternative techniques currently under development include nano-particle image velocimetry (nPIV) for measuring velocity fields within 100 nm of the channel wall and scanning confocal microscopy for measuring bulk velocity fields with less than 1 μm spatial resolution. Finally, new techniques for measuring bulk flow and wall temperature in microchannels emerge based on LIF and Brownian motion.

Originated as a microsampling tool, microfluidic devices have become more and more useful in biomedicine. Typical uses of microfluidics systems include sample

preparation for mass spectrometric analysis, fluid and particle routing, detection and control of chemical reactions, mixing of solutions, and separations. It is ultilized in a number of techniques such as process analysis, environment monitoring, clinical diagnostics, drug delivery, cell culture, cell manipulations, protein analysis, polymerase chain reaction (PCR), DNA sizing, and sequencing.

Anyway, to let nanoelectronics useful in biofluids environment, an integration of microfluidics with nanoelectronics could find a new solution. But the micro/nano mechanical and fluidics phenomena, electrical phenomena and also the electro-mechanical-optical interaction phenomena should be the main scientific issues necessary to be understood before the integration can be achieved in a sense of useful system.

1.4 Targets in the thesis

In this thesis, the material to be focused on is zinc oxide (ZnO), a semiconducting and piezoelectric material. Based on the work that has been done previously with ZnO nanobelts in our lab, we are trying to develop this type of nanostructures into a hierarchical and multifunctional building block for chemical and biological sensing devices. Aiming towards the biosensing application using the nanostructures to be synthesized, three targets are pursued. First is the controllable fabrication of the novel and hierarchical piezoelectric ZnO nanostructures. Second is to explore and understand the physical and chemical insights behind the involved growth phenomena by a variety of characterization techniques from structure characterization to chemical analysis. The third is to probe the device applications of piezoelectric ZnO nanostructures via in-situ

TEM resonance properties measurement, surface functionalization, device fabrication and electrical transport measurement.

CHAPTER 2

EXPERIMENTAL METHODOLOGIES

This research is focused on ZnO, an important semiconductor and piezoelectric material, as has been reviewed in chapter 1. The thesis work will be conducted on three major parts: synthesis, characterization and device application.

For the synthesis, a solid-vapor growth process was used; the specific growth conditions will be described in the relevant chapters. During the experiments, the growth kinetics and chemical reaction kinetics will be controlled via control of a series of controllable parameters; and chemical thermodynamics and physical characteristics of materials will also be involved in the optimization and design for desired nanomaterials synthesis.

Two types of characterization techniques were used in the work: 1, structure characterization and analysis; 2. device fabrication and characterization. The first is mainly for identification of structures and compositions of as-grown nanostructures, leading to an interpretation of physics and chemistry insight involved in the growth process. The second is for application development purpose.

As for the device application part, three stages for applications towards biosening are probed in the current work, which include the surface functionalization, resonance measurement, device fabrication and characterization based on ZnO nanostructures.

2.1 Vapor Phase Synthesis Techniques

In the past four years since the semiconducting oxide nanobelt was discovered, synthesis of belt-like oxide and sulfide based one dimensional (1D) nanostructures has attracted more and more attention due to their unique geometrical structure and functional properties like electrical and optical properties, and their potential applications in building nanoscale electronic and optoelectronic devices. So far most of the belt-like morphological nanostructures are achieved by using the solid-vapor deposition process.

The solid vapor deposition process represents the simplest method for the synthesis of one-dimensional nanostructures. By using this method, various types of 1D oxide nanobelts, such as ZnO, SnO_2, CdO, Ga_2O_3, In_2O_3, PbO_2, and other based nanobelts, such as ZnS, GaN, CdSe and CdS, were successfully fabricated. The set-up of the solid vapor deposition is an equipment shown in Figure 2.1.

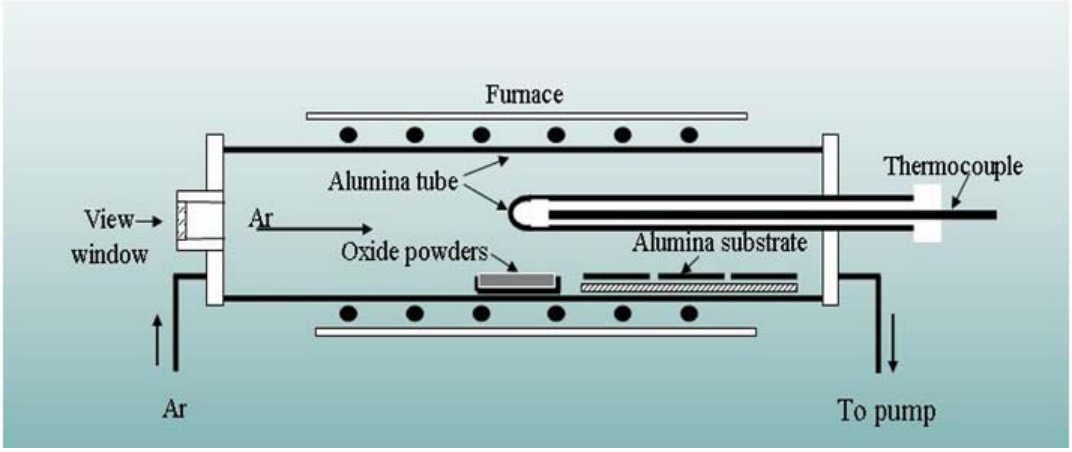

Figure 2.1 Schematic of Experimental set-up for synthesis of ZnO nanostructures.

In figure 2.1, the desired source materials (in the form of powders generally) were placed in the center of a horizontal tube furnace, where the temperatures, gas flow rate, pressure and deposition times were controlled. Before deposition, the chamber was

evacuated to 1~6x10^{-3} torr by a mechanical rotary pump. At the reaction temperature, the source materials were heated and evaporated, the vapor then was transported by the carrier gas such as Ar, to the downstream end low temperature region of the tube, and finally deposited on to either a growth substrate or the inner wall of the alumina tube or quartz tube. So this process consists of two processes, the vaporization of materials at high temperature, and condensation of materials at low temperature. During the process, there could be chemical reaction due to the self-instability (chemically) of materials at high temperature or the involving of reducing agent or catalysts.

For the solid vapor deposition process, the experiments generally were carried out at a high temperature due to the high melting point and low vapor pressure of oxide materials. For example, for ZnO nanobelt synthesis, the ZnO powders need to be heated to ~1400 ^{o}C, which is very high. To reduce the temperature, graphite can be introduced as the vapor-generating agent to reduce the oxide to metal vapor, which can be oxidized soon at low temperature so as to form the nanobelts.

There are a variety of parameters that control the synthesis of nanobelts using the solid vapor deposition. In addition to the basic parameters like temperature, pressure, gas flow rate, and duration time, other special parameters could be introduced for specific purpose for desired synthesis. For example, external fields such as electrical and magnetic can be involved in the synthesis process to get oriented growth of specific nanostructures. And the substrate and chemical composition can be the other alternating factors for different purposes during the growth.

During the syntheses, controlling the parameters in the chamber such as pressure, temperature gradient and gas flow rate, especially the source materials composition, is a key to design and synthesize desired nanostructures.

Two growth modes have been involved in the synthesis of ZnO nanostructures. One is a well-known Vapor-Liquid-Solid growth process, the so-called VLS growth mechanism. The other is a un-clarified Vapor-Solid growth process, namely VS growth mechanism. VLS mechanism has been proposed over four decades. The main point in this process is that a metallic or alloy catalyst such as Au, Ni, Co, Fe etc. has to be involved during the growth. Figure 2.2 shows a schematic classification of these two growth modes. Figure 2.2a shows the schematic growth process involving Au catalyst for Si whisker growth, which was firstly named as a VLS process.

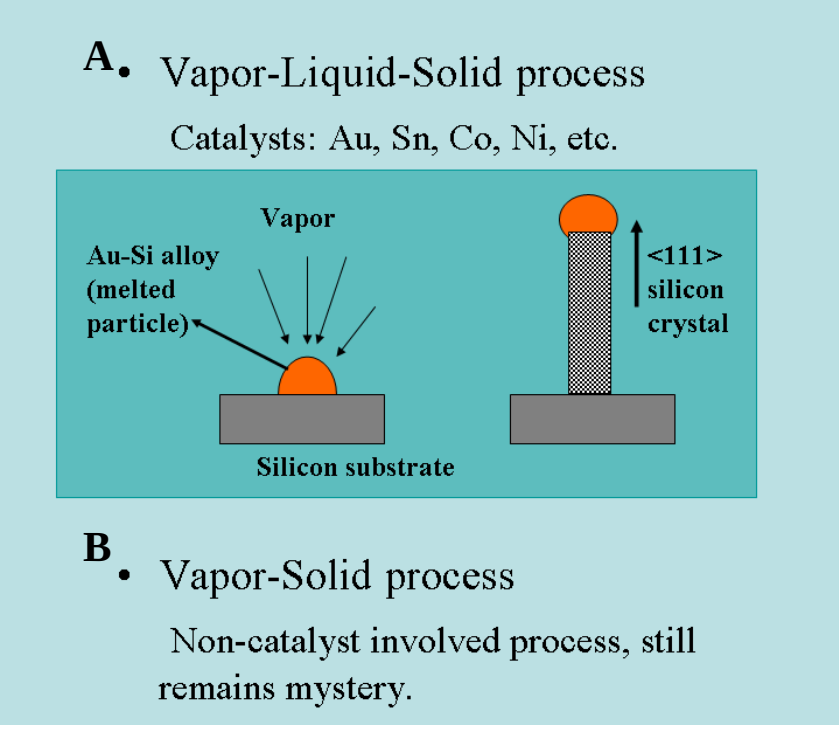

Figure 2.2 Schematic classification of two growth modes: VLS and VS growth.

The process includes three steps: the dissolution of deposition materials **v**apor in the catalysts **l**iquid droplets at local high temperature, saturation and supersaturation of deposition materials in liquid droplets, then precipitation of solid deposition materials along specific direction.

For the nanobelts syntheses, according to the availability of catalysts, it can be classified into two types of growth process: non-catalyst involved deposition and deposition involving catalysts such as Au, Sn, Ni, etc. During the non-catalyst involved deposition, two processes could be involved, one is the self-catalyzed vapor-Liquid-Solid (SVLS) process, the other is a Vapor-Solid (VS) process. When catalysts are involved in the growth process, it could be a VLS process, or combination of VLS and VS processes, even some researchers propose an Oxide-assisted growth process.

In the reaction without involving the catalysts, the nanobelt growth may be controlled by a way that is different from the VLS process. Since no liquid catalysts present in such case, it is likely that the growth is governed by VS process, for example, the formation of ZnO nanobelts by heating ZnO powders at ~1400 ^{o}C, where the oxide vapor directly deposits on the substrate or the inner wall of the alumina (or quartz) tubes. However, recent research results on the polar surface induced asymmetric growth of ZnO nanocantilevers showed that the growth could involve a self-catalyzed VLS process during the cantilever array's formation at the Zn terminated polar surfaces, where the Zn cluster in the growth front likely functions as the catalyst guiding the growth of nanocantilevers.

2.2 Structure Characterization and Analysis

Structure characterization was carried out using a variety of facilities, including scanning electron microscope, transmission electron microscope, etc. Scanning electron microscopy (FE-SEM) (field emission LEO 1530 FEG at 5 & 10 kV) and transmission electron microscopy (TEM) (JEOL 100C, field emission TEM Hitachi HF-2000 at 200 kV and JEOL 400X at 400 kV), and energy-dispersive X-ray spectroscopy (EDS) attached to the SEM and TEM, respectively were used to investigate the morphology, crystal structure and composition of as-grown nanostructures. Transmission electron microscopy is a key tool in this study for structure characterization and composition analysis, in the following paragraphs, a brief introduction on this unique instrumentation will be involved.

As shown in figure 2. 3 is the structure schematic of a typical transmission

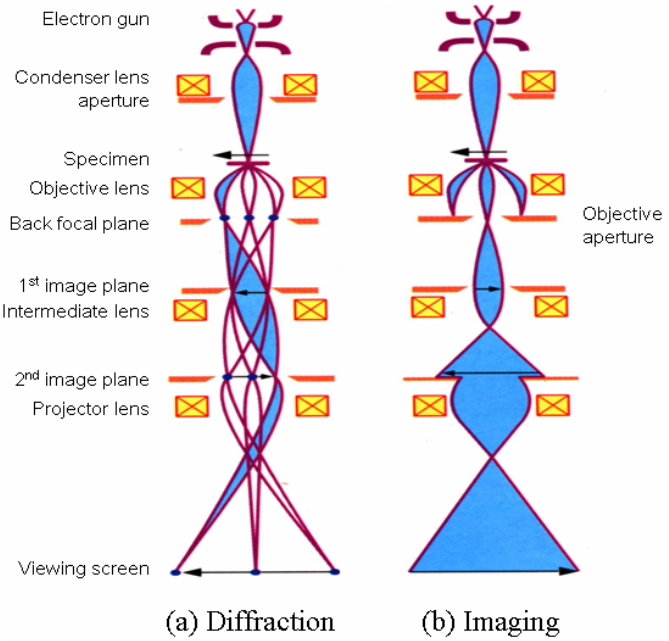

Figure 2.3 Electron column structure and the ray diagram for TEM operated for (a) diffraction mode and (b) imaging mode.

electron microscope together with basic electro-optics involved in two basic modes in TEM: the diffraction mode (figure 2.3a) and the imaging mode (figure 2.3b)

Currently, a typical transmission electron microscope consists of an illumination system, a sample loading stage, an electromagnetic optics system, image recording system and the chemical analysis system, as schemed in Figure2.3. The electron gun is the heart of the illumination system. LaB_6 thermionic emission source or a field emission source could be utilized for electron emission. Field emission source is of high brightness and high coherent electron emission, which is good for high coherence lattice imaging and high spatial resolution microanalysis. The electromagnetic optics system is comprised of the analogized functional lens realized via electromagnetic coils surrounding the column, which will alternate the accelerated electron beam path. The objective lens determines the limit of image resolution. The intermediate lenses and projection lenses give the system ability to magnify the local imaging area on sample to an over million magnification. The data recording system tends to be digital with the use of a charge coupled device (CCD), allowing quantitative data processing and quantification. Finally, the energy-dispersive X-ray spectroscopy (EDS) and electron energy loss spectroscopy (EELS) are capabilities for the chemical analysis system, which can be used to quantify the chemical composition of the specimen. A complementary application of the diffraction, imaging, and spectroscopy techniques available in a TEM is its unique strength to give a precise and reliable determination of the crystal structure and chemistry.

Two types of imaging techniques can be used to tract information: diffraction contrast imaging and phase contrast imaging, which are respectively used for traditional projection morphology imaging of the specimen and lattice structure imaging.

For the case of diffraction contrast, through the contrast amplitude difference from a single beam diffraction interaction with the corresponding specimen area, the imaging information can be obtained in the perspectives of phase variation, thickness variation, defects, bending strain, etc. As for the phase contrast imaging , it is the basis for the lattice structure imaging through imaging mode, which is complementary to the diffraction mode.

2.3 Surface Modification and Functionalization

Zinc oxide is an important resource for human being to obtain a certain amount of Zn, the second most abundant transition metal in the human body, which is vital for biological functions, such as gene expression, apoptosis, enzyme regulation, and neurotransmission. And also the everyday products like sun-proof cream contain a large fraction of ZnO. Billion dollars' business has been set up only based on this kind of everyday product. Anyway, it has been comprehensively noted that ZnO is very beneficial to the human's normal life including maintaining normal metabolism in self-body.

Seemly ZnO is very "biocompatible". However, to enable its function as a device material or functional component in human body, regardless of how it functions, through interaction with human body biofluid, or need of survival in a certain life-time period, ZnO materials have to be tested in different perspectives. For example, it has been known

that normally at room temperature and normal atmosphere, bulk ZnO has a very small solubility of around 1 mg in a liter of water. Since dissolution is a type of degradation in biomaterials, in the nano-scale we have to be concerned about this issue.

Molecular recognition is the most important step in the generation of a sigal (response) by a biosensing system. The specificity and affinity of this step will generally determine the overall device performance regardless of the detection methods employed. The goal of the surface modification and funtionalization in biosensing in fact is to achieve specific molecule recognition components with good enough stability, selectivity and sensitivity.

Therefore, from the functional points of view, as a biosensing building block, ZnO nanostructure employed not only has to be able to survive in biofluid, but has to be of high sensitivity and selectivity in recognizing certain biomolecules via certain types of surface modification. Generally, two types of binding could exist between the to-be-modified surface and the modification molecules: the non-specific binding via physical adsorption, which can be hydrophobic or electrostatic in nature; the other is specific binding via chemical adsorption, which is strong with covalent-bonding. Generally speaking, these two types of bindings could be useful respectively for disposable biosensing and long-life-time biosensing.

In this thesis, two sets of surface modification and functionalization experiments have been designed and carried out. Firstly, based on the polar surface dominated piezoelectric ZnO nanostructures, a great interest is to prove the selectivity of the two (0001) surfaces for different functional groups from the electrostatic force point of view. Furthermore, if it is selective, then different functional groups modified on polar surfaces

will give a tremendous space for further bio-functional group modification. Secondly, for biosensing purpose, ZnO nanostructures are designed to directly or indirectly to attach some certain biological organic species such as saccharides and proteins through physical adsorption and chemical adsorption.

As shown in figure 2.4, a cartoon schematic illustrates the process of the designed selective adsorption of magnetite nanoparticles on two types of polar surfaces in ZnO. Assume the electrostatic interaction between ZnO polar surfaces and NPs is the dominant deposition process, then it will be predicted that a selective adsorption process will happen to functionalize the two polar surfaces with "-" and "+" sign with different functional groups.

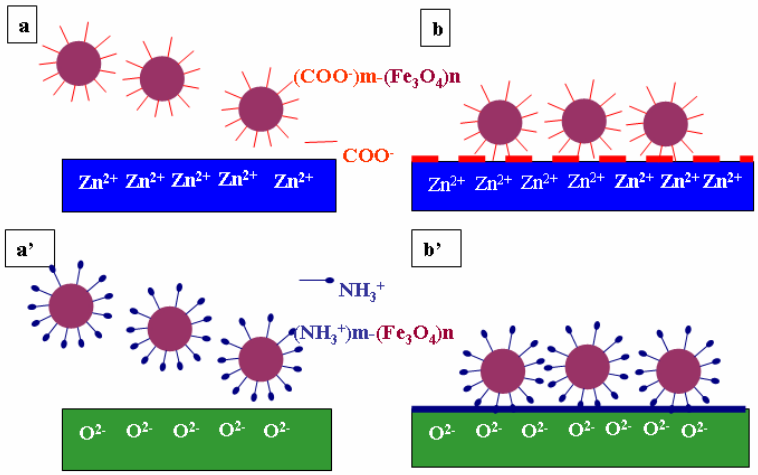

Figure 2.4 Selective charged Fe_3O_4 nanoparticles adsorptions on polar surfaces of ZnO.

For biofunctional group modification experiments, we have designed two types of biosurface functionalization experiments. One is to modify ZnO nanostructures with a stable surface coating via physical adsorption which can be further specifically bonded with certain types of saccharides such as prutose. The other is composed of three

experiments: a). find the suitable biological buffer for ZnO nanostructures to work in b). Silanization of ZnO nanostructures surfaces; c).direct protein attachment such as EYFP, a green fluorescence protein onto ZnO nanostures surfaces.

Physical attachment, silanization, and self-assembly using Langmuir-Blodgett technique represent three of the main methods for biosurface modification on inorganic substrates such as glass and metal oxide. As shown in figure 2.5 is the process of silanization, the most common method for metal oxide surface functionalization.

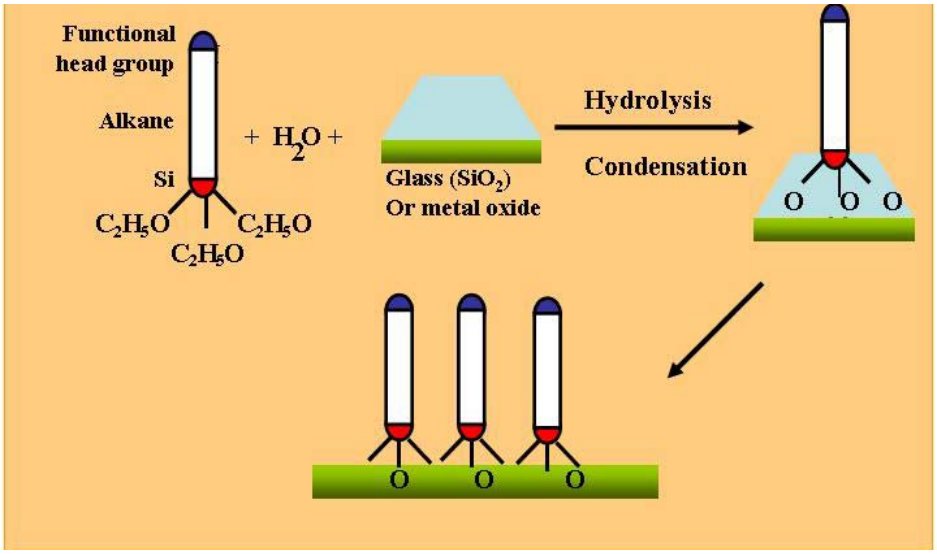

Figure 2.5 Silanization process for glass and metal oxide surface.

Silanization is a standard method which has been well documented. The oxide surfaces can easily be modified with silanes. In the silanization process, the oxide surface is treated with an organosilane containing an organic functional group at the head and an alkoxysilyl group at the tail. The tail alkoxysilyl group will couple with the metal oxide or silanol group on the substrate. The most commonly used silanes are aminosilanes and phenethylsilanes. After this step, a biofunctional linker head group is attached, followed by the coupling of the desired molecular recognition agent such as protein via its

functional groups such as $–NH_2$, -SH etc. to the head group of the silane. Alternatively, the linker silane could be first attached to the desired protein before the silanization.

2.4 Nano-device Fabrication and Characterization

2.4.1 Device design and fabrication

As shown in figure 2.5 is a simplified cross sectional schematic for the nanodevice to be fabricated. Si wafer with (110) orientation is used. The native oxide layer on the Si wafer, thermally growth oxide layer or SiN layer made by plasma enhanced chemical vapor deposition functions as an insulating layer to the two terminal electrodes made of Au or Pt and the bridged ZnO nanobelt across the two terminals. The Si layer underleath the insulating layer could function as the gate terminal upon necessary for field effect transistor measurement purpose, for which the two Au/Pt terminals will be the source and train electrodes. Generally the ZnO nanobelt bridge between the two Au/Pt terminals will be inevitably in contact with the SiO_2 or SiN insulation layer for the basic electronic transport measurement of ZnO nanobelt. Upon biosensing and resonating purposes, the bridged nanobelts or the other nanostructures will be designed to suspend across the two Au/Pt electrodes, leaving an enough space and all the nanostructures surfaces to involve the biosurface functionalization layer and the target molecules, or keep the resonating behavior the origin of the nanostructures themselves. The way to do that is through a microchannel fabrication underneath ZnO nanostructures (for detail, see chapter 6).

Figure 2.6 A simplified cross-sectional schematic of the device structure.

Electron beam nanolithography and photolithography are used to fabricate the silicon based nanodevices using ZnO nanostructures as the sensing materials.

For the microchannels fabrication, transparent silica and Si wafer (110) were chosen as the substrate. Photolithography and focused ion beam lithography were used for microchannels fabrications.

Two dual-beam Focused Ion beam systems (FEI, NOVA 200 and Quanta 30) were used for ion milling and Pt deposition.

2.4.2 Electrical measurement

Electrical characterization will be carried out by a volt-amperometric technique at certain bias with current change measured by picoamperometer. Two-probe electrical measurement method was used for measuring the current-voltage characteristics in terms of different pairs of terminals such as the source-drain, source-gate in the field effect transistor measurement.

As shown in figure 2.7 is a schematic of the electrical measurement circuit setup. An alternating bias voltage with certain frequency (typically 0.001Hz -30MHz in triangle waveform or sine waveform) will be applied across the two Au/Pt terminals. The voltage range will be 0-5V_{p-p}. Upon necessary, a DC voltage will be applied across the Si gate

electrode and one of the Au/Pt terminal as the gate bias. A SRS DS345 synthesized functional generator is used as the voltage source. And the picoammeter we used is the Keithley 6485 5-1/2 digit Picoammeter with 10fA resolution. A voltage divider box is used for providing the protection and voltage bias for the device under test. Another voltage divider box could be set up for the gate bias as well. Labview 7.0 software is used for a computer to acquire digital data via PCI data acquisition board with separate ports respectively connected with the analogue outputs of current and voltage.

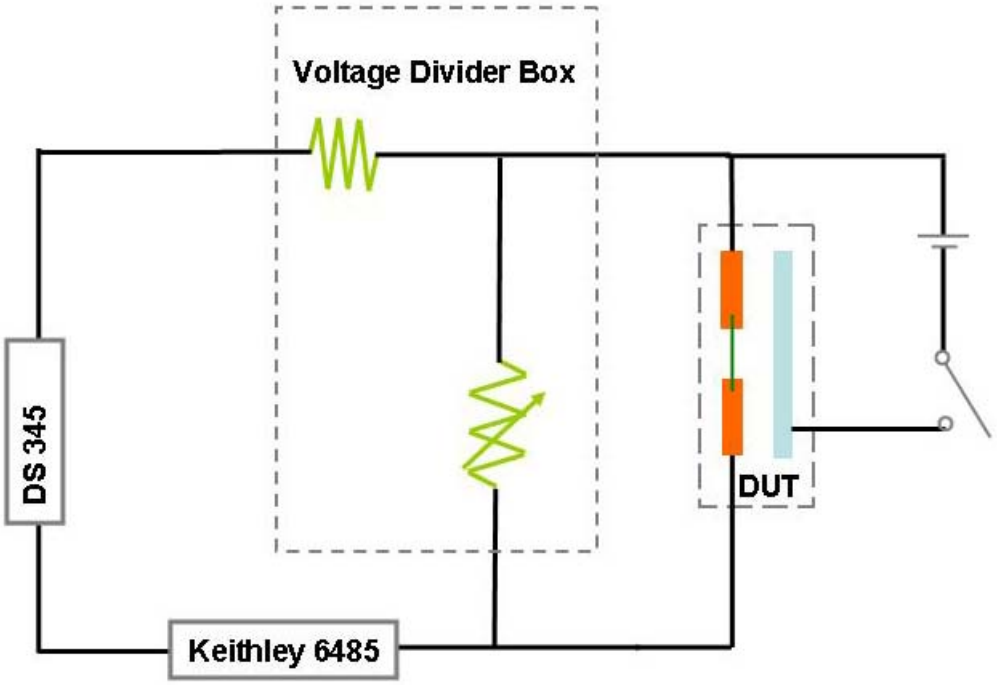

Figure 2.7 A schematic of the electrical measurement circuit setup.

2.4.3 Integration of microfluidics and nanoelectronics for biosensing application

For research on microflows, many of the traditional techniques of measuring fluid behavior have been adapted or replaced due to the small size and the planar format of these systems. For example, integrated probes, such as shear stress sensors and thermal

anemometers, have been developed for measuring gas and liquid flows in microsystems[101]. The integration of the probe directly into the device is attractive because it may facilitate closed-loop control of flows in devices that include both microfluidic and microelectronic elements.

Most other measurements of microflows have been performed with optical microscopes. An adaptation of particle image velocimetry (PIV) known as micro-PIV can yield a spatial resolution of the flow field of approximately one micron[102]. Fluorescence microscopy has also been used to observe microflows. In one variant, a spatially localized pulse from a high-intensity laser is used to generate a fluorophore photochemically in a small volume of fluid in the channel. The advection of this fluorescent volume is observed by fluorescence microscopy in order to visualize the flow profile and speed of the flow[103]. Confocal fluorescence microscopy has also been used to observe the three-dimensional structure of steady flows in microchannels[104].

To probe the piezoelectricity of ZnO polar nanostructures as well as to find biomedical applications of this unique type of nanomaterials, a platform involving both the sensing electrodes together with ZnO piezoelectrical nanostructures and specifically designed and fabricated microfluidic system is to be utilized for the purpose.

As shown in figure 2. 8 is a schematic for the test platform of the integrated devices and testing setup.

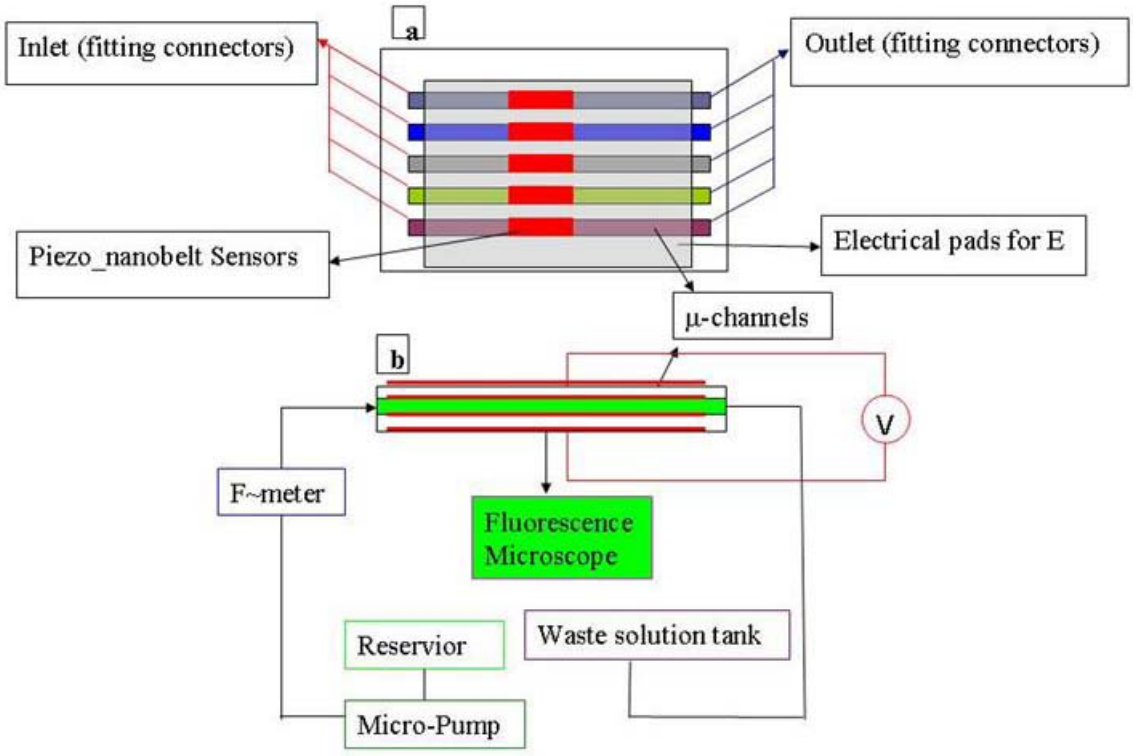

Figure 2.8 A schematic for the test platform of the integrated microfluidic/nanoelectronic device.

The principle of this measuring platform is: ZnO nanostructures (e.g., piezoelectric nanobelts, nanohelices and nanopropellers) as a flow sensor to correlate the biofluid flow rate (pressure or wall shear stress) with the voltage signal induced by the piezoelectric nanoribbons. During the fabrication and testing processes, parameters such as microfluidic channel diameter, microflow rate and pressure will be controlled by precise microfabrication experiments, flow meter (or precise output of micropump) and pressure transducer respectively. In addition, based on this setup, a through and systematic biosensing application study could be conducted by integration of simultaneous real-time biofluidics control and electrical characterization.

The techniques necessary to be used in device fabrication include photolithography and focused ion beam lithography (microfluidic channels), E-beam

nanolithography (sensing electrodes). The characterization tools include the real-time flow monitoring by the syringe pump and the current-voltage measurement via calibrated nanovoltmeter and picoammeter.

CHAPTER 3

HIERARCHICAL NANOSTRUCTURES OF SN-CATALYZED PIEZOELECTRIC ZINC OXIDE

To understand the chemical and physical process involved in the growth of one dimensional nanostructures of zinc oxide is essential for the rational design and control of the synthesis process so as to get desired nanostructures with reasonable yield.

In this chapter, we will focus on the study on Sn-catalyzed ZnO nanostructure, a systematic investigation that has been carried out from two perspectives. One is to improve understanding of the chemical and physical process occurred in the growth of hierarchical nanostructures, i.e., to understand how the Sn functions as a catalyst in a VLS growth process, so as to capture some of the important physical and chemical insights via crystallographic study on the interface between catalyst and the as grown nanostructures.. The other perspective is to design and fabricate desired hierarchical ZnO nanostructures with self-aligned and ordered arrangement.

As shown in table 3.1 is the summary of the experimental conditions for the Sn-catalyzed piezoelectric ZnO nanostructures discussed in this chapter.

Table 3.1 Summary of the experimental conditions for the synthesized Sn-catalyzed ZnO nanostructures.

Parameters / Results	Source (atm%) ($ZnO:SnO_2:C$)	Ar flow rate (sccm)	Pressure (mbar)	Temperature & Duration	Morphologies/ Reproducibility
(1) Crystallographic alignment & Catalytic growth study	2:1:1	20	200	1150 °C × 5, 15, 30 or 60 min	Nanorods & nanobelts/100%
(2) Nanowire-nanoribbon junction arrays	1:1:0	50	400-500	1300 °C × 60 min	Junction arrays/100%
(3) Nanopropeller arrays	3:4:1.5	20 (N_2)	200	1100 °C × 60 + 1300°C × 30 min	Nanopropeller arrays/100%

3.1 Crystallographic-orientation alignment of ZnO nanorods and nanobelts[105]

In synthesis of aligned one dimensional (1D) ZnO nanostructures, catalysts like Au[106, 107], Co[108] and NiO[109] have been introduced in the synthesis process to guide the oriented growth of ZnO nanowires, while aligned growth without catalysis has also been achieved using low temperature Chemical Vapor Deposition (CVD)[110] and ultra-high vacuum deposition technique like Metal-organic Chemical Vapor Deposition (MOCVD)[111,112] and Metal-organic Vapor Phase Epitaxy (MOVPE)[113]. All these involved the VLS growth process via introducing the catalysts.

To find the intrinsic characteristics from the chemical and physical understanding points of view during the VLS growth process, the growth phenomena of aligned ZnO nanorods and nanobelts catalyzed by metallic tin have been detailed investigated for the specific synthesis system of ZnO-SnO_2-C.

A chemical vapor transport process[2,3,114,115,116] was used for synthesis of aligned ZnO nanorods and nanobelts. The experimental apparatus includes a horizontal tube furnace; a rotary pump system and a gas supply system. A mixture of commercial ZnO, SnO_2 and graphite powders in certain ratio (Zn:Sn:C = 2:1:1.) was placed in an alumina boat as the source material and positioned at the center of the alumina tube. To investigate the duration time dependence on the growth of desired nanostructures, deposition processes were conducted at 1150 ^{o}C for 5, 15, 30 and 60 minutes, respectively, under a constant pressure of 200 mbar and an Ar flow rate of 20 sccm (standard cubic centimeters per minute). The entire length of the tube furnace is 50 cm. The desired nanostructures were deposited onto polycrystalline alumina substrates located 21 cm away from the furnace center in a temperature range of 550~600 ^{o}C.

Figure 3.1 is a group of typical SEM images of the as-synthesized nanostructures on an alumina substrate after 5 minutes deposition at 1150 ^{o}C, showing the initial growth characteristics of the desired nanostructure. Micro-size ZnO rods (micro-rods) of irregular side surfaces but uniform-flat (0001) surfaces of ~ 3 μm are formed on the alumina substrate, which sometime show faceted side surfaces (Figure 3.1b). On each micro-rod, there are a number of nanorods oriented perpendicularly to the (0001) plane, as were clearly depicted in Figs 3.1c and 3.1d, which are respectively the top and side view of the oriented ZnO nanorods. At the tip of each nanorod and nanobelt there is a comparable sized Sn ball. The oriented nanorods dispersively distribute on the flat c-plane of the micro-rods with uniform diameters ranging around 20-40 nm and average height about 40-80 nm.

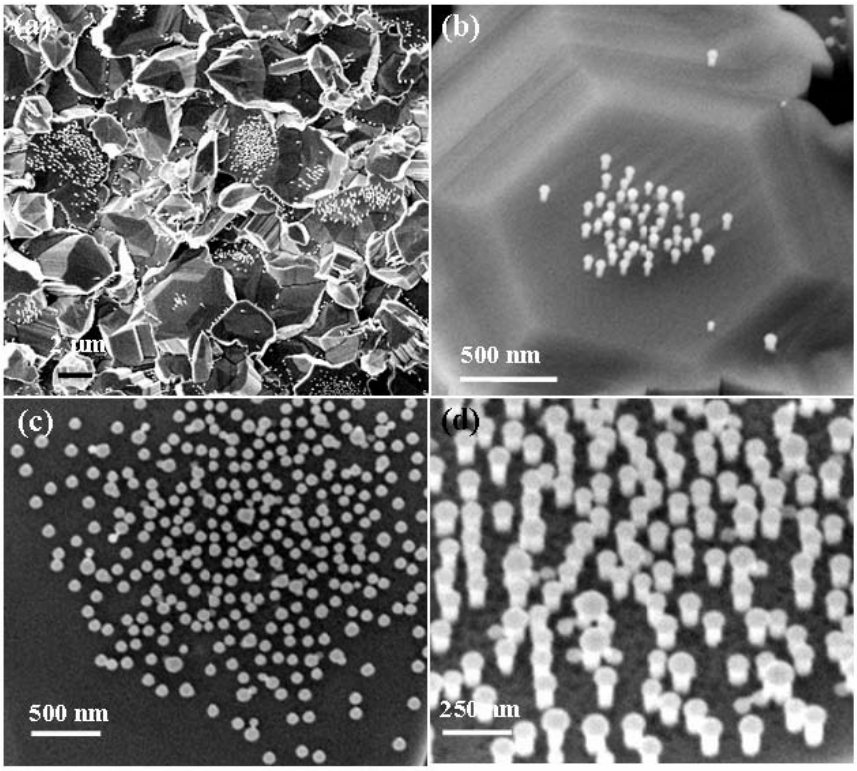

Figure 3.1 Initial growth of oriented nanorods using metallic Sn as the catalyst at 1150 ^{o}C with growth time of 5 minutes. a). Micron-scale ZnO short rods rooted on Al_2O_3 substrate, with aligned nanorods dispersively distributed on the top surfaces of the micro-rods; b). hexagonal faceted ZnO micro-rod with aligned ZnO nanorods on its top (0001) surface; c) and d) are the top and side view, respectively, of the oriented ZnO nanorods on the top of a single crystal micro-rod.

Upon extending the growth time at 1150^{o}C to 15 minutes, it is shown in Figure 3.2 that the oriented ZnO nanorods get longer and some nanobelts growing out of the side surfaces of the micro-rods. Higher magnified picture clearly describes the perpendicular directional growth of the nanobelts (as indicated in the inset in Figure 3.2), where the nanorods have dimensions of 30-50 nm in diameter and 100-200 nm in length, and nanobelts of 10-30 nm in width and 300-500 nm in length.

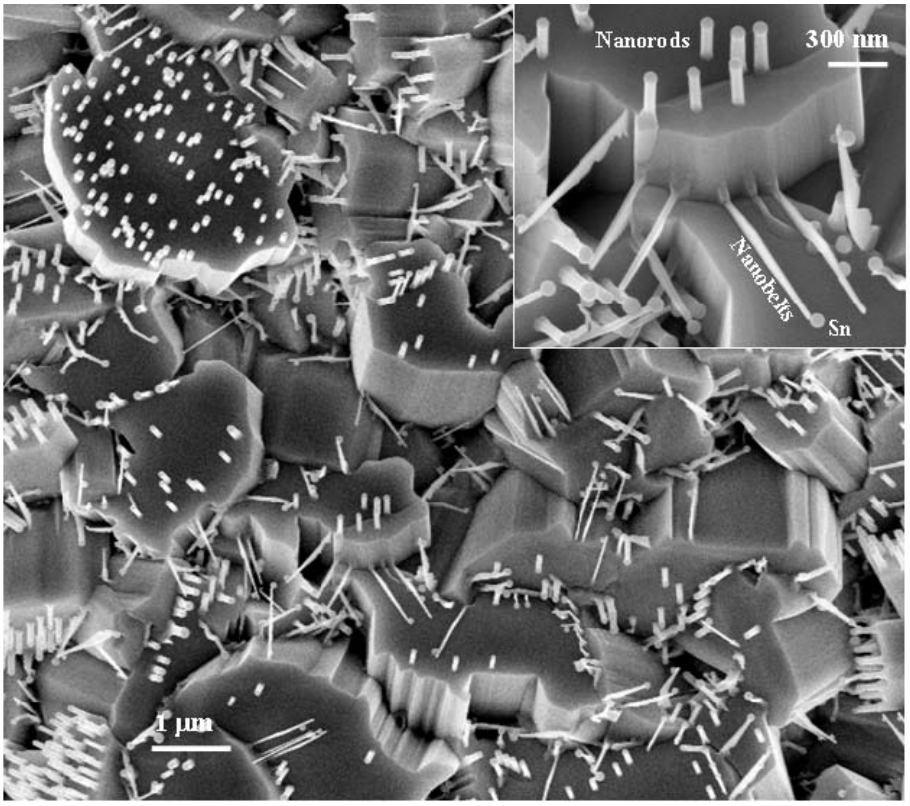

Figure 3.2 ZnO nanorods and nanobelts grown at the top and the side surfaces of the ZnO micro-rods, respectively, after extending the growth time to 15 minutes. Inset is a magnified SEM image.

The data suggest that the diameters of the nanorods are well confined by the size of the metallic Sn ball on the tip, and the growth time has a little influence on the diameter of the nanorods. Figs 3.3a and b give a good description of the oriented growth of the nanorods on the c-plane of the ZnO micron-rods. A closer examination at the root of each nanorod in Figs 3.3c and d shows that each nanorod tends to grow along the same crystallographic orientation as the micron-rod with six parallel faceted surfaces of $\{2\bar{1}\bar{1}0\}$, which indicates an orientation alignment of the ZnO nanorods and a coherent epitaxial relationship with the base ZnO micron-rod.

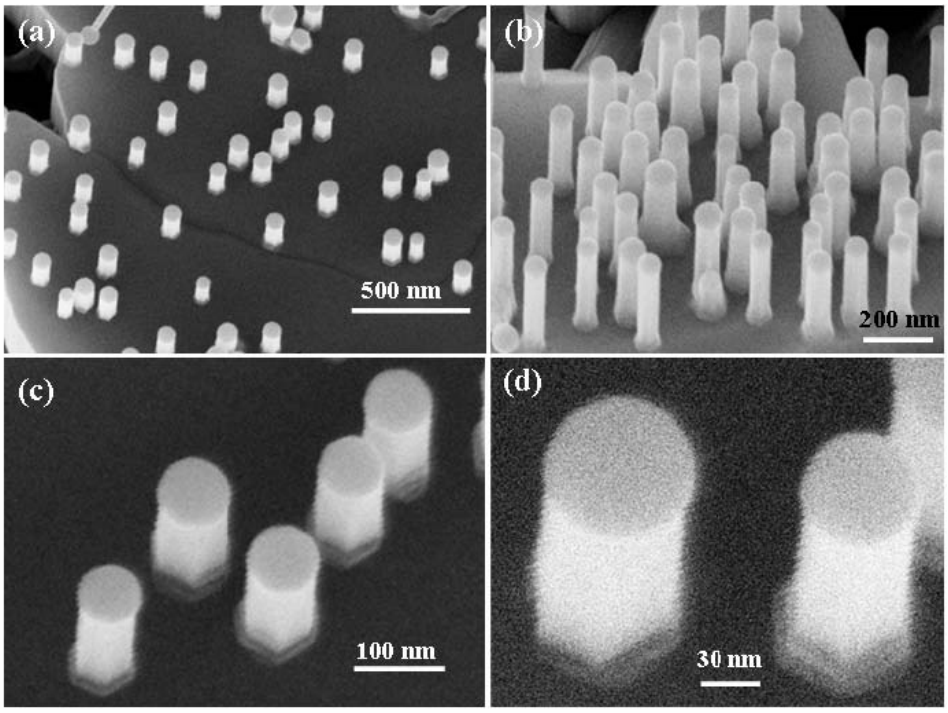

Figure 3.3 Perpendicular growth of nanorods on the c-plane of ZnO micro-rods. a) and b) are the dispersively oriented nanorods with inter-rod distance of ~400 and ~100 nm, respectively; c) and d) show the epitaxial growth of the ZnO nanorods, forming arrays with an identical crystallographic orientation, as represented by the parallel side surfaces.

Transmission electron microscopy imaging of a ZnO nanorod is presented in Figure 3.4. An Sn ball with faceted surface[117] is located at the growth front (Figure 3.4a). A high-resolution TEM image presented in Figure 3.4b shows that the ZnO nanorod grows along [0001] and its volume is free from dislocation. The interface between the Sn particle and the ZnO nanorod is atomically sharp and there may be a coherent relationship between the atomic lattices at the interface (Figure 3.4c), but the Sn is not well crystallized. From the image contrast across the nanorod presented in the low-magnification image (Figure 3.4a) and in the high-magnification TEM image in Figure 3.4b, a uniform contrast region at the middle of the nanorod (see the region indicated by arrowheads in Figure 3.4b and the enlarged image in Figure 3.4e) indicates its constant

projected thickness, while the side edges are very thin (see Figure 3.4d). Based on the image information, the six side surfaces of the nanorods are defined to be $\{2\bar{1}\bar{1}0\}$, the electron beam direction is $[2\bar{1}\bar{1}0]$. A schematic model of the nanorod cross-section is inserted in Figure 3.4a.

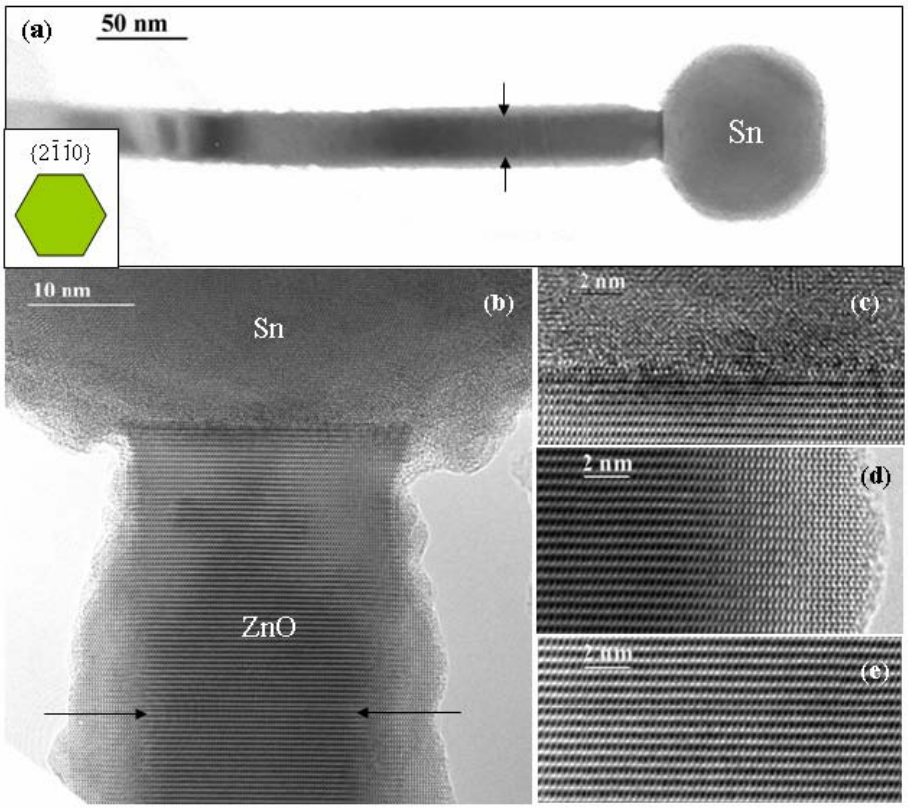

Figure 3.4 a) Low-magnification TEM image of a ZnO nanorod. The inset is a model of its cross-section. B) High-resolution TEM image of the nanorod with the incident electron beam along $[2\bar{1}\bar{1}0]$. (c, d, e) Enlarged images from the Sn-ZnO interface, the edge of the nanorod and the central region of the nanorod, respectively.

With increasing growth time, the oriented nanorods and nanobelts grew longer and longer. Figure 3.5 shows a typical morphology of the as-synthesized

nanostructructures upon 60 minutes at 1150 ^{o}C. Figure 3.5a shows the as-deposited nanostructures composed of the orientation-aligned ZnO nanorods and nanobelts out of

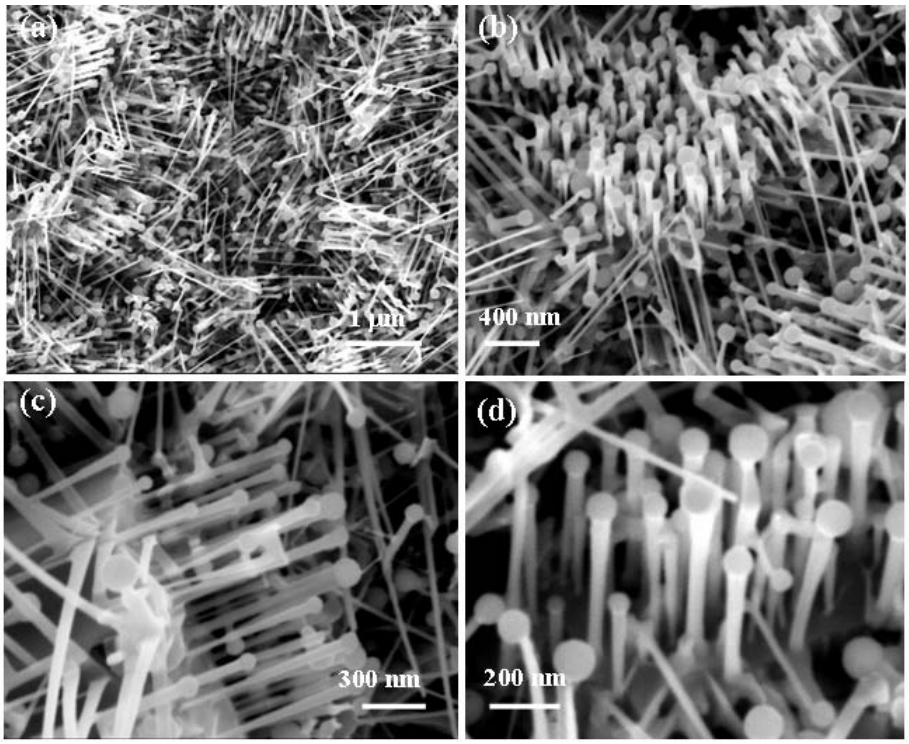

Figure 3.5 Typical morphology of the as-synthesized nanorods and nanobelts after 60 minutes' growth at 1150 ^{o}C. a) shows the aligned ZnO nanorods and side branched nanobelts on micro-rods; b) and c) demonstrate the perpendicular orientation relationship between the oriented ZnO nanorods and the surrounding nanobelts on a single micro-rod as viewed from the top and the side, respectively; d) gives the magnified view of the oriented nanorods rooted on a micro-rod.

the top and side surfaces of the micro-rods (Figs 3.5b and c). The ZnO nanorods grow out of the c-plane with a uniform length of 0.5-1.0 μm, while the diameter remains around 30-60 nm. Compared to those grown for a shorter time and separated by 100 nm - 1 μm, these oriented nanorods grew densely with a separation of 50-150 nm, suggesting an increase in nucleation sites during the growth. A slight increase in the diameter at the upper part of the nanorod is likely due to an increase in the size of the Sn catalyst particle

during the growth. High magnification images (Figs 3.5b and d) show that the micro-rods are rougher than those grown for 5 minutes. Along the perpendicular directions to the oriented nanorods, the number of side branched nanobelts of uniform length of 1 μm also dramatically increases. It is interesting to note that the metallic Sn head on the top of the nanorod is about one third larger in diameter than the nanorod diameter, while the size of the Sn head on a nanobelt is about 2~3 times larger than the width of the nanobelt.

To study the effect of graphite as a vapor generation agent for the growth of the desired nanostructures, an experimental session was conducted by adjusting the molar ratio of corresponding Zn: Sn: C from 2:1:1 to 2:1:2, but keeping the other parameters the same as for the experiments presented above. The growth time was one hour. Surprisingly, well-aligned nanowire-nanobelt junction arrays (for detail see section 3.3) formed perpendicularly oriented on the alumina substrate. Figure 3.6 is a top view of the as-grown junction arrays in a large area, where the six-fold symmetric feature of each junction array is clearly seen. Inset is a typical magnified micrograph of a single junction array. The junction array consists of a central nanowire of 100-200 nm in diameter and is surrounded by six-fold symmetric nanobelts of 50-100 nm in width that grow along the six crystallographic equivalent directions of $<01\bar{1}0>$.

The role of graphite in the raw material is to increase the creation rate of Zn and Sn vapors. Carbon can reduce ZnO and SnO_2 into Zn and Sn vapors at relatively lower temperature. It is expected that doubling the content of graphite in the raw material would increase the concentration of Sn liquid droplets, giving rise to many more nucleation sites[118], leading to the growth of high density nanorods and nanobelts. According to the studies on junction arrays which will be elaborated in the later section 3.3, it is known

that the side branched nanobelts would like to grow along six crystallographic equivalent orientations <01$\bar{1}$0>, giving a six-fold symmetric nanowire-nanobelt junction arrays presented in Figure 3.6.

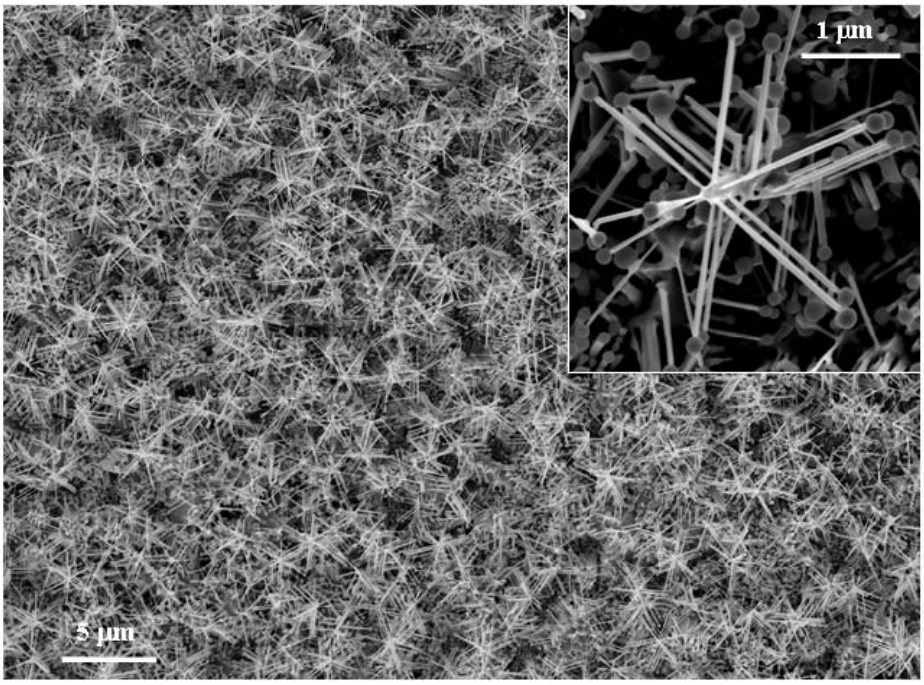

Figure 3.6 Top view of the well aligned nanowire-nanobelt junction arrays on an alumina substrate. Inset is a magnified micrograph of a single set of junction arrays with six-fold symmetric structure feature.

To optimize the desired morphology of the oriented ZnO nanorods, we tested some more parameters. Figure 3.7 is a typical morphology of the as-prepared nanorods and nanobelts after 30 minutes' growth at 1100 ^{o}C, where we used only two-thirds the amount of SnO_2 used in the other experiments and kept the pressure and argon flow rate the same. In Figure 3.7a, it is clearly shown that, in addition to the oriented ZnO nanorods, there are also some ZnO belt networks normal to and in between the oriented nanorods, as indicated by arrowheads. These networks are parallel to the nanobelts

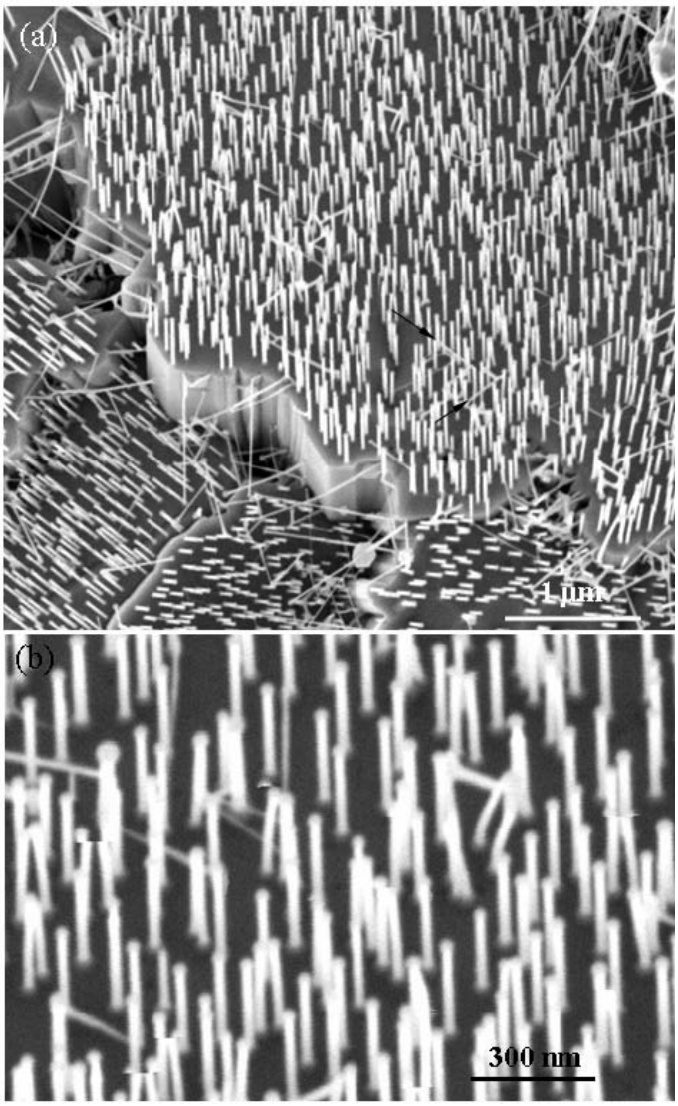

Figure 3.7 Typical morphology of the as-synthesized nanorods and nanobelts after 30 minutes' growth at 1100 ^{o}C. a) shows the well-aligned nanorods on a larger surface area. Nanobelts grown out of the nanorods in a perpendicular direction are also identified, as indicated by arrowheads. The alignment in the nanobelt directions indicates the crystallographic-orientation ordering among the nanorods. b) is a magnified view of the crystallographic-aligned ZnO nanorods arrays.

directly growing from the side surfaces of the micro-rod base due to the homoepitaxial orientation relationship[119]. Figure 3.7b is a magnified view of the vertically crystallographic-orientation aligned ZnO nanorods on a ZnO micro-rod, displaying uniform diameter of ~ 25 nm and height of ~250 nm.

There are two processes for the growth of ZnO nanorods. One is the oxidation of the reduced and vaporized Zn following the vapor-liquid-solid (VLS) growth process[120]; the other process is the direct deposition of the ZnO vapor (so called vapor-solid (VS) process). Based on our experimental data presented here and published previously[121,122], reductions of ZnO and SnO_2 into Zn and Sn vapors, respectively, are possible in the high temperature zone. The carrier gas transfers the reduced and vaporized Zn and Sn to the lower temperature region. The oxidation of Zn vapor and its subsequent deposition onto the substrate forms single crystal ZnO micro-rods with flat (0001) surfaces. Simultaneously, Sn vapor would transform to liquid droplets falling down on the surface of the ZnO micro-rods. Then on these flat planes, dispersed metallic Sn droplets function as catalysts to guide the oriented growth of ZnO, which in fact is a homoepitaxial process with the bulk ZnO micro-rods. The oriented nanorods remain an identical orientation with the micro-rods, resulting in the crystallographic-orientation-aligned growth of the nanorods on the (0001) surface. On the other hand, the liquid tin droplets in contact with the side surface of the ZnO micro-rods guide the growth of ZnO nanobelts along $<01\bar{1}0>$ perpendicular to the ZnO nanorods. A continuous deposition of the Sn vapor at the growth front results in a continuous increase in the size of the Sn particle, leading to a continuous increase in the size of the nanorods/nanobelts as growth proceeds.

Our data suggests that the VLS process is dominant, while the VS process is supplementary. As presented in Figs 3.1d, where the micro-rods as the growth platforms are quite rough at the very beginning in between the oriented nanorods and even form deep notches as if they were etched off upon longer growth time. Then it is expected that, as the growth time increases, the source materials were being consumed and the supply of vapors is short, the vapor pressure may fall below the supersaturation threshold required for the VLS growth. The growth can only be continued by vaporizing the micro-rods below the nanorods, resulting in the deep notches on micron-rod surfaces.

In summary, by using a simple vapor transport deposition method, well-aligned ZnO nanorods with six identical facets of $\{2\bar{1}\bar{1}0\}$ and orientation ordering have been successfully synthesized. Reduced Sn from SnO_2 acts as catalysts that guide the aligned growth of ZnO nanorods. By controlling the growth time at high temperature, nanorods of uniform lengths have been achieved. By increasing the content of graphite as the vapor-generating agent, well-aligned nanowire-nanobelt junction arrays have also been received. This study demonstrates that Sn can be an effective catalyst, which can be used to grow crystallographic-orientation aligned nanorods.

3.2 VLS mechanism understanding based on Sn-catalyst for growth of ZnO nanostructures[123]

To further probe the crystallographic-orientation alignment phenomena as described in section 3.1, we investigated in detail the crystallographic relationship between ZnO nanostructures and Sn particles which functioned as catalysts during the growth using X-ray diffraction (XRD) analyses and high resolution transmission electron

microscopy (HRTEM). The high-resolution transmission electron microscopy (HRTEM) work was carried out using a JEOL-4000EX operated at 400 kV.

Two batches of experiments are designed respectively for the purposes of X-ray diffraction followed by HRTEM work. Firstly, we use sapphire single crystal substrate with (0001) orientation for growth of oriented nanorods catalyzed by Sn, which later on proved to be an ideal sample for XRD analysis as a whole. As inspired by the results given by XRD analyses, which will be shown in the following section, detailed HRTEM work has been done for clearly clarifying the catalytic effect that the Sn particle plays during the orientation aligned growth of ZnO nanowires and nanobelts.

As shown in Figure 3.8 is a typical SEM image of as-grown aligned ZnO nanorods on sapphire (0001) substrate. It is clearly seen the ZnO nanorods grow normal to the substrate with spherical Sn ball at the tips.

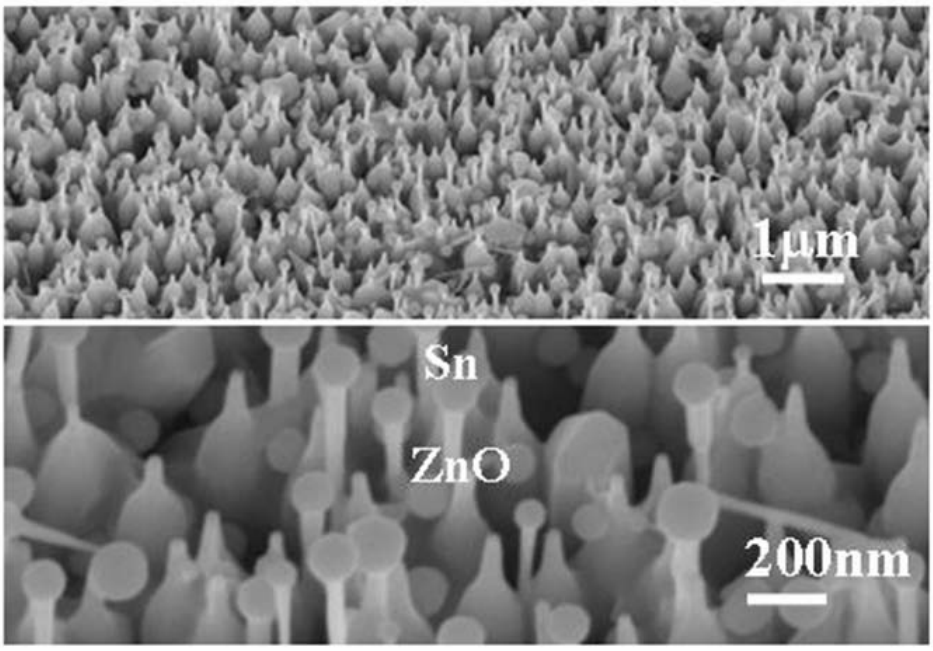

Figure 3.8 A typical SEM image of as-grown aligned ZnO nanorods on sapphire (0001) substrate.

The corresponding X-ray diffraction pattern in Figure 3.9 revealed that only strong peaks with respect to {0002} showed up, and the β-Sn peaks are corresponding to {200}, alumina peaks did not show up because the whole substrate has been covered with a layer of ZnO nanorods. It is suggested that there must be certain orientation relationship between ZnO nanorods and their Sn catalysts. To clarify this question, HRTEM investigation is necessary to be carried out on the crystallographic relationship between ZnO and Sn.

Vapor-liquid-solid (VLS) process has been an important approach in growth of quasi-one-dimensional (1D) nanowires and nanotubes (referred to as 1D nanostructures). In the VLS process, a metal catalyst is rationally chosen. It is generally believed that

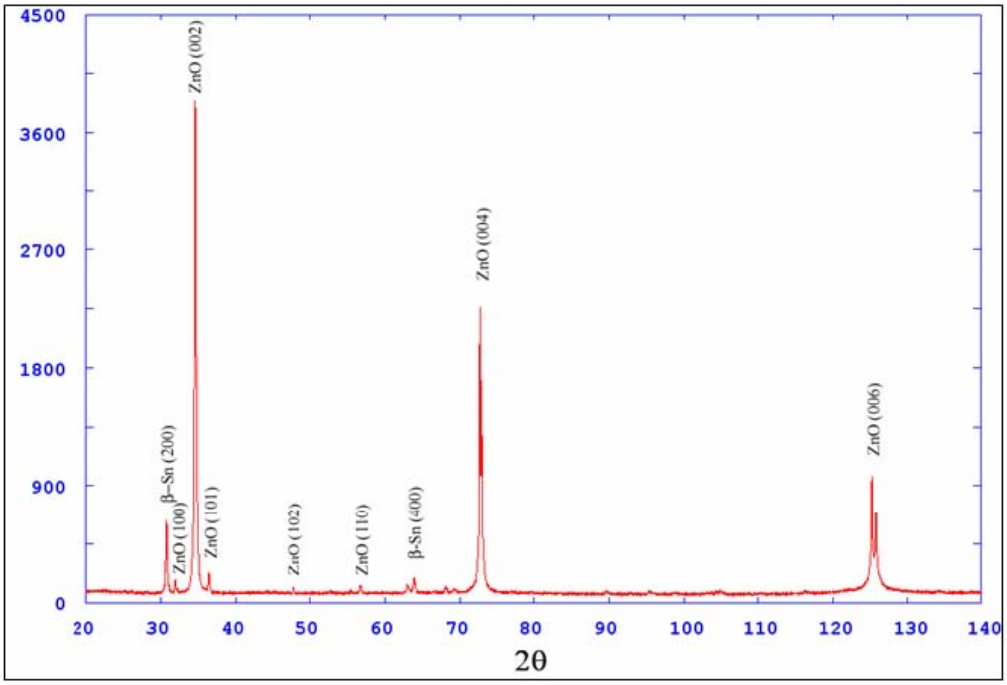

Figure 3.9 A typical X-ray diffraction pattern of as-grown aligned ZnO nanorods on sapphire (0001) substrate. It is shown there is a specific orientation relationship between ZnO nanorods and Sn particles on tip.

the metal particle is a liquid droplet during the growth and its crystal structure in solid may have no influence on the structure of the nanowires/nanobelts to be grown. Using tin particle guided growth of ZnO one-dimensional nanostructures as a model system, we show that the interface between the tin particle and the ZnO nanowires/nanobelts could be partially crystalline or ordered during the VLS growth although the local growth temperature is much higher than the melting point of the bulk tin, and the crystallographic structure and lattice mismatch at the interface is important in defining the structure characteristics of the grown nanowires/nanobelts. The interface prefers to take the least lattice mismatch, thus, the crystalline orientation of the tin particle may determine the growth direction and the side surfaces of the nanowires/nanobelts. The results may have important impact to understanding the physical chemical process involved in the VLS growth.

Vapor-liquid-solid (VLS) process has been an important approach in growth of quasi-one-dimensional (1D) nanowires and nanotubes. In the VLS process, a metal catalyst is rationally chosen from the phase diagram by identifying a metal that is in liquid at the growth temperature and serves as the site for adsorbing the incoming molecules, but the metal does not form a solid solution with the nanowire, thus it is phase separated at the growth front and leads the growth. The metal liquid droplet serves as a preferential site for absorption of gas phase reactant. Nanowire growth begins after the liquid becomes supersaturated in reactant materials and continues as long as the catalyst alloy remains in a liquid state and the reactant is available.[124] During the growth, the catalyst droplet directs the nanowire's growth direction and defines the diameter of the

nanowire. Ultimately, the growth terminates when the temperature is below the eutectic temperature of the catalyst alloy or the reactant is no longer available. As a result, the nanowires obtained from the VLS process typically have a solid catalyst nanoparticle at the ends with sizes comparable to diameters of the connected nanowires. Metal particles such as Au and Fe are effective for growing nanowires of Si[125,126], III-V compound, II-VI compound, and oxide: such as Au/ZnO[127], Fe/SiO_2[128], Co/SiO_2[129], Ni/Ga_2O_3[130], Ga/SiO_2[131].

It is generally believed that the metal particle is a liquid droplet during the growth and its crystal structure in solid may have no influence on the structure of the nanowires/nanobelts to be grown. In the following study, by using tin particle guided growth of ZnO 1D nanostructures as a model system, we found that the interface between the tin particle and the ZnO nanowire/nanobelt could be partially crystalline or ordered during the VLS growth although the local growth temperature is much higher than the melting point of the bulk tin, and the crystallographic structure and lattice mismatch at the interface is important in defining the structure characteristics of the grown nanowires/nanobelts. The interface prefers to take the least lattice mismatch, thus, the crystalline orientation of the tin particle may determine the growth direction and the side surfaces of the nanowires/nanobelts. The results may have important impact to understanding the physical chemical process involved in the VLS growth.

3.2.1 Sample preparation

The samples used for this study was prepared using a process the same as that in section 3.1. A mixture of commercial ZnO, SnO_2 and graphite powders in certain ratio (Zn:Sn:C = 2:1:1.) was placed in an alumina boat as the source material and positioned at

the center of the alumina tube. The entire length of the tube furnace is 50 cm. The desired nanostructures were deposited onto alumina substrate located in a temperature range of 550-600 ^{o}C. The high-resolution transmission electron microscopy (HRTEM) work was carried out using a JEOL-4000EX operated at 400 kV.

3.2.2 Experimental observation

Figure 3.10 is a typical scanning electron microscope (SEM) image, which shows ZnO nanowires/nanobelts with Sn particles on their tips. Classified from their morphology, the ZnO nanostructures show wire and belt morphologies. Judged from their

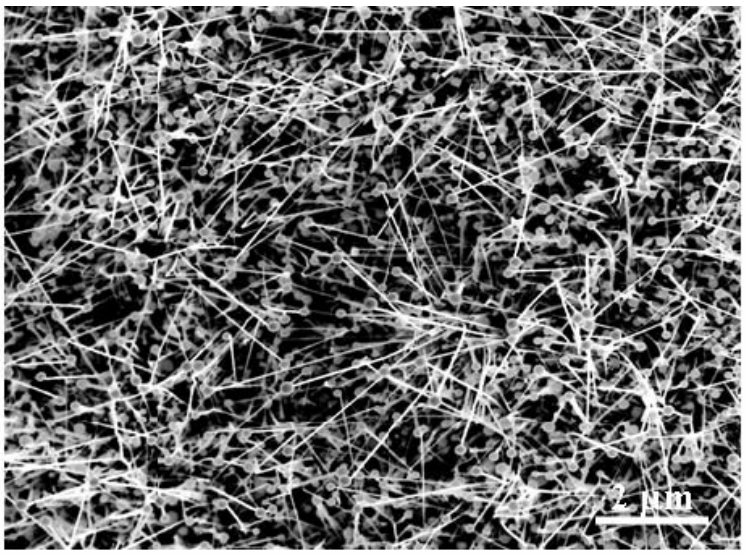

Figure 3.10 A typical SEM image of the Sn guided ZnO nanowires and nanobelts.

corresponding selected area electron diffraction (SAED) patterns, we found that ZnO nanowires grow along [0001] direction and the nanobelts have two growth directions, $[01\bar{1}0]$ and $[2\bar{1}\bar{1}0]$. No matter which growth direction they take, single crystal Sn particles always exist at their tips, which means that Sn catalyst can guide not only [0001]

growth ZnO nanostructures, but also $[01\bar{1}0]$ and $[2\bar{1}\bar{1}0]$ growth ZnO nanostructures. In the follows, we will present the orientation relationships in the neck-interfaces between Sn particles and the ZnO 1D nanostructures growing along [0001], $[01\bar{1}0]$ and $[2\bar{1}\bar{1}0]$.

3.2.2.1 Case 1: [0001] nanowires

Figure 3.11(a) and (b) show bright-field and dark-field images of a nanowires (thickness fringes indicates its wire morphology) with a particle at its tip. The SAED patterns recorded from the particle, the wire and both the wire and the particle are shown in Figure 3.11(c), (d) and (e), respectively, and each of them is single crystal. The SAED pattern of the particle (Figure 3.11(c)) can be indexed as $[10\bar{1}]_{Sn}$ pattern of the β phase tin with tetragonal structure (a = 0.5831 nm, c = 0.3182 nm, space group as $I4_1/amd$)[132]. The SAED pattern of the wire (Figure 2(d)) belongs to hexagonal ZnO structure with $a = 0.3249\,\text{nm}$, $c = 0.5206\,\text{nm}$, space group $P6_3mc$[133], and can be indexed to be $[2\bar{1}\bar{1}0]_{ZnO}$ pattern. The bright-field TEM image combined with SAED pattern reveals that the ZnO nanowire grows along [0001] and its side surfaces are $\{2\bar{1}\bar{1}0\}$. The interface orientation relationship between the ZnO wire and the Sn particle is $(020)_{Sn} \parallel (0001)_{ZnO}$, $[\bar{1}01]_{Sn} \parallel [2\bar{1}\bar{1}0]_{ZnO}$. Hereafter we index ZnO using the four-axis notation and the Sn using three-axis nation.

Figure 3.11(f) is a high-resolution electron microscopy (HRTEM) image of the white rectangle enclosed area in Figure 3.11(a), which depicts the interface structure between ZnO nanowire and the Sn particle. It is clear that $[0001]_{ZnO}$ is the growth direction of ZnO nanowire.

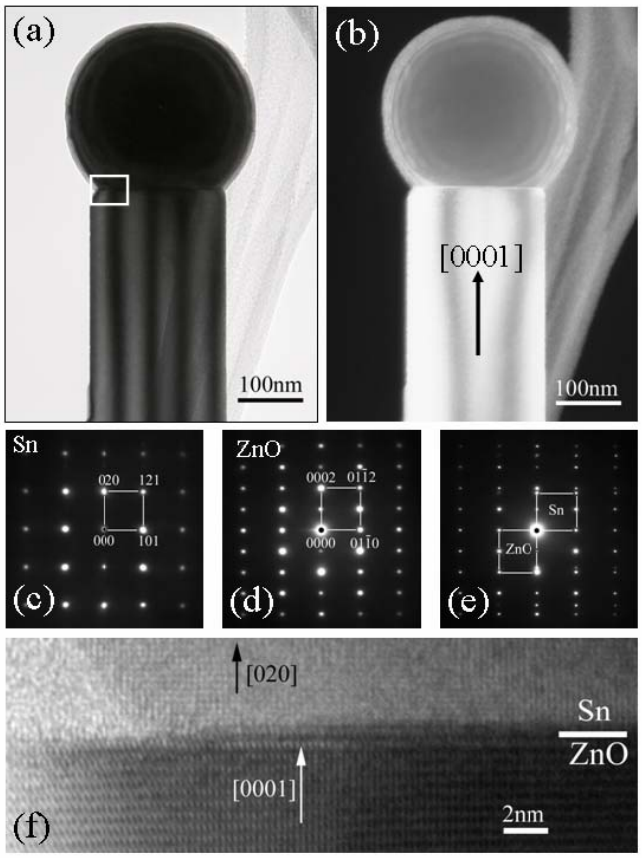

Figure 3.11 (a) and (b) are bright-field and dark-field images of a [0001] growth ZnO nanowire with an Sn particle at the growth front. (c), (d) and (e) are SAED patterns recorded from the particle, the rod, and both the particle and the rod in (a), respectively. (f) is an HRTEM image from the white rectangle enclose area in (a) from the interface region.

After measuring the lattice spacing, the $[020]_{Sn}$ direction of the Sn particle corresponds to ZnO growth direction $[0001]_{ZnO}$. It is noticed that the interface is flat and the width of the nanowire is comparable to the diameter of the Sn particle. Above the ZnO $(0001)_{ZnO}$ interface plane, there are two distinction regions, single crystal Sn particle core and an amorphous shell at the uncovered particle surface, as presented by the dark-field TEM image in Figure 3.11b. Chemical analysis using energy dispersice X-ray spectroscopy (EDS) indicates that the amorphous layer is SnO_x. It is important to note that the

amorphous shell covers only the exposed surface, which may be induced by subsequent oxidation of the Sn particle post growth.

3.2.2.2 Case 2: [01$\bar{1}$0] nanobelts

Figure 3.12(a) and (b) are bright-field and dark-field TEM images of [01$\bar{1}$0] growth ZnO nanobelts, respectively. The uniform contrast across its width is distinct from the wire presented in Figure 3.11(a) and (b). The nanobelts are defined by side surfaces of (2$\bar{1}\bar{1}$0) and (0001). The

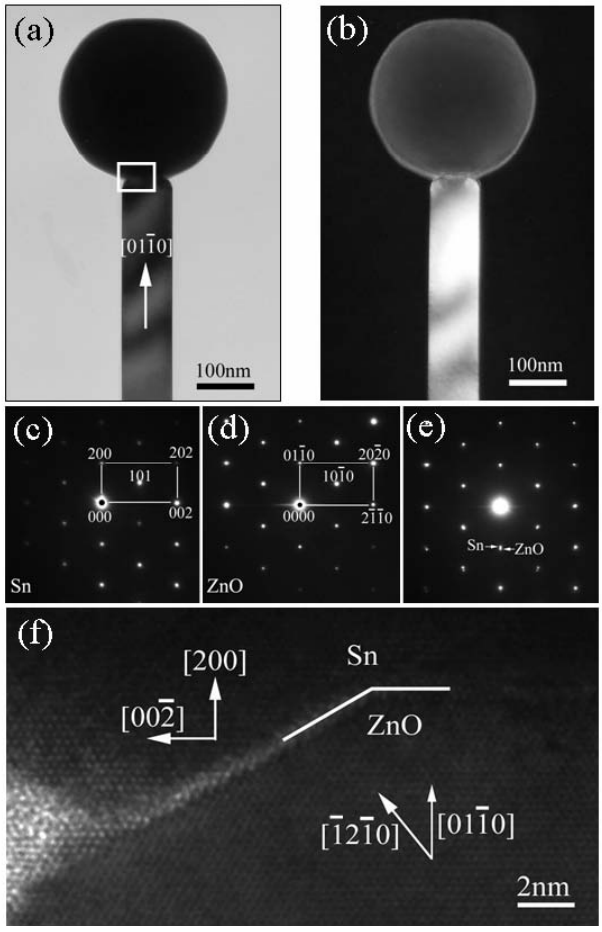

Figure 3.12 (a) and (b) are bright-field and dark-field images of a [01$\bar{1}$0] growth ZnO nanobelt with an Sn particle at its tip. (c), (d) and (e) are SAED patterns recorded from the particle, the belt ,and both the particle and the belt in (a), respectively. (f) is an HRTEM image from the white rectangle enclosed area in (a).

SAED patterns recorded from the Sn particle, the ZnO belt and both the particle and the belt are shown in Figure 3.12(c), (d) and (e), respectively. The interface orientation relationship between the particle and the nanobelt is described as $(200)_{Sn} \parallel (01\bar{1}0)_{ZnO}$ and $[020]_{Sn} \parallel [0001]_{ZnO}$. Figure 3.12(f) is an HRTEM image from the white rectangle enclosed area in Figure 3.12(a) from the interface. Compared to the flat interface in the [0001] growth ZnO nanowires, the interface between $[01\bar{1}0]_{ZnO}$ growth ZnO nanobelt and Sn particle is composed of $(01\bar{1}0)_{ZnO}$ and $(\bar{1}2\bar{1}0)_{ZnO}$ planes (corresponding to $(200)_{Sn}$ and $(30\bar{1})_{Sn}$, respectively), with a 30° rotation between them. The width of the nanobelts is much smaller than the diameter of the Sn particle.

3.2.2.3 Case 3: $[2\bar{1}\bar{1}0]$ nanobelts

Figure 3.13(a) and (b) are bright-field and dark-field TEM images of a $[2\bar{1}\bar{1}0]$ growth ZnO nanobelt with an Sn particle at its tip. The SAED patterns recorded from the Sn particle, ZnO belt and both the particle and the belt are shown in Figure 3.13(c), (d) and (e), respectively. The nanobelt is defined by side surfaces of $(01\bar{1}0)$ and (0001). The interface orientation relationship can be described as $(200)_{Sn} \parallel (2\bar{1}\bar{1}0)_{ZnO}$ and $[020]_{Sn} \parallel [0001]_{ZnO}$. Figure 3.13(f) is an HRTEM image from the interface. The clear ZnO lattice image in Figure 3.13(f) indicates that $[2\bar{1}\bar{1}0]_{ZnO}$ growth ZnO belt is thin and the thickness of the belt is uniform. The interface between the particle and belt is flat and composed of $(2\bar{1}\bar{1}0)_{ZnO}$ and $(200)_{Sn}$ planes.

As a summry of our data, among the total of 40 nanowires we have studied by TEM, 20 nanowires grow along [0001], 10 grow along $[2\bar{1}\bar{1}0]$, and 10 grow along

[$01\bar{1}0$]. The three cases are the only configurations we have identified, and there is no other orientation relationship being found.

3.2.3 Catalytic Growth Discussion

Catalytic growth of ZnO 1D nanostructures by vapor transport is a vapor-liquid-solid (VLS) crystal growth process. In our synthesis, the SnO_2 powders were first reduced by carbon

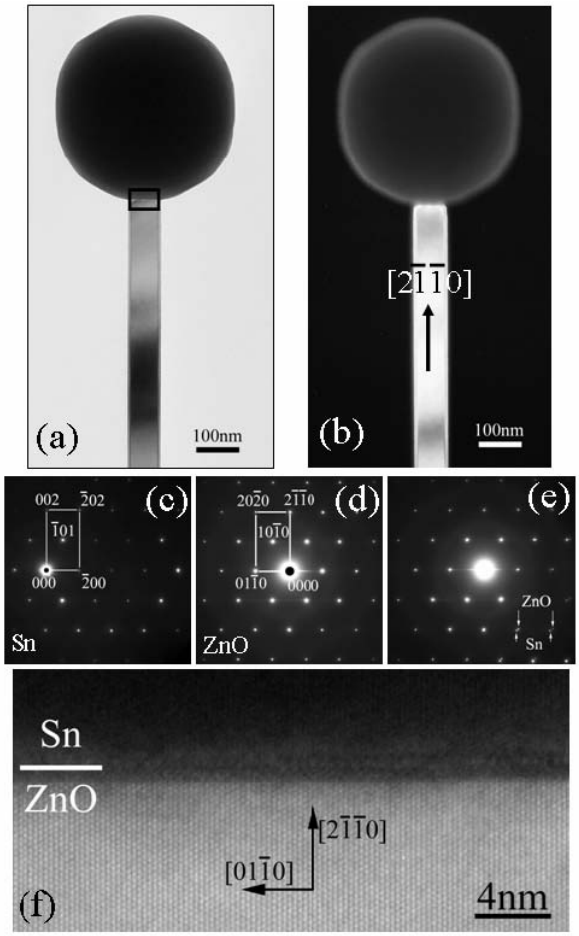

Figure 3.13 (a) and (b) are bright-field and dark-field images of a [$2\bar{1}\bar{1}0$] growth ZnO nanobelt with an Sn particle at its tip. (c), (d) and (e) are SAED patterns recorded from the particle, the belt, and both the particle and the belt in (a), respectively. (f) is an HRTEM image from the white rectangle enclosed area in (a).

into Sn vapor and CO/CO_2 vapor in the high temperature region, then the Sn droplet formed on the substrate served as the catalyst. ZnO vapor is transported and adsorbed on the surface of the catalyst. When the alloy droplets become supersaturated, ZnO will be phase separated and crystallized to form the nanowire/nanobelt. Normally, ZnO nanowires prefer to grow along $[0001]_{ZnO}$ and its diameter is considered to be defined by the catalyst droplets. By choosing a proper substrate, such as $(2\bar{1}\bar{1}0)$ sapphire, ZnO nanowires can grow epitaxially, which means that the ZnO-substrate interface might control the growth orientation of the ZnO nanostructure. However, no detailed study has been reported on crystal orientation relationship between catalyst and ZnO nanostructures.

When Sn is used as catalyst, some new phenomena appear in our growth, which are different from those observed conventionally in nanowire growth: (i) Not only [0001] growth ZnO nanowires, but also considerable amounts of $[01\bar{1}0]$ and $[2\bar{1}\bar{1}0]$ growth ZnO nanobelts have been found, which were grown previously without using catalyst.[134] (ii) ZnO nanostructures with different growth directions show apparently different sizes although the catalyst Sn particles have about the same size. The ratios between the diameter of the Sn particles and the size of the [0001], $[01\bar{1}0]$ and $[2\bar{1}\bar{1}0]$ growing ZnO 1D nanostructures in Figure 3.11, Figure 3.12 and Figure 3.13 are 1:0.71, 1: 0.3 and 1:0.18, respectively. (iii) SAED patterns indicate that ZnO 1D nanostructures in different growth directions have different orientation relationships with the catalyst Sn particle. There are two possibilities for this growth effect: 1) the Sn particle is locally crystallized or atomically ordered at the interfacial region with the ZnO at the initial nucleation and subsequent growth of the 1D nanostructure, so that the crystalline structure of the Sn

determines the growth direction and subsequently the side surfaces of the ZnO nanostructure; 2) the Sn particle was in liquid state during the growth and it crystallized post the growth according to the orientation of the 1D nanostructure. The following experimental result gives an unambiguous answer.

An amazing structure observed in the growth product is that one Sn particle results in the growth of two 1D nanostructures along well-defined growth directions. As shown in the SEM images in Figure 3.14, two 1D ZnO nanostructures can be guided by a single Sn particle. And their morphology indicates that they are in different growth directions. The thin and wide belts from the left Sn particle in Figure 3.14(a) grow along $[2\bar{1}\bar{1}0]$ and $[01\bar{1}0]$, respectively; the growth direction of the ZnO wire in Figure 3.14(b) is [0001], while a thin ZnO nanostructure that shares the same Sn catalyst particle shows a belt morphology, with a growth direction of either $[2\bar{1}\bar{1}0]$ or $[01\bar{1}0]$.

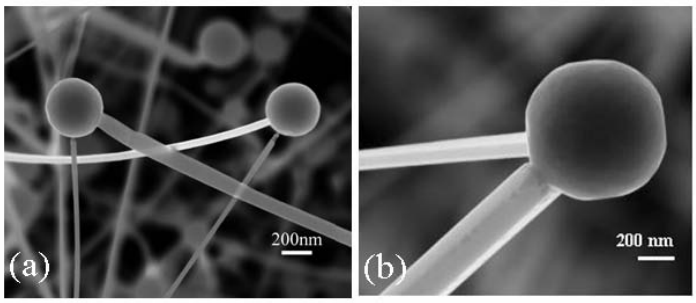

Figure 3.14 (a) is an SEM image, which shows each of the two Sn particles guiding the growth of two ZnO nanobelts. The Sn particle in (b) leads the growth of a ZnO wire and a ZnO belt.

Figure 3.15(a) is a TEM image of two 1D ZnO nanostructures sharing a single Sn catalyst particle. Figure 3.15(b) and (c) are the SAED patterns recorded from the Sn particle and the wide ZnO wire, which indicates that the Sn particle is a single crystal and

the wide ZnO wire grows along [0001]. The orientation relationship between the ZnO wire and the Sn particle is the same as the case discussed in Figure 3.11. After tilting the sample, a zone axis pattern is received from the thin belt (Figure 3.15(d)). The projected direction of the nanobelt perpendicular to the beam is $[\bar{1}\,\bar{1}\,24]$, indicating that the true growth direction of the belt is $[\bar{1}\,\bar{1}\,20]$. The result presented in Figure 3.15 indicates that well-defined crystallographic orientation relationships between the Sn particle and the

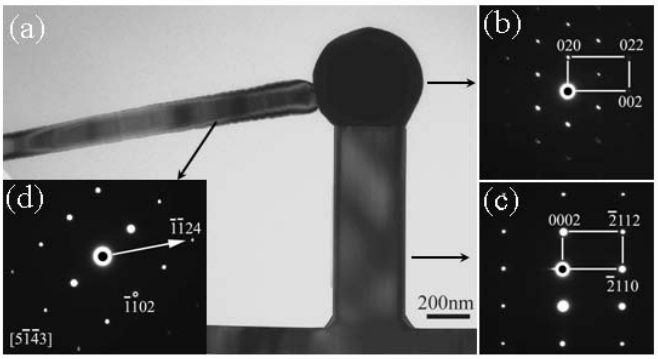

Figure 3.15 (a) is a TEM image, which shows an Sn particle guided a [0001] growth nanowire and a $[\bar{1}\,\bar{1}\,20]$ growth nanobelt at the same time. The SAED pattern of the Sn particle and the [0001] growth nanowire are shown in (b) and (c). (d) SAED pattern recorded from the nanobelt after a small tilting. The incident beam direction is $[5\,\bar{1}\,\bar{4}\,3]$.

two 1D nanostructures. With consideration the single crystal structure of the Sn particle after the growth, the fixed orientation relationship is only possible if the Sn particle is locally atomically ordered at its surface, although the local growth temperature of 550~600 ^{o}C is much higher than the bulk melting point of Sn (232 ^{o}C).[135] This may be possible if there is a very thin layer, of a few atomic layers, of possibly Sn-O on the surface of the Sn particle due to the presence of the oxygen vapor in the growth chamber. Such a local ordering may need to preserve to only a few atomic layers in thickness, while the rest of the tin particle is in molten state during growth. Since ZnO has a high

melting temperature of 1975 ^{o}C, the coherent interfacial "pinning" may raise the local melting temperature of Sn at the interface.[136]

The epitaxial orientation relationships between the Sn particle and the ZnO 1D nanostructure can be explained from the *lattice mismatch* at the interface. The schematics in Figure 3.16 are used to depict the mismatch at the Sn-ZnO interfaces for the three cases presented above. Based on the SAED patterns in Figure 3.11, the interface of [0001] growth nanowire is composed of $(0001)_{ZnO}$ and $(020)_{Sn}$ planes. It is known that the atoms in the ZnO $(0001)_{ZnO}$ plane have six-fold symmetry. For the $(020)_{Sn}$ plane matched to $(0001)_{ZnO}$, the angle between $(101)_{Sn}$ and $(\bar{1}01)_{Sn}$ is 57.1°; it is acceptable to consider that the atoms in the $(020)_{Sn}$ plane have quasi-six-fold symmetry. The low-indexed planes at the interface of ZnO nanostructures are the three sets of $\{01\bar{1}0\}_{ZnO}$ planes with 120° angle between them (Figure 3.16(a)); two of them match with the $\{101\}_{Sn}$ planes with a lattice mismatch as small as 0.7% in reference to ZnO, the third one matches to the $\{200\}_{Sn}$ with a lattice mismatch of 3.6%. Thus, hexagon is preferred to be the cross-section at the interface, corresponding to a wire/rod-morphology.

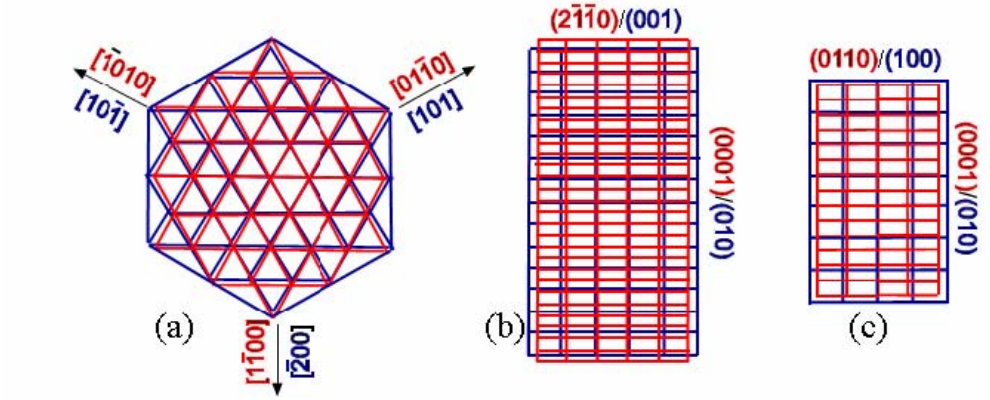

Figure 3.16 (a), (b) and (c) are the schematics of atomic planes at the epitaxial interfaces between the Sn particle and the [0001], $[01\bar{1}0]$ and $[2\bar{1}\bar{1}0]$ growth ZnO nanostructures, respectively.

The interface of $[01\bar{1}0]$ growth ZnO nanobelts is composed of $(01\bar{1}0)_{ZnO}$ and $(200)_{Sn}$ planes. The $(0001)_{ZnO}$ and $(2\bar{1}\bar{1}0)_{ZnO}$ are the low-indexed perpendicular planes that are matched to $(010)_{Sn}$ and $(001)_{Sn}$ planes with lattice mismatches of 12.0% and 2.1%, respectively. The rectangle strain pattern is likely to induce the rectangular belt form. Because the lattice mismatches between $\{2\bar{1}\bar{1}0\}_{ZnO}$ and $(002)_{Sn}$, and $\{01\bar{1}0\}_{ZnO}$ and $(101)_{Sn}$ are 2.1% and 0.7%, respectively, a possible case is that the lattice mismatch can be reduced by changing the interface from $(01\bar{1}0)_{ZnO}$ to $(\bar{1}2\bar{1}0)_{ZnO}$, possibly resulting in the deflection in the interface plane, as observed in Figure 3.11(f).

The asymmetric lattice mismatch also exists in the low-indexed planes of $(0001)_{ZnO}$ and $(01\bar{1}0)_{ZnO}$ at the interface of $[2\bar{1}\bar{1}0]$ growing ZnO nanobelts (Figure 3.16(c)). The lattice mismatches between $(0001)_{ZnO}$ and $(020)_{Sn}$, $(01\bar{1}0)_{ZnO}$ and $(200)_{Sn}$ planes are about 3.6% and 12.0%, respectively. Different from the $[01\bar{1}0]$ growing nanobelts, a larger lattice mismatch of 3.6% exists at the interface between $(01\bar{1}0)_{ZnO}$ and $(100)_{Sn}$, thus, the size of the nanobelt is reduced to decrease the interface mismatch energy. The comparably large size of [0001] growth ZnO nanowires is consistent with their small lattice mismatch at the interface.

The orientation relationships between Sn particles and ZnO 1D nanostructures in our synthesis suggest that the Sn particle is partially crystallized or atomically ordered at least at the interface between the particle and the ZnO 1D nanostructure during the growth. The ordered layers appear taking an important role in initiating the nucleation and growth of the ZnO 1D nanostructure, resulting in morphology control. It may be the reason why the 1D ZnO nanostructures from a single Sn particle can take different

growth directions, in spite of the preferred [0001] growth. After the temperature was dropped to room temperature, the Sn particle forms a single crystal particle and it preserves the orientation as defined by the interface with the ZnO 1D nanostructure.

3.2.4 Conclusions

Using electron diffraction and high-resolution electron microscopy, we studied the interface relationship between catalyst Sn particles and their guided ZnO 1D nanostructures. Tin catalyst not only can guide [0001] growth nanowires, but also can guide $[01\bar{1}0]$ and $[2\bar{1}\bar{1}0]$ growth nanobelts. The orientation relationship between the [0001] growth ZnO nanowire and the single crystal β phase Sn particle is: $(020)_{Sn}$ || $(0001)_{ZnO}$, $[\bar{1}01]_{Sn}$ || $[2\bar{1}\bar{1}0]_{ZnO}$. For nanobelts growing along $[01\bar{1}0]$ and $[2\bar{1}\bar{1}0]$, the orientation relationships are $(200)_{Sn}$ || $(01\bar{1}0)_{ZnO}$, $[020]_{Sn}$ || $[0001]_{ZnO}$ and $(200)_{Sn}$ || $(2\bar{1}\bar{1}0)_{ZnO}$, $[020]_{Sn}$ || $[0001]_{ZnO}$, respectively. One tin particle can initiate the growth of two 1D nanostructures; the tin particle is single crystal post the growth and it preserves epitaxial relationships with the grown nanostructures.

Our results provide new insights in revealing the process involved in VLS growth. Using Sn/ZnO as a model system, we showed that the interfacial region of the tin particle with the ZnO nanowire/nanobelt could be crystalline or atomically ordered during the VLS growth, although the local growth temperature is much higher than the melting point of tin, and it may play a key role in initiating 1D nanostructure. The interface prefers to take the least lattice mismatch, thus, the crystalline orientation of the tin particle may determine the growth direction and the side surfaces of the nanowires/nanobelts.

3.3 Self-assembled Nanowire-nanoribbon Junction Arrays and Nanopropeller arrays[137]

Now, we have captured some kind of sense on the growth of ZnO nanorods and nanobelts. For hexagonal nanorods, the fast growth direction is along [0001], one of the major easy axis of wurtzite structured ZnO. While for ZnO nanobelts, three fast growth directions become choices for directional growth. There is a large amount of space for playing the crystal growth of nanobelts. Then if we can control the orientation relationship between catalyst and as-grown nanostructures as well as the exposing facets of as-grown nanostructures, desired hierarchical nanostructures could be assembled.

It is known that quasi-one-dimensional nanostructures for a variety of functional materials have been successfully synthesized by using various approaches including thermal evaporation[138], sol-gel[139], arc discharge[140], laser ablation[141] and template-based method[142]. To date, extensive research work has been focused on ZnO. Many different morphological ZnO nanostructures, including wires, belts, and rods[143], etc., have been fabricated. However, towards the integration of nanostructures elements into variety of nanodevices, self-assembled types of hierarchical nanostructures from the atomic level have become necessary.

3.3.1 Nanowire-nanoribbon Junction Arrays

Thermal evaporation was used in the present study for synthesis of ZnO nanostructures. The experimental set-up consists of a horizontal high temperature tube furnace of length ~ 50 cm, an alumina tube (~ 75 cm in length), a rotary pump system and a gas controlling system. Commercial (Alfa Aesor) ZnO and SnO_2 powders with

weight ratio of 1:1 (5 grams in total) were fully mixed by grounding the powder mixture for 15 minutes and then used as the source material. The source material was loaded on an alumina boat and positioned at the center of the alumina tube. After evacuating the tube to 2×10^{-3} Torr, thermal evaporation was conducted at 1300 ^{o}C for one hour under pressure of 300~400 Torr and Ar carrier gas flow rate of 50 sccm (standard cubic centimeters per minute). The synthesized nanostructures grew on the top of the inner-wall of the alumina tube in a region of ~ 4 cm in width, located downstream ~ 15 cm away from the source material (located in the middle of the furnace), and the local growth temperature was in the range of 700~800 ^{o}C.

The yield of the synthesis is reasonably high. Typical scanning electron microscopy (SEM) images of the as-synthesized products are given in Figure 3.17. Figure 3.17a shows a low-magnification image of the as-synthesized products with a uniform feature consisting of sets of central axial nanowires, surrounded by radial oriented "tadpole-like"[144] nanostructures. The morphology of the string appears like a "liana", and the axial nanowire is the "rattan", which has a uniform cross-section with dimension in the range of a few tens of nanometer. The "tadpole-like" branches have spherical balls at the tips (Figure 3.17b). EDS analysis shows that the tadpole-like structure and the central nanowire are ZnO, while the ball at the tip is Sn.

It is apparent in Figure 3.18a that the top and bottom strings have a dense and ordered stacking of tadpole-like nanostructures with maximum widths of ~ 300 nm, while the central one is a string assembled with sparsely distributed tadpole-like nanostructures along a thin nanowire. A high magnification SEM image given in Figure 3.18b shows the ribbon shape of the tadpole-like structures, with a fairly uniform thickness, and their

surfaces are rough with steps. The contact point between the nanoribbon with the axial nanowire is rather small in the order of a few tens of

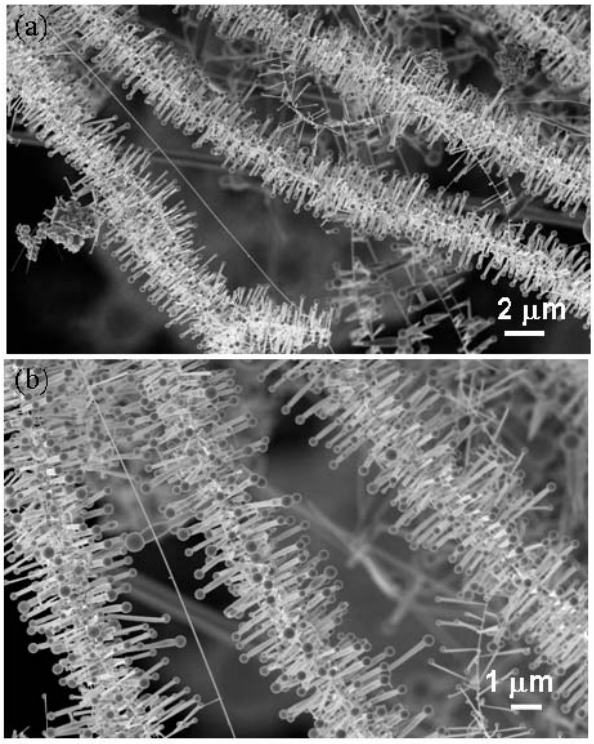

Figure 3.17 SEM images of the as-synthesized ZnO nanostructures, showing strings of "tadpole-like" nanostructures.

nanometers, while far away from the contacting point, the nanoribbon size is rather large in the order of 100 – 200 nm.

An interesting phenomenon observed in Figure 3.18c is that the distribution of the nanoribbons around the axial nanowire has an angle interval of ~ 60^{o}. A typical front view of the nanowire indicates a six-fold symmetrical ordered assembly (Figure 3.18d).

Figure 3.19a is a typical TEM image of the nanowire-nanoribbon junction structures. The axial nanowire is as thin as ~ 30 nm, while the width of the nanoribbon is rather large and increases as the growth continue. The contrast introduced by the surface

steps on the ribbons is apparent. Figure 3.19b shows a case that two nanowires grow from a nanoribbon. The TEM image

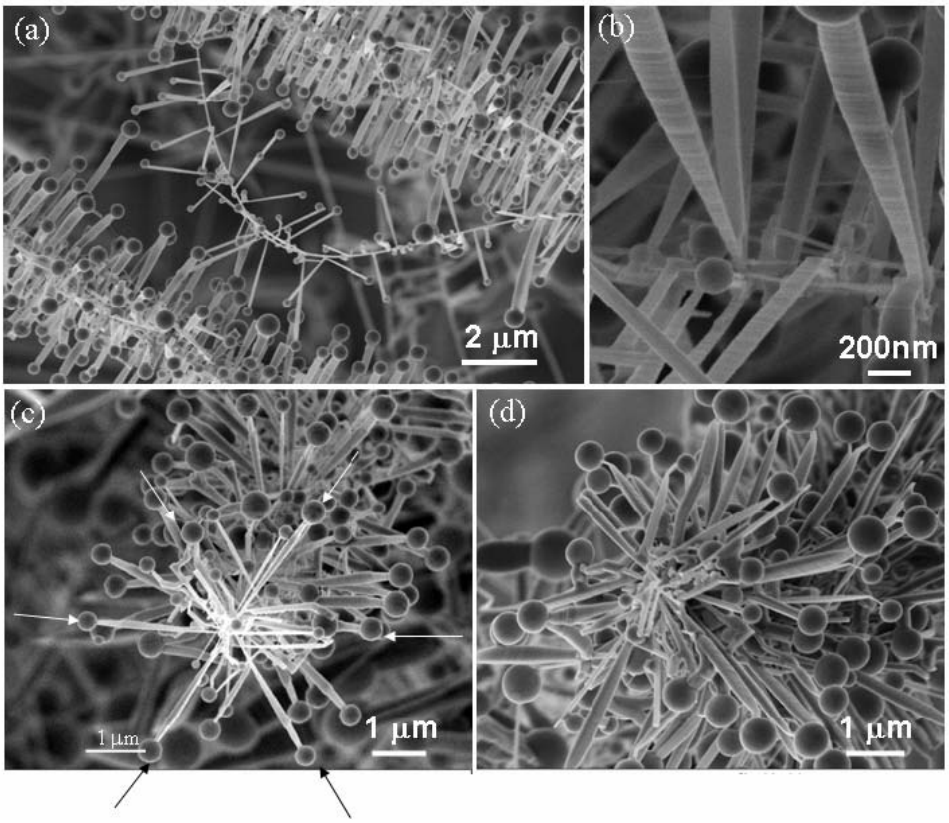

Figure 3.18 High magnification SEM images of the ZnO nanostructures showing (a, b) the ribbon shape of the "tadpole-like" nanostructure, (c, d) and their quasi-six-fold radial distribution around the axial nanowire.

and the corresponding electron diffraction pattern show that the nanoribbon and the nanowire have the wurzite (hexagonal) structure. The most commonly observed growth direction of the nanoribbons is $[01\bar{1}0]$ (and equivalent directions), and the nanowires are [0001]; the top surfaces of the nanoribbon are $\pm(2\bar{1}\bar{1}0)$.

Figure 3.20a shows a junction consisting of an axial nanowire and two branches of nanoribbons. The nanowire and nanoribbons are of the same crystal piece and they

share a common $(2\bar{1}\bar{1}0)$ plane; their growth directions are [0001] and $\pm$ $[01\bar{1}0]$ (Figure 3.20b), respectively.

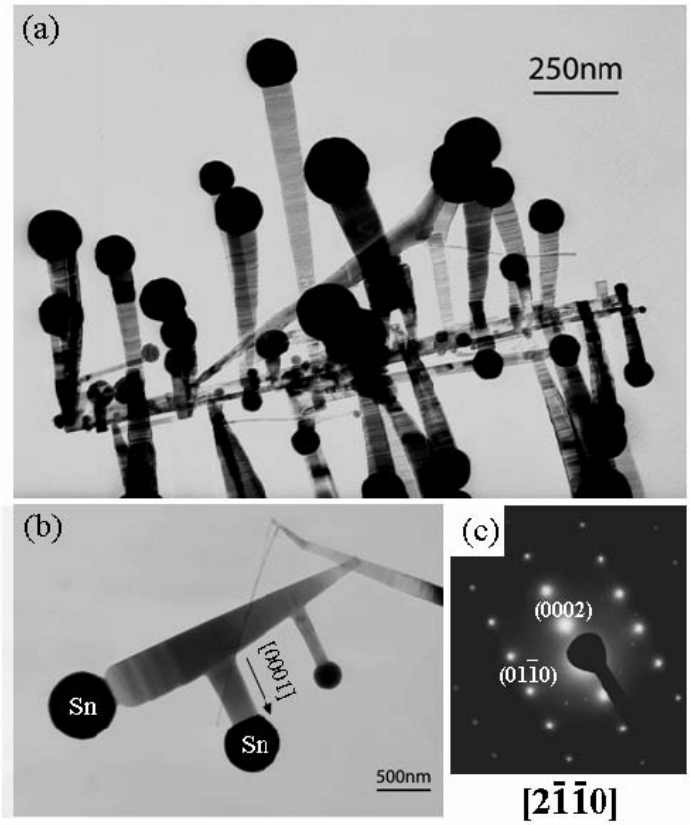

Figure 3.19 (a) Low-magnification TEM image of the as-synthesized ZnO nanowire-nanoribbon junction arrays. (b, c) TEM image of two junctions and the corresponding electron diffraction pattern.

Electron diffraction, bright and dark-field TEM images (Figs 3.20c and d) recorded from the junction area prove that the nanoribbon and nanowire have the same crystal structure and orientation.

In the present study, a mixture of SnO_2 and ZnO powders was used as the source material. It is known that SnO_2 can decompose into Sn and O_2 at high temperature[145,146,147], thus, the growth of the nanowire-nanoribbon junction arrays is the

result of vapor-liquid-solid (VLS) growth process, in which the Sn catalyst particles are responsible for initiating and leading the

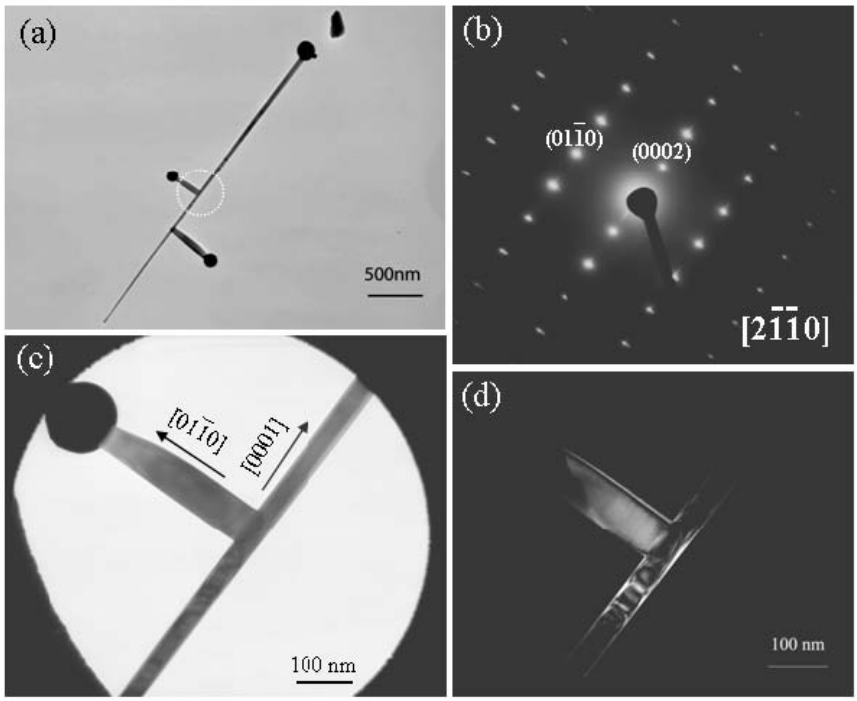

Figure 3.20 (a) TEM image of two junctions and (b) the corresponding electron diffraction pattern from the junction region as indicated by a white circle in (a) (excluding the Sn particle). (c, d) Bright-field and (0002) dark-field TEM images from the junction region.

growth of ZnO nanowires and nanoribbons. Our previous study of ZnO nanobelts shows that the fast growth directions of ZnO are [0001] and $<10\bar{1}0>$. [30]

The growth of the novel structure presented in the present study can be separated into two stages. The first stage is a fast growth of the ZnO axial nanowire along [0001] with Sn as the catalyst (Figure 3.21a). The growth rate is so high that a slow increase in the size of the Sn droplet has little influence on the diameter of the nanowire, thus the axial nanowire has a fairly uniform shape along the growth direction.

The second stage of the growth is the nucleation and epitaxial growth of the nanoribbons due to the arrival of the tiny Sn droplets onto the ZnO nanowire surface (Figure 3.21b). This stage is much slower than the first stage because the lengths of the nanoribbons are uniform and much

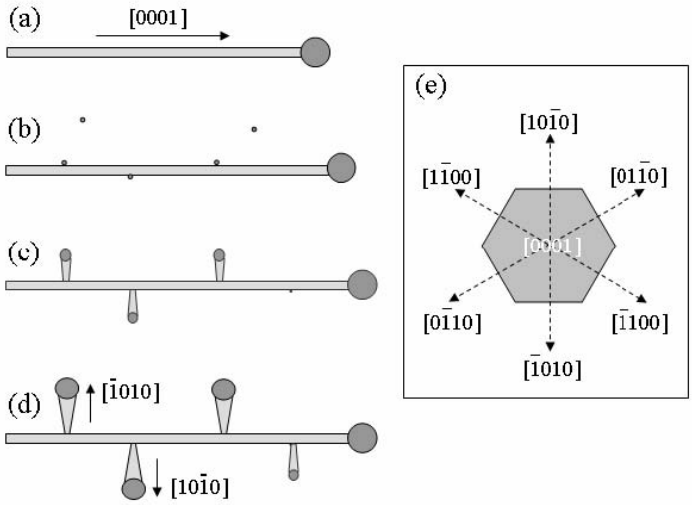

Figure 3.21 (a-d) Schematic diagram showing the two-stage growth of the ZnO junctions. (e) A cross-section model illustrating the isotropic epitaxial growth of the nanoribbons around the nanowire.

shorter than that of the nanowire. Since Sn is in liquid state at the growth temperature, it tends to adsorb the newly arriving Sn species and grows into a larger size particle (i.e., coalescing) (Figure 3.21c). Therefore, the width of the nanoribbon increases as the size of the Sn particle at the tip becoming larger, resulting in the formation of the tadpole-like structure observed in TEM (Figure 3.21d).

The ZnO nanowire is likely to have a hexagonal cross-section bounded by ±(10$\bar{1}$0), ±(01$\bar{1}$0) and ±($\bar{1}$100), which are six crystallographic equivalent planes.[1-2] The Sn liquid droplets deposited onto the ZnO nanowire lead to the simultaneous growth of

the ZnO nanoribbons along the six growth directions: $\pm[10\bar{1}0]$, $\pm[0\bar{1}10]$ and $\pm[\bar{1}100]$ (Figure 3.21e). The angles between the two adjacent growth directions is 60^o, resulting in the six-fold symmetric distribution of the nanoribbons around the nanowire, in agreement with the observation shown in Figs 3.18c and d.

In summary, by thermal evaporating a mixture of ZnO and SnO_2, self-assembled nanowire-nanoribbon junction arrays of ZnO have been synthesized. The growth is dominated by the VLS mechanism and Sn particles reduced from SnO_2 serve as the catalyst for the growth. The axial nanowires (the "rattans") are the result of fast growth along [0001], and the surrounding "tadpole-like" nanoribbons are the growth along $\langle 10\bar{1}0\rangle$. An isotropic growth along six $\langle 10\bar{1}0\rangle$ results in the ordered radial distribution of the nanoribbons around the axial nanowire. The junction arrays of ZnO structures reported here are likely to have ultra-high surface sensitivity due to the unique structure, and they are a candidate for building sensors with ultra-high sensitivity.[148] It may be possible that, through further adjustment of synthesis parameters including temperature, pressure, source composition, etc., more perfectly and orderly self-assembled junction arrays could be prepared.

3.3.2 Nanopropeller Arrays

When we introduced the carbon as reducing agent, then a mixture of ZnO and SnO_2 and graphite powders in a certain weight ratio was used as the source material, another type of complex ZnO nanostructure was successfully grown: the self-assembled polar surface dominated nanopropeller arrays.

The polar surface dominated nanopropeller arrays of ZnO in this work were grown by a two-step high temperature solid-vapor deposition process. The experimental

set-up consists of a horizontal high temperature tube furnace of length ~ 50 cm, an alumina tube (~ 75 cm in length), a rotary pump system and a gas controlling system. Commercial (Alfa Aesor) ZnO and SnO_2 powders as well as graphite with molar ratio of 3:4:1.5 were mixed, ground and then loaded on an alumina boat and positioned at the center of the alumina tube. The evaporation was conducted at 1100 ^oC for 60 minutes (step I) and then up to 1300 ^oC for half an hour (step II) under pressure of 200 mbar. The N_2 carrier gas flow rate is controlled at 20 sccm (standard cubic centimeters per minute). The nanopropeller arrays grew on a polycrystalline Al_2O_3 substrate in a temperature zone ranging of 600~700 ^oC and 800~900 ^oC corresponding to the steps I and II, respectively.

Figure 3.22(a) shows a top view of the well-aligned ZnO nanopropeller arrays on a polycrystalline Al_2O_3 substrate grown in a relatively higher temperature zone (~680 ^oC (step I)). Each column of nanopropeller arrays consists of six arrays of triangular shaped blades of 4-5 μm in length, and a propeller array of diameter ~ 10 μm. Columns of the nanopropellers remain their six-fold arrays of parallel nanoribbon blades around the central nanowire (Figure 3.22(b)). There is a small Sn ball of a diameter ~50 nm at the tip of the blade, which is less than half of the average width of the blade (~ 400 nm). All of the blades have a uniform isosceles triangular shape. Figure 3.22(c) gives a typical morphology of the other type of ZnO nanopropeller arrays grown on an alumina substrate. With a similar six-fold symmetry and branching phenomena as for the first case in figs. 3.22(a) and (b), a magnified image of the nanopropeller arrays in Figure 3.22(d) shows some rougher stepped top surfaces of the blades than the flat smooth surfaces as observed in Figure 3.22(b). Unlike the previous case with a bare flat node at the tip of the central axis, there are several fine nanowires sticking out of the growth front. The

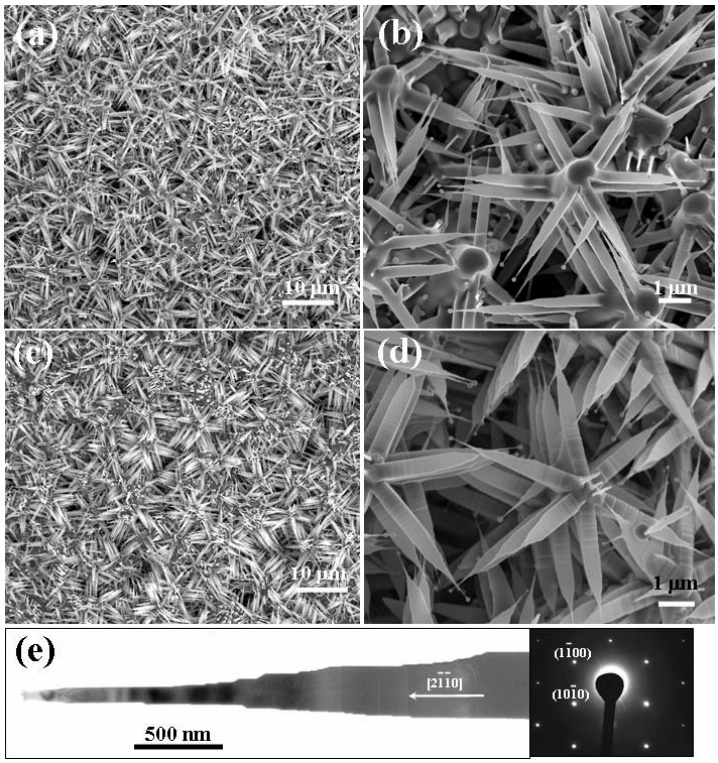

Figure 3.22 (a) SEM image of bunches of ZnO nanopropeller arrays rooted at Al_2O_3 substrate; (b) magnified picture of the six-fold symmetrical ZnO nanopropeller arrays with flat top surfaces; (c) nanopropeller arrays with stepped rough top surface; (d) high magnification SEM images of nanopropeller arrays with stepped rough top surface, on which there are normal oriented nanowires along the central axis; (e) TEM image of a nanopropeller blade, showing a stepped surface. The corresponding electron diffraction shows the nanoblade is along [0001] and growth direction $[2\bar{1}\bar{1}0]$.

contrast in a TEM image recorded from a nanoblade reveals that the blade always has a stepped surface (Figure 3.22(e)), consistent to the SEM observation. The corresponding electron diffraction pattern indicates that the blade surfaces are ±(0001), and growth direction $[2\bar{1}\bar{1}0]$ (*a*-axis).

Figure 3.23(a) shows nanopropeller arrays grown in a lower temperature zone (600~650 ^{o}C, step I), and each column is as large as 2-5 μm in diameter. There are aligned nanowires and isosceles triangular-shape nanoblades growing perpendicularly. Fine nanowires (~ 50 nm) grow vertically on the top surface of the nanoblades (Figure

3.23(b)) [note: the wires are only grown on one side of the nanoblades]. The nanoblades are at 60^{o} angle, corresponding to the six-fold symmetry in the c-plane (Figure 3.23(c)). Uniform Sn particles of 50 nm in size are located at the tip

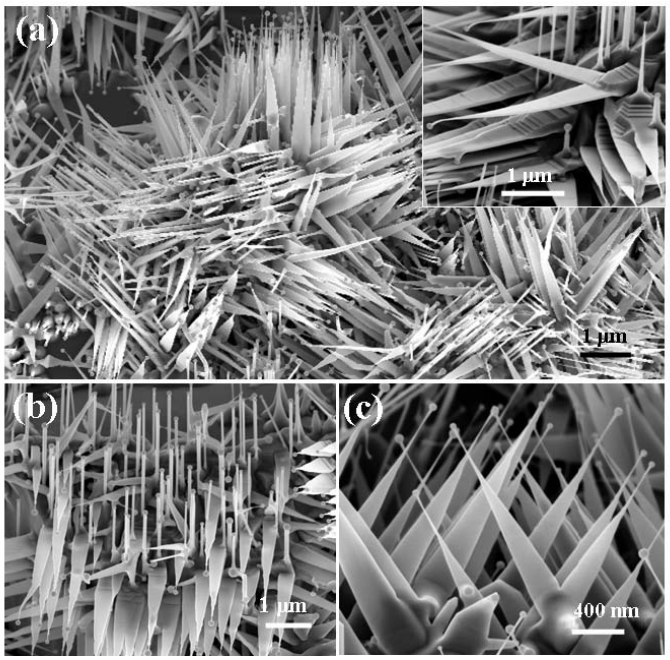

Figure 3.23 (a). SEM image of the as-synthesized ZnO nanostructures, showing arrays of nanowires and nanopropeller blades. Inserted image shows surface steps at the root of the nanoblades. (b) Side view of a bunch of aligned ZnO nanopropeller blades with perpendicularly ordered ZnO nanowires, and (c) top view of 60^{o} crossed nanopropeller blades.

of the nanoblades, and they are eight times smaller than the largest width of the nanoblade. Magnified side view of the nanoblades presents their rectangular cross-section, as inserted in Figure 3.24(a). The smallest width of the triangular-shape nanoblade is ~ 20 nm and the maximum width is ~ 500 nm. The nanoblade has a stepped top surface towards the growth direction, while the surface against the growth direction is smooth. A closer examination at the junction between the nanoblades and the axial nanowire shows major steps.

In addition to the closely packed columns of nanopropeller arrays, freestanding nanopropeller arrays have also been found. Figure 3.24(a) is a side view of a single column of freestanding ZnO nanopropeller arrays formed at relatively low temperature region (~620 ^{o}C (step I)), which is apparently composed of hexagonal symmetrical arrays of ZnO triangular-shape

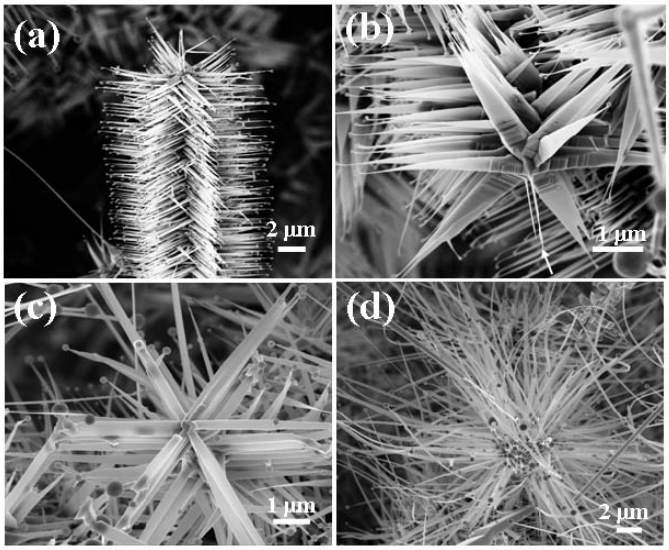

Figure 3.24 Temperature dependence of the grown nanopropeller arrays. (a) SEM image of a single column of the as-synthesized ZnO nanopropeller arrays. (b) Front view of a column of ZnO nanopropeller arrays with nanowires at the central axis, which was collected from a lower temperature zone (~ 620 ^{o}C in Step I); c) a column of ZnO nanopropeller arrays with uniform nanoribbon shape and smoother surface, which was collected from a medium temperature zone (~ 650 ^{o}C in Step I); (d) a column of ZnO nanopropeller arrays with long nanoribbons, which was collected from a higher temperature zone (~ 680 ^{o}C in Step I).

blade of 20-500 nm in width and 4-5 μm in length. There are two nanowires standing out the tip of the symmetry axis, as indicated by an arrowhead in Figure 3.24(b).

Different from the triangular-shaped nanoblades presented in the sample grown in a lower temperature zone (Figure 3.24(b)), nanoblades with uniform widths are found in

a medium temperature zone (Figure 3.24(c)) (~650 ^{o}C (step I)). In a higher temperature zone (~680 ^{o}C (step I)), the nanoblades are long and curved (Figure 3(d)).

The top and bottom surfaces of the nanoblades have different surface morphology. Figure 3.25(a) is a closer side view of the top surfaces of two nanoblades, showing steps perpendicular to the blade direction of $[2\bar{1}\bar{1}0]$. The steps are responsible for the increased blade thickness approaching the root. The bottom surface of the nanoblades is flat and much smoother (fig 3.25(b)). A broken blade reveals its trapezoid cross section (Figure 3.25(c)), indicating that the side surface is not exactly $(01\bar{1}0)$. The shorter width side of the trapezoid corresponds to the stepped top surface, while the longer side to the flat bottom surfaces.

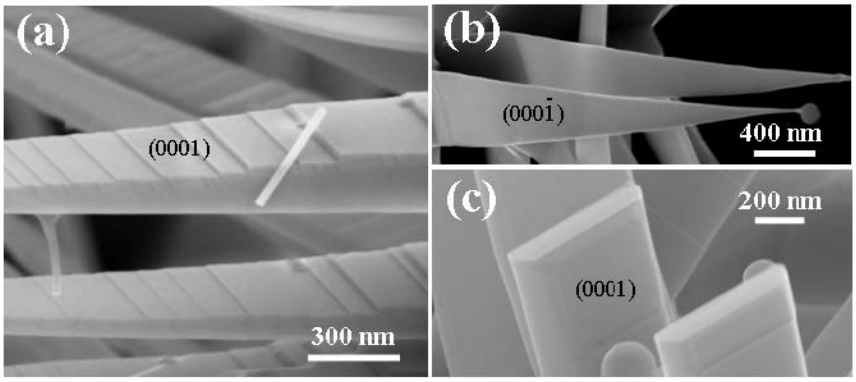

Figure 3.25 (a) Front view of two individual blades, showing surface steps; (b) Back side view of the bottom surfaces of nanoblades, showing smoother surface; (c) trapezoid cross section of a nanoblade.

The growth of ZnO is dominated by the vapor-liquid-solid (VLS) process guided by the Sn catalyst and by the self-catalysis process[149]. ZnO nanobelts have been grown without using catalyst, and ZnO can be self-catalytic active. Initially, the ZnO and SnO_2 powders were reduced by graphite and vaporized in the form of Zn, ZnO, Sn and O vapors. In a lower temperature zone, Sn vapor condenses onto the substrate, which lead

to the growth of ZnO nanowires along [0001] and enclosed by $\{2\bar{1}\bar{1}0\}$ surfaces[1] (Figure 3.26(a)). This is a fast growth process. Then, the Sn vapor condensed later on the surface of the nanowire lead the epitaxial growth of ZnO nanobelts out of the surface of the nanowire, which extend along the six radial

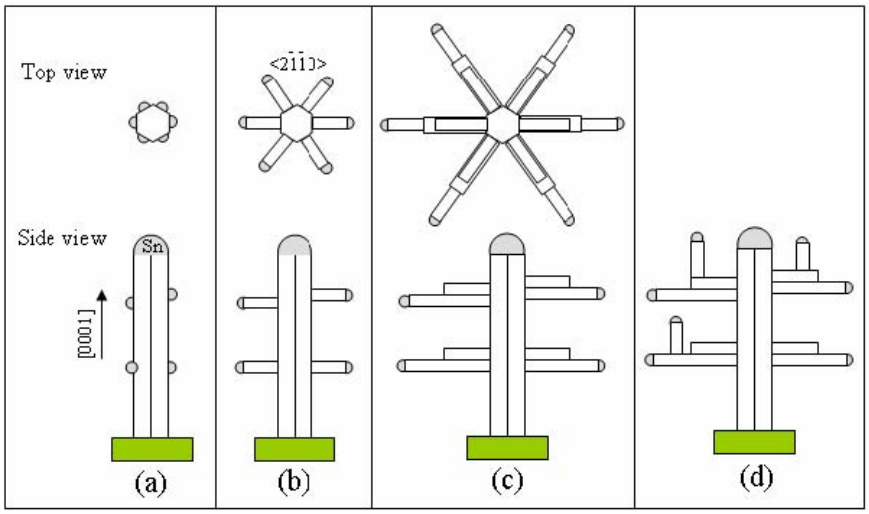

Figure 3.26 Schematic growth process of the nanoblade arrays. The diagram shows only one column of nanopropeller array for simplicity of illustration.

directions: $\pm[2\bar{1}\bar{1}0]$, $\pm[11\bar{2}0]$, $\pm[1\bar{2}10]$, forming the hexagonal symmetric nanoblades (Figure 3.26(b). The nanoblades also grow transversely along $<01\bar{1}0>$ as the growth proceeds along $<2\bar{1}\bar{1}0>$, resulting in growth steps towards the tip (Figure 3.26(c). The later condensed Sn droplets on the surface of the nanoblades lead to the growth of secondary nanowires along c-axis (Figure 3.23(b)), and this growth is along +*c*-axis rather than –*c*-axis due to higher catalytic activity of the Zn-terminated basal plane, which will be discussed next.

The growth morphology depends on the local temperature, surface diffusion rate and availability of Zn-O vapor. In a lower temperature region, a relatively slower surface

diffusion and the decrease in supply of the vapor as more source material being consumed, a triangular-shape structure is formed. On the other hand, a transverse growth along <$10\bar{1}0$> can extend the width of the nanoblades as the growth proceeds along <$2\bar{1}\bar{1}0$>, resulting in the formation of triangular nanoribbon blades (Figure 3.24(b)). In the medium temperature region, a faster diffusion of the Zn-O vapor and higher surface mobility may lead to the formation of uniform and longer nanoblades (Figure 3.24(c)). By the same token, a faster growth along <$2\bar{1}\bar{1}0$> forms longer nanoblades in a higher temperature zone (Figure 3.24(d)).

The c-plane of ZnO is a polar surface, with Zn-terminated (0001) and oxygen-terminated ($000\bar{1}$). Our recent study has found that the (0001)-Zn surface is chemically active in growing nanostructures, but the ($000\bar{1}$)-O is inert.[45] Therefore, further growth along [0001] is possible on the top surface of the nanoblade, resulting in secondary growth of nanowires (Figure 3.23(b), see Figure 3.26(d)) as well as the formation of growth steps, but the ($000\bar{1}$)-O bottom surface is flat without growth although Sn particles may be deposited on the surface. The reason for the formation of the trapezoid shaped cross-section of the nanoblade (with shorter side on (0001)) and surface steps is likely due to a continuous growth along [0001], because the growth tends to reduce the area of the (0001) surface to decrease the surface energy due to polarization, resulting in a shrinkage in the width of the nanoblade along [0001].

In conclusion, this paper presents a two-step high temperature solid-vapor deposition process for synthesis of polar surface dominated ZnO nanopropeller arrays. The axis of the nanopropellers is a straight nanowire along the *c*-axis and enclosed by {$2\bar{1}\bar{1}0$} surfaces; the six-fold symmetric nanoblades are later formed along the

crystallographic equivalent *a*-axes (<$2\bar{1}\bar{1}0$>) perpendicular to the nanowire. The top surface of the nanoblade is the Zn-terminated +*c*-plane, showing surface steps and possible secondary growth of nanowires, while the back surface is the oxygen-terminated –*c*-plane, which is smooth and inert.

3.4 Substrate atomic-termination induced anisotropic growth[150]

Using as-provided Sn as catalyst, a variety of 1D ZnO nanostructures have been achieved. The three fastest growth directions will lead to a diversity group of hierarchical complex ZnO nanostructures. A full understanding of physical and chemical phenomena involved in the growth process is the key for controlled growth of aligned ZnO nanostructures and complex nanostructures. During the process, there are several important highlights needed to be mentioned: 1) upon introducing metallic Sn as catalyst, the ZnO growth becomes complicated, but the three fastest growth directions and specific wurtzite structured ZnO make the three directional growth of nanostructure in an ordered way, which in fact is a self-organization process; 2) during the synthesis, there in fact is a phenomenon of competitive catalyst effect with respect to different growth directions. For example, upon the growth time increase, more and longer piezoelectric nanobelts along [$2\bar{1}\bar{1}0$] or [$01\bar{1}0$] directions formed in comparison with c-directed nanowires. 3). Selective catalyst effect of Sn on polar surfaces of ZnO proved that the charged surfaces could be ultilized for growth of aligned nanowires or nanotrunk islands, which is to be discussed in the following section.

In the vapor-liquid-solid (VLS) growth, it is generally believed that it is the catalyst particle at the tip that determines the size and growth rate of the nanowire, and

the surface termination of the substrate may have little effect on the growth. Controlling the size of the catalyst particles can effectively control the size of semiconductor nanowires.[21] In this section, taking the Sn catalyzed growth of one-dimensional nanostructures of ZnO on a single crystal ZnO substrate as a model system, we show that the substrate atomic termination can critically affect the growth rate and morphology of the grown nanowires in the VLS growth. The growth features on the $\{2\bar{1}\bar{1}0\}$, $\{01\bar{1}0\}$, and ±(0001) surfaces will be elaborated. It is suggested that the interaction between the surface ionic charge with the catalyst particle is likely responsible for the observed growth phenomena.

The sample used in this study was prepared using a two-step high temperature vapor-solid deposition process, which was used for growing the polar surface dominated nanopropeller arrays of ZnO. The solid vapor deposition here involves using the same experimental set-up as that for nanojunction arrays. Commercial (Alfa Aesor) ZnO and SnO_2 powders, and graphite with molar ratio of 3:4:1.5 were mixed, ground and then loaded on an alumina boat and positioned at the center of the alumina tube. The evaporation was conducted at 1100 ^oC for 60 minutes (step I) and then up to 1300 ^oC for half an hour (step II) under pressure of 200 mbar. The N_2 carrier gas flow rate is controlled at 20 sccm (standard cubic centimeters per minute). The desired structures grew on a polycrystalline Al_2O_3 substrate in a temperature zone ranging of 600~700 ^oC and 800~900 ^oC respectively corresponding to lower and higher temperature duration periods.

The as-grown sample has many large crystals of ZnO formed on the alumina substrate, and these ZnO crystals serve as the substrate for growing ZnO nanostructures.

Figure 3.27a shows a typical scanning electron microscopy (SEM) image of a large block of the as-grown ZnO nanostructures, which appears like a “brush” of 40-50 μm in length, 10-15 μm in width and several micron in thickness. A large ZnO crystal is the substrate with aligned ZnO nanostructures growing out of the five exposed surfaces and displaying different growth features. Energy dispersive spectroscopy (EDS) analysis in SEM proves that the as-grown base and the as-grown nanostructures are ZnO with Sn balls at the tips. The nanostructures grown at the left- and right-hand side facets are distributed symmetrically, while the top and bottom surfaces have asymmetrical nanostructures of different dimensionality and morphology. On the top facet, the grown elements are short and cone-like trunks of ~1 μm in height and 800 nm in width. While on the bottom surfaces, uniform nanowires with diameter around 100 nm and height around 2 μm are grown. Based on our recent study on ZnO nanopropellers the Zn-terminated (0001) planes is active for nanowire growth, while the oxygen-terminated $(000\bar{1})$ plane is inert with Sn guided growth, the top and bottom surfaces in Figure 3.27a are respectively $(000\bar{1})$ and +(0001).

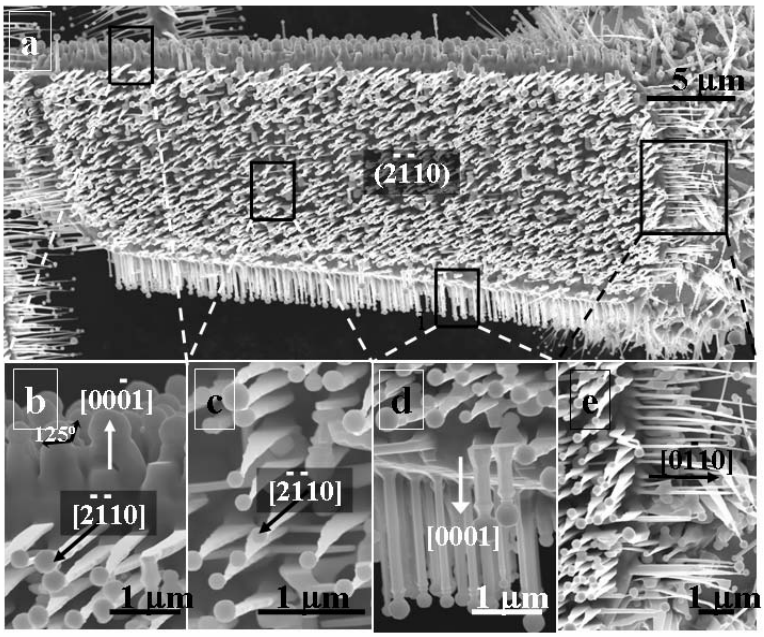

Figure 3.27 SEM images of the as-synthesized ZnO nanostructures growing out of the five surfaces of a ZnO substrate. (b-e) Enlarged areas as marked in (a). The asymmetric growth of nanostructures on the substrate surfaces of different structure characteristics are presented (see text).

For the nanotrunks grown on the $(000\bar{1})$ surface, the contact angle between the Sn ball and the trunk top is ~125 ± 5° (Figure 3.27b). Figure 3.27d is the magnified side view of the as-grown nanowires on the Zn-terminated (0001) surface. The aligned ZnO nanowires grown out of the Zn-terminated (0001) surface have a uniform diameter of ~ 100 nm and length ~ 2 μm, and six side surfaces $\{2\bar{1}\bar{1}0\}$ (Figure 3.27d). The nanowires are aligned and they have an epitaxial orientation with the substrate. The contact angle between the Sn particle and the nanowire growth front is ~150 ±5°.

Figure 3.27c shows the well-aligned ZnO nanoribbons growing out of the $(2\bar{1}\bar{1}0)$ surface of the substrate, with epitaxial growth direction $[2\bar{1}\bar{1}0]$, top and bottom faces ±(0001), and side stepped $(01\bar{1}0)$ surfaces. The width of the nanoribbon is not uniform

along the entire length. The nanoribbon has the largest width of ~ 300 nm at the contact point with the substrate, the smallest width of ~10 nm at the contact with the Sn catalyst, and a length ~ 1 μm. Figure 3.27e shows the normally orientated nanoribbons on the right-hand side facet of the substrate, which grow along $[01\bar{1}0]$. It is also shown that the widths of the nanoribbons along $[2\bar{1}\bar{1}0]$ and $[01\bar{1}0]$ are at the same order of magnitude, tens of nanometers, and the length of the nanoribbons along $[01\bar{1}0]$ is around 3 μm.

The non-polar surface shows symmetric growth. Figure 3.28 is a top view along the c-axis of the nanowires grown on a ZnO substrate. It is apparent that the triangular nanoribbons grown symmetrically on the top and bottom non-polar facets of $\pm(2\bar{1}\bar{1}0)$. From Figure 3.28b it was found that the cone trunks formed vertically on the O-terminated $(000\bar{1})$ top surface have roughly faceted side surfaces, defined by $\{2\bar{1}\bar{1}0\}$ and displaying hexagon-based pyramid. In Figure 3.28c, the broken triangular nanoribbons clearly present their rectangular cross-section of ~300 nm in width and ~ 40 nm in thickness. A closer image at the top surface of the nanoribbon displays a smooth top surface (Figure 3.28d), corresponding to the chemically sluggish O-terminated $(000\bar{1})$ polar surface of ZnO, in consistence to our previous results.

Figure 3.29a shows another SEM image viewing from the top of the brush structure. On the top and bottom O-$(000\bar{1})$ and Zn-(0001) ZnO surfaces, aligned shorter and wider pyramidal ZnO trunks and longer and narrower hexagonal ZnO nanowires are grown, respectively. Different

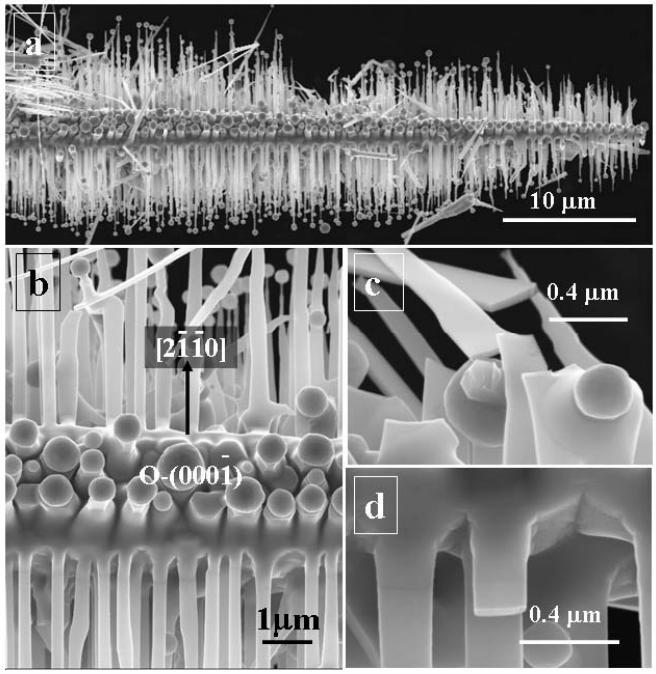

Figure 3.28 [0001] directional top view of the as-grown ZnO nanostructures, showing symmetric growth of triangular nanoribbons along ±[2$\bar{1}\bar{1}$0]. (b) A closer top view of the nanotrunks grown out of the O-terminated (000$\bar{1}$) ZnO surface, revealing the hexagonal base contour of nanopyramids; (c) broken triangular nanoribbons showing rectangular cross sections; (d) smooth top surfaces of triangular nanoribbons corresponding to the O-terminated (000$\bar{1}$) polar surface of ZnO.

from the cases in Figs 3.27 and 3.28, the nanoribbons grown on the large (2$\bar{1}\bar{1}$0) substrate surface could have a smaller width-to-thickness ratio. The grown nanoribbons are enclosed by relatively larger and smoother ±(01$\bar{1}$0) surfaces and smaller ± (0001) surfaces. Steps are introduced on the side surfaces, and the nanoribbon becomes sharper toward the tip (Figure 3.29b). Interval between the nanoribbons is quite regular and the aligned ribbons are spaced close to periodic (Figure 3.29c).

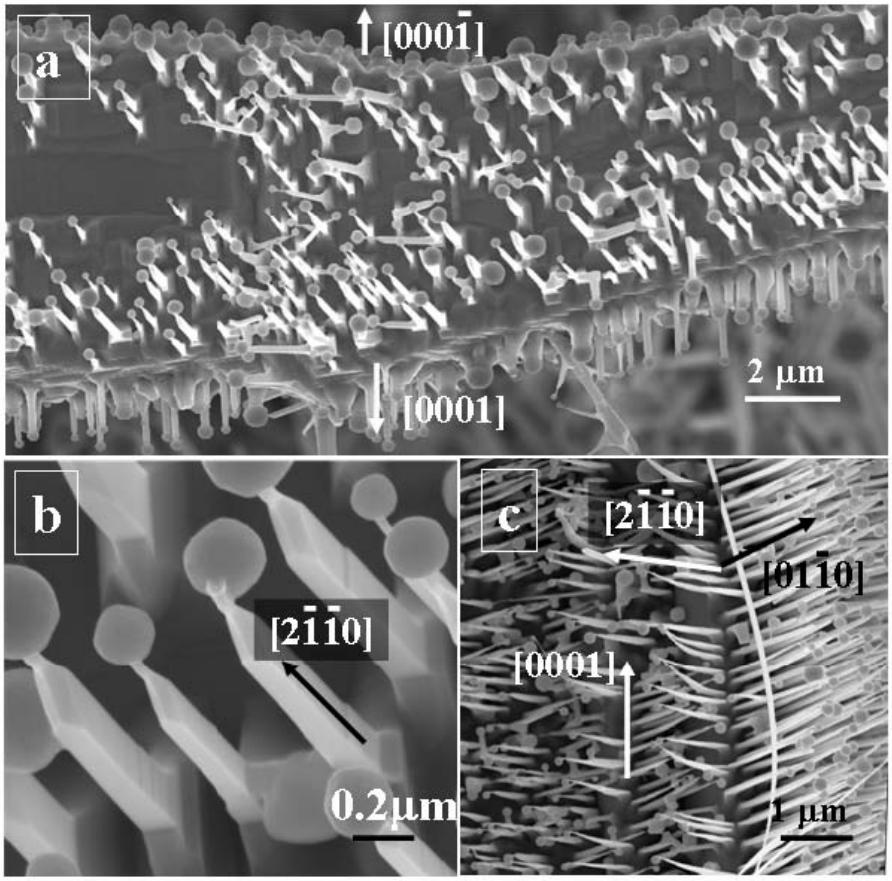

Figure 3.29 (a) The as-grown ZnO nanostructures with sparsely covered (2$\bar{1}\bar{1}$0) plane by ZnO nanoribbons; (b) a closer view of the nanoribbons normal to (2$\bar{1}\bar{1}$0) plane, indicating nanoribbons with small width-thickness ratio; c) periodically aligned arrays of ZnO nanoribbons with growth directions [2$\bar{1}\bar{1}$0] and [01$\bar{1}$0] on the two surfaces, respectively.

Based on the SEM image in Figure 3.27, we have calculated the volumes of the as-grown ZnO nanostructures and the Sn particles covering on unit substrate surface area of the ± (0001) polar surfaces. We assume the nanostructures on both polar surfaces are uniformly distributed, and the Sn particles are spherical, ZnO nanowires are cylindrical, and the ZnO pyramidal trunks have a hexagon-base. The estimated volumes of ZnO nanostructures and Sn catalysts per unit area are: 197 ± 5 (ZnO nanowires) and 600 ± 10 nm (Sn catalysts) for the (0001) substrate surface; and 318 ± 9 (ZnO pyramidal trunks)

and 854 ± 20 nm (catalyst Sn) for the $(000\bar{1})$ substrate surface, respectively. The volume ratio of the ZnO material per unit area on the (0001) and $(000\bar{1})$ substrate surfaces is 1:1.6, and the volume ratio of the Sn material per unit area on the (0001) and $(000\bar{1})$ substrate surfaces is 1:1.42. The volume ratios of ZnO:Sn on the (0001) and $(000\bar{1})$ substrate surfaces are 3 and 2.7, respectively, indicating that the sticking rates of the ZnO vapor onto the Sn surfaces does not have significant difference on the two substrate surfaces, but the amounts of ZnO and Sn deposited on the $(000\bar{1})$ substrate surface are about 50% more than that onto the (0001) substrate surface, indicating high surface adsorption rate of Sn onto the $(000\bar{1})$ substrate surface.

From Figs 3.27b and d, the contacting angle between the Sn particle and the ZnO nanowire is ~150^o on the Zn-terminated (0001) substrate surface, and is ~125^o on the oxygen-terminated $(000\bar{1})$ substrate surface, indicating that the $(000\bar{1})$ surface has a higher degree of wetting contact with the Sn particle than the (0001) surface.

Based on the experimental data presented, a growth model for the ZnO nanostructure growth on ± (0001) polar surfaces is proposed. The entire growth is dominated by VLS. The Sn catalyst was reduced from SnO_2 added in the source material. Thermal reduction of SnO_2 may result in some charged species and neutral species:

$$SnO_2 \leftrightarrow xSn^{2+} + (1\text{-}x)Sn + 2xO^{2-} + (1\text{-}x)O_2$$

Where x represents the percentage of charged Sn^{2+} ions after the decomposition. The charged species may recombine and condense onto the substrate to form a charged catalyst particle $(Sn)^+$. A neutral Sn particle can also be positively charged since metal atoms tend to lose electrons. For the Zn^{2+}-terminated (0001) ZnO substrate surface with positive charges, the positively charged $(Sn)^+$ particle has a small repulsion with the

substrate due to the electrostatic interaction, but it still tends to stick onto the surface due to a stronger adhesion force. The consequence of the electrostatic repulsion results in a larger contact angle between the particle and the substrate (Figure 3.30a). The Sn particle initiates the growth of ZnO nanowire (Figure 3.30b), and the nanowire has an epitaxial orientation relationship with the substrate due to least lattice mismatch. The nanowire continues to grow following the VLS growth process (Figure 3.30c).

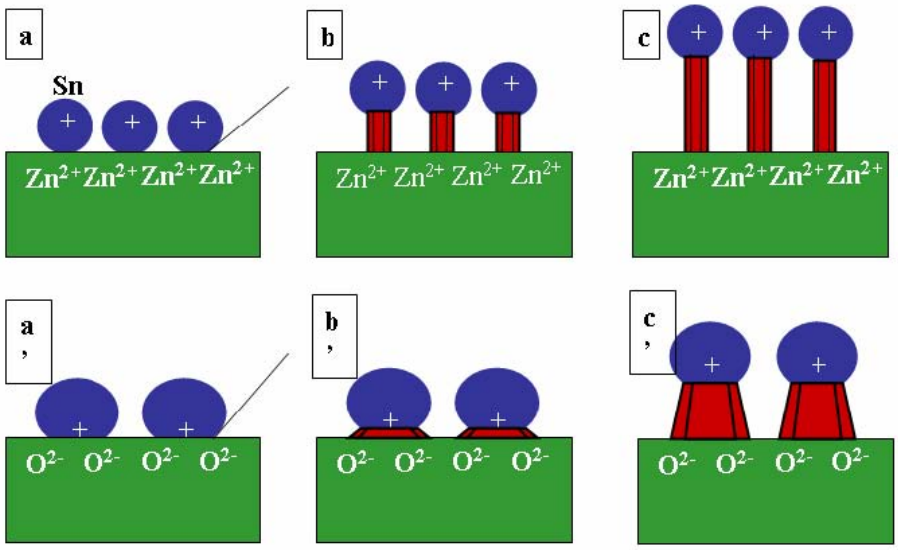

Figure 3.30 Growth model of the ZnO nanowires on Zn-terminated (0001) polar surface (a-c) and O-terminated ($000\bar{1}$) polar surface (a'-c') (see text).

For the oxygen-terminated ($000\bar{1}$) ZnO substrate surface with negative charges, the attraction between the substrate surface and the positively charged $(Sn)^+$ particle results in a smaller contact angle and larger contact area (Figure 3.30a'). Naturally, there is less population density of Sn particle on the substrate surface and each of them is larger. The large Sn particle initiates the growth of nanorods (Figure 3.30b'). As the growth continue and the distance between the particle and the substrate surface is further away, the contact area between the particle and the ZnO nanorod may reduce slightly due

to the reduced electrostatic attraction, possibly resulting in a shrinkage in nanorod size as the growth proceed, and forming a short nanotrunk with a hexagon-base (Figure 3.30c').

In comparison to the growth on the (0001) substrate surface, the electrostatic attraction between the $(000\bar{1})$ substrate surface and the Sn particles tends to attract a high density of Sn onto the surface at the early growth stage. These Sn particles are most effective in attracting the ZnO molecular species, resulting in a higher density of ZnO deposition on the $(000\bar{1})$ substrate surface. But the ratio of ZnO:Sn in each case remains approximately a constant, as expected from the VLS process in which it is the catalyst surface that is responsible for adsorbing the incoming molecular species.

For the non-polar $\pm(2\bar{1}\bar{1}0)$ and $\pm(01\bar{1}0)$ substrate surfaces, the growth on the surfaces shows symmetric features and the growth still follows the VLS growth process. Take the $(2\bar{1}\bar{1}0)$ substrate surface as an example, nanoribbons grow epitaxially on the substrate and they are enclosed by large $\pm(01\bar{1}0)$ and small ± (0001) surfaces, and a gradual lateral growth along $\pm[01\bar{1}0]$ results in a triangular-like shape (See Figure 3.27c).

In summary, Sn catalyzed ZnO nanostructure growth on a single crystal ZnO substrate has been used as a model system for elaborating the effect of polar surfaces on VLS growth of nanowires. For the Zn-terminated (0001) substrate surface, due to an electrostatic repulsion between the Sn particle and the substrate, uniform, long and epitaxially aligned nanowires have been grown. For the oxygen-terminated $(000\bar{1})$ substrate surface, short nanotrunks have been grown, which are attributed to a stronger adhesion between the substrate and the particle at the initial stage of growth. These asymmetric growth features are related to the atomic-termination of the substrate, surface

charges and interface adhesion. But the volume ratio of ZnO:Sn on the two polar surfaces remains about the same, indicating that the VLS process is dominant. For the non-polar surfaces such as $\pm(2\bar{1}\bar{1}0)$ [or $\pm(01\bar{1}0)$], symmetric nanoribbons have been grown. The growth model proposed here might provide some new insight in understanding the physical chemical process involved in VLS growth.

3.5 Summary

Through a systematic investigation on the Sn-catalyzed ZnO nanostructure, an improved understanding of the chemical and physical process occurred in the growth of hierarchical nanostructures has been achieved:

1. By using a simple vapor transport deposition method, well-aligned ZnO nanorods with six identical facets of $\{2\bar{1}\bar{1}0\}$ and orientation ordering have been successfully synthesized. Reduced Sn from SnO_2 acts as catalysts that guide the aligned growth of ZnO nanorods. The dimensions and morphological distribution of nanorods could be tuned by controlling the growth time and the content of graphite as the vapor-generating agent. It is suggested that Sn can be an effective catalyst, which can be used to grow crystallographic-orientation aligned nanorods;
2. Using electron diffraction and high-resolution electron microscopy, we studied the interface relationship between catalyst Sn particles and their guided ZnO 1D nanostructures. Tin catalyst not only can guide [0001] growth nanowires, but also can guide $[01\bar{1}0]$ and $[2\bar{1}\bar{1}0]$ growth nanobelts. The orientation

relationship between the [0001] growth ZnO nanowire and the single crystal β phase Sn particle is: $(020)_{Sn}$ || $(0001)_{ZnO}$, $[\bar{1}01]_{Sn}$ || $[2\bar{1}\bar{1}0]_{ZnO}$. For nanobelts growing along $[01\bar{1}0]$ and $[2\bar{1}\bar{1}0]$, the orientation relationships are $(200)_{Sn}$ || $(01\bar{1}0)_{ZnO}$, $[020]_{Sn}$ || $[0001]_{ZnO}$ and $(200)_{Sn}$ || $(2\bar{1}\bar{1}0)_{ZnO}$, $[020]_{Sn}$ || $[0001]_{ZnO}$, respectively. One tin particle can initiate the growth of two 1D nanostructures; the tin particle is single crystal post the growth and it preserves epitaxial relationships with the grown nanostructures.

3. Using Sn/ZnO as a model system, we showed that the interfacial region of the tin particle with the ZnO nanowire/nanobelt could be crystalline or atomically ordered during the VLS growth, although the local growth temperature is much higher than the melting point of tin, and it may play a key role in initiating 1D nanostructure. The interface prefers to take the least lattice mismatch, thus, the crystalline orientation of the tin particle may determine the growth direction and the side surfaces of the nanowires/nanobelts.

4. Sn catalyzed ZnO nanostructure growth on a single crystal ZnO substrate has been used as a model system for elaborating the effect of polar surfaces on VLS growth of nanowires. For the Zn-terminated (0001) substrate surface, due to an electrostatic repulsion between the Sn particle and the substrate, uniform, long and epitaxially aligned nanowires have been grown. For the oxygen-terminated $(000\bar{1})$ substrate surface, short nanotrunks have been grown, which are attributed to a stronger adhesion between the substrate and the particle at the initial stage of growth. These asymmetric growth features are related to the atomic-termination of the substrate, surface charges and interface adhesion. But

the volume ratio of ZnO:Sn on the two polar surfaces remains about the same, indicating that the VLS process is dominant. For the non-polar surfaces such as $\pm(2\bar{1}\bar{1}0)$ [or $\pm(01\bar{1}0)$], symmetric nanoribbons have been grown. The growth model proposed here might provide some new insight in understanding the physical chemical process involved in VLS growth.

5. By thermal evaporating a mixture of ZnO and SnO_2, self-assembled nanowire-nanoribbon junction arrays of ZnO have been synthesized. The growth is dominated by the VLS mechanism and Sn particles reduced from SnO_2 serve as the catalyst for the growth. The axial nanowires (the "rattans") are the result of fast growth along [0001], and the surrounding "tadpole-like" nanoribbons are the growth along $[10\bar{1}0]$. An isotropic growth along six $[10\bar{1}0]$ results in the ordered radial distribution of the nanoribbons around the axial nanowire. The junction arrays of ZnO structures reported here are likely to have ultra-high surface sensitivity due to the unique structure, and they are a candidate for building sensors with ultra-high sensitivity. It may be possible that, through further adjustment of synthesis parameters including temperature, pressure, source composition, etc., more perfectly and orderly self-assembled junction arrays could be prepared.

6. A two-step high temperature solid-vapor deposition process has been successfully used for achieving polar surface dominated ZnO nanopropeller arrays. The axis of the nanopropellers is a straight nanowire along the *c*-axis and enclosed by $\{2\bar{1}\bar{1}0\}$ surfaces; the six-fold symmetric nanoblades are later formed along the crystallographic equivalent *a*-axes ($<2\bar{1}\bar{1}0>$) perpendicular to

the nanowire. The top surface of the nanoblade is the Zn-terminated +*c*-plane, showing surface steps and possible secondary growth of nanowires, while the back surface is the oxygen-terminated –*c*-plane, which is smooth and inert.

CHAPTER 4

POLAR SURFACE DOMINATED NANOARCHITECTURES OF PIEZOELECTRIC ZINC OXIDE

As inspired by carbon nanotubes, research in 1D nanomaterials is the forefront in nanotechnology due to their unique electronic, optical, mechanical and chemical properties. For non-carbon based 1D nanostructures, devices have been fabricated utilizing semiconductor nanowires, such as Si and InP. Piezoelectric effect, an important phenomenon that couples electro-mechanical behaviors, appears to be forgotten in nanomaterials research. None of the well-known nanostructures, such as quantum dots and carbon nanotubes, exhibits an intrinsic piezoelectricity. This is an area that remains to be explored because piezoelectric effect at nano-scale is critical in electromechanical sensors, actuators and resonators.

In 2001, semiconducting oxide nanobelts (nanoribbons) have been discovered, giving rise to a brand new configuration with respect to the nanowire configuration. The nanobelt is a 1D nanostructure that has a rectangular cross-section with well-defined crystal surfaces. As inspired by this discovery, research in functional oxide based 1D nanostructures is rapidly expanding and is becoming a forefront research in nanotechnology. In the past four years, synthesis of belt-like oxide, sulfides, and selenided based 1D nanostructures has drawn a lot of attention due to their unique geometrical structure and functional properties as well as their potential applications as building blocks for nanoscale electronic and optoelectronic devices. It is worth mentioning that a variety of functional nanodevices such as field effect transistors and

ultra-sensitive nano-size gas sensors, nanoresonators and nanocantilevers have been fabricated based on individual nanobelts. In this section, the main focus will be on the belt-like ZnO nanostructures.

4. 1 Polar Surface dominated Zinc Oxide nanobelts[151 ,152]

Wurtzite zinc oxide has a hexagonal structure (space group *C6mc*) with lattice parameters a = 0.3296, and c = 0.5206 nm, which is of a number of alternating planes composed of tetrahedrally coordinated O^{2-} and Zn^{2+} ions, stacked alternatively along the *c*-axis (Figure 4.1a). The tetrahedral coordination in ZnO results in non-central symmetric structure, and consequently the piezoelectricity and pyroelectricity. Another important characteristic of ZnO is the polar surfaces. The most common polar surface is the basal plane. The oppositely charged ions produce positively charged Zn-(0001) and negatively charged O-$(000\bar{1})$ surfaces, resulting in a normal dipole moment and spontaneous polarization along the *c*-axis.

For the (0001) polar surface dominated nanobelt, its structure can be approximated to be a capacitor with two parallel charged plates (Figure 4.1b). The polar nanobelt tends to roll over into an enclosed ring to reduce the electrostatic energy. A spiral shape is also possible for reducing the electrostatic energy. The formation of the nanorings and nanohelixes can be understood from the nature of the polar surfaces. If the surface charges are uncompensated during the growth, the spontaneous polarization induces electrostatic energy due to the dipole moment, but rolling up to form a circular ring would minimize or neutralize the overall dipole moment, reducing the electrostatic energy. On the other hand, bending of the nanobelt produces elastic energy. The stable

shape of the nanobelt is determined by the minimization of the total energy contributed by spontaneous polarization and elasticity. If the nanobelt is rolled uniradically loop-by-loop, the repulsive force between the charged surfaces stretches the nanohelix, while the elastic deformation force pulls the loops together; the balance between the two forms the nanohelix/nanospring. In all of the cases illustrated here, the polar-axis *c* is pointing towards the center.

A new structure configuration is introduced if the direction of the spontaneous polarization is rotated for 90^{o}. The nanobelt has polar charges on its top and bottom surfaces (Figure 4.1c). If the surface charges are uncompensated during growth, the nanobelt may tend to fold itself as its length gets longer to minimize the area of the polar surface. One possible way is to interface the positively charged Zn-(0001) plane (top surface) with the negatively charged O-$(000\bar{1})$ plane (bottom surface), resulting in neutralization of the local polar charges and the reduced surface area, thus, forming a loop with an overlapped end. The long-range electrostatic interaction is likely to be the initial driving force for folding the nanobelt to form the first loop for the subsequent growth. As the growth continues, the nanobelt may be naturally attracted onto the rim of the nanoring due to electrostatic interaction and extends parallel to the rim of the nanoring to neutralize the local polar charge and reduce the surface area, resulting in the formation of a self-coiled, co-axial, uni-radius, multi-looped nanoring structure.

Structurally, ZnO has three-types of fast growth directions: $<2\bar{1}\bar{1}0>$ ($\pm[2\bar{1}\bar{1}0]$, $\pm[\bar{1}2\bar{1}0]$, $\pm[\bar{1}\bar{1}20]$); $<01\bar{1}0>$ ($\pm[01\bar{1}0]$, $\pm[10\bar{1}0]$, $\pm[1\bar{1}00]$); and $\pm[0001]$. Together with the polar surfaces due to atomic terminations, ZnO exhibits a wide range of novel

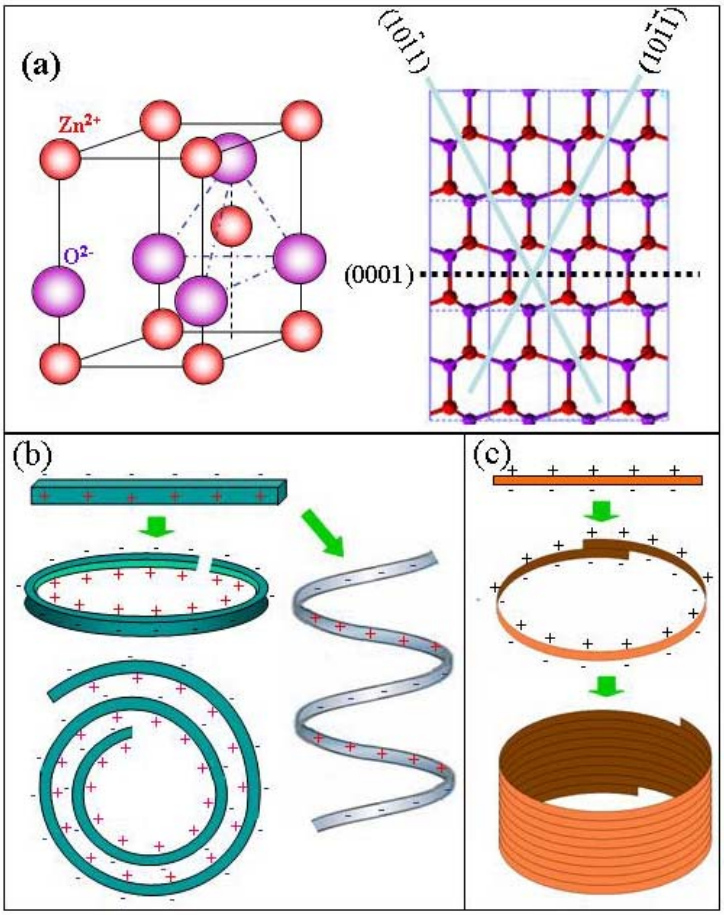

Figure 4.1 (a) Three-dimensional structure model of the unit cell of ZnO, and the corresponding projection along *a*-axis, showing the polar surfaces terminated with Zn and O, respectively. (b) Schematic model of a polar nanobelt, and the possible nanostructures created by folding the polar nanobelt with it polar direction pointing towards the center, forming nanoring, nanospiral and nanohelixes. (c) Model of a polar nanobelt and its self-coiling process for forming a multi-looped ring by folding the nanobelt with its polar direction pointing to the axial direction of the ring. The nanoring is initiated by folding a nanobelt into a loop with overlapped ends due to long-range electrostatic interaction among the polar charges; the short-range chemical bonding stabilizes the coiled ring structure; and the spontaneous self-coiling of the nanobelt is driven by minimizing the energy contributed by polar charges, surface area and elastic deformation.

structures that can be grown by tuning the growth rates along these directions. These are the fundamental principles for understanding the formation of numerous ZnO nanostructures.

The polar surface dominated ZnO nanostructures were grown by a high temperature solid-vapor deposition process. The raw material could be pure ZnO or a mixture of ZnO (melting point 1975 ^{o}C) with a certain amount of some doping materials, such as indium oxide and lithium carbonate powders, which was placed at the highest temperature zone of a horizontal tube furnace. Before heating to a desired temperature, the tube furnace was evacuated to ~ 10^{-3} torr to remove the residual oxygen. ZnO decomposes into Zn^{2+} and O^{2-} at high temperature (1350-1400^{o}C) and low pressure (~ 10^{-3} torr), and this decomposition process is the key step for controlling the anisotropic growth of the nanobelts. The Ar carrier gas was introduced at a flux of 25-50 sccm (standard cubic centimeters per minute). The condensation products were deposited onto an alumina/silicon substrate placed in a lower temperature zone under Ar pressure of 200-500 torr.

4. 2 Nanobows and Nanorings [153, 154, 155, 156]

Nanobows are novel nanostructures found recently in growth of nanorings. Continuous and uniform bending of nanobelts into semi-rings is a characteristic of all nanobows. Two types of nanobows have been found. One is the free standing nanobows extended from nanowires or nanorods. The other is the nanobows directly rooted on the deposition substrate. Figure 4.2(a) shows a hexagonal ZnO rod with a ZnO nanobelt grown from one of its six primary crystallographic facets, ended on the other side facet of

the hexagonal nanorod. The rod grows along [0001] with side surfaces of $\{2\bar{1}\bar{1}0\}$ or $\{01\bar{1}0\}$. Based on the characteristics of ZnO nanostructures, the inner arc of the nanobow will be Zn-terminated or O-terminated. In Figure 4.2b, two other types of nanobows of ~3 μm in width directly rooted at polycrystalline alumina substrate. Figure 4.2c shows a circular platelet formed by {0001} polar surfaces. Figure 4.2d displays a conjuctional structure of a nanobow and a bow-like platelet.

A mechanism about the formation of nanorings has been proposed as following[97]. For a thin, straight polar-surface-dominated (PSD) nanobelt, the spontaneous polarization-induced electrostatic energy decreases upon rolling into a circular ring due to the neutralization of the dipole moment. However, the elastic energy introduced during

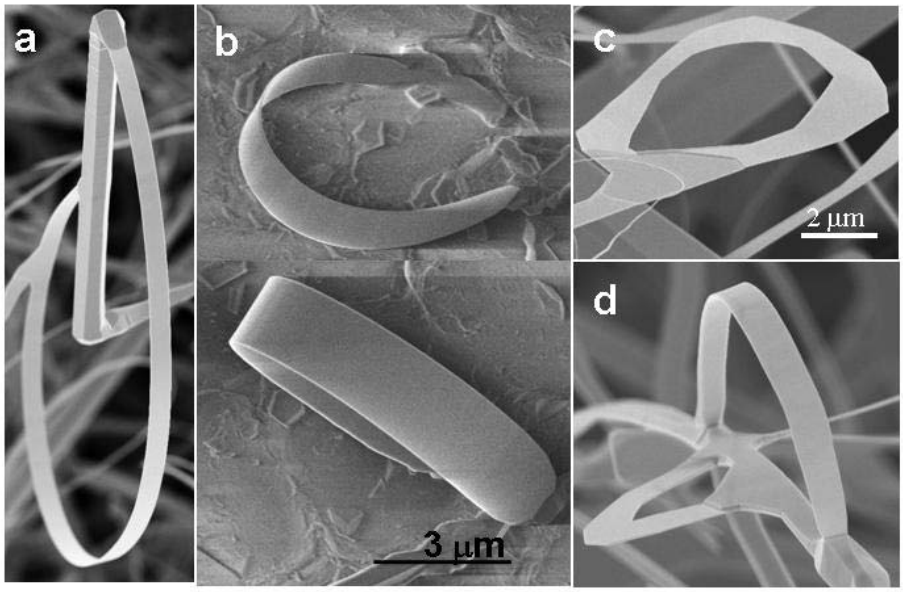

Figure 4.2 (a) ZnO nanobows made from individual polar-surface-dominated single-crystal nanobelt in conjunction with a hexagonal ZnO nanowire. (b) two ZnO nanobow directly rooted on polycrystalline alumina substrate. (c) bow like circular platelet of ZnO. (d). A combination nanoarchitecture of a nanobow and a bow like circular platelet of ZnO.

deformation increases. If the nanobelt is sufficiently thin (~10 nm), the former can overcome the latter, so that the total energy reduces by forming a ring. The stable shape of the ring is dictated by the minimization of the total energy contributed by spontaneous polarization and elasticity. This is the electrostatic polar-charge model.

By adjusting the raw materials with the introduction of impurities, such as indium, a seamless nanoring structure of ZnO has been synthesized (Figure 4.3). TEM imaging and diffraction analysis have proved that the nanoring is a single-crystal entity with circular shape. The single-crystal structure referred here means a complete nanoring that is made of a single crystalline ribbon bent evenly at the curvature of the nanoring. Although the radius of the ring is large, its thickness could be ranging from less than 10

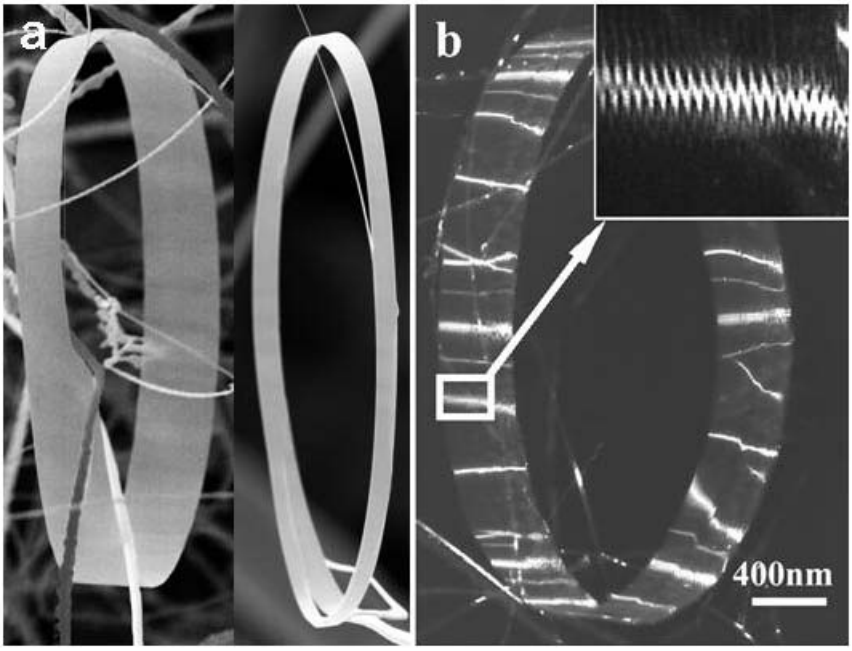

Figure 4.3 Seamless single-crystal nanorings of ZnO. (a) SEM images of two nanorings. (b) A dark field TEM image of a nanoring, the inset in (b) is an enlargement of a local region, displaying the contrast produced by the uni-radius, loop-by-loop self-coiling nanobelt.

nm to over 50 nm. The nanoring is made of a loop-by-loop co-axial, uni-radius, epitaxial-coiling of a nanobelt, which is shown in the dard field TEM image Figure 4.3b, the inset enlarged image corresponding to the white squared area shows the contrast due to the periodical looping circles.

The growth of the nanoring structures can be understood from the polar surfaces of the ZnO nanobelt. The polar-nanobelt shown in Figure 4.3b grows along $[10\bar{1}0]$, with side surfaces $\pm(1\bar{2}10)$ and top/bottom surfaces $\pm(0001)$, and has a typical width of ~15 nm and thickness ~10 nm. The nanobelt has polar charges on its top and bottom surfaces (Figure 4.4a). If the surface charges are uncompensated during growth, the nanobelt may tend to fold itself as its length getting longer to minimize the area of the polar surface. One possible way is to interface the positively charged Zn-(0001) plane (top surface) with the negatively charged O-(0001) plane (bottom surface), resulting in neutralization of the local polar charges and the reduced surface area, thus, forming a loop with an overlapped end (Figure 4.4b). This type of folding is 90^o with respect to the folding direction for forming the nanospring or nanospiral, possibly due to the difference in aspect ratio of the nanobelts and relative size of the polar surfaces. The radius of the loop may be determined by the initial folding of the nanobelt at the initial growth, but the size of the loop cannot be too small to reduce the elastic deformation energy. The total energy involved in the process coming from polar charges, surface area and elastic deformation. The long-range electrostatic interaction is likely to be the initial driving force for folding the nanobelt to form the first loop for the subsequent growth. This is the nucleation of the nanoring.

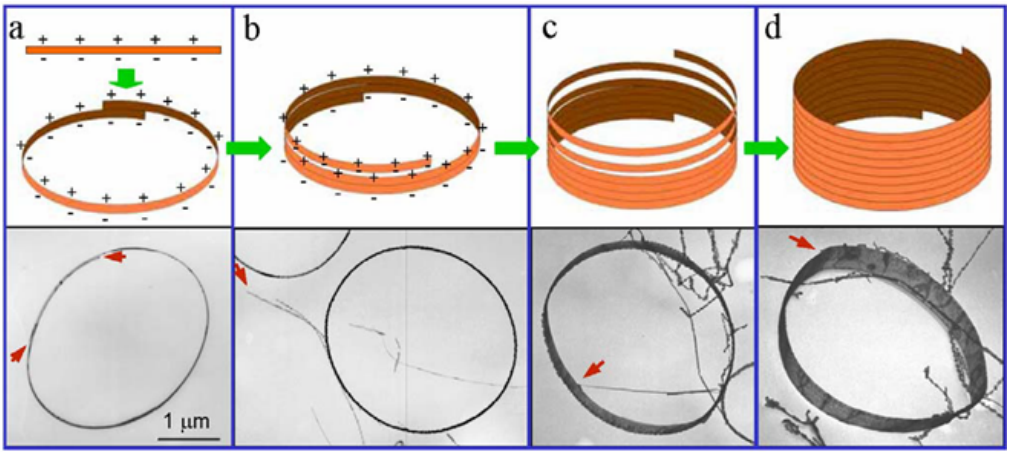

Figure 4.4 a) Model of a polar nanobelt. Polar surface induced formation of (b) nanoring, (c) nanospiral and (d) nanohelixes of ZnO and their formation processes.

As the growth continues, the nanobelt may be naturally attracted onto the rim of the nanoring due to electrostatic interaction and extends parallel to the rim of the nanoring to neutralize the local polar charge and reduce the surface area, resulting in the formation of a self-coiled, co-axial, uni-radius, multi-looped nanoring structure (Figure 4.4c). The self-assembly is spontaneous, which means that the self-coiling along the rim proceeds as the nanobelt grows. The reduced surface area and the formation of chemical bonds (short-range force) between the loops stabilize the coiled structure. The width of the nanoring increases as more loops winding along the nanoring axis, and all of them remain in the same crystal orientation (Figure 4.4d). Since the growth was carried out in a temperature region of 200-400 ^{o}C, “epitaxial sintering” of the adjacent loops forms a single-crystal cylindrical nanoring structure, and the loops of the nanobelt are joined by chemical bonds as a single entity. A uni-radius and perfectly aligned coiling is energetically favorable because of the complete neutralization of the local polar charges

inside the nanoring and the reduced surface area. This is the “slinky” growth model of the nanoring. The charge model of the nanoring is analogous to that of a single alpha helix.

4. 3 Single Crystal Nanosprings[157]

Helix or spiral is a unique shape from the nature. In nature, a good example can be the DNA double-helices[158]. In the artificial nano regime, a number of inorganic materials have been achieved in helical/spiral shape. For example, carbon nanotube coils [159] are created when paired pentagon-heptagon atomic-rings arrange themselves periodically within the hexagonal carbon network[160]. Formation of nanosprings of amorphous silica has been thought to occur through a perturbation during the growth of a straight nanowire[161]. Helical structures of SiC[162] are proposed to be a screw-dislocation-driven growth process. Using the difference in surface stress on the two surfaces, rings and tubes of strained bi-layer thin films, such as Si/SiGe, have been made[163].

ZnO is a good example to show a unique capability to display in a spiral shape. It is known that, due to differences in surface energies among (0001), $\{01\bar{1}0\}$ and $\{2\bar{1}\bar{1}0\}$, freestanding nanobelts and nanowires of ZnO are usually dominated by the lower energy, non-polar surfaces such as $\{01\bar{1}0\}$ and $\{2\bar{1}\bar{1}0\}$. There are two types of synthesis that can produce the single crystal nanospirals. One is through introducing doping, such as In and/or Li, ZnO nanobelts dominated by the (0001) polar surfaces can be grown. The other is that pure ZnO will be used as the only source, which is the main focus of this section.

In the doping case, the nanobelt grows along $[2\bar{1}\bar{1}0]$ (the *a*-axis), with its top/bottom large surface ±(0001) and the side surfaces ± $(01\bar{1}0)$. The typical thickness is of 5 – 20 nm and the belt has a large aspect ratio of ~1:4, allowing a great flexibility and toughness for the nanobelts. It has been mentioned in section 4.2, a polar surface dominated nanobelt can be approximated to be a capacitor with two parallel charged plates (Figure 4.5a). The polar nanobelt tends to roll over into an enclosed ring to reduce the electrostatic energy (Figure 4.5b). A spiral shape is also possible for reducing the electrostatic energy (Figure 4.5c).

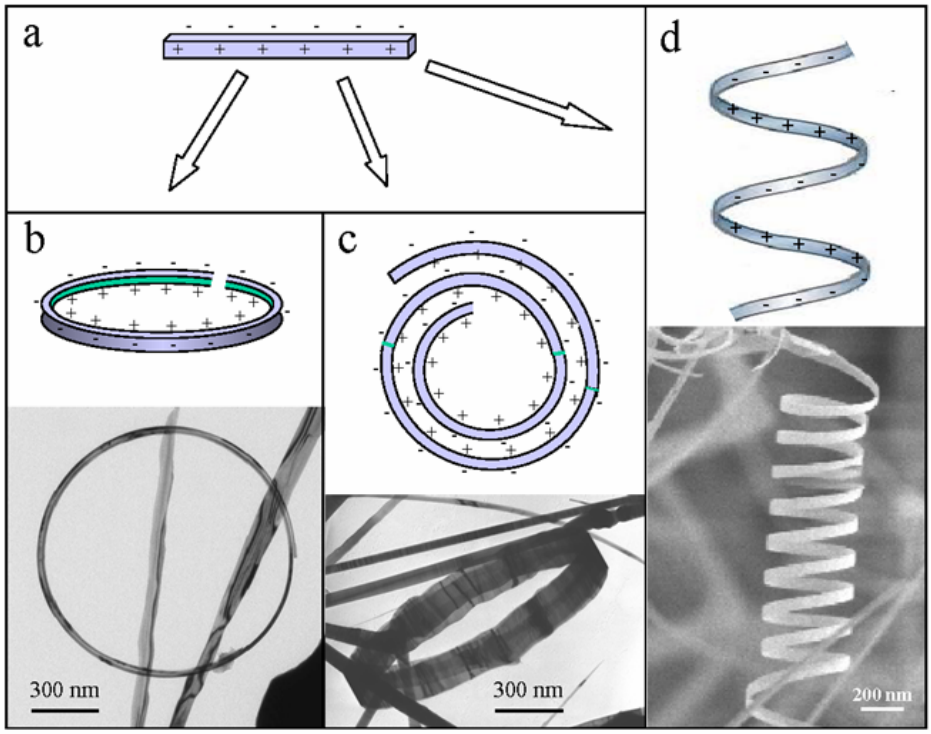

Figure 4.5 (a) Capacitor approximation of a polar nanobelt. (b, c, d) nanoring, nanospiral and nanospring formations interpretated by polar charge model.

The formation of the nanorings and nanohelixes can be understood from the nature of the polar surfaces. If the surface charges are uncompensated during the growth,

the spontaneous polarization induces electrostatic energy due to the dipole moment, but rolling up to form a circular ring would minimize or neutralize the overall dipole moment, reducing the electrostatic energy. On the other hand, bending of the nanobelt produces elastic energy. The stable shape of the nanobelt is determined by the minimization of the total energy contributed by spontaneous polarization and elasticity.

If the nanobelt is rolled loop-by-loop, the repulsive force between the charged surfaces stretches the nanospring, while the elastic deformation force pulls the loops together; the balance between the two forms the nanospring that has elasticity (Figure 4.5d). The nanospring has a uniform shape with radius of ~ 500 – 800 nm and evenly distributed pitches. Each is made of a uniformly deformed single-crystal ZnO nanobelt.

The diversity and splendid nanostructures of ZnO could make it to be of the same importance as carbon nanotubes for exploring nano-scale phenomena and devices. The single-crystal nanorings and nanosprings of ZnO, for example, are potential candidates for building semiconducting and piezoelectric resonators, actuators and sensors for chemical and biological detections. It is necessary, as the first step, to synthesize nanosprings at high-yield.

However, the formation of the nanosprings relies on the nanobelts that are dominated by the {0001} polar surfaces, which have higher energy than the $\{01\bar{1}0\}$ and $\{2\bar{1}\bar{1}0\}$ and are energetically unfavorable to form during growth. An energy barrier has to be overcome by controlling growth kinetics to form polar surface dominated nanosprings. Therefore, the yield of the nanosprings was lower than 5%,[13] greatly limiting its applications in electromechanical-coupled nanodevices. Through a systematical work, we have succeeded in maneuvering the growth kinetics for

synthesizing single-crystal ZnO nanorings at a yield of >50%. This work pushes ZnO nanosprings from a scientific phenomenon to a practical material for carrying out a wide range of physical, mechanical, chemical and biological experimental studies. The rational control of high-yield synthesis of piezoelectric ZnO nanosprings could open a new era in ZnO based electromechanical-coupled nanodevices.

Our synthesis is based on a high temperature vapor-solid process. In comparison to our previous experiments,[164] we did not introduce any doping such as Li or In in the source materials. The key is to control growth kinetics. A systematic characterization of the as-grown nanostructures at different deposition areas of different local growth temperature was conducted by scanning electron microscope by examining the morphology and chemical composition. In a region of 500 - 600 ^{o}C, it was observed that a high-yield of nanosprings was successfully achieved on a polycrystalline alumina substrate. This type of experiments was repeated over 5 times.

Among the as-synthesized product, the most frequently found nanostructure is single-crystal nanosprings. Figure 4.6a displays a typical low magnification SEM picture of the as-grown ZnO nanosprings at a yield of > 50%, distributed densely and uniformly on a polycrystalline Al_2O_3 substrate. The typical dimensions of an individual nanospring are 1-4 μm in diameter, 1-3 μm in pitch distance and tens of microns long (Figure 4.6b). The coiled nanobelt is about tens of nanometer in thickness, 0.2~1 μm in width. Some of the nanosprings tend to be entangled with each other, but a majority of nanosprings are separated and randomly located on the substrate. The high-magnified SEM picture in Figure 4.6c reveals the surface morphology of an individual ZnO nanospring. The nanospring has a width about 300 nm, a diameter of ~3 μm, while the pitch distances

range form 1-3 μm. Both side surfaces of the coiling nanobelts across the width are of a zig-zag shape. The pair of large surfaces is rather smooth in comparison to the side surfaces. Both the right-handed and left-handed chiralities have been found.

The structure of the nanosprings is characterized by transmission electron microscopy (TEM). A nanospring of diameter ~ 5 μm was projected from the top view in figure 4.7a, where a circular shaped looping was clearly revealed. Figure 4.7b is a projected image of a nanospring from the side view. The projected nanospring has a width of ~250 nm, a pitch distance of ~ 4 μm and a diameter of around 4 μm. Figure 4.7c shows a magnified TEM image of the nanospring, where the bending contours are clearly shown, indicating its single crystal structure. A high-resolution TEM image of the nanoring is given in Figure 4.7d. Electron diffraction pattern in the inset of figure 4.7d shows that the nanobelts forming the nanosprings are dominated by the {0001} polar surfaces and grow along $[11\bar{2}0]$ (a-axis).

Structurally, the wurtzite structured ZnO can be described as a number of alternating planes composed of tetrahedrally coordinated O^{2-} and Zn^{2+} ions, stacked alternatively along the *c*-axis. The oppositely charged ions produce positively charged (0001)-Zn and negatively charged $(000\bar{1})$-O polar surfaces, resulting in a normal dipole moment and spontaneous polarization along the *c*-axis as well as a divergence in surface energy. In the synthesis, the high growth temperature and inert gas environmentin the growth chamber may greatly limit the adsorption of foreign molecules on the surface. If the ionic charges on the surface are uncompensated, the nanobelt tends to fold over in order to reduce the electrostatic energy. If the nanobelt is rolled uniradically loop-by-loop, the repulsive force between the charged surfaces stretches the nanospring,

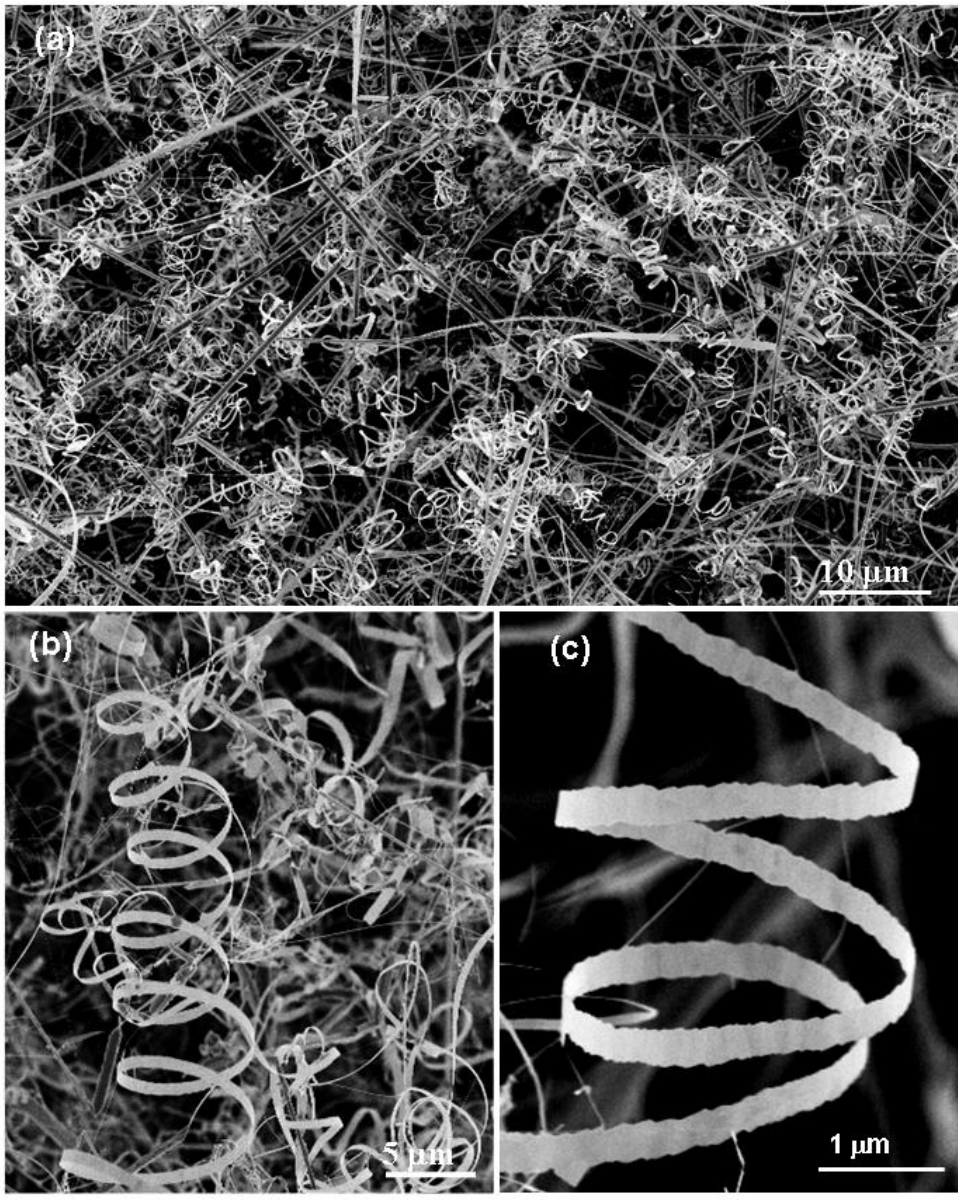

Figure 4.6 (a) A low magnification SEM image recorded from the as-synthesized ZnO sample, demonstrating a predominance of nanosprings in the product. (b, c) Enlarged SEM images displaying detailed morphology of individual nanosprings.

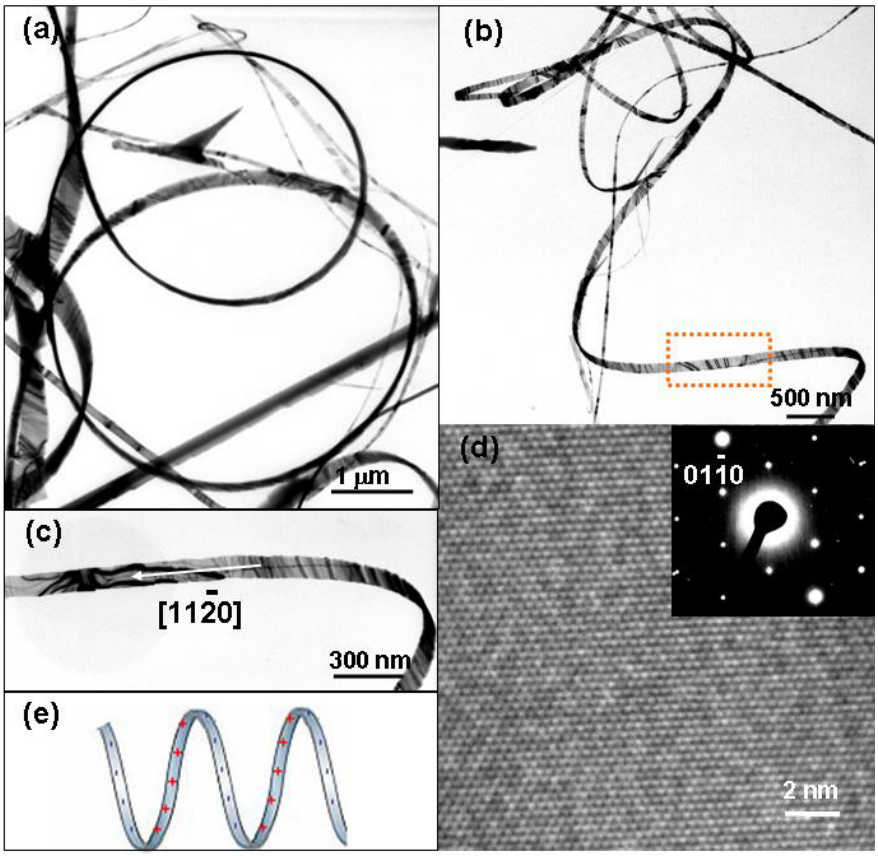

Figure 4.7 (a) A top view and (b) a side view TEM image of a ZnO nanospring; (c) A magnified TEM image presents the single crystal structure of the nanospring and the growth direction of the nanobelt. (d) High resolution TEM image and the corresponding electron diffraction pattern recorded from the nanobelt coiling into a nanospring. The image shows that the nanobelt is dominated by {0001} polar surface, its growth direction [2$\bar{1}$ $\bar{1}$0], and its dislocation-free volume.

while the elastic deformation force pulls the loops together; the balance between the two leads to the formation the nanospring/nanohelix (Figure 4.7e).

The other type of frequently observed structures is nanoloops, nanospirals, or unclosed nanorings. Figures 4.8a, 4.8b and 4.8c display three typical configurations of nanoloops, which are formed by rolling the nanobelts circularly. TEM imaging and electron diffraction analysis indicate that the nanobelts forming the nanoloops are dominated by the {0001} large flat surfaces and grow along [10$\bar{1}$0] (Figure 4). The

formation of the nanoloops is to reduce the electrostatic energy created by the polar charges on the {0001} surfaces. If the inner surface of the loop is Zn^{2+} terminated and the outer surface is O^{2-} terminated in one case, from the energy point of view it should be identical to have the reverse case in which the inner surface of the loop is O^{2-} terminated and the outer surface is Zn^{2+-} terminated, as shown in Figure 4.8d. An experimental evidence of such a case is given in Figure 4.8e, in which the two rings have opposite charges on the surfaces. This result excludes the dominant effect of surface stress in the formation of nanoloops.

A spiral shape is also possible for reducing the electrostatic energy (Figure 4.8f), which is formed by a nanobelt whose thickness may increase slightly along its length. An in-plane spiral curling of the nanobelt tends to minimize the electrostatic energy among the ionic charges on the polar surfaces (Figure 4.8g). If the distance between the loops is small, a densely packed spiral is formed (Figure 4.8h). The key result presented in this paper is the high-yield synthesis of nanosprings, which opens the possibility of their property characterization and applications. The question we tend to answer is what is the kinetics that is important for the growth of high percentage of nanosprings? It is a common fact that the {0001} polar surfaces are the dominant facets of single-crystal nanosprings and nanoloops of ZnO. And there is no doubt that the polar charges induce the formation of these unique structures. Since the polar surfaces {0001} have higher surface energy than either $\{2\bar{1}\bar{1}0\}$ or $\{10\bar{1}0\}$, finding experimental conditions that make it possible for forming the higher energy {0001} surface is the key. To find a clue, Table 4.1 summarizes the experimental conditions, growth morphology and dominant surfaces of ZnO nanostructures that we have synthesized using the same experimental set-up

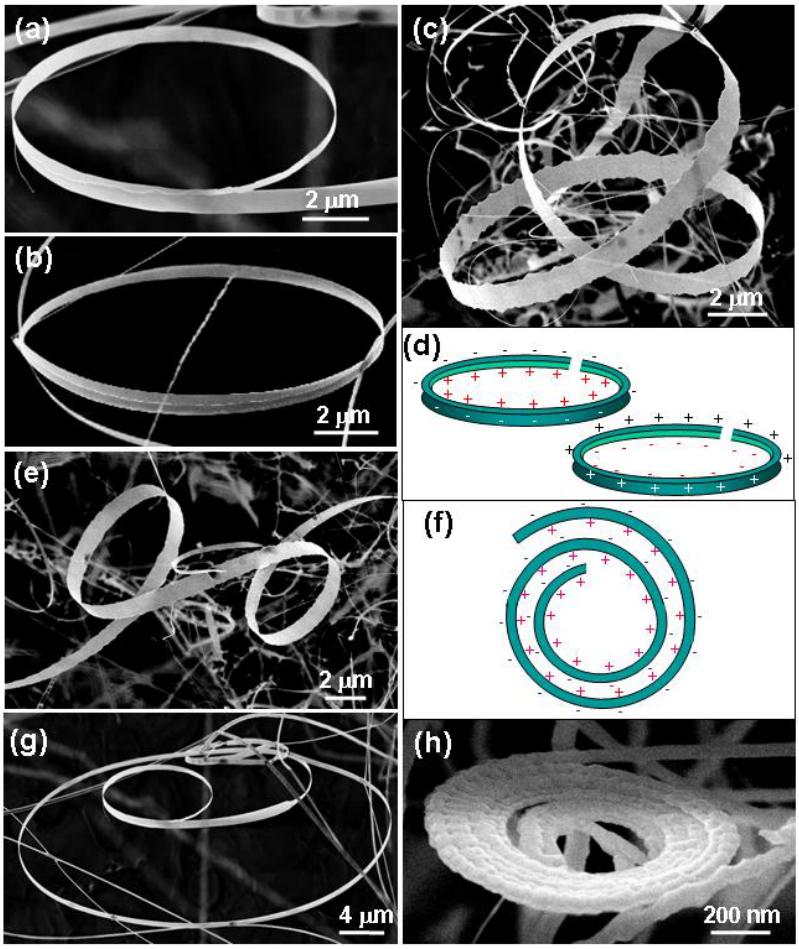

Figure 4.8 (a-c) SEM images of ZnO nanoloops (or nanorings) formed at the ends of nanobelts. (d). Schematic models about the formation of the nanoloop, where "+" is the Zn^{2+} and "-" is the O^{2-}. (e) SEM image of "twin" nanoloops corresponding to the model shown in (d). (f) Schematic model about the formation of a nanospiral, and (g, h) are two corresponding experimental images.

during the last 5 years. In the table, it is shown that, despite the source peak temperature in the range of 1300-1400 ^{o}C and a variation in vaporization time, unanimously both polar surfaces dominated and non-polar surface dominated nanobelts could be produced. In the column of source materials used, it is clearly seen that polar surface dominated nanobelts were synthesized with or without doping in ZnO. The pressure of the gas flow appears also not critical to the formation of polar surfaces unless the pressure becomes

very low. A common and striking fact is that a pre-evacuation of the growth chamber to ~ 10^{-3} torr appears to be necessary for growing {0001} dominated nanobelts. It is suggested a pre-pumping would reduce the content of oxygen and other gas species in the growth chamber, thus, greatly reduces the possibility of molecular adsorption on the {0001} polar surfaces. This step appears to be the key for high-yield growth of polar surface dominated nanostructures. In the current work, the synthesis was conducted at 1390 ^{o}C for 2~6 hours under a confined pressure range of 250~300 mbar after the temperature of reaction chamber was ramped to 800 ^{o}C, where argon carrier gas was kept with a flow rate of 50 sccm throughout the high-temperature synthesis and cooling processes. Before inletting argon carrier gas, the pre-growth pressure of $2x10^{-2}$ torr was maintained for 3 to

Table 4.1 A summary of belt-like ZnO nanostructures by vapor-solid growth process.

Parameters / Nanostructures	Nanobelt growth direction / dominant flat surfaces	Yield (%)	Peak Temperature (°C); Time at peak temperature; Source materials	Flow rate of Ar Gas (sccm)	Pre-growth pressure; Pressure during growth (mbar)
Nanobelts [10]	[0001]/{10-10}; or [10-10]/{2-1-10}	100	1400 °C; 120 min; ZnO	50	400; 400
Nanosprings & nanorings [151,152]	[2-1-10]/{0001}	~5	1350 °C; 30 min; ZnO: Li_2O	25	~10^{-3} ; 330
Nanorings [11]	[10-10]/{0001}	~ 20	1400 °C; 30 min; ZnO:In_2O_3: Li_2CO_3	50	~10^{-3} ; 660
Nanobows [153]	[10-10]/{0001}	5	1350 °C; 120 min; ~10 hrs; ZnO	50	~10^{-2} ; 300 , Evacu Pr=0.1
Nanosprings [157]	[2-1-10]/{0001}	50-100	1390 °C; 120 - 360 min; ZnO	50	~10^{-3}; 250~300
Nanorings & nanospirals [157]	[10-10]/{0001}	20	1390 °C; 120 - 360 min; ZnO	50	~10^{-3}; 250~300

8 hours. In a separated experiment, we have found that a sudden drop in chamber pressure can also lead to formation of polar surface dominated nanobows.

Structurally, we found that planar defects like stacking faults confined in the {0001} plane are present in the nanobelts dominated by {0001} facets. Figure 4.9c shows a bright-field TEM image recorded from the twisting point of a nanospring where the incident electron beam is closely parallel to the (0001) plane. A corresponding dark-field TEM image from the area (Figure 4.9d) clearly indicates the presence of planar defects (see the arrowheads in Figure 4.9d). We know that planar defects lie in the {0001} plane, and they tend to lead fast growth along the plane of the defects, making it possible to form {0001} dominated nanobelts. The driving force for this fast growth is unclear, but the planar defects are found to be the key in the growth of platelet nanocrystals. It is possible that the presence of planar defects could lower or overcome the energy barrier required for growing the polar surface dominated nanostructures.

In summary, by controlling the growth kinetics through refining parameters such as temperature, pressure and duration time, especially the pre-growth pressure level, single crystal ZnO nanosprings were synthesized at high yield (> 50%). Our experiments indicate that doping is not necessary for forming the polar surface dominated nanosprings and nanoloops, but a pre-growth low pressure seems to be the key. The nanobelts that form the nanosprings grow along $[2\bar{1}\bar{1}0]$, and the ones that form the nanoloops/nanospirals grow along $[10\bar{1}0]$. It is suggested that planar defects are usually present in the polar surface dominated nanobelts. This work demonstrates that a simple control on the pre-growth condition results in a largely improved yield of nanosprings. This study makes it possible to synthesize high purity, high yield nanosprings, opening the door for systematically understanding the properties and exploring the applications of semiconducting and piezoelectric nanosprings of ZnO.

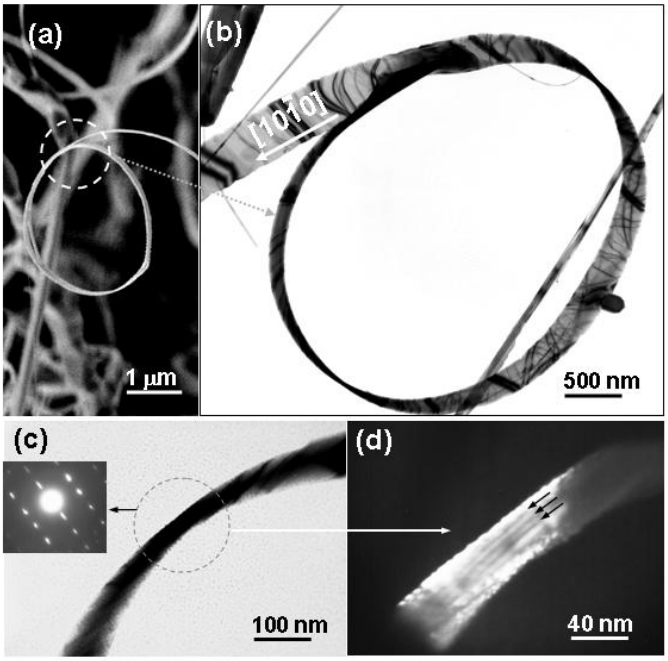

Figure 4.9 (a) An SEM image showing a nanoloop, and (b) a corresponding TEM image indicating that the nanobelt is dominated by {0001} polar surfaces and its growth direction [01$\bar{1}$0]. (c) Bright-field and (d) corresponding dark-field TEM image recorded from a twist point of a polar nanobelt for forming a nanospring, showing the presence of planar defects parallel to the large surface. The inset is an electron diffraction pattern recorded from the twisting area.

4. 4 Circular Structures and Combinated Nanoarchitectures[165]

Generally, crystallographic characteristics will determine the growth habit of the specific nanocrystal growth. For example, structurally ZnO has three-types of fast growth directions: <2$\bar{1}\,\bar{1}$0> (±[2$\bar{1}\,\bar{1}$0], ±[$\bar{1}$2$\bar{1}$0], ±[$\bar{1}\,\bar{1}$20]); <01$\bar{1}$0> (±[01$\bar{1}$0], ±[10$\bar{1}$0], ±[1$\bar{1}$00]); and ±[0001]. Together with the polar surfaces due to atomic terminations, ZnO could exhibit a wide range of novel structures that can be grown by tuning the growth rates along these directions. These are the fundamental principles for

understanding the formation of numerous ZnO nanostructures. For hexagonal nanorods, the fast growth direction is along [0001], one of the major easy axis of wurtzite structured ZnO. While for ZnO nanobelts, three fast growth directions become choices for directional growth. There is a large amount of space for playing the crystal growth of nanobelts. Then if we can control the orientation relationship between catalyst and as-grown nanostructures as well as the exposing facets of as-grown nanostructures, desired hierarchical oxide nanostructures could be self-assembled.

As discussed in previous section, ZnO has two important structure characteristics: the multiple and switchable growth directions: $<01\bar{1}0>$, $<2\bar{1}\bar{1}0>$ and <0001>; and the {0001} polar surfaces. With the three types of stable facets of $\{01\bar{1}0\}$, $\{2\bar{1}\bar{1}0\}$ and {0001}, the three types and 13 fastest growth directions create a lot of freedom for the growth morphology. Nanobelts of different crystal facets have been synthesized. Another key factor is the polar surfaces. The Zn-terminated (0001) surface is positively charged, and the O-terminated $(000\bar{1})$ surface is negatively charged, thus, there is a spontaneous dipole moment along the c-axis. If the crystal thickness is large, the effect of the dipole is small, but once the nanobelt is as thin as 10-50 nm, the spontaneous polarization can produce a few unusual growth features, such as nanorings, nanobows, nanohelixes and nanospirals, which are the results of minimizing the electrostatic energy due to the polarization. Recent work on a combinated ZnO nanoarchitectures has shown that these fundamental growth features co-exist during the growth, and their recombination produces a diversity group of nanoarchitectures including several types of nanorings, nanobows, platelet circular structures, Y-shape split ribbons, and crossed ribbons. In the

following section, the switch growth phenomena of ZnO nanostructures will be elaborated.

4. 4. 1 Switch Growth in Circular architectures

Figure 4.10 shows a series of SEM images indicating the switching growth modes of ZnO circular architectures. The morphology shown in Figure 4.10a gives a good example of a nanobelt that switched its growth direction during the syntheses. The belt grew along a specific direction, then it switched for ~ 30^o into another direction, and finally rotated 60^o and then self-coiled into a full ring. Figure 4.10b is a case of a switching growth mode within a nanoring, in which seemly the starting end of the nanoring could not find the end point when it crosses the curved nanobelt, so a growth along a switched direction can be a choice for leading to the eventual meeting with the original nanobelt. As shown in the right, the enlarged section shows a three-time switching growth made the loop closed. Figure 4.10c is a case in which three branches grew first along three $<01\bar{1}0>$ directions, and then one of the two side branches crossed the middle branch underneath its surface, and then rejoin the other branch. The joining point is not flat due to the mismatch (as indicated by a dotted ellipse) caused by passing the middle branch. The structure of this kind is a pair of “bow and arrow”. It is worth mentioning that such a

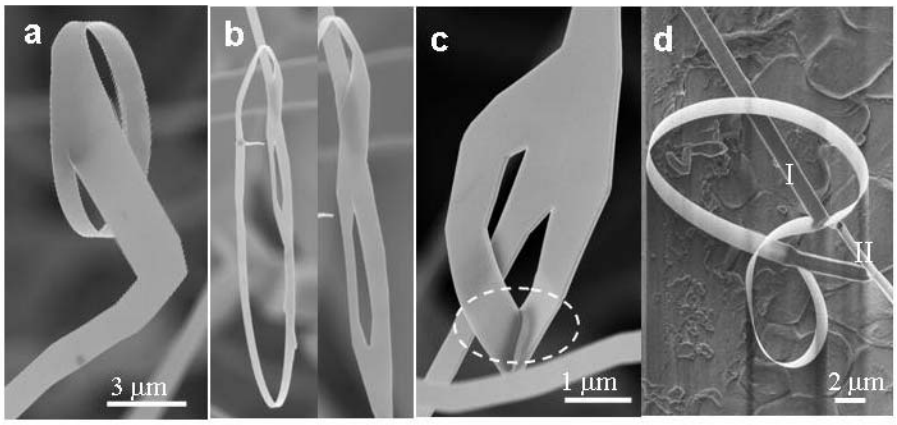

Figure 4.10 Switching growth directions in formation of ZnO nanoarchitectures. (a) A nanoring started and ended at the same ZnO rod. (b) A nanoring formed after the nanobelt switching its growth direction. (c) A nanoring formed by a double-loop coiling of a nanobelt. (d) A curved and twisted ZnO nanobelt that constructs an architecture.

combined structure is still single crystalline, although at the interface there is apparently a mismatch. Under TEM, it has been found that the two side ribbons could miss each other at the joining point. And the top and bottom surfaces have been revealed to be the {0001} polar surfaces under TEM. It must be pointed out that the planar circular-like structure presented here is formed by changing the growth direction among the six crystallographic equivalent directions, rather than the minimization of electrostatic energy. As seen in Figure 4.10d, the nanobelt could twist itself into a configuration that matches the local crystallography and surface charge. Secondary growth is responsible for the unusual twisting configuration of the nanobelt.

An architecture can be made by combining the growth configurations presented in Figures 4.2 and 4.3. Figures 4.11a and b are a combination of a nanorod, a semi-circular bow and a perfect ring. The nanorod grows along [0001] and is enclosed by six $\{01\bar{1}0\}$ side facets. A nanobelt grows perpendicularly to the nanorod along $[01\bar{1}0]$ and bends uniformly and finally

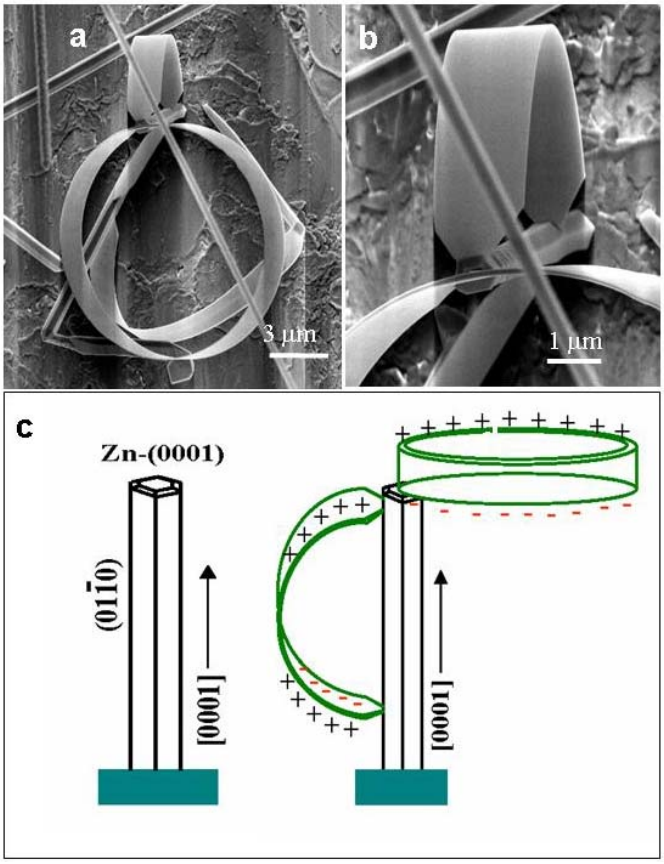

Figure 4.11 (a) An nanoarchitecture composed of a rod, a bow and a ring. (b) Magnified SEM images to capture the orientation relationships among the three components. (c) A structure model of the architecture**.**

ends at the nanorod, forming a nanobow. This nanobelt is dominated by the {0001} polar surfaces and the polar charges enforce the bending of the nanobelt. The joint point between the nanobelt and the rod is a neck structure. A complete ring on the top of the nanorod has a solid conjunction with the rod, and its large surfaces are $\pm(01\bar{1}0)$, and its top and bottom rims are the {0001} polar surfaces. The growth direction of the self-coiled belt is $[2\bar{1}\bar{1}0]$, similar to the seamless nanoring reported previously (Figure 4.3b).

The combined growth structure presented in Figure 4.11 is the first observation of its kind. This type of combination directly proves the co-existence of the polar belt rolled

rings/bow and the polar belt self-coiled seamless nanoring. Figure 4.11c is a schematic model for this integrated growth phenomenon. The first step is a growth of a hexagonal rod along [0001]. The top facet is dominated by Zn-terminated (0001) plane, which is self-catalytically active, and the side facets are likely to be the six crystallographically equivalent $\{01\bar{1}0\}$ surfaces. As growth continues, the stepped side facets as shown in Figure 4.11b would function as a good nucleation site for the secondary growth, leading to the formation of a belt along a normal direction of $[01\bar{1}0]$. Due to the spontaneous polarization of the ZnO nanobelt across its thickness, bending into a ring would reduce the electrostatic energy, provided the thickness-to-radius ratio is less than ~ 4%. But the bending is ended if the nanobelt reaches the rod and rejoins the single crystal rod, forming a semi-circular bow. On the other hand, with the growth of the rod, the growth front of Zn-(0001) plane could be the nucleation site for the other fast growth belt along $[2\bar{1}\,\bar{1}0]$ parallel to the side facet of the rod, and it tends to fold back to form a loop, such as the model shown in Figure 8c. A perfect ring is formed by epitaxial self-coiling of a polar belt. The bottom surface of the ring tends to be O-$(000\bar{1})$ surface, while the top surface is Zn-(0001).

4. 4. 2 Y shape single-crystal nanoribbons

Splitting of a single crystal could occur and the side branch growth leads to the formation of Y shape nanoarchitecture of ZnO. Figure 4.12 gives a typical example for the split growth phenomena. Figure 4.12a shows that a ribbon of large-aspect-ratio (around 5-10) and smooth polar surfaces splits into two high aspect ratio ribbons of equal width but half in thickness. The ribbon was too thick to be bent by polar charge prior

splitting, but bending is possible after splitting (bottom enlarged section). In Figure 4.12b, TEM imaging and diffraction show that the splitting is due to an initiation of a side branch along $[01\bar{1}0]$ away from the original branching direction of $[11\bar{2}0]$, but both branches are still dominated by {0001} polar surfaces. Figure 4.12c shows that a curly ribbon splits out of a straight ribbon, later it rejoins the straight ribbon. The curly ribbon is due to its small thickness, and is due to the surface polar charge. These growth features are rather unique.

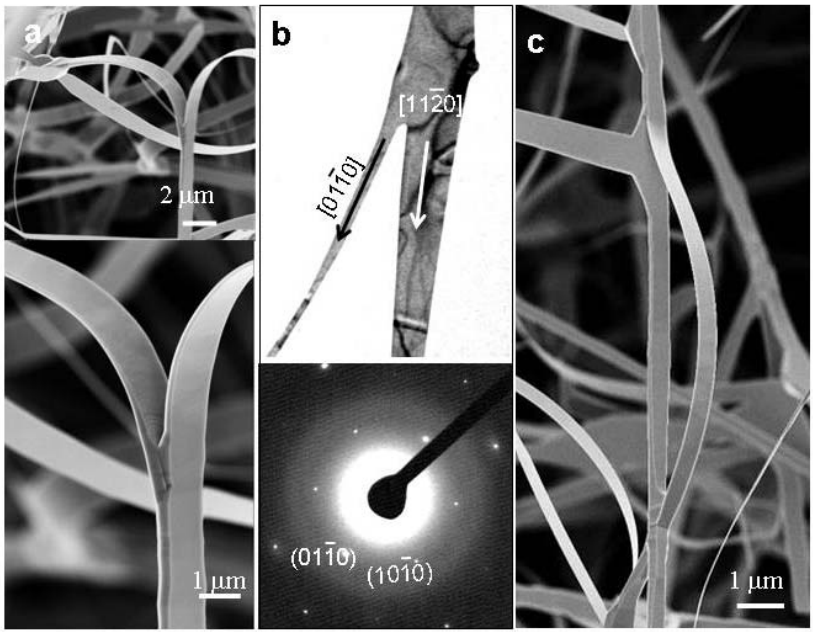

Figure 4.12 (a) SEM images of two tangential split ribbons. (b) TEM image and corresponding [0001] diffraction pattern of a Y structure, which is produced by separating the growth along $[01\bar{1}0]$ from the original $[2\bar{1}\bar{1}0]$ direction. (c). A bow structure formed by the split growth of a belt and its later rejoining to the straight ribbon.

Joining two nanostructures together could occur in two ways. One is a natural crystallographic matching so that two of them are integrated as a single crystal. The other is a sintering during growth. Figures 4.13a and b show two nanobelts that are joined together. It is possible that both crystallographic bonding and sintering play a role in

holding them together. But a case shown in Figure 4.13c is likely due to sintering. The nanostructure shown in Figure 4.13d is a result of self-splitting.

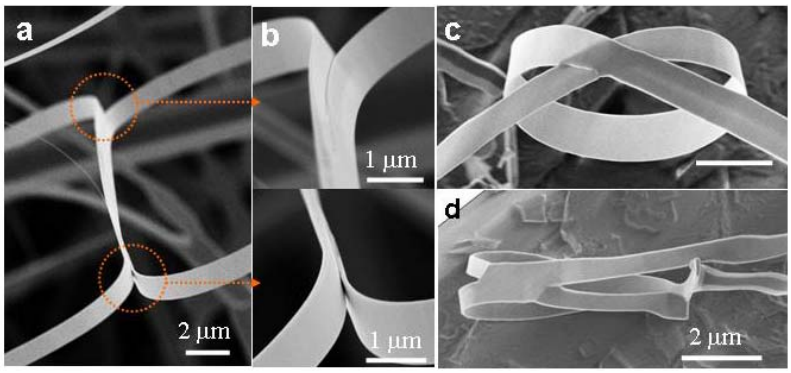

Figure 4.13 Joining of nanostructures via high temperature sintering. (a) Two micron sized ribbons merged in parallel in the contact region, and (b) are the enlarged views of the top and bottom sides of the joining points, respectively. (c) A self-bent and twisted ribbon into a closed loop. (d) A polar surface dominated full-ring split out another nanoribbon, which overlapped and merged with the original loop.

4. 4. 3 Crossed Nanoribbon Architectures

Crossed ribbon structures have been observed with some unusual configurations. One way of creating crossed structures is the switching/splitting in grow directions among <01$\bar{1}$0> and <2$\bar{1}$$\bar{1}$0>. These type of structures usually have a smooth surface and all of the branches share the same flat {0001} surface (Figures 4.14a, b). The two branched nanoribbon in Figure 4.14c grow along [1$\bar{2}$10] and [2$\bar{1}$$\bar{1}$0]. For the three-branched nanoribbons in Figure 4.14d, electron diffraction pattern shows that the three nanoribbons are a single crystal and are along [1$\bar{1}$00], [01$\bar{1}$0] and [$\bar{1}$010].

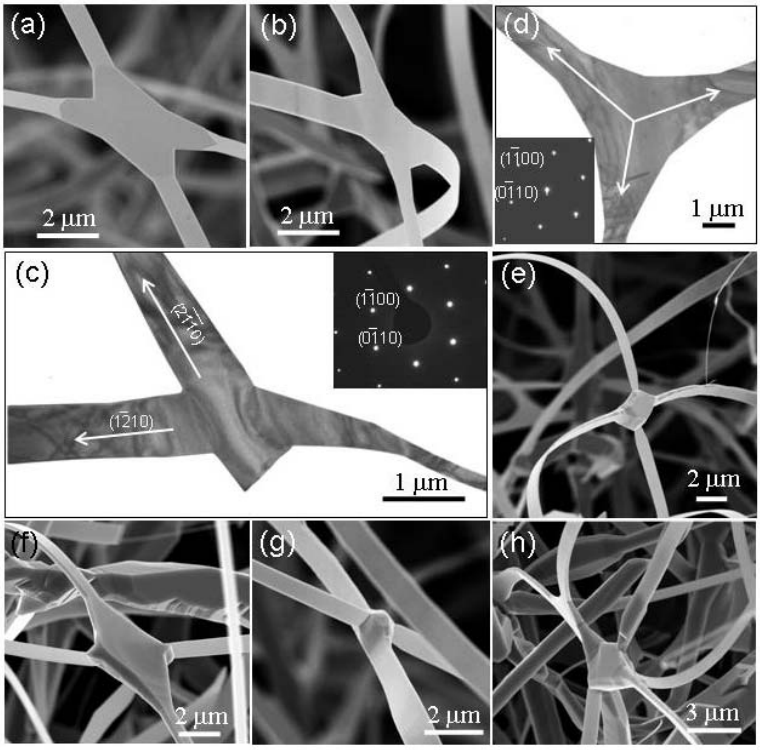

Figure 4.14 Crossed junctions of ZnO. (a-d) SEM and TEM images of the crossed nanobelts that share the same polar surface of (0001). The junction branches could be along $[01\bar{1}0]$ or $[2\bar{1}\bar{1}0]$. (e-g) Cross-junctions of nanobelts with twisted ribbons, so that they do not share a common polar surface. (h) A multi-junction structure of over four ribbons.

The other group of crossed structure is complex because there is a crystal at the joint point of the nanobelts, and sometime the two nanobelts do not share a common flat surface (Figures 4.14(e-g)). This type of structure could involve the formation of twins at the central crystal and/or sintering. The two ribbons could grow perpendicularly from a cross-junction area, and they do not share a common flat surface. Figure 4.14h is a more complicated case, where multiple ribbons grew from one junction, forming a 3D complex structure. These nanostructures demonstrate the diversity of ZnO growth.

4. 4. 4 Zig-zag Chain Architectures

Zig-zag chain type of nanostructures has also been found for ZnO. Figure 4.15 shows two typical configurations of the zig-zag structures.

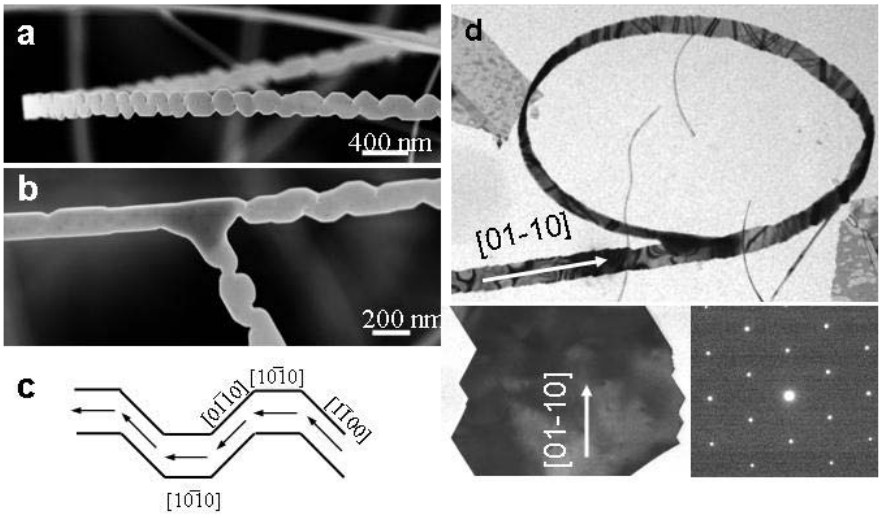

Figure 4.15 (a, b) Polar-surface-dominated ZnO ribbons with zig-zag chain structure, which are formed by a periodic change in growth direction. (c) A model of the chain structure, (d) nanorings made of zig-zag nanoribbon, where the electron diffraction analysis proves the validation of chain model.

The chain structures are dominated by the large {0001} polar-surfaces, but its growth direction changes periodically, as shown in Figure 4.15c, leading to the formation of chain structures. For the same family of growth directions of <01$\bar{1}$0>, for example, there are six equivalent directions and there is a 60^o rotation between the two adjacent directions. Therefore, a periodic change in growth direction following a periodicity of [$\bar{1}$100] $\rightarrow$ [10$\bar{1}$0] $\rightarrow$ [01$\bar{1}$0] $\rightarrow$ [10$\bar{1}$0], and a fixed length growth results in the formation of zig-zag chain structure, similar to the one reported previously. The junction shown in Figure 4.15b is due to a split growth of the nanoribbon along one of the directions. Figure 4.15d shows a TEM image of a closed loop with extension, the nanoribbon is in a zig-zag shape, the inset TEM diffraction pattern proved the switching growth model in Figure 4.15c.

4.5 Superlattice Structured Nanohelices [166]

We have known that zinc oxide can form single-crystal nanosprings, nanorings, and nanobows by bending/folding polar-surface-dominated nanobelts. These growth processes are dominated by a minimization of the electrostatic energy contributed by the cation and anion terminated surfaces of this ionic material, and their shapes are determined by balancing the electrostatic energy with the elastic deformation energy. The structural configurations of ZnO nano-objects could form the basis for fabricating nano-scale sensors, transducers, and resonators.

We now here introduce a distinctive helical structure of ZnO, made of a superlattice-structured nanobelt that is formed spontaneously in a solid-vapor growth process. The superlattice nanobelt is a periodic, coherent, epitaxial and parallel growth of two alternating nanostripes of ZnO crystals oriented with their c-axes perpendicular to each other. The role played by polar-surfaces in the structural transformation is demonstrated, and the nanohelix has been manipulated by atomic force microscopy (AFM) to measure its elastic properties.

The ZnO nanohelices were grown with high reproducibility by a vapor-solid process by using temperature to controll growth kinetics. The experimental set-up consists of a horizontal high-temperature tube furnace, an alumina tube, a rotary pump system, and a gas controlling system. First, 2 g of commercial ZnO powder (Alfa Aesar) was compacted and loaded into an alumina boat and positioned at the center of the alumina tube as the source material. The system was pre-pumped to ~2 x 10^{-2} mbar, and

the ramp rate was controlled at 20^{o} to 25^{o}C/min when the temperature was raised from room temperature to 800 ^{o}C. The furnace was then held at 800 ^{o}C for 20 min and the temperature was ramped at 20^{o}C/min from 800^{o} to 1400^{o}C. When the temperature reached 1000 ^{o}C, argon was introduced as a carrier gas to raise the pressure from ~2 x 10^{-2} mbar to the desired synthesis pressure of 200 to 250 mbar within ~2.5 min. The solid-vapor deposition was carried out at 1400 ^{o}C for ~2 hours under a pressure of 200 to 250 mbar. The argon carrier gas was kept at a flow rate of 50 sccm (standard cubic centimeters per minute). The as-grown nanohelices of ZnO were deposited onto a polycrystalline Al_2O_3 substrate at a local temperature of 700^{o} to 800^{o}C, and characterized by a variety of microscopes, including scanning electron microscopy (SEM) (LEO 1530 FEG at 5 & 10 kV), high-resolution transmission electron microscopy (TEM) (Hitachi HF-2000 at 200 kV and JEOL 4000EX at 400 kV), atomic force microscopy (AFM) (Molecular Force Probe MFP-3D™ from Asylum Research), and focused ion beam microscopy (FIB) (FEI NOVA 200).

As shown in Figure 4.16 is a typical SEM image showing that the as-synthesized sample was composed of up to 10% of freestanding nanohelices. High-resolution SEM images show the high degree of uniformity of the nanohelices, which can be left- (Figure 4.17A, and C) or right-handed (Figure 4.17B, and D). Their population ratio is nearly 1:1 resulted from the statistics plot in Figure 4. 18. This statistics results revealed that the nanohelix diameters, widths and pitch distances range between 300 to 700 nm, 100 to 500 nm and 500 to 2500 nm, respectively. The length of the

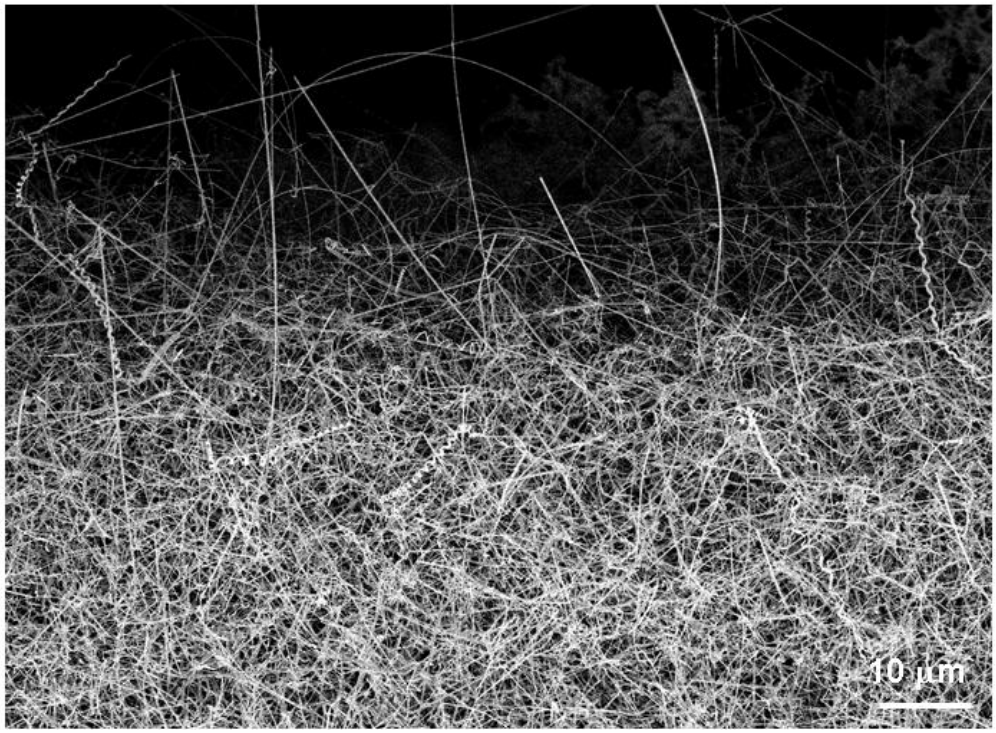

Figure 4.16 Low-magnification SEM image from the as-synthesized sample, showing the distribution of freestanding nanohelices of ZnO in the grown product.

nanohelix can be as long as 100 μm. Energy dispersive X-ray spectroscopy analyses indicate that the nanorings are ZnO without detectable impurity.

Low-magnification TEM images of the nanohelices (Figure 4.19A and B) revealed the crystalline structure and winding shape of the nanobelts. The electron diffraction (ED) pattern, acquired from a single period of a nanohelix, shows mirror symmetry. This mirror symmetry is caused by superposition of several ZnO diffraction patterns rotated around the axial direction of the nanohelix axial direction of the nanohelix. A dark-field TEM image recorded from a segment of a nanobelt (Figure 4.19C) shows that the nanobelt has a periodic superlattice-structure across its entire width, with a uniform periodicity of ~3.5 nm. With a 5º offset, the stripes are nearly

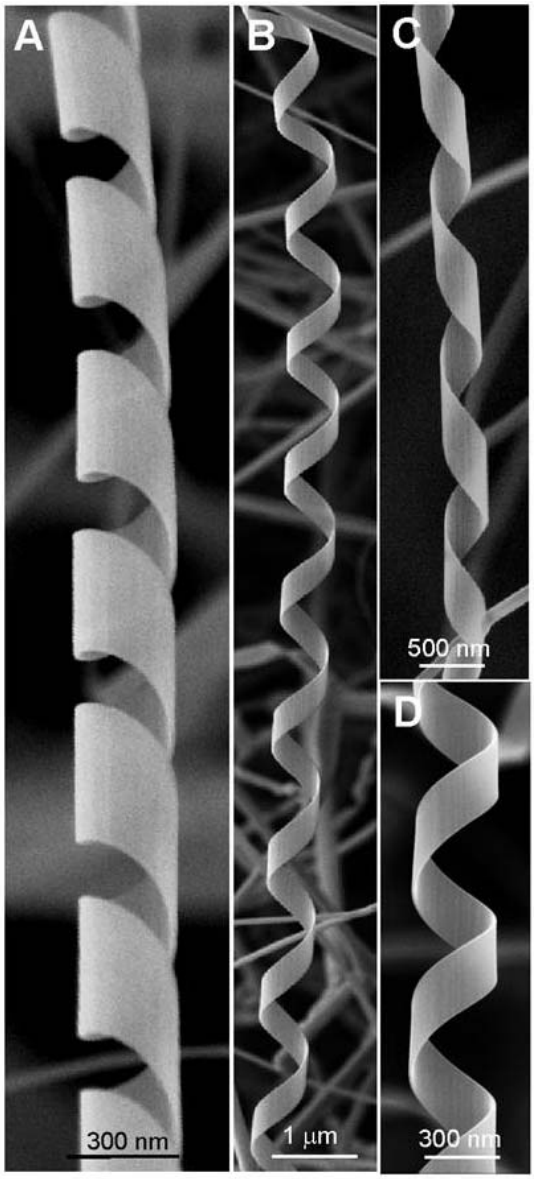

Figure 4.17 Morphology of nanohelices. (**A**-**C**) Typical SEM images of the left- and right-handed ZnO nanohelices. (**D**) A high-magnification SEM image of a right-handed ZnO nanohelix, showing a uniform and perfect shape. All of the nanohelices are directly received from the as-synthesized sample and they are freestanding on the substrate surface.

parallel to the nanobelt growth direction and run along the length of the nanohelix (Figure 4.20).

As mentioned in chapter 1, from crystallography, the wurtzite-structured ZnO crystal is described schematically as a number of alternating planes of tetrahedrally-coordinated O^{2-} and Zn^{2+} ions stacked alternatively along the c-axis. The oppositely charged ions produce positively charged (0001)-Zn^{2+} and negatively charged $(000\bar{1})$-O^{2-} polar surfaces (c-planes). High-resolution TEM revealed the superlattice-structure of the nanobelt with a periodic alternating arrangement of two types of stripes (Figure 4.19D), which are oriented epitaxially in the following orientations: Stripe I has a growth direction of $[1\bar{1}00]$, with top and bottom surfaces ±(0001) (polar surfaces); Stripe II has a growth direction of $[2\bar{1}\bar{1}2]$, with top and bottom surfaces±$(01\bar{1}0)$ (nonpolar surfaces). The corresponding ED pattern of the nanobelt shows that the growth directions of the two types of stripes have a small rotation of $\alpha \approx 4^{o}$ (Figure 4.19E), indicating that the adjacent stripes rotate in the plane of the nanobelt for the same magnitude of the angle when forming the superlattice. The angles between the ED spots also slightly deviate from the expected result of a large crystal and suggest rigid lattice twist in some atomic planes. The two stripes are coherent by aligning $(0\bar{1}10)$ of stripe I with (0002) of stripe II at a lattice mismatch of 2.9%, and $(\bar{2}110)$ of stripe I with $(\bar{2}110)$ of stripe II without lattice mismatch, so the interface energy is likely to be low. Viewing from the projected direction of the incident electron beam, the two stripes are aligned byfacing $(\bar{1}\bar{1}20)$ of stripe I parallel to the $(\bar{2}116)$ of stripe II, and aligning the [0001] of stripe I with $[01\bar{1}0]$ of stripe II. The true interface is inclined

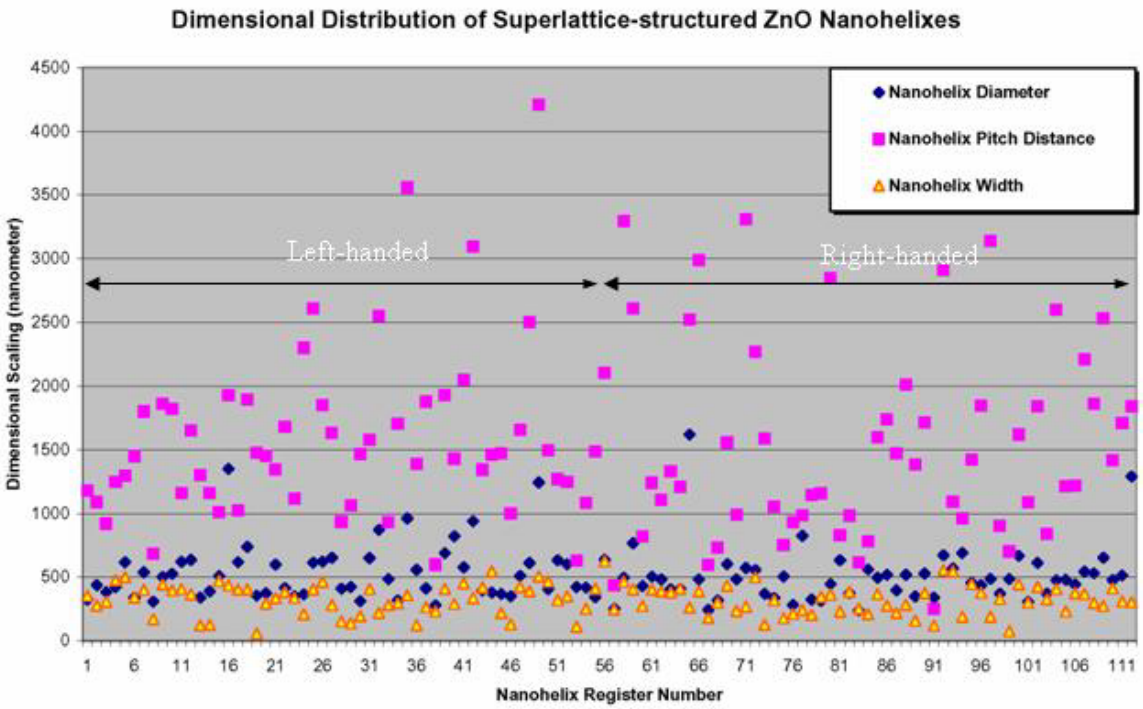

Figure 4.18 Distribution of the diameters and pitch distances of the nanohelixes and the width of the nanobelt. The data were derived from SEM images. The ratio between the left-handed to right-handed nanohelix is 56 : 57.

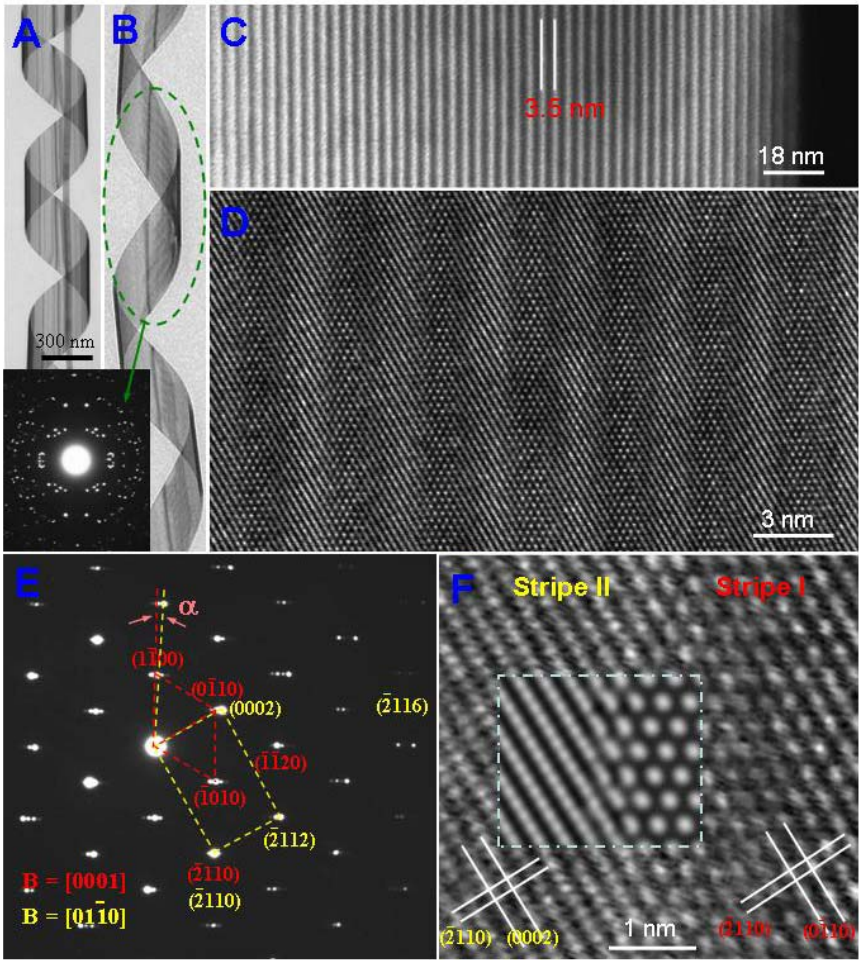

Figure 4.19 Crystal structure of the nanohelix. (**A**) Typical low-magnification TEM image of a ZnO nanohelix, showing its structural uniformity. Note a straight nanobelt was enclosed inside the helix during the growth. (**B**) Low-magnification TEM image of a ZnO nanohelix with a larger pitch-to-diameter ratio. The selected-area electron diffraction pattern (SAEDP) is from a full turn of the helix. (**C**) Dark-field TEM image from a segment of a nanohelix, showing that the nanobelt that coils into a helix is composed of uniformly, parallel, longitudinal, and alternatively distributed stripes at a periodicity of ~3.5 nm across its entire width. The edge at the right-hand side is the edge of the nanobelt. (**D, E**) High-magnification TEM image and the corresponding SAEDP of a ZnO nanohelix with the incident beam perpendicular to the surface of the nanobelt, respectively, showing the lattice structure of the two alternating stripes. The SAEDP is composed of two sets of fundamental patterns: as labeled and indexed in red for stripe I and yellow for stripe II. A careful examination of the image indicate that the true interface between the stripes is not edge-on in reference to the incident electron beam, but at a relatively large angle. (**F**) An enlarged high-resolution TEM image showing the interface between the two adjacent stripes. The inset is a simulated image using the dynamic electron diffraction theory. The interface proposed here is $(\bar{1}\bar{1}22)$ for stripe I, which is inclined with respect to the incident electron beam at an angle of 32°.

with respect to the direction of the electron beam, so that the contrast at the interface in the high-resolution TEM image is not very sharp (see Figure 4.19F). Based on the orientation relation presented above, the experimental image can be simulated using dynamic electron diffraction theory. The result is inserted in Figure 4.19F, showing quantitative agreement with the observation. Thus, the interface for stripe I is likely to be $(\bar{1}\bar{1}22)$.

The initiation of the nanohelix is a direct result of superlattice formation. From an SEM image of a nanohelix with both ends (Figure 4.21A), a straight stiff-nanoribbon is directly connected to the starting point of a nanohelix. TEM examination shows that the joining point between the nanoribbon and the nanohelix is the place where the superlattice is created (Figure 4.21B). The stiff-nanoribbon is a single crystal object dominated by large c-plane surfaces (Figure 4.21C). The superlattice is formed spontaneously and abruptly across the entire width of the nanoribbon. A striking feature is that the width of the nanobelt increases and its thickness decreases significantly after transforming into the superlattice structure (Figure 4.21B, see also Figure 4.22). The stripes hold the same orientation relation as defined in Figure 4.20E (see the selected-aread ED (SAED) inserted in Figure 4.21C). An enlarged local area shows the co-existence and spontaneous formation of periodically arranged, two alternating stripes at the transverse interface where the structural transformation occurred abruptly (Figure 4.21D). At the transverse interface, the lattice mismatch of

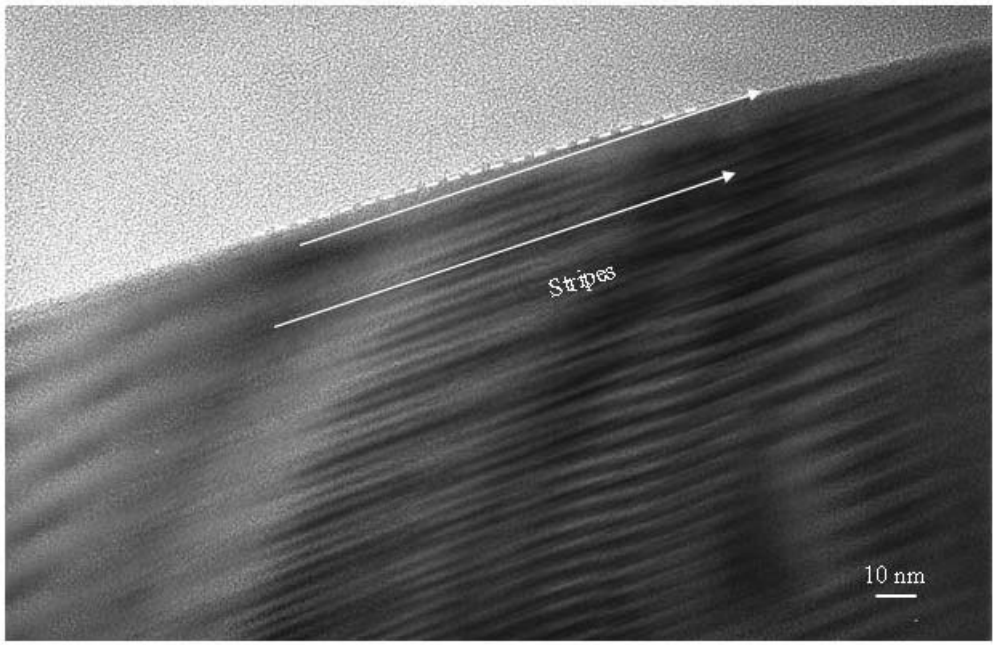

Figure 4.20 Low-magnification TEM image showing that the direction of the superlattice stripes is almost parallel to the direction of the nanobelt, but at an angle of ~ 5^{o}.

2.9% between $(0\bar{1}10)$ of the nanoribbon with (0002) of stripe II should create interface mismatch edge dislocations with a Burgers vector of $[0\bar{1}10]$, which are expected to be separated by 3.45 nm. In fact, the periodicity of the superlattice is ~3.5 nm, and mismatch edge dislocations have been identified at the turning point between the nanoribbon and the superlattice (see the circled areas in Figure 4.21D). The site of the mismatch dislocation could be the nucleation site of stripe II. The superior uniformity in periodicity of the superlattice is most likely to be a result of the lattice mismatch as defined by crystal structure, and rigid crystal twisting gives rise to the strain contrast observed in Figure 4.21B and even in the high-resolution TEM image in Figure 4.21D.

The termination of the nanohelix growth is caused by a complete conversion of the remaining polar-surfaces into non-polar-surfaces and an increase in nanoribbon

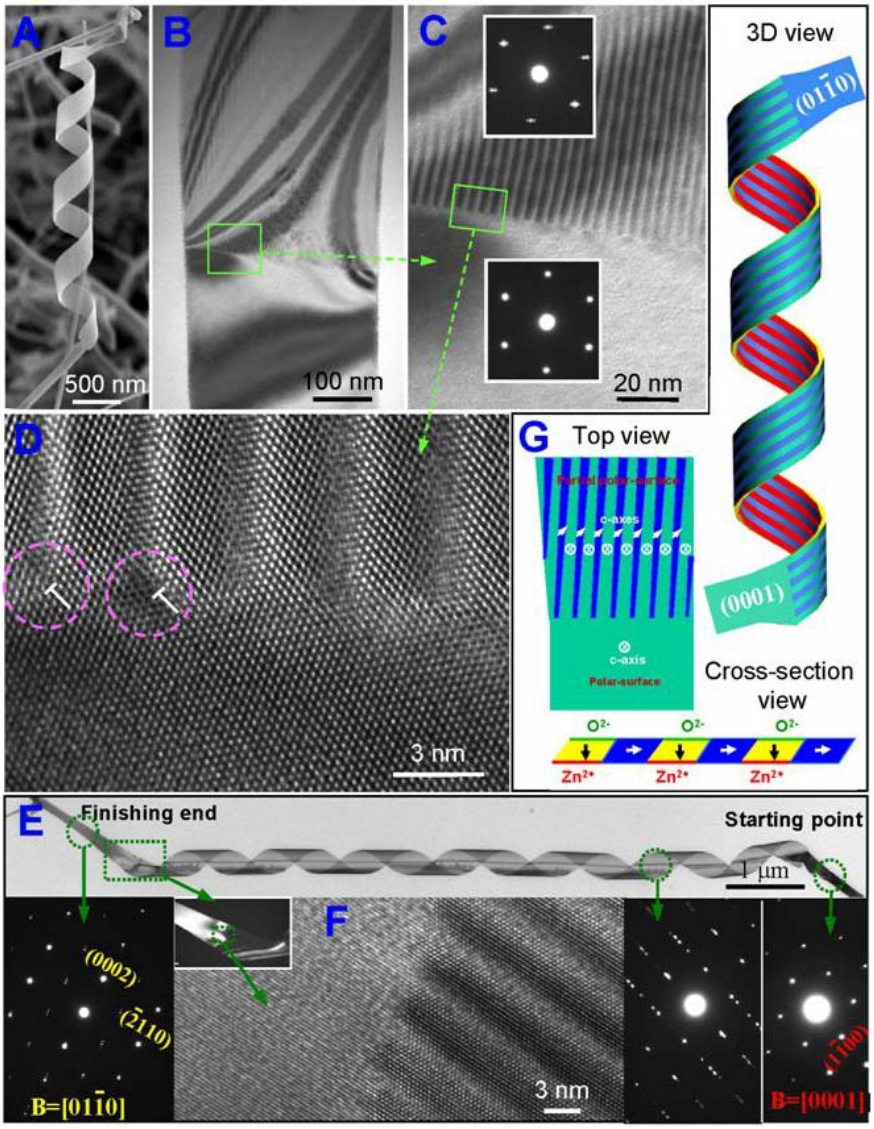

Figure 4.21 Initiation and formation process of a nanohelix. (**A**) A low-magnification SEM image of a ZnO nanohelix showing its starting point and finishing end. (**B**) A low-magnification TEM image from the starting-point of a nanohelix, showing a distinct and sharp contrast change across a transverse line and an increase in nanobelt width. (**C**) An enlargement of the boxed area in (B) and the corresponding diffraction patterns from the single crystal region and the superlattice-structured region. The bottom-segment is a c-plane dominated single-crystal stiff-nanoribbon, while the top-segment is a superlattice-structured flexible-nanobelt, and the corresponding electron diffraction pattern is the same as the one shown in Figure 2E. (**D**) High-magnification TEM image recorded from the interfacial region of the segments, showing a clear cutting-line from where the structural transformation occurs across the entire width of the nanobelt. Mismatch edge-dislocations are identified in the circled regions directly linked to stripe II. (**E**) Low-magnification TEM image of a nanohelix showing its entire structure from beginning to end. Three representing SAEDPs are recorded from areas selected from the starting-end,

the middle section, and the finishing end. The starting point is a nanoribbon oriented along [0001], which is fully dominated by the c-plane polar-surfaces; the middle section of the nanohelix is superlattice-structured, while the finishing end is a single-crystal nanoribbon that is dominated by non-polar-surfaces according to the dark-field TEM image (inset), [$01\bar{1}0$] diffraction pattern and (**F**) high-resolution TEM image recorded from the area, where a distinct and clear-cut transformation from the superlattice-structured nanobelt to an a-plane dominated nanoribbon is apparent. (**G**) Schematic models showing the top-view and cross-sectional view of the nanobelt for illustrating the corresponding directions of the c-axes and the distribution of polar charges (in green for O^{2-} and red for Zn^{2+}) and non-polar surfaces (in blue). A three-dimensional (3D) structure model of a nanohelix, showing its initiating point and finishing end. The periodicity of the superlattices may result in the formation of periodic piezoelectric domains.

thickness. From the TEM image and the corresponding SAED patterns recorded from a single nanohelix (Figure 4.21E), the formation of the nanohelix is a result of transforming a fully c-plane-dominated stiff-nanoribbon (starting point) into a superlattice-structured, partially polar-surface dominated, flexible nanobelt (middle section). The starting stiff-nanobelt is thick (~ 40 nm) and straight [see Figure 4.22]. After transforming into the superlattice-structured nanobelt, the thickness of the nanobelt is greatly reduced to less than 20 nm and its width is significantly increased [See Figure 4.22]. Finally, the ending of the nanohelix is a result of abruptly transforming the partially c-plane-dominated, superlattice-structured nanobelt into a single-crystal nanoribbon dominated by nonpolar surfaces at the finishing end (Figure 4.21E), where the corresponding dark-field TEM image and the high-resolution TEM image (Figure 4.21F) indicate that the top and bottom surfaces of the nanoribbon are the nonpolar $\pm(01\bar{1}0)$ surfaces. The thickness of the nanoribbon increases significantly as well after the transformation. The formation of the nanohelix is a rigid structural alteration caused by the alternating stripes in the superlattice, and the formation of a superlattice is likely to be a polar charge induced structural transformation (see the model in Figure 4.21G). In the synthesis, a pre-

pumping to 2 x 10^{-2} mbar creates the condition for growing polar surface dominated nanoribbons. The polar charges are preserved on the surface during the growth under

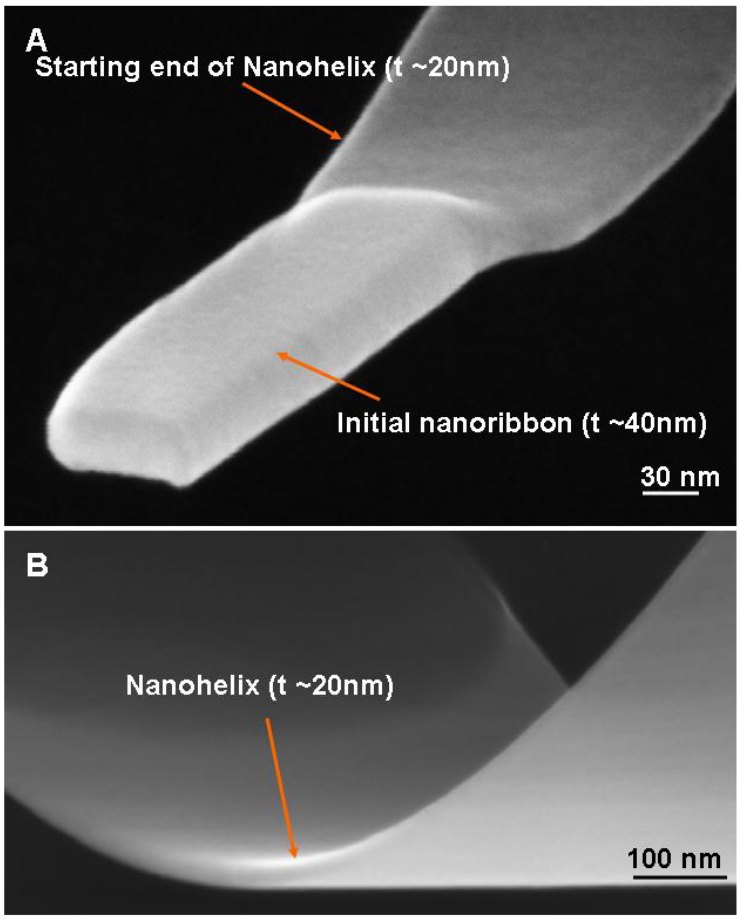

Figure 4.22 Thickness and width change at the joining interface between the initial stiff nanoribbon and the nanohelix.

conditions of high temperature and inert environment. As reported previously, the existence of the polar-surfaces results in the formation of ZnO nanosprings and nanorings. If the width of the nanoribbon is rather large (see Figure 4.21B), the electrostatic energy of the polar surfaces diverges with the extension of its length. A possible way of reducing the electrostatic energy is to transform the polar-surface into a nonpolar surface, provided the interface mismatch energy is reasonably low, forming

superlattice-structured stripes that are nearly parallel to the growth direction of the nanobelt. The introduction of argon gas at a later stage during the growth may be the initiation of superlattice formation. The switching in c-axis may indicate the formation of piezoelectric domains. The width of the nanobelt increases after the structural transformation from a single-crystal, c-plane-dominated stiff-nanoribbon (in green) into a superlattice-structured, flexible-nanobelt; the stripes are not exactly parallel to the growth direction of the nanobelt, and a small in-plane rotation for an angle of α exists between the growth directions of the two adjacent stripes, which induces the geometrical curvature required for rigidly twisting its shape. The polar charges remaining on the surfaces of stripe I also help to bend the nanobelt into a ring structure especially with the decrease of the nanobelt thickness. Thus, the accumulation of rigid structural rotation or twist across the width of the superlattice nanobelt and a continuous growth of the stripes along the length of the nanobelt results in the formation of a helical structure, which could be left-handed or right-handed. The winding of the nanobelt is terminated after the nanobelt fully transforms from a partial-polar-surface-dominated and superlattice-structured nanoobject into a single-crystal nanoribbon dominated by nonpolar surface (in blue), which is likely to be caused by a change in growth kinetics. The single-crystal nanoribbon is a straight structure without rigid lattice alteration or surface polar charges; thus, it will not continue to wind but will extend as a straight ribbon.

Manipulation of a nanohelix with AFM and FIB shows that it has a rigid structure. A nanohelix has been sectioned by FIB into a short segment of one period (Figure 4.23A), but the shape of the segment is still preserved and shows no visible relaxation. A nanohelix has also been cut by an AFM tip at two consecutive turns (Figure

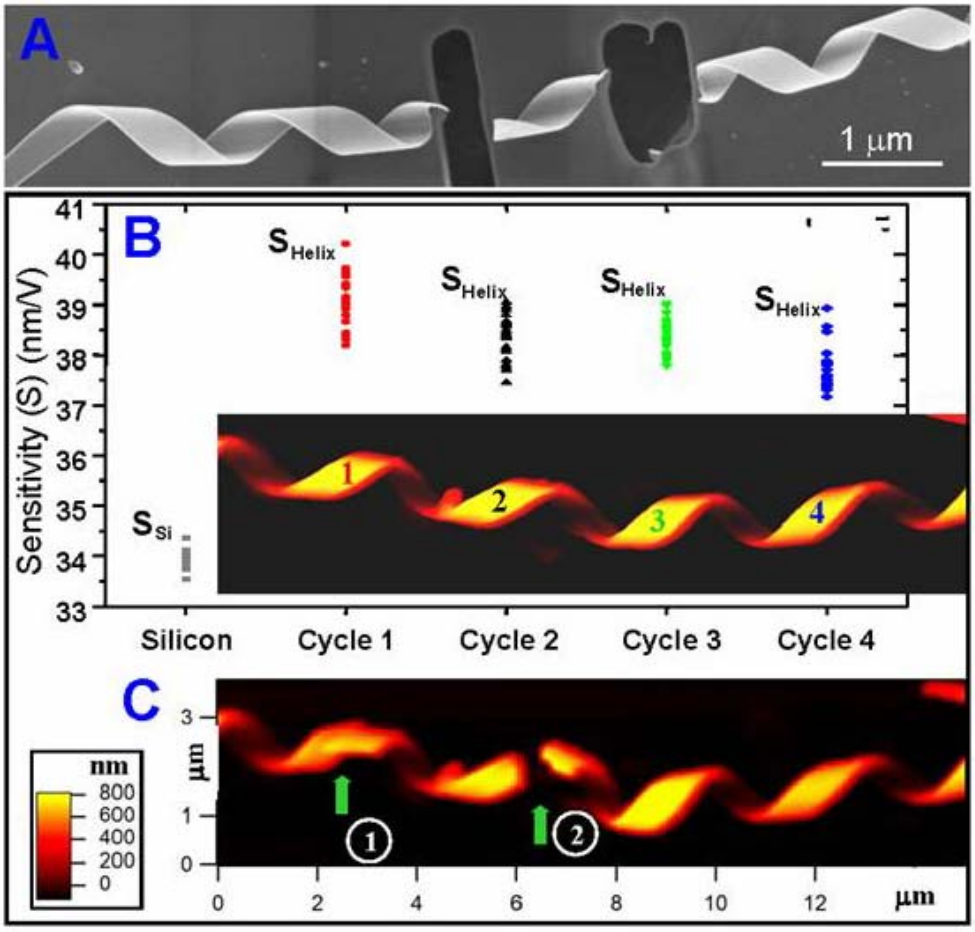

Figure 4.23 Manipulation of a nanohelix and measurement of its elastic properties. (**A**) SEM image of a nanohelix that was cut by an focused ion beam microscope (FIB), shows the preservation of the rigid geometrical shape after the cut, which suggests there is minimal stored elastic energy. (**B**) AFM contact mode measurement of the sensitivity (*S*) of the photo-detector for the silicon substrate and the four turns of a ZnO nanohelix, as indicated by 1 to 4 in the inserted AFM image. The sensitivity S of the photodetector is the inverse of the slope of the force-displacement (*F-Z*) curve, which is directly related to the elastic property. The measurement was done by positioning the tip on the surface of the up most middle-point of the turn of the helix. Each dot represents one measurement. The sensitivity S_{Si} for silicon is significantly lower than that for the ZnO nanohelix (S_{Helix}). (**C**) Fracture of the nanohelix at two consecutive turns of the nanohelix by the AFM tip, showing a preservation of helical shape in the sectioned region.

4.23C), and the preservation of the rigid shape by a single-turn helix after cutting suggests little if any stored elastic energy.

The transverse spring constant of the nanohelix, a quantity for describing the stiffness of the nanohelix perpendicular to its axial direction, has been measured by AFM using the force-displacement (*F*-*Z*) curve. Through the static compression of a nanohelix lying on a silicon substrate with an AFM tip (Figure 4.23B) [see Figure 4.24] and careful calibration of the sensitivity S

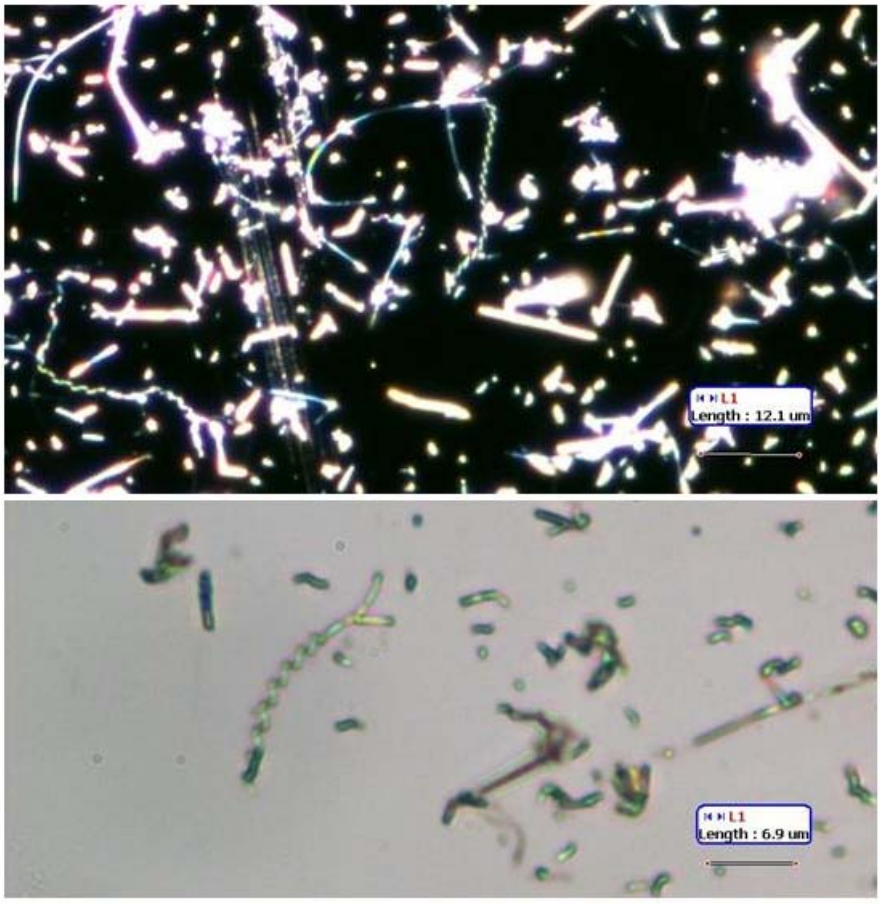

Figure 4.24 Optical images from the nanohelices lying on silicon substrate for AFM manipulation and measurements.

of the photodetector, which is the inverse of the slope of the *F-Z* curve [see Figure 4.25], the transverse spring constant K_{Helix} of the nanohelix was found to be: 3.9, 4.6, 4.5 an 5.3 N/m for 1 to 4 turns respectively, of the nanohelix as labeled in Figure 4.23B. The measured K_{Helix} is near the theoretically estimated transverse spring constant of 4.2 N/m, and so the elastic modulus E of the nanohelix derived from the measured spring constant is 42, 49, 48 and 57 GPa for the four turns respectively, which agrees well with the elastic modulus measured for straight ZnO nanobelts by mechanical resonance using in-situ TEM.

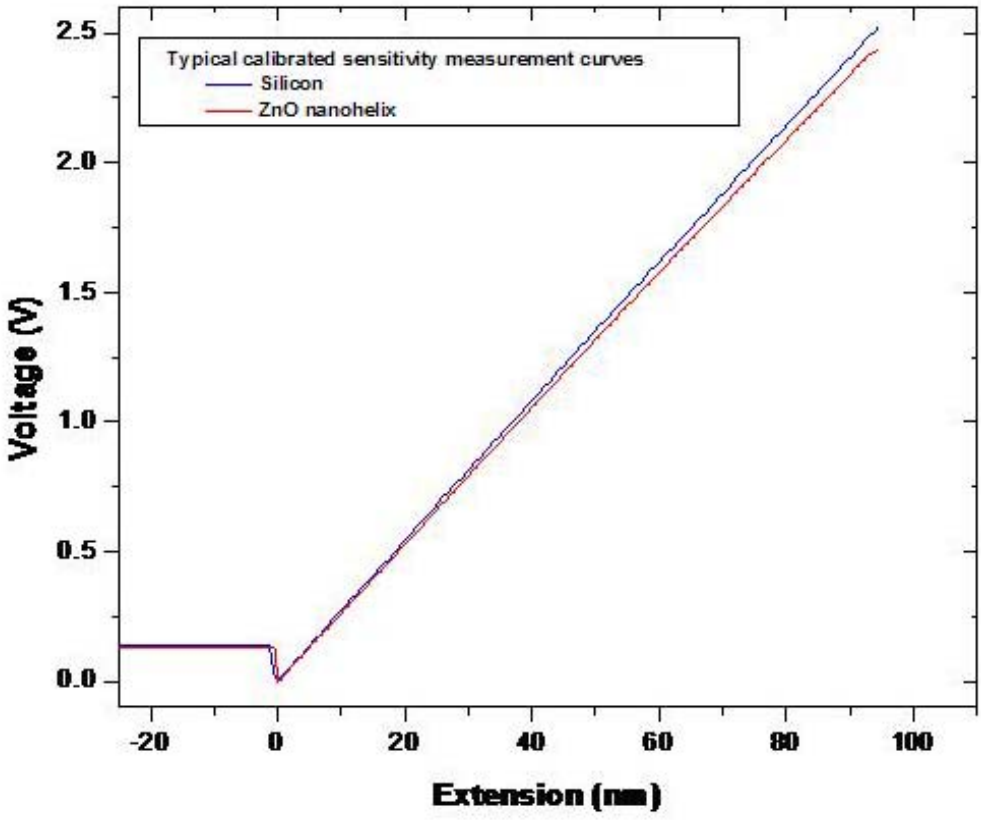

Figure 4.25 F-Z curves measured by AFM. Two typically calibrated sensitivity measurement curves for determining the spring constant of the nanohelix by AFM. The blue line is from silicon substrate, and the red from ZnO nanohelix. The slope of the curve is the most important quantity for our measurements.

The perfect helix shape we observed is of great interest not only for understanding the growth behavior of polar surface driven growth process in the wurtzite system, such as GaN, AlN and InN, but also for investigating fundamental physics and optical phenomena. The piezoelectric and semiconducting properties of ZnO suggest that the nanohelix could be a fundamental unit for investigating electromechanically coupled nanodevices by utilizing the superlattice piezoelectric domains. The nanohelix is likely to have important applications in sensors, transducers, resonators and photonics.

CHAPTER 5

SELF ASSEMBLY OF ZINC OXIDE NANOCRYSTALS: QUANTUM DOTS, NANODISKETTES, NANOTUBES AND NANOCAGES

Conjunction and integration of self-assembled process and structures with lithography based nanofabrication techniques is the key of bridging "bottom-up" with "top-down" approach in nanotechnology. As the first step toward this goal, exploration of techniques for building self-assembled nanostructures at all length scales and understanding the growth mechanisms are essential for achieving superior functionality. Biomaterial-like morphologies have been synthesized via self-assembled mesophase materials using solution based chemical approach[167,168], forming a group of structures such as ropes, helixes, spirals, gyroids, doughnuts, and discoids., and even hierarchically ordered mesophase crystals.[169,170,171] Structures formed by self-assembly of size-and shape controlled nanocrystals, passivated with surfactant and suspended in solution, have been demonstrated for a wide range of metallic [172,173,174,175,176,177], semiconductor [178,179,180] and oxide nanocrystals.[181,182]

In this chapter, we will focus on using the bottom-up approach to self assemble a variety configurations of ZnO nanostructures, ranging from 0-dimensional quantum dots, 1-dimensional nanotubes, 2-dimensional nanodiskettes to 3-dimemensional nanocages, etc. Two new strategies have been successfully probed and developed for fabrications of a versatile group of nanostructures building blocks for nanoelectronics and optoelectronics. First, a brand-new strategy involving electron-solid interaction is designed and demonstrated to successfully fabricate ultra-small quantum dots pattern on

bulk materials. Secondly, by using the simple vapor-sold growth process, in conjunction with the physical and chemical understanding of ZnO crystal growth process, a strategy for growing various types of nanostructures has been developed, which could be extended to a potential strategy for the other II-VI class and III-V group wurtzite structured semiconductors nanostructures.

5. 1 Self-organized ZnO Quantum Dots

Semiconductor quantum dots (QDs) provide an ultimate limit of quantization size in solids[183]. The strongest confinement of charge carriers in all three dimensions is a typical and unique property of QDs and is the basis for improved device characteristics and device innovations. The so-called Stranski-Krastanov (SK) technique is a favorable growth method of self-assembled quantum dots upon the existence of large lattice mismatchs within semiconductor heterostructures, where a switching from layer-by-layer to an island-growth mode occurs. Ion sputtering such as Ar+ bombarding represents another effective way to induce the formation of specifically homoepitaxial quantum dots or nanoisland arrays on the utilized semiconductor thin films such as Si, Ge, GaSb, InSb etc. It has been comprehensively believed that the surface instability led by ion beam energy illumination is the dominant factor for the self-assembly of semiconductor quantum dots.

A wide band-gap semiconductor, ZnO has seen important application potential in electronics and optoelectronics. ZnO quantum dots have been synthesized using a variety of approaches including wet chemical method, sol-gel method, and even gas-source chemical vapor deposition methods developed recently, etc. By using electron beam

illumination on ZnO nanobelt and nanowire, for the first time, locally pattern arrays of ZnO nanodots have been successfully fabricated. Through tuning the illumination intensity and dwell time, the nanodots size could be controlled as small as 1 nm, as large as tens of nanometer. The as-grown ZnO nanodots density could be as large as 1.8×10^{14} cm^{-2}. Electron beam induced self-assembly of quantum dots arrays has been demonstrated on the ZnO bulk single crystal as well. It is suggested that a large scale pattern of ZnO quantum dots array could be achieved by using unmasked e-beam lithography. And like ion sputtering, electron beam led surface instability could be utilized as another important approach for self-organized surface nanostructuring on semiconductor solids in a clean and cost-effective way.

As shown in Figure 5.1a is a low magnification SEM image of a ZnO nanobelt ~150 nm wide. It is interesting to find that after ~20 minutes of exposure under strongly convergent electron beam (acceleration voltage=10 kV, current density=0.54 nA/cm^2), local area as shown in square-boxed region of Figure 5.1b is rather brighter compared to the unexposed or less exposed area due to the more electron charges trapping. When the local exposed area was magnified in Figure 5.1c, it is observed that the surface of ZnO nanobelt has become rough with edged surface. It is significant that the surface of ZnO nanobelt has been covered by a great number of nanodots with diameter less than 10 nm, leading to a rather rough surface. Energy dispersive spectra analysis revealed that there is no the third element involved in the process except Zn and O.

To investigate the growth process of these nanodots, a video clip was recorded from the beginning of the exposure of a ~400 nm wide ZnO nanobelt under a strongly convergent electron beam in SEM with acceleration voltage and current density

respectively 10 kV and 0.54 nA/cm^2. Figure 5.2 is a set of four SEM images showing the nanodots growth moment respectively at 0″,1′33″, 2′14″and 6’34″. At the very beginning (~0′ E-beam exposure, Figure 5.2a), it is obviously that ZnO nanobelt surface is very smooth with no significant island emerging within the resolution range. While when exposure happened for about one and a half minutes, some visible grainy pattern began to

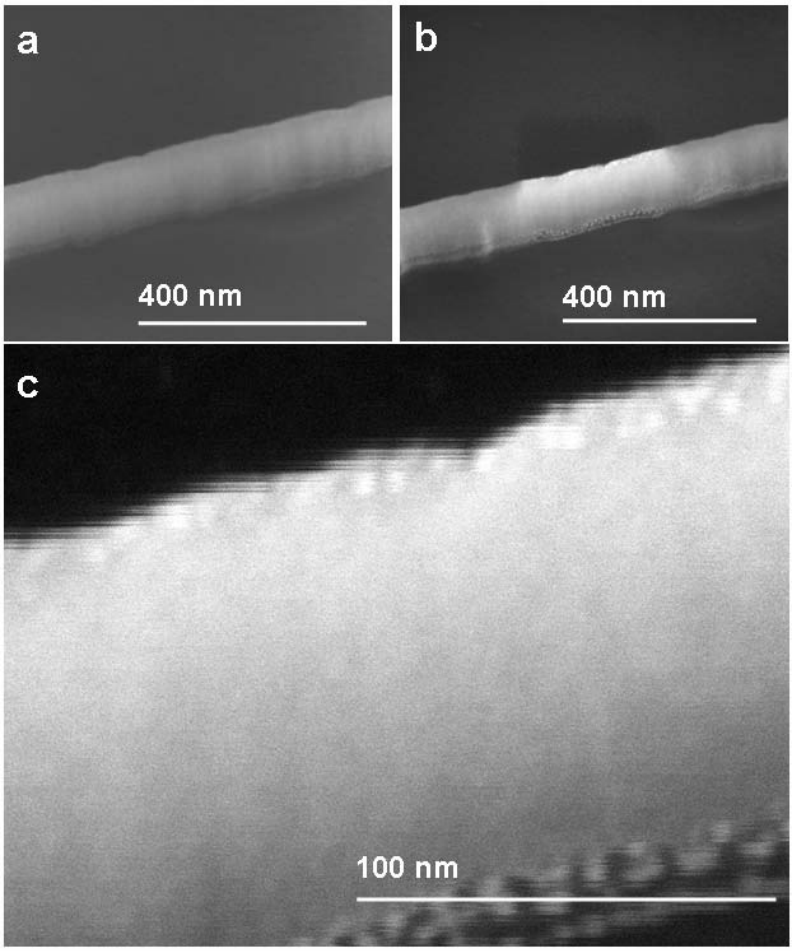

Figure 5.1 Surface morphologies of ZnO Nanobelts after electron beam exposure at (a) ~0 minute, (b) 20 minute, low-mag SEM image, (c) 20 min, high magnification SEM image. (V=10kv, I=0.54nA/cm^2).

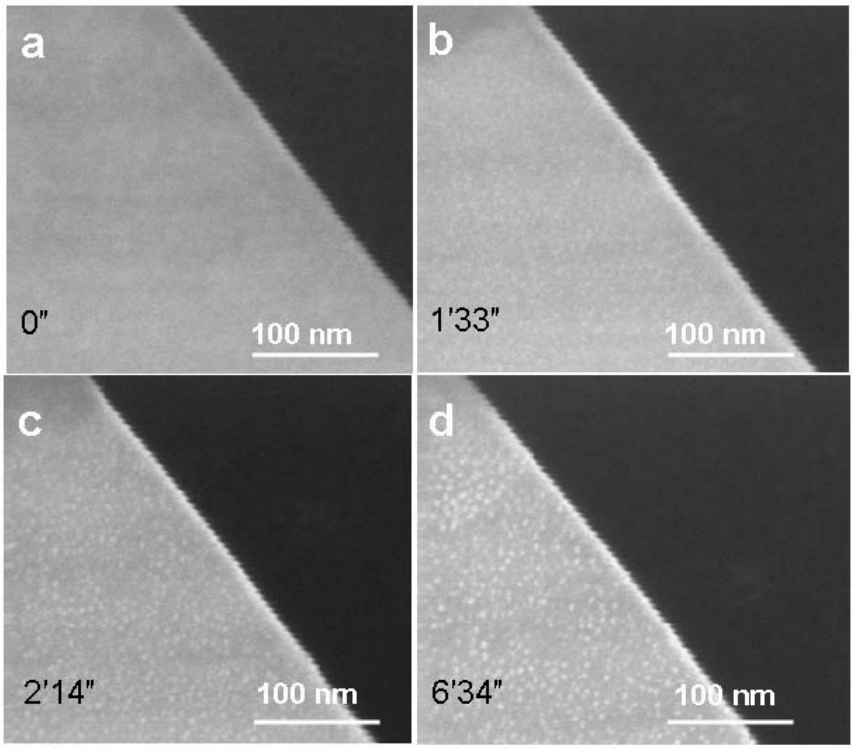

Figure 5.2 Formation process of ZnO quantum nanodots under electron beam illumination.

come out (Figure 5.2b). After 2′14″ (Figure 5.2c), nanodots with size around 2 nm were densely packed on the the surface of ZnO nanobelt. And as the exposure time increases, the nanodots size becomes bigger and bigger. At 6′34″ (Figure 5.2d), the nanodots are of a uniform size~5 nm. Based on the SEM images, the density of these nanodots is approximated as large as 1.8×10^{14} cm^{-2}.

In-situ transmission electron microscopy was used to characterize the structure and composition of the as-grown nanodots. Under TEM, a similar phenomenon happened as the case described in figs. 5.1 and 5.2. A high magnification TEM image is shown in Figure 5.3a, it is clear that under TEM electron illumination, the surface of ZnO nanobelt becomes rougher and rougher and covered by lots of nanoislands around 3.5 nm in diameter. Furthermore, under an electron acceleration voltage of 400 KV, the irradiation

effect becomes much stronger than under SEM, where the acceleration voltage is only 10 KV. The high resolution lattice image was shown in Figure 5.3b, the nanodots or nanoislands sprouted out with exactly same lattice pattern as that of the original ZnO nanobelt, "the substrate". It is suggested that the nanodots are ZnO nanodots homoepitaxially grown on ZnO nanobelts.

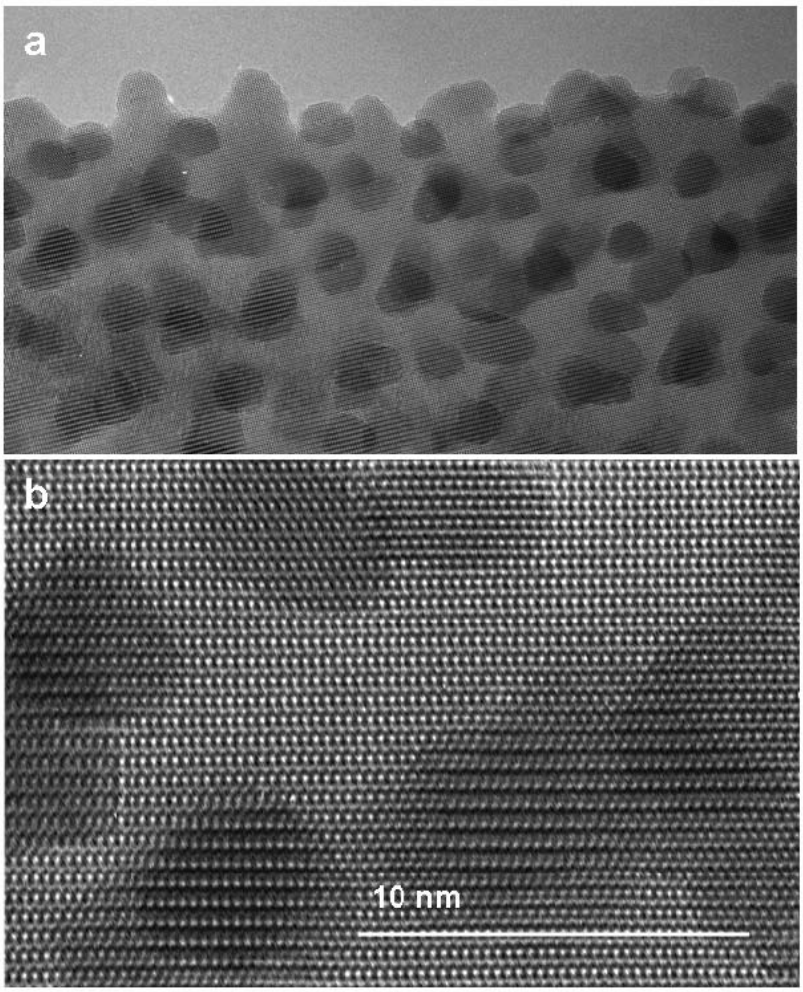

Figure 5.3 A low-magnification TEM image (a) and a high resolution TEM lattice image (b) displaying the homoepitaxial growth of ZnO quantum nanodots on a ZnO nanobelt.

During the growth of ZnO nanodots out of ZnO nanobelts "substrate", there is tendency that the nanodots grow bigger and bigger with the increase of the electron beam

exposure time. To find out the size distribution of ZnO nanodots correlating to the exposure time, the time dependence of ZnO nanodots' growth (V=10 KV, I=0.54 nA/cm^2) is plotted in Figure 5.4. The nanodots size at a certain exposure time is an average of 100 nanodots in the certain snapshot frame. From the plot, it is clear that the nanodots can grow from a very small diameter less than 1 nanometer upon an exposure time less than 30 second, to ~5 nm in diameter at the exposure time of ~7 minutes.

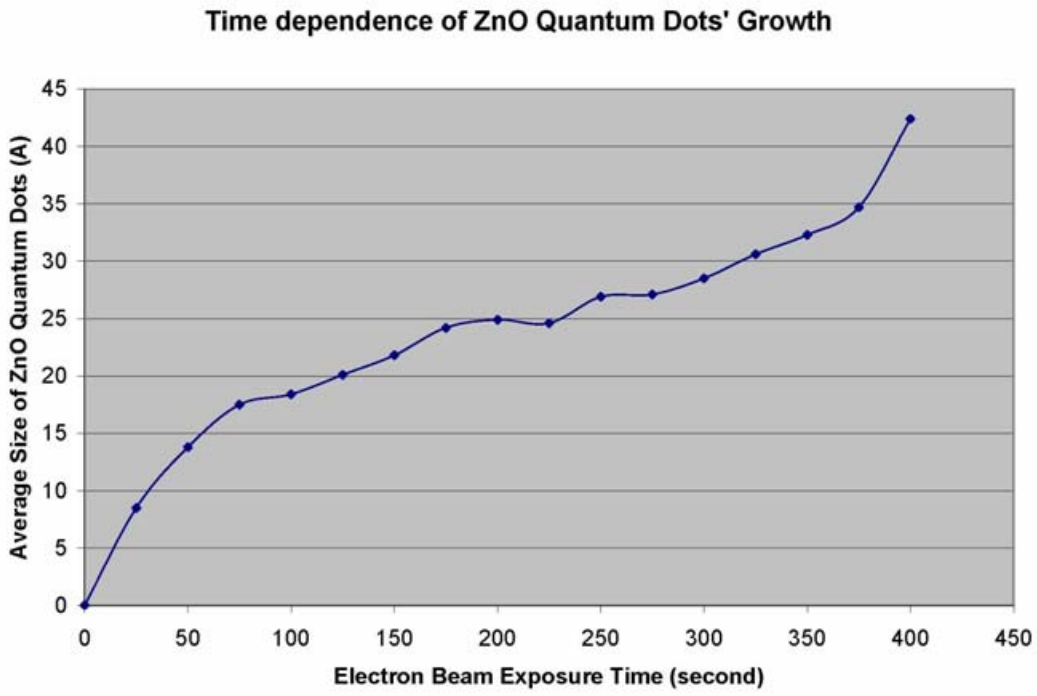

Figure 5.4 Time dependence of ZnO quantum nanodots' growth on ZnO nanobelts under electron beam exposure (V=10 KV, I=0.54 nA/cm^2).

To find out if the self-organized ZnO nanodots formation works for ZnO bulk single crystal, two types of ZnO single crystal wafers with orientations respectively [0001] and $[01\bar{1}0]$ have been used for electron-beam irradiation. As expected, self-assembly process of ZnO quantum dots happened on both types of wafer surface under electron beam exposure. As shown in Figure 5.5 are two SEM images respectively

representing the original polished (0001) ZnO surface (Figure 5.5a) and the surface post electron-beam exposure (Figure 5.5b). It is clearly seen that after 20 minutes electron beam exposure, on the originally atomically smooth surface of (0001), densely-packed ZnO quantum dots about 5 nm in diameter grow similar to the case on ZnO single crystal nanobelt.

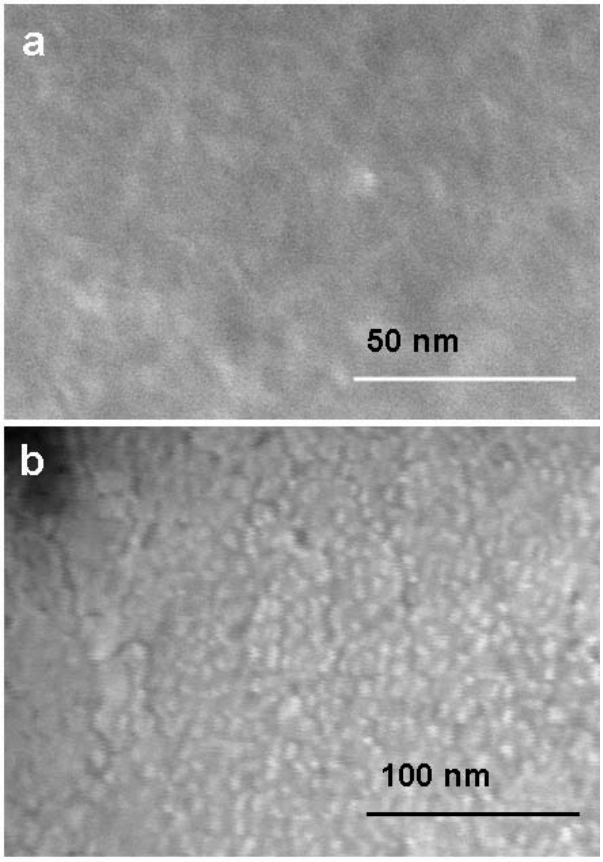

Figure 5.5 SEM images showing ZnO (0001) single crystal wafer (0001) surface morphologies before (a) and after (b) electron beam exposure with V=10kv, I=0.54nA/cm^2 for 20 minutes.

Since ZnO quantum dots will form on ZnO bulk surface under electron-beam illumination, it would be interesting to investigate the surface morphology evolution under a specific illumination intensity of electron beam. As for the illumination intensity, accelerating voltage and current density will be the key parameters. As shown in Figure

5.6 are two sets of electron beam illuminations with respectively 2KV, 0.21 nA/cm^2 (Figures 5.6a and 5.6b) and 5KV, 0.4nA/cm^2 (Figures 5.6c and 5.6d). Figure 6a is a low magnification SEM image of (0001) ZnO surface after 3 minutes exposure under 2 kV, 0.21 nA/cm^2 electron beam. After short time period exposure, it is evident that the smooth surface became rougher and the ZnO atoms and clusters on local area get rearranged under high E-beam intensity illumination. From the contour in the center of the image, it can be derived that the some of the center materials have diffused to the

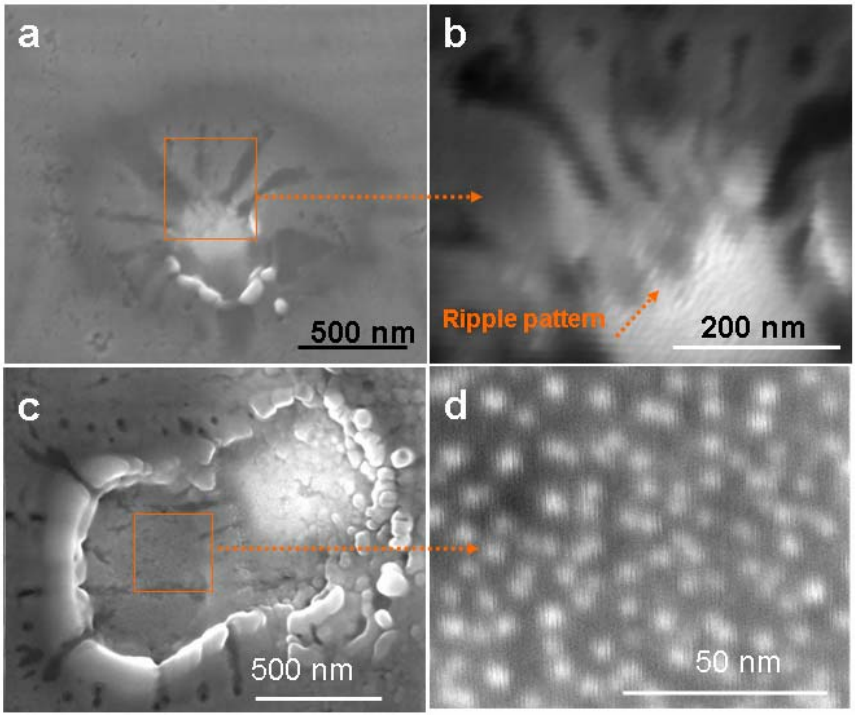

Figure 5.6 The surface morphology evolution under a specific illumination intensity of electron beam after certain time periods. (a)-(b). V=2 KV, I=0.21 nA, 3 min Exposure; (c)-(d). V=5 KV, I=0.4 nA, 30min exposure.

surrounding area, form a river-like radial corrugated pattern. The river pattern was not that significant in the bottom area of illumination, where there is a visible clump wall, a clump of diffused materials. This type of asymmetrical pattern may be induced by the

asymmetrical distribution of electron-beam illumination intensity caused by the electro-optics of the SEM.

The magnified SEM image in Figure 5.6b corresponds to the squared boxed area in Figure 5.6a. It has shown that there is a fine pattern inside the intensive-illumination area, a corrugated ripple pattern similar to the Si surface under Ar+ bombard. From the asymmetry of post-illumination surface morphology and the existence of ripple pattern, it is suggested that like the ion sputtering case on semiconductor surface, there could be an incident angle dependence on the surface diffusion led morphology evolution. Upon higher illumination intensity with higher accelerating voltage (5 KV) and higher current density ($0.4nA/cm^2$), after a longer period of ~30 minutes' illumination, it is found that the a cavity of about 1 um^2 comparable to the illumination area is formed on the bulk surface, the clump wall surrounded the irregular shaped cavity. The river pattern radically extends to the out side of the cavity, the unexposed ZnO bulk surface area. A high-magnification SEM image corresponding to the cavity bottom area in Figure 6d indicates that a densely packed ZnO quantum dots array has self-assembled under stronger and longer electron-beam illumination, instead of a ripple pattern in figs. 5.6a and 5.6b.

So far, the understanding of electron-illumination effect on semiconductor surface is still far from clear. It is suggested that like ion sputtering process, it could be a great scientific research topic in terms of light weight electrons and accumulation of scattering effect which are very rare for ion bombarding process. And it is suggested by design and control of the writing parameters under the e-beam lithography SEM, a large-scale quantum dots array of ZnO with desired and designed pattern could be achieved, which

would be of great interest for further design and creation of new class quantum devices involving quantum dots arrays as the intermediated band structure tunning layer.

5. 2 Textured ZnO Nanocages and Shells

In this section, by using a simple vapor-solid phase growth process, a new self-assembled nanostructure, mesoporous structured polyhedral cages and shells formed by self-assembly of ZnO, which are made by a novel self-assembly process during physical deposition. The cages/shells exhibit unique geometrical shapes and their walls are composed of mesoporous and textured ZnO nanocrystals. The structures of the cages and shells are studied and a growth mechanism is proposed.

5. 2. 1Materials Synthesis

Zinc oxide is a versatile smart material that has unique applications in catalysts, sensors, piezoelectric transducers and actuators [184], photovoltaic[185], and surface acoustic wave devices.[186] Growth of high quality (0001) textured ZnO thin films has received enormous attention due to its maximized piezoelectric performance.[187] Thin films composed of nanocrystalline ZnO are usually grown by chemical vapor deposition and e-beam sputtering. The structures reported here were synthesized by a solid-vapor deposition process, analogous to the process used for synthesis of oxide nanobelts.[188] The experimental apparatus includes a horizontal tube furnace, a rotary pump system and a gas supply system. A mixture of commercial ZnO, SnO_2 and graphite powders in atomic ration of 2:1:1 was grounded and then used as the source material, which is located in an alumina boat and positioned at the center of the alumina tube. After evacuating the tube to 2×10^{-3} Torr, thermal evaporation was conducted at 1150 ^{o}C for 15 minutes under

pressure of 200-300 Torr and Ar flow rate 25 sccm (standard cubic centimeters per minute), then cooled down to 1000 ^{o}C and kept isothermal for 30 minutes without supplying Ar gas. The gray-white products collected downstream in a temperature range of 300 -500 ^{o}C onto an alumina substrate are investigated by electron microscopy.

5. 2. 2 Results and Discussions

5. 2. 2. 1 Textured Cage and Shell Structures

For a typical synthesis, particles are observed to be dispersed uniformly on an alumina substrate (Figure 5.7). This process has very high repeatability following the

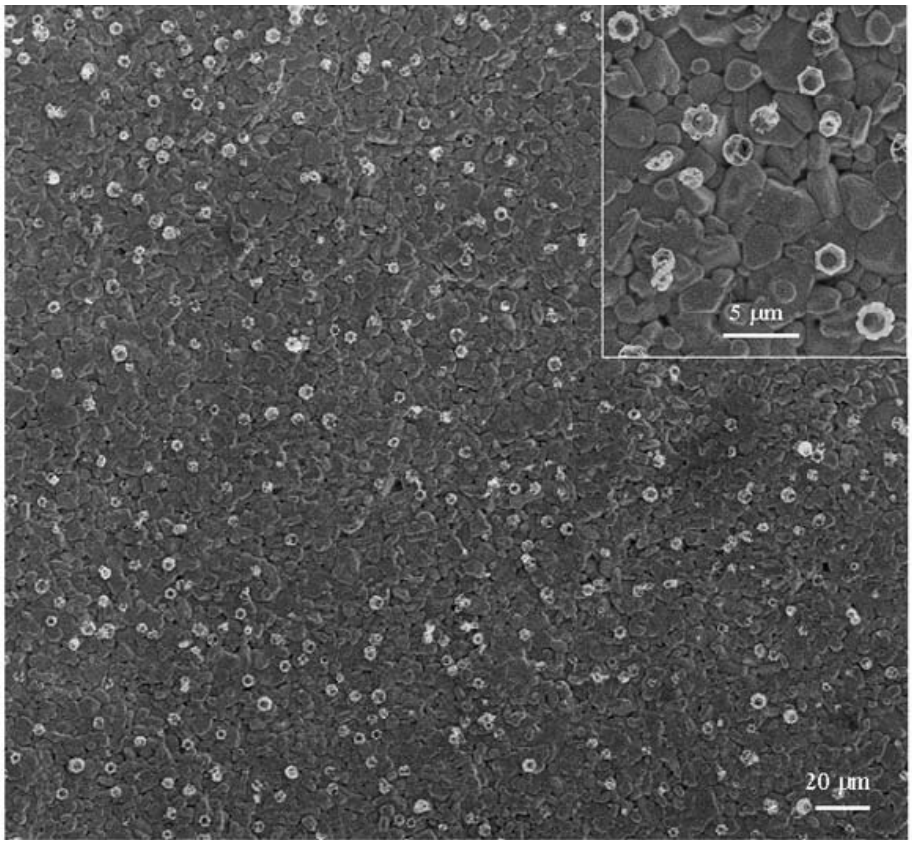

Figure 5.7 A typical low-magnification SEM image of the as-synthesized ZnO polyhedral cages and shells distributed uniformly on the substrate surface, showing high construability of the process.

procedures given in the experimental section. The dispersive distribution of the particles suggests that they were formed by individual nucleation and growth. A closer examination of the particles indicating that they are mostly hollow shells as presented in the enlarged image inserted in Figure 5.7, where some polyhedral cages and spherical shells are observed.

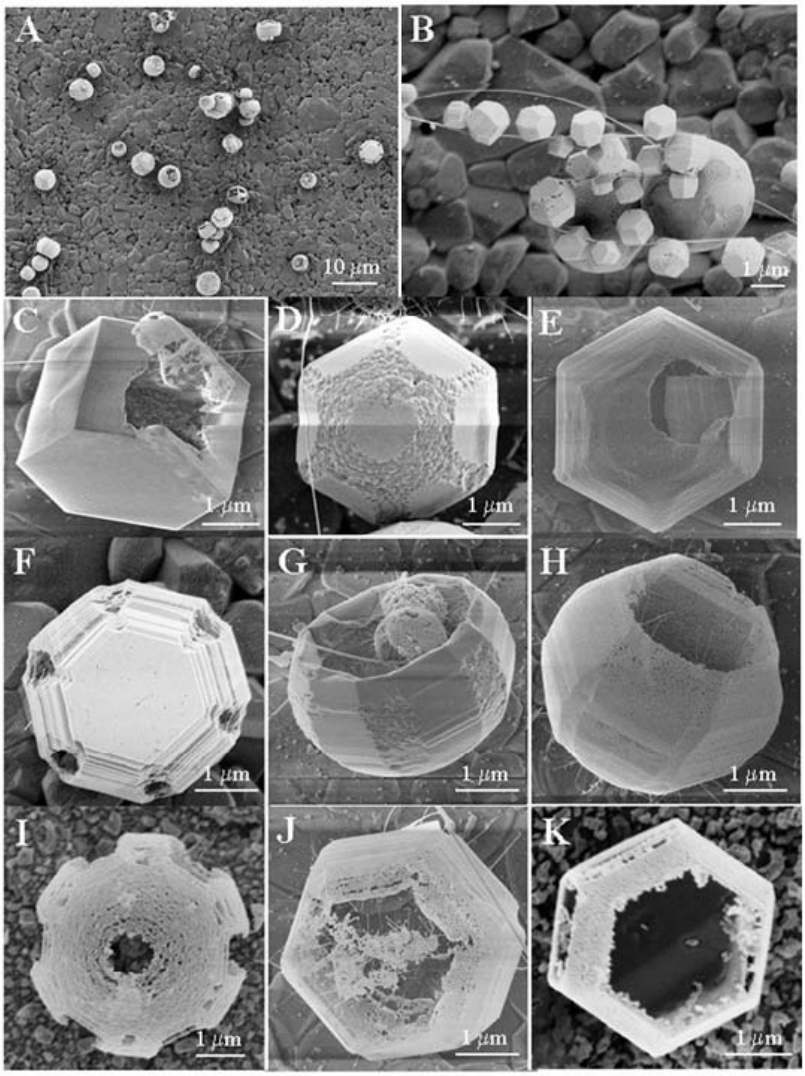

Figure 5.8 Low-magnification SEM images of ZnO polyhedral cages and shells distributed (A) dispersively on the substrate and (B) aligned along a nanobelt, respectively. (C-E) Typical drum shaped cages of truncated hexagon-based shells. (F-K) Open cage structures of mesoporous textured ZnO nanocrystals.

In the temperature zone that we are interested in, balls and polyhedra are observed, some of them are dispersed on the substrate and there appears no correlation among them (Figure 5.8A), while some of them line up along a ZnO nanobelt (Figure 5.8B) that was formed in a higher temperature zone of typically 700-900 ^{o}C. Details about the nanobelts have been reported previously. The nanostructures displayed by the scanning electron microscopy (SEM) images apparently exhibit the regular polyhedral shapes. The typical shapes observed are classified into two groups: hexagon-based drums and spherical/hemi-spherical shells.

In order to investigate the related shapes of the cages and shell, we have collected all of the possibly observed shapes through SEM observation to find their common characteristics for proposing a growth mechanism, and the results are collected in Figures 5.8C-K. The hexagon-based rods are often seen (Figure 5.8C) but they have the shell structure; some hexagon-based rods with truncated edges are also found (Figure 5.8D), which have a shape analogous to a drum. The polyhedron is enclosed by (0001) (top and bottom surface), $\{10\bar{1}0\}$ (side surfaces), stepped $\{10\bar{1}1\}$ (inclined surfaces) and high index planes with rough surfaces (Figs. 5.8D and E). Some truncated hexagon-based drums show open corners, as the one displayed in Figure 5.8F. In some cases, one side of the shell collapses possibly due to high growth temperature as well as the small shell thickness (Figure 5.8G). The local thickness of the shell depends on the crystallographic nature of the surface; the {0001} surface can be open (Figures 5.8H-K), the lower energy $\{10\bar{1}0\}$ surfaces can also be open in some cases (Figures 5.8I, K). A common feature is that the shell exhibits mesoporous structure, which will be discussed next.

Although the polyhedral shell structure appear to be composed of nanocrystals, transmission electron diffraction and imaging indicates that they have a "single crystalline" textured orientation (Figure 5.9A), and the side surfaces are $\{10\bar{1}0\}$. The three-dimensionally projected structure can be seen through a bright-field TEM image. Dark-field TEM image confirms that the shell structure is composed of nanocrystals, which are oriented with texturing (Figure 5.9B). High-resolution TEM image recorded along [0001] clearly shows the six-fold symmetric lattice image. Detailed analysis of the image indicates grain boundaries, as indicated by arrowheads, and holes introduced by the mesoporous structure (Figure 5.9C). The average size of the nanocrystals is 20-40 nm.

To trace the effect of Sn in the growth of the cages and shells, detailed TEM analysis was carried out. There are numerous of ZnO nanowires growing on the surfaces

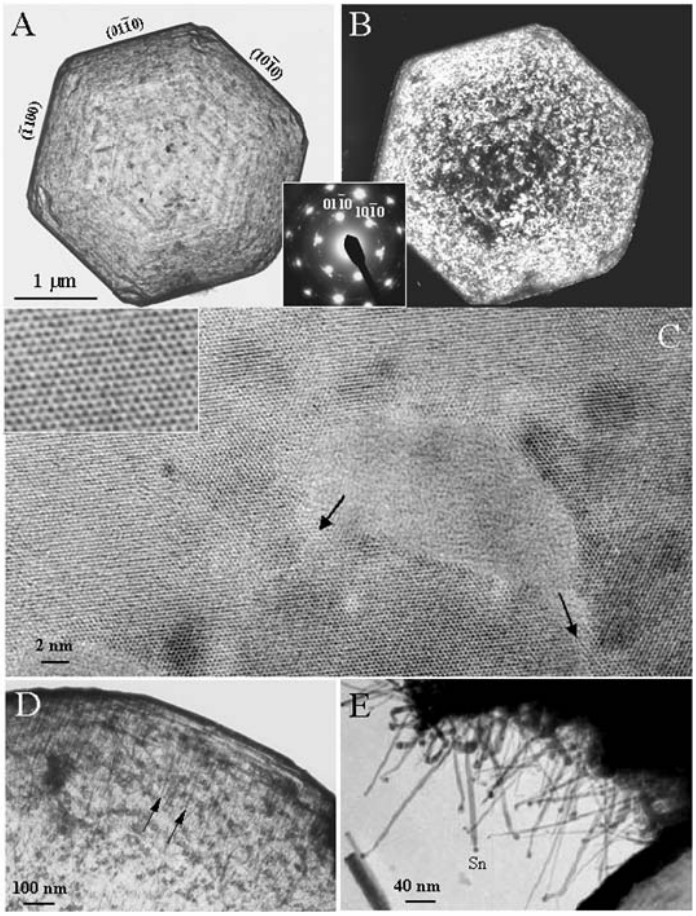

Figure 5.9 (A) Bright-field and (B) dark-field TEM images of a hexagon-based cage, where the inset electron diffraction pattern shows the textured orientation of the ZnO nanocrystals. (C) High-resolution TEM image recorded along [0001], showing the crystalline, mesoporous and textured grain structures of the cage. An enlargement of the image is inserted. (D) Low magnification TEM image showing the growth of ZnO nanowires inside the cage structure, as indicated by arrowheads. (E) TEM image of the ZnO nanowires grown outside of the cage with Sn particles at the tips.

of the cages and shells (Figure 5.9D). There are usually tiny Sn particles located at the growth front, which lead the growth of the ZnO nanowires (Figure 5.9E). EDS analysis, with a detection limit of 2 at.%, shows that the ZnO nanostructure has no Sn content in its volume.

Another major structure observed is spherical or hemispherical shell structure (Figure 5.10A), and they tend to align along a ZnO nanobelt. Enlargement of the shell

clearly presents the mesoporous structure with some open holes (Figure 5.10B). Spheres with thicker walls can also be identified (Figure 5.10C); an enlarged SEM image from the

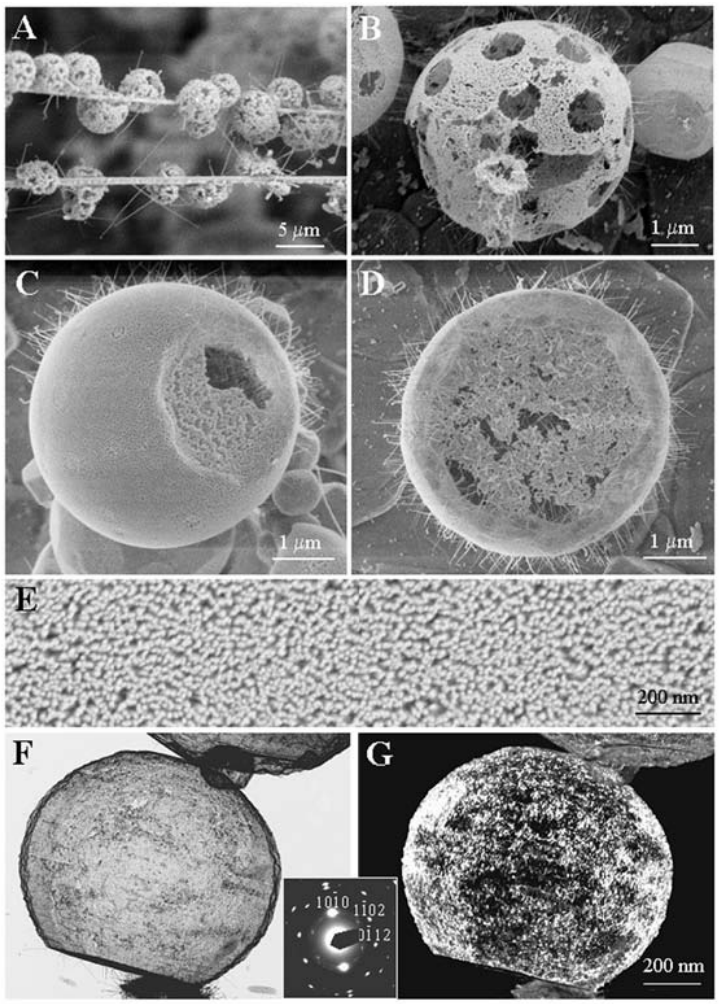

Figure 5.10 (A) Low-magnification SEM image of spherical shells distributed along a ZnO nanobelt. (B-D) Spherical shells composed of textured ZnO nanocrystals. (E) A high-magnification SEM image from the shell, showing mesoporous and nanostructured nature of the shell. (F, G) Bright-field and dark-field TEM images from a partial hemispherical shell. The corresponding electron diffraction pattern proves the textured orientation of the ZnO nanocrystals in the shell.

surface displays the mesoporous structure (Figure 5.10E), with nanocrystallites of sizes ~ 30 nm. The materials that fill in the sphere are also mesoporous with the presence of ZnO nanowires grow both inside and outside the shell (Figure 5.10D). Bright-field TEM

image proves the shell structure of the sphere, and the shell thickness is ~ 50 nm (Figure 5.10F). The patch and grainy type contrast observed in the dark-field TEM image (Figure 5.10G) proves that the shell is nanostructured. Electron diffraction pattern from the shell shows a single crystalline structure and is indexed to be $[\bar{2}4\bar{2}3]$, confirming the texturing of the ZnO nanocrystals.

5. 2. 2. 2 Growth Mechanism

The formation process of the polyhedral ZnO shell and cage structures is proposed to be a process comprised of solidification of liquid droplets, surface oxidation and sublimation (Figure 5.11). The introduction of graphite in the raw materials is to reduce the oxides into metals as given by:

$$2ZnO\ (s) + C\ (s) \rightarrow 2Zn\ (g) + CO_2\ (g), \quad (1)$$

$$SnO_2\ (s) + C\ (s) \rightarrow SnO\ (g) + CO\ (g), \quad (2)$$

and/or

$$SnO_2\ (s) + C\ (s) \rightarrow Sn\ (g) + CO_2\ (g), \quad (3)$$

Based on our previous study, the SnO vapor can be converted into Sn and SnO_2 vapor at temperatures as low as 900 ^{o}C,

$$2SnO\ (g) \rightarrow Sn\ (l) + SnO_2\ (s), \quad (4)$$

The sublimated Zn atoms are carried down stream by the Ar carrier gas. If the Ar flow gas is tuned off during the growth, the concentration of the Zn vapor increases; and in the lower temperature region, Zn atoms condense and form liquid clusters (Figure 5.11A), which tend to deposit fairly uniformly onto either the substrate or on the surface of the nanobelts, formed in the high temperature zone and carried to the lower temperature zone by the Ar gas. The liquid droplets quickly solidify on the substrate in the lower

temperature zone, forming faceted single crystalline Zn polyhedra, which are enclosed by $\{0001\}$, $\{10\bar{1}0\}$ and $\{10\bar{1}1\}$ facets (Figure 5.11B). Then, the residual oxygen in the growth chamber can oxidize the surface of the Zn polyhedron. Since the oxidation rates on different crystal surfaces are different: the surface

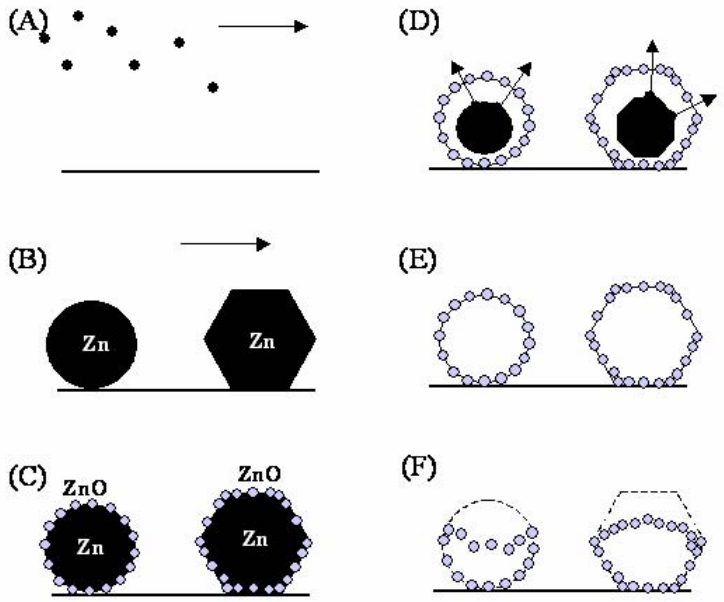

Figure 5.11 A proposed growth mechanism for the formation of the cages and shells composed of textured ZnO nanocrystals. (A): Zn vapor phase carried by the Ar gas. (B) Deposition of the Zn droplets at different substrate temperature region results in the formation of single crystalline spherical and hexagon-based rods Zn particles. (C) Surface oxidation produces textured ZnO nanocrystals on the Zn surface. (D, E) Vaporization/sublimation of the Zn core results in the formation of ZnO cage/shell structure. (F) The cage/shell could collapse due to sintering at the growth temperature.

with lowest energy tend to be most stable and may resist to be oxidized, while the high energy surfaces will be quickly oxidized, resulting in the formation of an oxide layer with a non-uniform thickness on the Zn polyhedral surface (Figure 5.11C). Both Zn and ZnO have the hexagonal crystal structure with lattice constants of a = 0.2665, c = 0.4947 and a = 0.3249, c = 0.5206 nm [189], respectively, ZnO tends to have an epitaxial orientation

relationship with the base crystal Zn. But the large lattice mismatch of 23.7% in the basal plane makes it impossible to form large size ZnO crystals covering on the Zn surface. Instead, ZnO nanocrystallites are formed as islands and they preserve the same orientation as the Zn crystal, and leave gaps/pores between the nanocrystallites owing to large local mismatch strain. The mesoporous structure is formed due to the distribution and growth of multi-nuclei on the Zn surface. Moreover, Zn has a much lower melting point of 419 ^{o}C than that of 1975 ^{o}C for ZnO, an increase in local temperature between 300 – 500 ^{o}C during the growth leads to the sublimation of Zn but not ZnO (Figure 5.11D), resulting in the formation of the textured ZnO shell/cage structure (Figure 5.11E). In some cases, the shell collapsed after the vaporization of the Zn core due possibly to that the oxide layer is thin and the local temperature is high enough to cause sintering (Figure 5.11F), forming various collapsed structures observed by SEM.

Temperature gradient may determine the equilibrium shapes for original Zn particles and the subsequent shapes of the nanostructured ZnO shells/cages (Figs. 5.11B-F). At a lower temperature region (below the melting point of Zn, 419 ^{o}C), the cages tend to have equilibrium shapes enclosed by (0001), $\{10\bar{1}0\}$ and $\{10\bar{1}1\}$ faces with relatively lower energy [190] due to a more spontaneous solidification process. In a higher temperature region (close to or above the melting point of Zn, 419 ^{o}C), spherical-like shells/cages may be formed due to the small undercooling level for the solidification process, with appreciable tendency to remain spherical shaped liquid droplets [190,191] while their surfaces are being oxidized.

5. 2. 2. 3 “Flower”-like Structure and Tin Content

The reduced Sn metal would serve as catalysts for the growth of ZnO nanowires [192] inside and outside the ZnO shell/cage (Figure 5.10). Energy dispersive X-ray spectroscopy (EDS) chemical analysis from the polyhedral shell structure indicates that the content of Sn is, if any, less than the EDS detection limit of typically 1-2 at. %. To trace the distribution of Sn in the final products, all of the structural configurations have been examined by EDS.

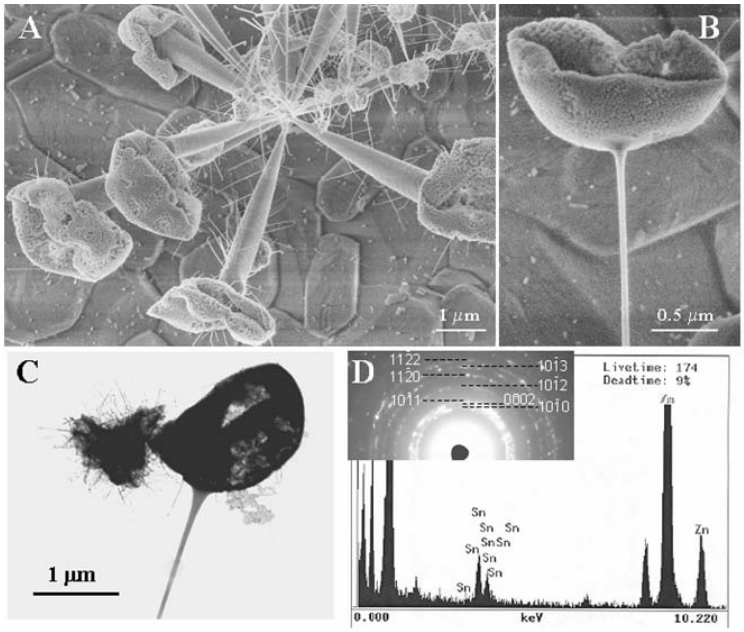

Figure 5.12 (A) ZnO rods supported Zn-Sn-O "flower-like" structures. (B) A high-magnification TEM image of the structure. (C) TEM image of the structure, and (D) corresponding electron diffraction pattern and EDS spectrum from the top flower region, showing polycrystalline structure without texturing. The electron diffraction pattern matches very well to the X-ray diffraction data for wurtzite structured ZnO, suggesting the Sn may be present in a form of tiny clusters.

Figure 5.12A shows the growth of a flower-like structure, where the branches are ZnO rods growing along [0001] (Figure 5.12B), and the "flower" is a nanocrystal composite (Figure 5.12C) with Sn content of ~ 8 at. %. Electron diffraction from the "flower" shows that the nanocrystals are oriented randomly, distinctly different from the cage and shell

structures presented in Figures 5.7-10, but the diffraction pattern still fits the ZnO structure. It may be suggested that the Sn could be present in tiny particles mixed in the nanocrystals that compose the flower-like structure. It must be pointed out that the flower-like structure was observed only occasionally. The structure observed in Figure 5.12A is the sintering result of the collapsed Zn-Sn-O shells after the vaporization of the Zn core.

5. 2. 3 Conclusions

We have successfully fabricated a new structure, mesoporous structured polyhedral drum and spherical cages and shells formed by textured self-assembly of ZnO nanocrystals, which are made by a novel self-assembly process during epitaxial surface oxidation. The cages/shells exhibit unique geometrical shapes and their walls are composed of mesoporous and textured ZnO nanocrystals. The structures of the cages and shells are studied and a growth mechanism is proposed to be a process following solidification of the Zn liquid droplets, surface oxidation and sublimation.

5. 3 ZnO Nanodiskettes

By tuning the synthesis parameters such as pressure in this study, various configurations of diskette-like ZnO nanostructures were achieved. The vapor phase transport synthesis parameters are: source materials: ZnO powders + graphite (C); evaporation temperature: 1100-1150 ^{o}C, evaporization time at the peak temperature: 30-60 minutes; short time pause for 0-10 min at 1000 ^{o}C (this step is designed for a comparative study to the case of tubular nanostructures to be presented in Section 4) during the cooling process; and pressure: 20-400 mbar. In the temperature zone we are

interested in, diskette-like nanostructures were observed to be in the form of clumps. The observed ZnO nanodiskettes can be classified into three types of morphologies with slightly different composition: textured core-shell Zn-ZnO nanodiskettes, "single-crystal-like" textured ZnO nanodiskettes, nanostructured polycrystalline ZnO diskettes and mesoporous ZnO diskettes. The as-deposited samples were collected at a temperature range of 400 to 600 ^{o}C.

5. 3.1 Textured Zn-ZnO Core-shell Nanodiskettes

For a typical synthesis by evaporating a mixture of ZnO and graphite at 1100 ^{o}C for 30 minutes (pressure was controlled around 20 mbar), textured diskette like ZnO and core-shell Zn-ZnO nanoparticles are received (Figures 5.13-16). It is worth noting that this process is of high reproducibility and high-yield.

Figs. 5.13a-d is a series of SEM images displaying the diskette-like ZnO nanostructure. A low magnification SEM image of the densely grown diskettes with uniform size of 1-2 μm was illustrated in Figure 5.13a. These diskettes are always in connection with zig-zag shaped nanowires. A side-view magnified image of a ZnO nanodiskette in Figure 5.13b presents a clear description that each diskette has a regular hexagonal faceted shape. The thickness of the disk is 100-200 nm. It is indicated by a white arrowhead in Figure 5.13b that an extended nanowire with a similar hexagonal cross-section grew normal to the hexagonal nanodiskette in the center area. It is also found that the normally emerging nanowire in fact could also extend from the side edge of the hexagonal nanodiskette (as displayed in Figure 5.13c). In general, one large surface of the nanodiskette is rather smooth while the other side is rough. The diameter of

nanodiskette could be as small as 300 nm, and its thickness could be as thin as 50 nm. The cross-section of the extended nanowire could also be irregular. Figure 5.13d shows a

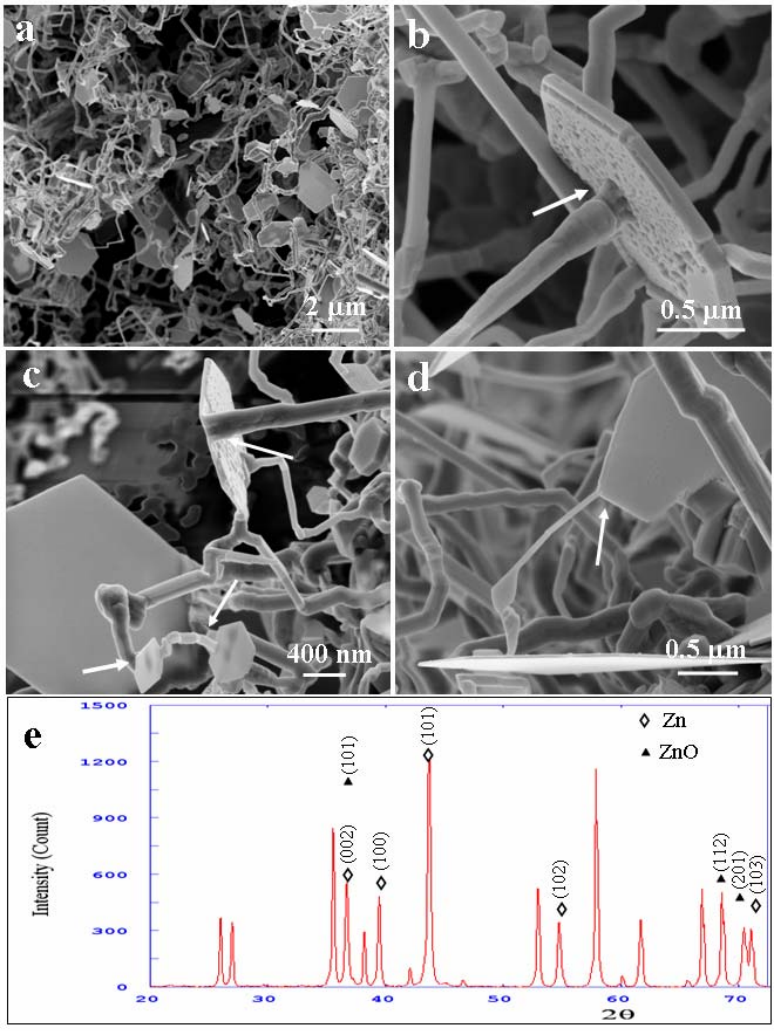

Figure 5.13 (a) A typical SEM image showing the densely distributed nanodiskettes of ZnO on alumina substrate. (b) A bottom side view of a nanodiskette, revealing a normally extruded nanowire from the center of the rough large surface of the nanodiskette. (c) Three irregular shaped nanowires grew from the side surfaces of nanodiskettes or their edges (as indicated by arrowheads). (d) A nanoribbon grown in the plane of the large surface of a nanodiskette. (e) A typical X-ray diffraction spectrum indicating majority peaks from ZnO and Zn (as indicated with a solid triangle and a diamond symbols respectively), the extra peaks come from the alumina substrate.

nanowire that directly grew from the edge in the plane of the hexagonal diskette (as pointed at by an arrowhead). X-ray diffraction spectrum of the as-prepared sample is

shown in Figure 5.13e, which proves that the majority of the peaks come from ZnO and Zn, whose diffraction peaks are marked by "▲" an "◊" respectively. The extra peaks were contributed by the alumina substrate used for collecting sample.

To find out the crystal structure of an individual nanodiskette, a systematic TEM imaging and diffraction analysis was conducted. Figure 5.14a is a TEM image of two hexagonal nanodiskettes of ~3 μm in width. The corresponding electron diffraction pattern in Figure 5.14b is a single crystal [0001] pattern of ZnO, which reveals that the top and bottom large surfaces of the nanodiskette are a pair of (0001) and $(000\bar{1})$ c-planes, while the six side facets are $\{01\bar{1}0\}$. Figure 5.14c is a TEM image showing a ZnO nanodiskette with three normally extended nanowires from the edge of the side surface (A), the center of the bottom rough surface (B), and the edge of the side surface

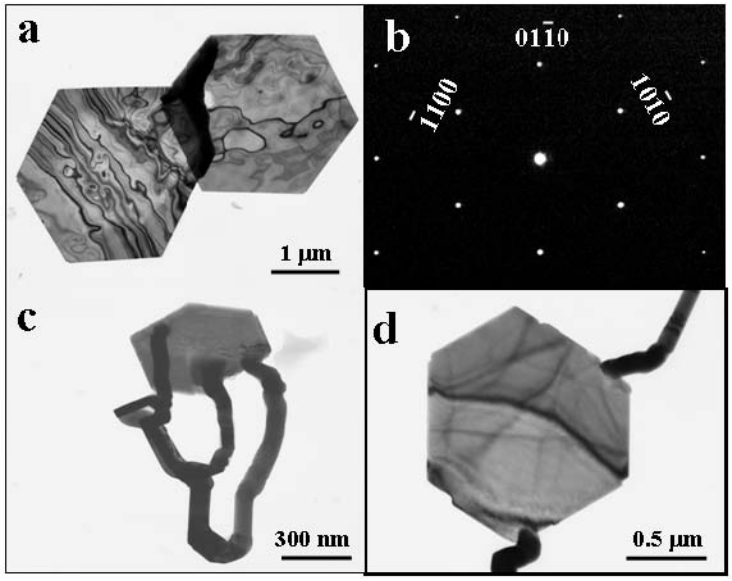

Figure 5.14 (a) and (b) are respectively a TEM image of two overlapped hexagonal nanodiskettes and the corresponding single crystal [0001] diffraction pattern from a diskette. (c, d) Nanowires grown out of the top and side surfaces of a ZnO diskette.

(C). The size of the nanodiskette is about 600 nm. The recorded top view of a 2 μm nanodiskette in Figure 5.14d displayed two extended nanowires from the edge of the nanodiskette.

Further TEM analysis was conducted to investigate the fine structure in the nanodiskette. Figure 5.15a is a bright field TEM image of a nanodiskette, which shows that the dominant surface of the diskette is rough. The corresponding dark field TEM image in Figure 5.15b clearly demonstrates the surface roughness, where nanosized nanocrystals were exposed. The diffraction pattern is composed of two sets of [0001] diffraction patterns corresponding to elemental Zn and ZnO, between which an epitaxial orientation relationship is preserved. Figure 5.15d is an HRTEM image recorded from the middle part of the nanodiskette in Figure 5.15a. The image depicts a two-dimensional Moire´ pattern with electron beam parallel to the *c*-axis of the two overlapping Zn and ZnO lattices. Considering that a Moire´ fringe pattern is produced by two sets of parallel overlapped lattice planes of Zn and ZnO, respectively, there are three sets of intersecting Moire´ fringes; every individual pattern is rotated with respect to the other by 60°, forming a Moire´ pattern as shown in Figure 5.15d. This is due to the epitaxial orientation relationship between Zn and ZnO as well as the perfect alignment in c-axes. Considering the lattice mismatch between Zn and ZnO, the inter-fringe spacing of the Moire´ pattern is about 1.30 nm, which corresponds to one Moire´ fringe every 4.6 atomic planes of ZnO or 5.6 atomic planes of Zn [193]. An HRTEM image from the edge part of the hexagonal nanodiskette is shown in Figure 5.15e. The lattice image displays the interface between Zn core and ZnO shell as indicated by two arrowheads. The upper part of the image

reveals the lattice image of the ZnO shell, while the bottom part corresponds to the elemental core Zn. The thickness of the ZnO shell is 1.5-2 nm.

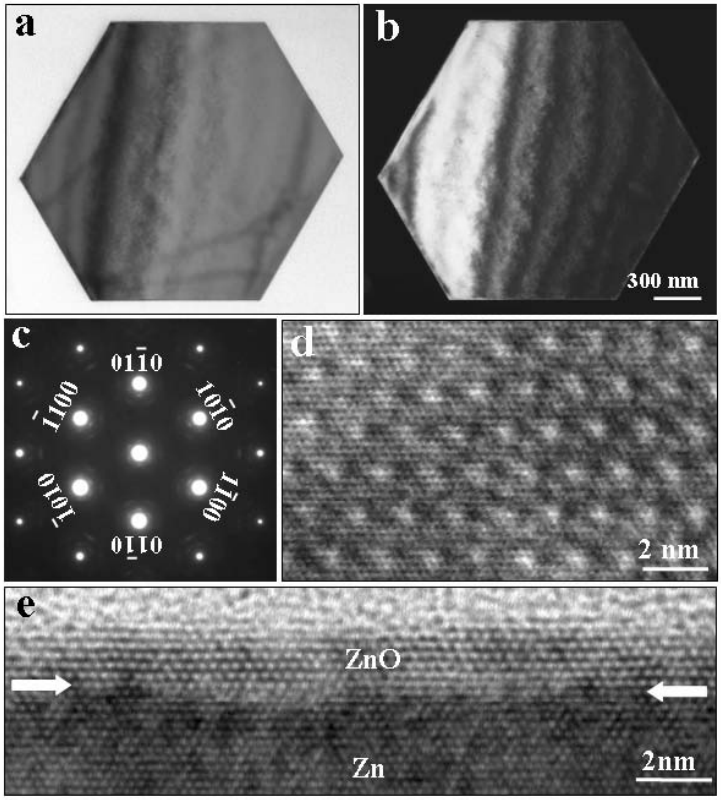

Figure 5. 15 (a, b) Bright field (BF) and the corresponding dark field (DF) TEM images of a Zn-ZnO core-shell nanodiskette composed of ZnO nanocrystals. (c) The corresponding diffraction pattern of the nanodiskette that is composed of two sets of [0001] diffraction spots from Zn and ZnO, respectively, showing their epitaxial orientation relationship. (d) High resolution TEM image from the diskette showing a two-dimensional Moire' frings. (e) HRTEM lattice image displaying the side wall of the ZnO and the middle Zn core, where two arrowheads point out the interface between the Zn core and ZnO shell.

To further investigate the lattice structure at the Zn-ZnO interface, the HRTEM image has been digitally processed. By taking a Fourier transform of the raw image displayed in Figure 5.16a, selecting only the reflections from Zn and ZnO, respectively, two sets of images corresponding to Zn and ZnO are presented in Figs. 5.16b and c. The Zn lattice is rather perfect without much distortion due to the fact that Zn was the

"mother"crystal formed first at the core. The ZnO is formed via oxidation so that the lattice exhibits imperfection due to the multiple nuclei's of the oxide grains on the surface. Mismatch dislocations and strains are apparent in the lattice image from the thin ZnO shell (see Figure 5.16c).

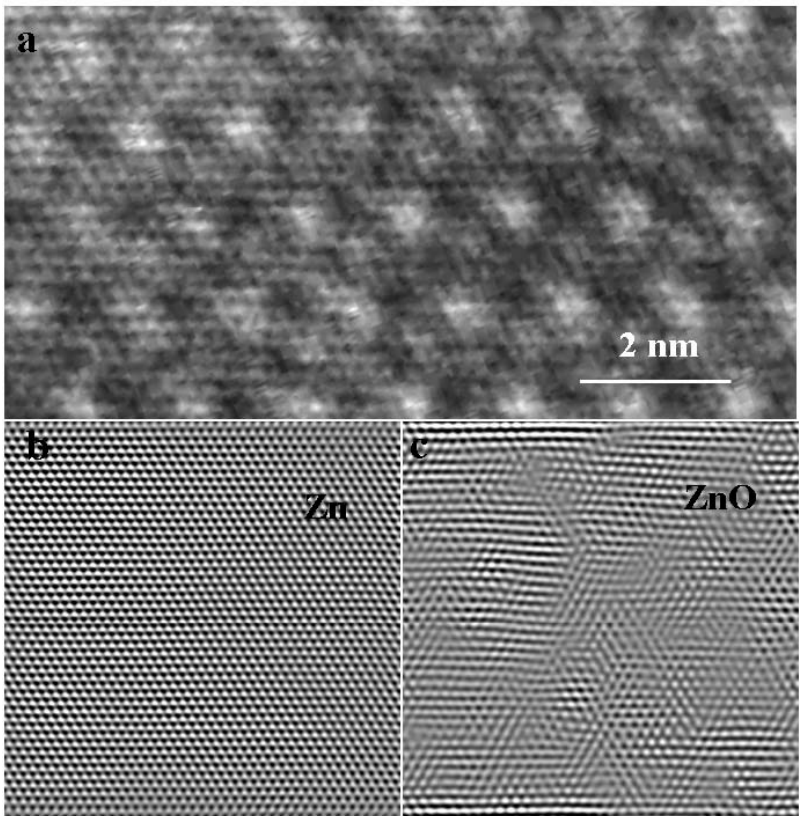

Figure 5.16 (a). HRTEM image recorded from a Zn-ZnO diskette. (b, c) Fourier filtered images of (a) showing the lattices from Zn core and ZnO shell, respectively.

5. 3.2 Nanostructured Polycrystalline ZnO Diskettes and Mesoporous ZnO Diskettes

To investigate the effect of pressure variation on the formation of ZnO nanodiskettes, we tuned the pressure from original 20 mbar to 200 mbar, and kept the other parameters the same as the one described in Section 5.3.1. It is interesting to find out that similar hexagonal diskette-like nanostructures of ZnO were grown in the form of clumps in a temperature range of 400-600 ^{o}C. Typically, three types of nanodiskette have

been observed under SEM, which are respectively single crystal ZnO nanodiskettes, polycrystalline nanodiskettes and mesoporous nanodiskettes as the substrate temperature increasing from 400 ^{o}C to 600 ^{o}C.

Figure 5.17a is a clump of densely packed ZnO nanodiskettes found in low 400 ^{o}C area, which have a uniform size of around 5 μm. Between the nanodiskettes, lots of tiny nanowires were grown. The magnified SEM image in Figure 5.17b clearly displayed that the thickness of each nanodiskettes is about 10 nm. Figure 5.17c describes that on one large surface of a nanodiskette, secondary growth of nanowires are clearly visible (as indicated by arrowheads). A typical low magnification TEM image in Figure 5.17d is a front projection view of a ~5 μm wide nanodiskette. The corresponding enlarged image on the left corner of the nanodiskette in Figure 5.17e reveals its grainy and patch dominated surface, an indication of a possible polycrystalline structure. While in Figure 5.17f the corresponding electron diffraction pattern proved it to be textured and self-assembled by ZnO nanocrystals that are approximately oriented in the same orientation.

As the local growth temperature increases to ~500 ^{o}C, the morphology and structure of the diskettes were changed. In Figure 5.18a, it is shown that more densely packed ZnO nanodiskettes/nanosheets form a big clump of flower-like morphology. The nanodiskettes tend to be wavy (Figures 5.18b and c) instead of the flat-like nanodiskettes collected in low 400 ^{o}C temperature region (Figures 5.17b and c). To determine if the nanodiskettes still kept the single-

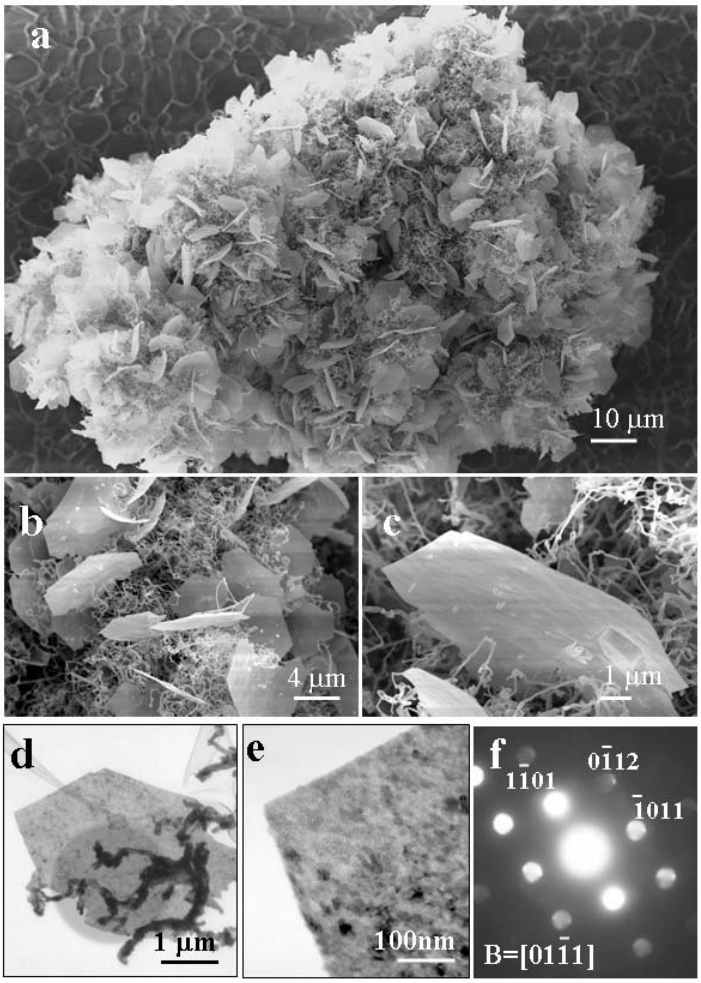

Figure 5.17 (a) A clump of ZnO nanodiskettes intermediated with lots of tiny nanowires. (b) A magnified SEM image showing the small thickness of the ZnO nanodiskettes and the intermediated tiny ZnO nanowires. (c) An enlarged side-view SEM image of a ZnO nanodiskket, revealing the secondary growth of ZnO nanorods on the large surface. (d, e, f) are respectively a low-magnification TEM image of a ZnO nanodiskette, an enlarged TEM image corresponding to the corner of the ZnO nanodiskette, and its corresponding electron diffraction pattern, showing textured grains of the ZnO nanocrystals composing of the nanodiskette.

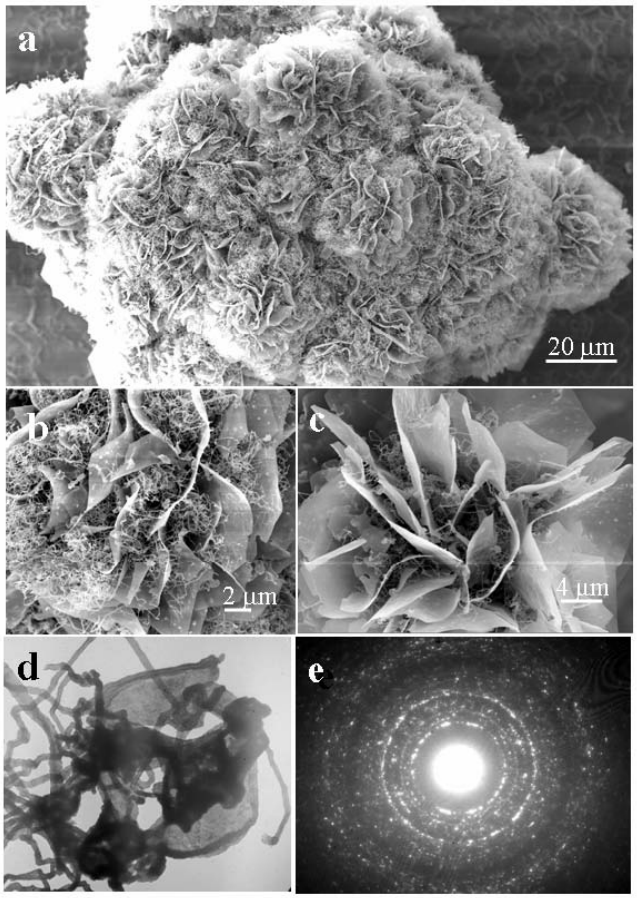

Figure 5.18 (a) A flower-like clump of packed ZnO nanodiskettes intermediated by nanowires. (b) A magnified SEM image showing a flower-like nanodiskettes with curved large surfaces. (c) Curved flakes of nanodiskettes with a uniform thickness as thin as ~30 nm. (d) a typical TEM image of two curved nanodiskettes with nanowires surrounding them. (e) The corresponding electron diffraction pattern revealing the polycrystalline structure of the curved nanodiskette.

crystal-like textured structure, TEM results are displayed in Figures 5.18d and e. Figure 5.18d is an TEM image showing two curved nanodiskettes with a diameter around 10 μm, between them quite a few Zn nanowires are around. The imaging difference between Zn nanowires and ZnO nanowires is that the former is curly and the latter is straight. The selected area electron diffraction pattern shown in Figure 5.18e is from a local small part of a curly nanodiskette. The ring pattern clearly shows that the nanodiskette is made of

nanocrystallites that are randomly oriented. This is very different from the single-crystal-like textured structure of the nanodiskettes collected at a lower temperature zone.

As the local temperature goes higher to ~600 ^{o}C, it is found that mesoporous nanodiskettes are the dominant morphological configurations. Figures 5.19a and b show two low magnification SEM images of the mesoporous nanodiskettes that still kept a uniform hexagonal shape. The thickness of the diskettes is as thin as tens of nanometers and the pore size is ~50 nm. Figures 5.19c and d are respectively the TEM images and its corresponding electron diffraction pattern of a mesoporous nanodiskette. The mesoporus feature is apparent, where the nanosized grains are uniformly distributed and interconnected to form a "net-like" structure. The electron diffraction pattern proves the random orientation of the nanocrystallites that compose the mesoporous diskette.

5. 3.3 Growth Mechanism of ZnO Nanodiskettes

In previous work on the textured polyhedral ZnO shell and cage structures, the formation process has been proposed to be a process comprised of solidification of liquid droplets, surface oxidation and sublimation. In our current work, similarly, the epitaxial oxidation on Zn surfaces is the fundamental process of forming the core-shell structure. The introduction of graphite in the raw materials is to reduce the oxides into metals as given by:

$$2ZnO\ (s) + C\ (s) \rightarrow 2Zn\ (g) + CO_2\ (g) \qquad (1)$$

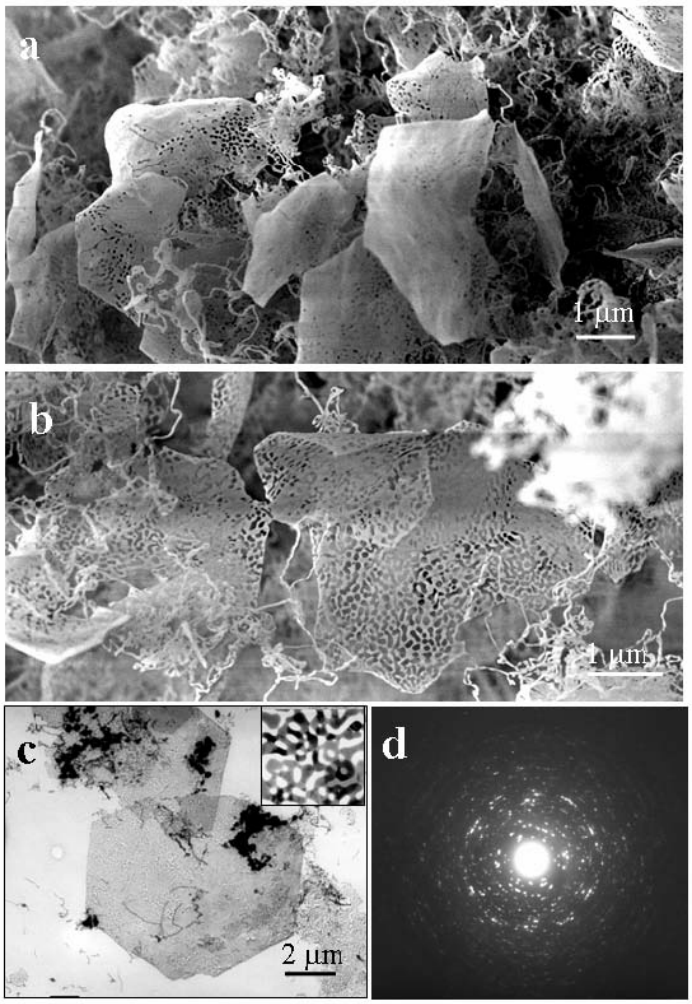

Figure 5.19 (a, b) Mesoporous nanodiskettes with a uniform hexagonal shape, small thickness (tens of nanometers) and pore structure. (c) and (d) are respectively a TEM image of a mesoporous nanodiskette and its corresponding electron diffraction pattern, the inset in (c) is a magnified TEM image showing the pores with size about 50 nm.

The sublimated Zn atoms are carried down stream by the Ar carrier gas. In the lower temperature region, Zn atoms condense and form liquid clusters (as schematically shown in Figure 5.20a), which tend to deposit fairly uniformly onto the alumina substrate. The liquid droplets quickly solidify on

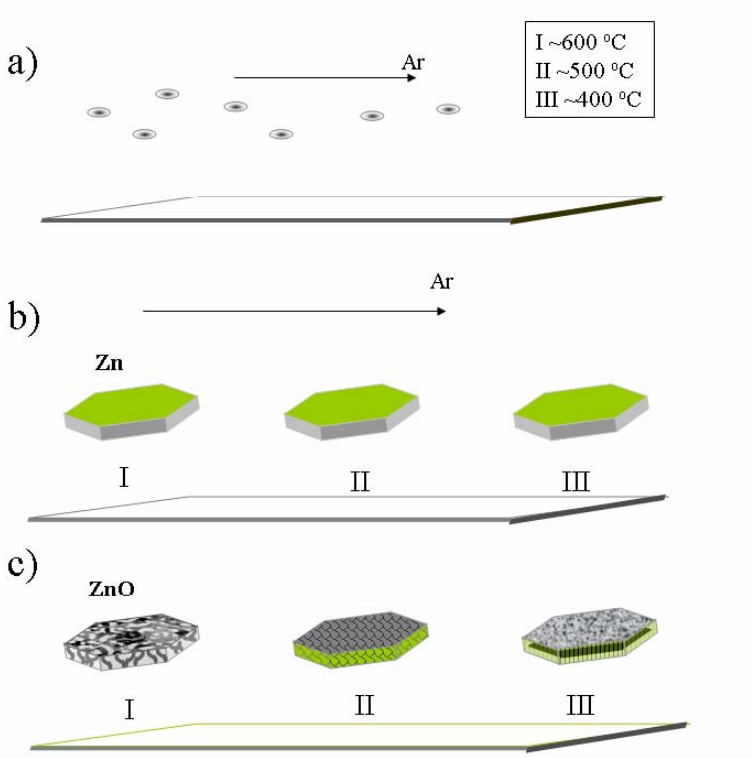

Figure 5 .20 A proposed growth model of the ZnO nanodiskette (see text for details).

the substrate in the deposition temperature zone of 400-600 ^{o}C. From the surface energy point of view, the lowest energy facets for Zn are {0001}, and then $\{10\bar{1}0\}$ and $\{2\bar{1}\bar{1}0\}$. Thus, the faceted single crystalline Zn hexagonal diskettes tend to form, which are enclosed by {0001} top and bottom surfaces and $\{10\bar{1}0\}/\{2\bar{1}\bar{1}0\}$ side surfaces, as shown in Figure 5.20b. With consideration of the lower local growth temperature, the residual oxygen in the growth chamber is likely to oxidize the surface of the Zn nanodiskettes, but the degree to which the diskettes to be oxidized depends on the local temperature. As shown in Figures 5.17, 18 and 19, with the local growth temperature increased from ~400 °C to ~500 °C and until ~600 °C, the hexagonal nanodiskettes

evoluted from single-crystal-like core-shell Zn-ZnO nanodiskettes and ZnO nanodiskettes (III) to nanostructured and polycrystalline textured nanodiskettes (II) and to mesoporous nanodiskettes composedof randomly oriented ZnO nanocrystals (I), respectively, as sketched in Figure 5. 20c. A slight difference between the work reported here from the cages and shells reported previously is that Sn catalyst is absent in the current study, thus, the formation of ZnO nanocrystal is contributed from the surface oxidation of Zn and the deposition of ZnO vapor directly vaporized from the source material:

$$ZnO\ (s) \rightarrow ZnO\ (g) \qquad (2)$$

At the lower temperature region of ~400 ^{o}C, epitaxial surface oxidation is the major contribution to the growth of textured Zn-ZnO diskettes and ZnO diskettes. The difference between textured Zn-ZnO diskettes and ZnO diskettes is the degree of oxidation being incomplete or complete. Since the local temperature is low, a slow oxidation is likely and a strong interaction with the Zn core is possible, resulting in single-crystal-like structure (see Figs 5.13-16).

With the increased local growth temperature to ~500 ^{o}C, the oxidation rates are likely to be higher, resulting in a quick formation of larger size ZnO nanocrystallites and non-uniform thickness of the ZnO nanodiskettes (Figure 5.20c II). In this case, the deposition of the coming ZnO vapor may become significant, which may directly deposit on the surfaces of the ZnO nanocrystals or form new nanocrystals on the nanodiskettes, thus, the epitaxial growth of ZnO nanocrystals is partially terminated because of the quick surface oxidation and the re-deposition of ZnO vapor at a faster rate, forming nanostructured polycrystalline objects (see Figure 5.15).

When the local temperature is as high as ~600 ^{o}C, a re-sublimation of Zn is possible; the sublimation rate of Zn nanodiskettes may be so fast that the deposition of polycrystalline and nanostructured ZnO is not enough to cover the entire surface of the original Zn nanodiskette. The areas covered or oxidized into ZnO are preserved, while the uncovered areas are resublimated, leaving behind a polycrystalline ZnO "skeleton" and the formation of holes or pores in the body of the nanodiskettes (Figure 5.20c I). In this case, the mesoporous structured ZnO is formed (see Figure 5.19).

Growth pressure could have significant effect on the nanostructure morphology. Figs. 5.13-16 and Figs. 5.17-19 are the data acquired when the the pressure in growth chamber was set at 20 and 200 mbar, respectively. For the case of 20 mbar, the limited amount of residue oxygen makes the temperature variation a dominating effect for the selective surface oxidation process, leading to a morphological transition from Zn particle (non-oxidized), Zn-ZnO core-shell textured nanodisk (incompleted selective-oxidation), to textured (single-crystal-like) ZnO nanodisk (completed selective-oxidation) in a temperature zone of 400-600 ^{o}C. While when the growth pressure was changed to 200 mbar, the residue oxygen amount became significant, the selective oxidation process can be fully completed in the entire temperature range. However, the temperature variation has become a dominant effect on the structural transition of ZnO nanodisk from textured, polycrystalline, to mesoporus and polycrystalline. In this transition process, excess amount of oxygen has led to the direct deposition of ZnO from the vapor phase. The epitaxial growth of ZnO nanodisk on Zn nanodisks may be terminated due to a simultaneous deposition of randomly oriented ZnO nanocrystals onto the selectively-

oxidized Zn base crystal. When the temperature reaches to high 500 ^{o}C, the fast sublimation of Zn will result in a mesoporous structure of polycrystalline ZnO nanodisks.

5. 4 ZnO Nanotubes

Tubular structure is of a special and important morphological configuration in nature. Synthetic nanoscale tubular structures have caught great research attention since the discovery of carbon nanotube. In addition to famous carbon nanotube, some important engineering and functional compounds such as MoS_2[194], MoS_3[195] and BN [196] have been synthesized into tubular structures. Using tungsten-comprised precursors, Al-rich mullite as an important engineering material has been fabricated in tubular shape [197]. GaN, an important blue light emission material, has been fabricated into nanotube arrays using a conjunctional of MOCVD and Thermal CVD, in which ZnO nanowire arrays were taken as the template for growing GaN nanotube arrays[198]. Via combustion assisted chemical vapor deposition method, nanotube arrays of SnO_2 have also been achieved [199], which could be of importance in nanosensing.

Using nanotube, nanobelt, and nanowires as templates, tubular structures can be synthesized for a wide range of materials. Most of these materials have to be inert to the environment, which can be removed later, or can be completely convertible by a chemical reaction. In this section, ZnO will be taken as a typical example for illustrating the self-assembly process of tubular oxide nanostructures during a simple solid-vapor deposition process.

To date, ZnO has been one of the most extensively explored inorganic materials besides carbon in the nanoscale science and technology. Recently there have been quite a

few reports about the successfully synthesis of ZnO microscale tubes [200, 201], and also some nanotubes [202, 203,204, 205] with polycrystalline or textured crystal structures.

Chemically, solid ZnO is an ionic bonded crystal. The bonding between cation Zn^{2+} and O^{2-} is so strong that the melting point of ZnO is as high as 1975°C. Zn metal is of a melting point as low as 411°C and can be easily oxidized in air [206]. Both Zn and ZnO have a similar hexagonal crystal structure. A low melting point of Zn and the high melting point of ZnO as well as their hexagonal crystal structures have given us a great advantage for designing and fabricating various metal-semiconductor core-shell nanostructures and tubular structures [207].

5. 4. 1 ZnO Microtubes and Nanotubes

Using a thermal evaporation approach, as well as taking advantage of selective surface oxidation on the as-formed Zn nano-object, tubular ZnO nanostructures have been synthesized. We now examine how the oxidation rate of Zn depends on the surface energy. During a systematic growth study of ZnO nanodiskettes, it is interesting to find that short micro tubes were formed with clean hexagonal faceted surface. Figure 5.21a shows an inclined view of a typical hexagonal tube of ZnO about 3-5 μm in length, 2-3 μm in width, and wall thickness of ~200 nm. An enlarged open-end of the tube is illustrated in Figure 5.21b, where the inner surface of the tube is stepped, rough and without facets, revealing a possible sublimation process of the material from the center. Figure 5.21c displays a front view of a ZnO tube of ~2 μm in width and ~4 μm in length with a rather sharp inner surface, and the hexagonal facets are clean but not perfect. In Figure 5.21d, a tube with ~4 μm in height and ~4 μm in diameter is shown. The hollow core of the tube can be

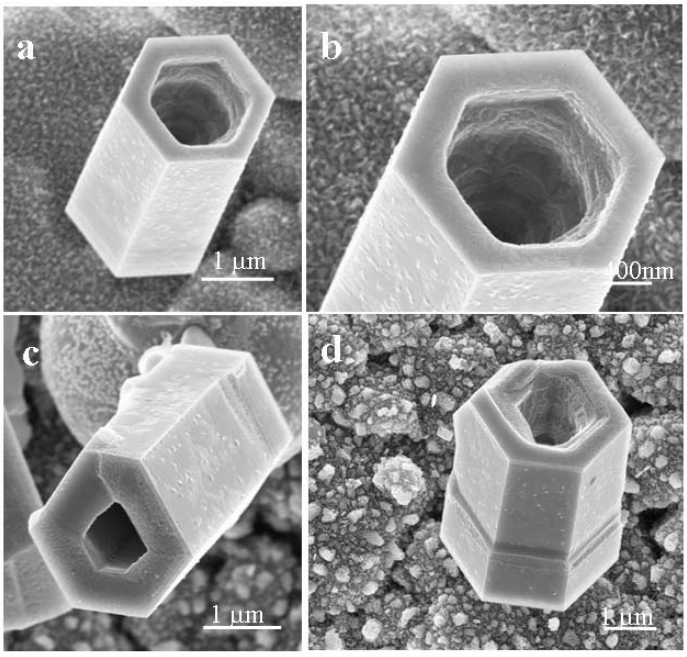

Figure 5.21 A series of SEM images displaying individual short microtubes with rough outer and inner surfaces. (a, b) Low magnification SEM images showing the outer hexagonal faceted surfaces and the inner rough and stepped surfaces of the ZnO tubes. (c) and (d) are two short micron sized tubes with hexagonal facets

clearly seen, where the inner diameter at the entrance is larger than that in the middle of the tube, suggesting that the original material filling the core was not completely sublimated. It is evident from Figure 5.21 that the template for forming the tube was a hexagonal Zn rod; the oxidation of the surface formed the wall of the tube, and the re-sublimation of the Zn core created the hollow tube.

By adjusting the pressure in the synthesis has led the growth of high quality tubular structures. Figs. 5.22a and b show two microtubes of ZnO with irregular shaped cross-

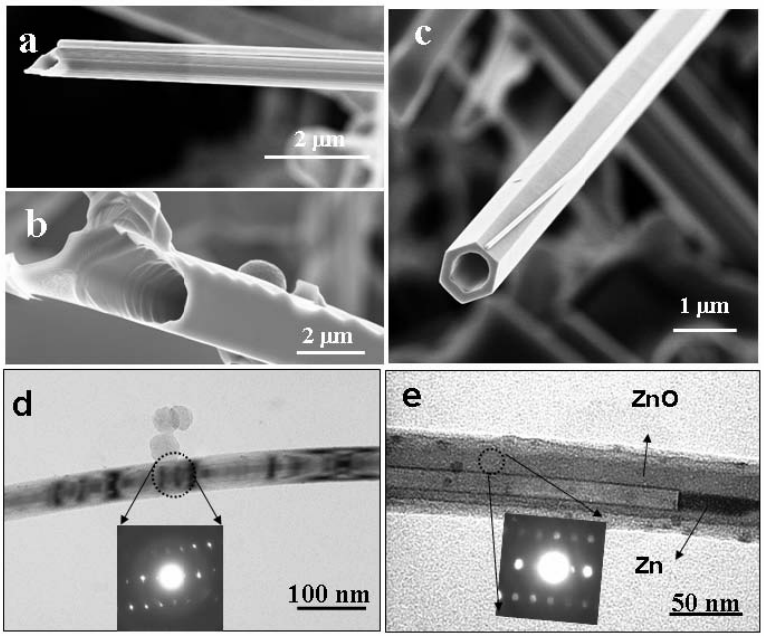

Figure 5 .22 (a, b) SEM images displaying individual microtubes of ZnO with irregular shaped cross sections. (c) Hexagonal faceted tubes of ZnO. (d, e) TEM images showing a Zn-ZnO core-shell nanocable and a ZnO nanotube with residual Zn core, the inset electron diffraction patterns indicate their single crystal structures.

sections respectively from the side and front views. The two microtubes have possible circular cross-section, and rough side surfaces. The stepped inner surface of the microtube in Figure 5.22b revealed that, despite a possible single crystal structure, the formation of microtube still follows a possible sublimation process of core material. Figure 5.22c gives a clear description of an intact, smooth and long freestanding microtube of ZnO, which should be of single crystal. Two typical TEM images showing a Zn-ZnO core-shell nanocable and a ZnO nanotube with remaining Zn core inside are respectively displayed in Figs. 5.22d and e. The diameters of the two Zn-ZnO nanocable and nanotube are 50-100 nm. The partially left or residual Zn inside the tube and inner wall is apparent in Figure 5.22e. The inset select area nano-diffraction patterns indicate that they are single crystals with the same orientation and growing along c-axis.

5. 4. 2 ZnO Nanotube Arrays on ZnO Cages

As illustrated above, a low melting point of Zn and the high melting point of ZnO have given us hints to design and fabricate various functional nanostructured ZnO nano-objects. Controlling the growth kinetics would allow us to control the formation process of the Zn-ZnO system. Lower-temperature synthesis of 1D ZnO nanostructures is very attractive because it gives the hope to integrate the process with other synthesis and fabrication processes. Here, we show a case of synthesis of nanotube arrays on large shells.

In the deposition region at growth temperature around 450 ^{o}C, ZnO nanotube arrays on ZnO cages were observed, as shown in Figure 5.23a. Microspheres of ZnO with sizes ~30 μm grew freestanding on alumina substrates. Radical branched tubes surround the central microsphere (Figure 5.23b). A broken microsphere in Figure 5.23c reveals that the microsphere in fact is a hollow shell-like structure, inside which, radially distributed nanotube arrays with a uniform diameter of ~1.5 μm grew directly out of the inner cage surface. The outer surface of ZnO cage is covered by radially extruding nanotube arrays of ZnO (Figure 5.23d). Further close examination at the inner surface of ZnO cage found that, besides the hexagonal nanotubes, some wavy ZnO nanowalls are present. A typical TEM image of a broken nanotube from hollow ZnO cages is shown in Figure 5.23f, where the hollow inside is in a visible bright contrast. Its corresponding electron diffraction pattern shown in the inset (bottom) proves its single-crystal growth along [0001] direction.

It is interesting to find out in Figure 5.24 that the outer surfaces of some ZnO cages are enclosed by regularly arranged hexagonal pyramid-like domains; the six intersection lines of the

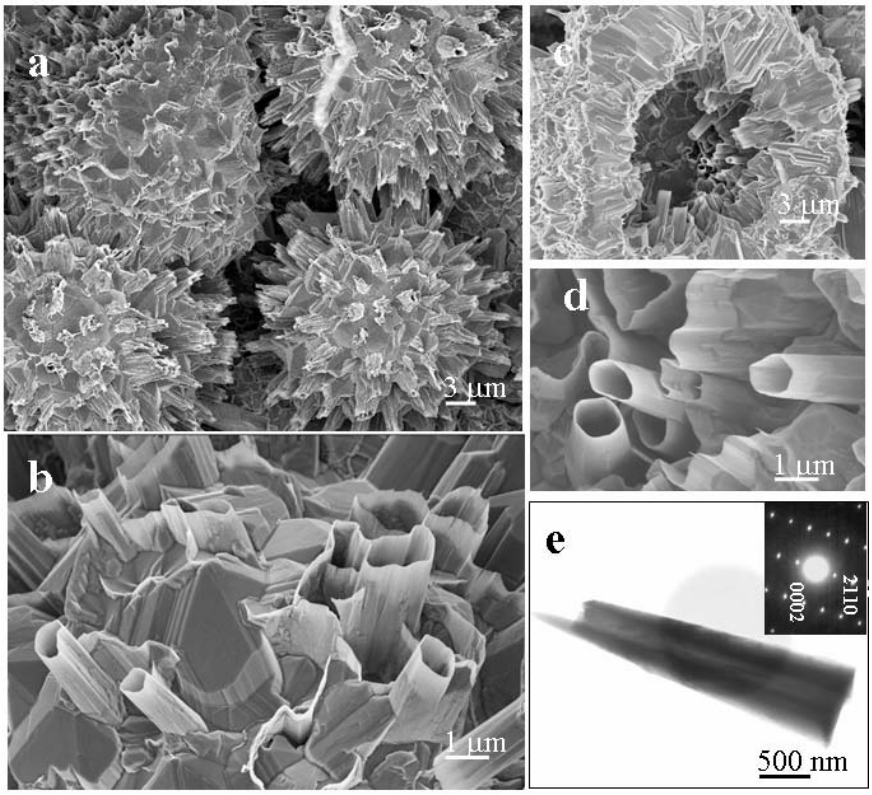

Figure 5. 23 (a-d) A series of SEM images showing ZnO nanotube arrays distributed on the inner and outer surfaces of a large-size hollow shell-like structure. (e) A typical TEM image of a broken ZnO nanotube from hollow shell-like structure, the right side corresponding electron diffraction pattern indicates its single-crystal growth direction along [0001].

pyramid are visible from the front (Figs. 5.24b, c and d). Each pyramid is about 2 μm in width and 1-1.5 μm in height. On the tip of each ZnO pyramid, there is a single standing out nanorod of ~300 nm in wide and ~600 nm in height (Figs. 5.24b and d). A single nanotube with diameter of ~200 nm has been observed sometimes at the tip of the pyramid (Figs. 5.24a and c).

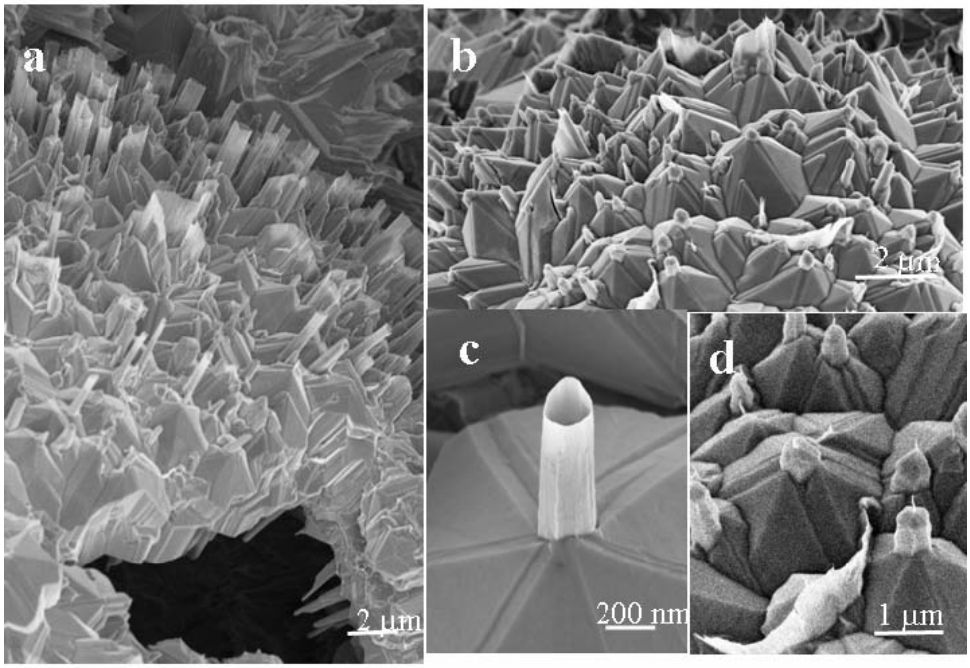

Figure 5.24 A SEM image displaying a collection of hexagonal nanotubes (a) and nanorods (b) of Zn-ZnO ; On each island there is only one nanotube or grown nanorod on its top, closer views in (c) and (d) respectively.

5. 4. 3 Growth Mechanism of ZnO Microtubes and Nanotubes

There are three important factors on the growth of ZnO tubular structures: the kinetics in the Zn and ZnO system, the lower energy facets, and the oxidation rates of different surfaces. The oxidation rates on different crystal surfaces as well as at different temperature regions are distinct. The Zn surface with lowest energy such as {0001} planes tend to be most stable and may resist to be oxidized, while the higher energy surfaces such as $\{10\bar{1}0\}$ are likely to have a higher oxidation rate. It is evident from the above experimental results that the selective and epitaxial oxidation growth of ZnO on Zn rod is an effective way to design and synthesize tubular nanostructures of ZnO in a dimension ranging from nanometers to micrometers.

Similar to the growth mechanism proposed on ZnO nanodiskettes and nanocages [208], a growth mechanism on ZnO nanotubes is illustrated in Figure 5.25. The first step (Figure 5.25a) is still

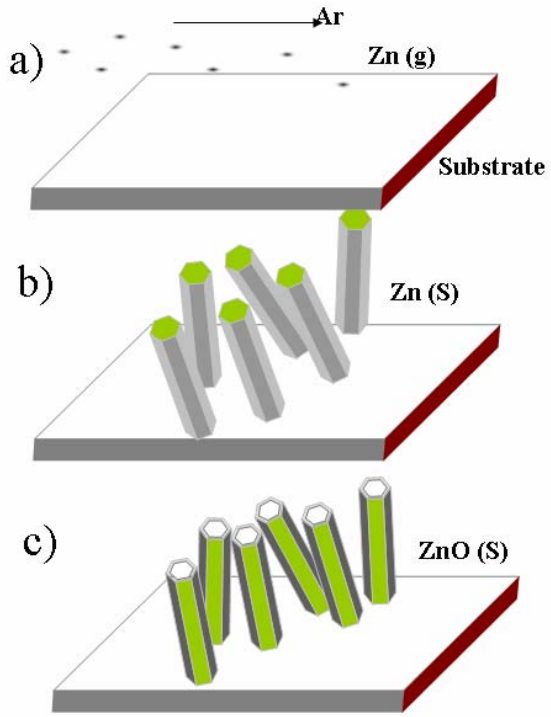

Figure 5.25 A proposed formation model of freestanding or rooted ZnO nanotubes.

the necessary vapor transfer of reduced Zn droplets by Ar gas to the deposition area of temperatures 400~500 ^{o}C. A faster growth along c-axis direction leads to the formation of hexagonal based Zn rods (Figure 5.25b). Since the Zn {0001} surfaces have lower energy than the $\{10\bar{1}0\}/\{2\bar{1}\bar{1}0\}$ surfaces, they are more stable and resistive to oxidation. As a result, the side surfaces of the hexagonal nanorod are oxidized first, forming a ZnO shell. At the same time, the low melting point Zn has a lower vaporization temperature, the remaining Zn inside the rod can be re-sublimated through the open ends at the {0001}

surfaces, leaving behind a ZnO tube that has relatively smooth facets as defined by the Zn rod (Figure 5.25c). The sublimation may not be complete, thus, the inner surface of the tube is rough possibly with some residual Zn. If the sublimation is terminated at the early stage, the half-tubular structures would be formed.

The growth of the structures in Figure 5.24 is more complex, but they are still governed by the process illustrated in Figure 5.25. It is likely that a large Zn liquid droplet was deposited on the substrate, which was too large to be a single crystal, thus, a polycrystalline Zn ball was formed, but with many hexagonal pyramids forming on the surface, each of which was initiated from a Zn nuclei. Then, the small Zn vapor could deposit on the surface at the tips of the pyramids to reduce the local surface energy, forming a hexagonal rod at the tip. Then, an oxidation and subsequent sublimation process as illustrated in Figure 5.25 is possible, forming the tubular structure at the tip (see Figure 5.24c).

5. 5 Summary

Two new strategies have been successfully probed and developed for fabrications of a versatile group of nanostructures building blocks for nanoelectronics and optoelectronics. First, a brand-new strategy involving electron-solid interaction is designed and demonstrated to successfully fabricate ultra-small quantum dots pattern on bulk materials. Secondly, by using the simple vapor-sold growth process, in conjunction with the physical and chemical understanding of ZnO crystal growth process, a strategy for growing various types of nanostructures has been developed, which could be

extended to a potential strategy for the other II-VI class and III-V group wurtzite structured semiconductors nanostructures.

CHAPTER 6

BIOSENSING APPLICATION STUDY ON PIEZOELECTRIC ZINC OXIDE NANOSTRUCTURES

Besides the popularly used optical biosensing devices, there are another two types of sensors that have been developed for biosensing based on two different sensing mechanisms. One is built on the small amount of mass change in terms of combination of intrinsic resonance frequency and external loading led frequency shift. The other is based on the electrical signal, either conductivity or resistivity variation upon environment changes.

In the category of the first biosensing mechanism, there has been lots of on-going research. The cantilever-based sensor research is a big part of it, which actually has present wide range of applications in the field of physical, chemical and biochemical sciences.[209,210,211] The second one so far is still very challenging in terms of signals extraction and processing difficulties due to the high aqueous environment noise. Rarely there is a successful work in this area by using the intensively explored electrical measurement methodology developed for solid state sensing. Recently, by using Si nanowires as sensing building blocks, and via surface functionalzation of the nanowires surface, especially through a distinct electrical conductivity variation, selective binding events have been demonstrated between the antibody modified Si nanowires and the virus nanoparticles happened in different biofluids, leading to a highly sensitive range of detection which might go to single virus particle detection.

In this chapter, both types of sensing mechanisms will be explored respectively by using *in-situ* microscopy measurement technique and by conducting a systematic biosensing study based on the piezoelectric ZnO nanostructures. As for the *in-situ* microscopy measurement, we will focus on the fundamental resonance phenomena study and a work-function measurement and a mass measurement by using resonance phenomena. For the biosensing study, a systematic work from biosurface functionalization, device fabrication to electrical measurement will be elaborated in later subsections following the first subsection on *in-situ* microscopy measurement exploration.

6.1 *In-situ* Microscopy measurement[212,213]

Miniaturization of the cantilever dimensions towards the nanometer scale has drawn a great attention for enabling an improvement on sensitivity, spatial resolution, energy efficiency and time of response, etc..[214,215] Semiconducting oxide nanobelts [216] and nanowires[217], as a new class of nanostructures, are showing novel electronic, chemical and optical properties.[218, 219]They have become the fundamental building blocks for fabricating nanoscale sensors and logic circuits.[220,221] As mentioned before, the nanobelts are of a distinct structural morphology with a rectangular cross-section and a uniform structure, which could be directly used as nanocantilevers and nanoresonators in nanoelectromechanical systems (NEMS).[222, 223]A key phenomenon for applying nanobelts in NEMS technology is their electromechanical resonance behavior, and an important physical quantity for cantilever applications is their bending modulus.

Recently, a new experimental approach, based on the electric-field-induced resonant excitation, has been developed for direct measurement the mechanical properties of individual nanowire-like structures by *in-situ* transmission electron microscopy (TEM).[224,225,226] Using this method, mechanical properties of carbon nanotubes, silicon nanowires,[227] and silicon carbide-silica composite nanowires[228] have been investigated.

In this subsection, first we will explore the *in-situ* TEM measurement of ZnO nanobelts in terms of resonance property and work function measurement, and then move on to the *in-situ* optical microscopy measurement technique for mass detection using ZnO nanowire.

6.1.1 Dual-mode Resonance of ZnO Nanobelt

In this section, we studied the electromechanical resonance behavior of a single ZnO nanobelt, induced by an alternative electric field by using the above mentioned *in-situ* TEM technique. Due to the rectangular cross-section of the nanobelt, we have successfully observed two fundamental resonance modes in corresponding to the two orthogonal transverse vibration directions. The electromechanical resonant behavior is directly correlated with their distinct structural feature, showing a possibility for versatile applications as nanoresonators and nanocantilevers for biosensing. The bending modulus of the ZnO nanobelts was measured to be ~52 GPa and the damping time constant of the resonance in vacuum of 10^{-8} Torr was ~1.2 ms.

Scanning electron microscopy (SEM) image of the as-synthesized ZnO nanobelts is given in Figure 6.1 (a), which reveals a large quantity of nanobelts with lengths over several tens to hundreds micrometer. Figure 6.1 (b) shows a typical TEM image of the

ZnO nanobelt, displaying high structural uniformity. The selected area electron diffraction pattern indicates that the

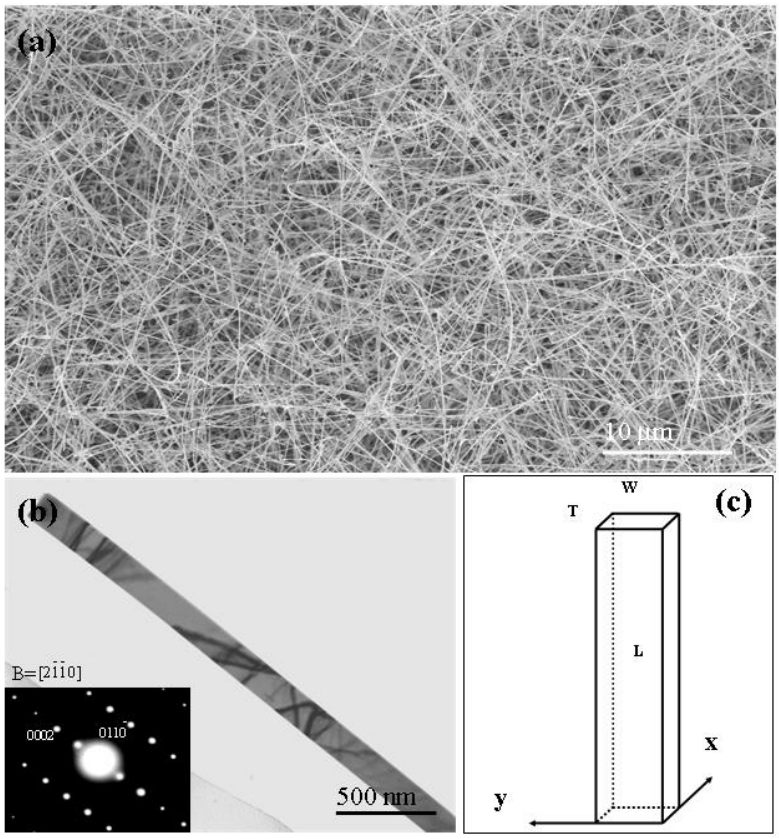

Figure 6.1 (a) SEM image of the as-synthesized ZnO nanobelts. (b) A typical TEM image of a ZnO nanobelt and its electron diffraction pattern (inset). (c) Schematic geometrical shape of the nanobelt.

nanobelt grows along [0001] and is enclosed by $\pm(2\bar{1}\bar{1}0)$ and $\pm(01\bar{1}0)$ facets. Figure 6.1 (c) represents the geometry of a nanobelt with length *L*, width *W*, and thickness *T*. In our experiment, the nanobelts were glued at one end onto a copper wire, while the other end near the counter electrode was free. This is a simple one-end clamped cantilever with a rectangular cross section. To carry out the mechanical property measurements of a nanobelt, a specimen holder for a Hitachi HF-2000 TEM (200 kV) was built for applying a voltage across a nanobelt and its counter electrode, as shown in Figure 6.2. An

oscillating voltage with tunable frequency was applied on the nanobelt. Mechanical resonance of the nanobelt can be induced if the applied frequency matches the natural vibration frequency (Figure 6.3). From the classical elasticity theory for a

Figure 6.2 A top view of a home-made sample holder for *in-situ* TEM measurement.

rectangular beam, the fundamental resonance frequency corresponding to the thickness direction (x-axis) (Figure 6.1c) is[229]

$$\nu_{xi} = \frac{\beta_i^2 T}{4\pi L^2}\sqrt{\frac{E_x}{3\rho}}, \qquad \text{Equation (1)}$$

where β_i is a constant for the *i*th harmonic: $\beta_1 = 1.875$ and $\beta_2 = 4.694$, E_x is the bending modulus for the vibration along the x-axis, L is length of the nanobelt, ρ is mass density; and the corresponding resonance frequency in the width direction (y-axis) (Figure 6.1c) is given by

$$\nu_{yi} = \frac{\beta_i^2 W}{4\pi L^2}\sqrt{\frac{E_y}{3\rho}}\ . \qquad \text{Equation (2)}$$

A selected ZnO nanobelt at stationary is given in Figure 6.3(a). By changing the frequency of the applied voltage, we have found two fundamental frequencies in two orthogonal transverse vibration directions. Figure 6.3(b) shows a harmonic resonance with its vibration plane nearly parallel to the viewing direction, and Figure 6.3(c) shows the harmonic resonance with the vibration plane closely perpendicular to the viewing direction. For calculating the bending modulus, it is

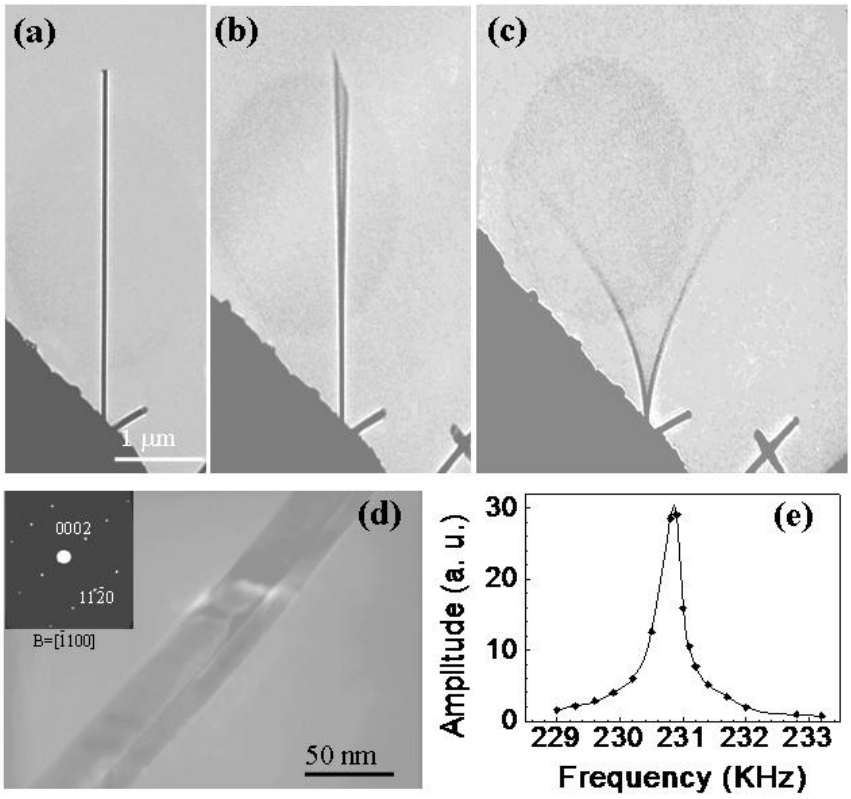

Figure 6.3 A selected ZnO nanobelt at (a) stationary, (b) the first harmonic resonance in x direction, ν_{x1} = 622 kHz, and (c) the first harmonic resonance in y direction, ν_{y1} = 691 kHz. (d) An enlarged image of the nanobelt and its electron diffraction pattern (inset). The projected shape of the nanobelt is apparent. (e) The FWHM of the resonance peak measured from another ZnO nanobelt. The resonance occurs at 230.9 kHz.

critical to accurately measure the fundamental resonance frequency (ν_1) and the dimensional sizes (*L*, *W* and *T*) of the investigated ZnO nanobelts. To determine ν_1, we have checked the stability of resonance frequency to ensure one end of the nanobelt is tightly fixed, and the resonant excitation has been carefully checked around the half value of the observed resonance frequency to ensure it is the fundamental frequency. The specimen holder is rotated about its axis so that the nanobelt is aligned perpendicular to the electron beam, thus, the real length (*L*) of the nanobelt can be obtained. The normal direction of the wide facet of the nanobelt could be firstly determined by electron

diffraction pattern, which was $[2\bar{1}\bar{1}0]$ for the ZnO nanobelt (Figure 6.1b). Then the nanobelt was tilted from its normal direction by rotating the specimen holder, and the tilting direction and angle were determined by the corresponding electron diffraction pattern. As shown in the inset of Figure 6.3d, the electron beam direction is $[1\bar{1}00]$. The angle between $[1\bar{1}00]$ and $[2\bar{1}\bar{1}0]$ is 30°, i.e. the normal direction of the wide facet of this nanobelt is 30° tilted from the direction of the electron beam. Using the projected dimension measured from the TEM image (Figure 6.3d), the geometrical parameters of this nanobelt are determined to be W = 28 nm and T = 19 nm. Based on the experimentally measured data, the bending modulus of the ZnO nanobelts is calculated using Eq. (1) and Eq. (2). The experimental results are summarized in Table 6.1. The bending modulus of the ZnO nanobelts was ~ 52 GPa. This value represents the modulus

Table 6.1 Bending modulus of the ZnO nanobelts, E_x and E_y reprent the bending modulus corresponding to the resonance along the thickness and width direction, respectively.

Nanobelt	Length L (μm) ($\pm$0.05)	Width W (nm) ($\pm$1)	Thickness T (nm) ($\pm$1)	Fundamental frequency (kHz)				Bending modulus (GPa)	
				W/T	ν_{x1}	ν_{y1}	ν_{y1}/ν_{x1}	E_x	E_y
1	8.25	55	33	1.7	232	373	1.6	46.6±0.6	50.1±0.6
2	4.73	28	19	1.5	396	576	1.4	44.3±1.3	45.5±2.9
3	4.07	31	20	1.6	662	958	1.4	56.3±0.9	64.6±2.3
4	8.90	44	39	1.1	210	231	1.1	37.9±0.6	39.9±1.2

that includes the scaling effect and geometrical shape, and it is in excellent agreement with the elastic modulus measured by nanoindenter.[230] Although nanobelts of different sizes may have slight difference in bending modulus, there is no obvious difference if the calculation was done using either Eq. (1) or Eq. (2). The ratio of two fundamental frequencies ν_{y1}/ν_{x1} is consistent to the aspect ratio W/T, as expected from Eqs. (1) and (2) ($\nu_{y1}/\nu_{x1} = W/T$).

The full width at half maximum (FWHM) of the resonance peak is shown in Figure 6.3e, and $\Delta\nu/\nu_1$ ~ 0.2 %. This value is independent of the vibration modes or the size of the nanobelt. To explore the intrinsic meaning of the measured $\Delta\nu/\nu_1$ value, we consider a one-dimensional harmonic oscillator with a natural frequency ν_1. When a viscous (or frictional) force is acting on the particle and the force is proportional to the instantaneous speed of the particle, the damping of the vibration amplitude is given by exp $(-t/\tau_0)$, where τ_0 is the damping time constant of the oscillator. The life time τ_0 is related to $\Delta\nu/\nu_1$ by following equation for $\Delta\nu/\nu_1 << 1$,

$$\tau_0 = \left[(\Delta\nu/\nu_1)\pi\nu_1/1.732\right]^{-1}. \qquad \text{Equation (3)}$$

For $\Delta\nu/\nu_1$ = 0.2%, ν_1 = 231 kHz, the lifetime is τ_0 = 1.2 ms. From the definition of τ_0, the viscosity (or friction) coefficient $\eta = 2M/\tau_0$, where M is the mass of the particle. Thus, the damping time constant depends on the viscosity coefficient of the nanobelt in the medium in which the measurement was carried out.

A ZnO nanobelt was set on resonance for 10 minutes at 622 kHz and at a vibration angle of ~ 30°, the shift of resonance frequency was less than 1%, and the resonance frequency and structure of the nanobelt are considerably stable under electron beam irradiation at 200 kV. The beam illumination intensity has no effect on the measurement.

ZnO nanobelts can be used as a force sensor. Figure 6.4a shows a selected ZnO nanobelt with a hooked end, which is equivalent to a cantilever with an integrated tip. Due to the two transverse vibration modes of the nanobelt, resonance along two orthogonal directions has been observed (Figure 6.4b and Figure 6.4c). The two

resonance modes just correspond to the two modes of the tip operation when the nanobelt-base cantilever is used as a force sensor: one is the tapping mode, and the other is the non-contact mode. Thus, the force sensor fabricated using the ZnO nanobelts is versatile for applications on hard and soft surfaces.

In summary, electromechanical resonance behavior of ZnO nanobelts has been characterized by *in-situ* TEM. The dual resonance modes with two orthogonal directions have been observed. The single crystalline, structurally controlled nanobelts could be used as a new type nanoresonator and nanocantilever with dual operation modes, which

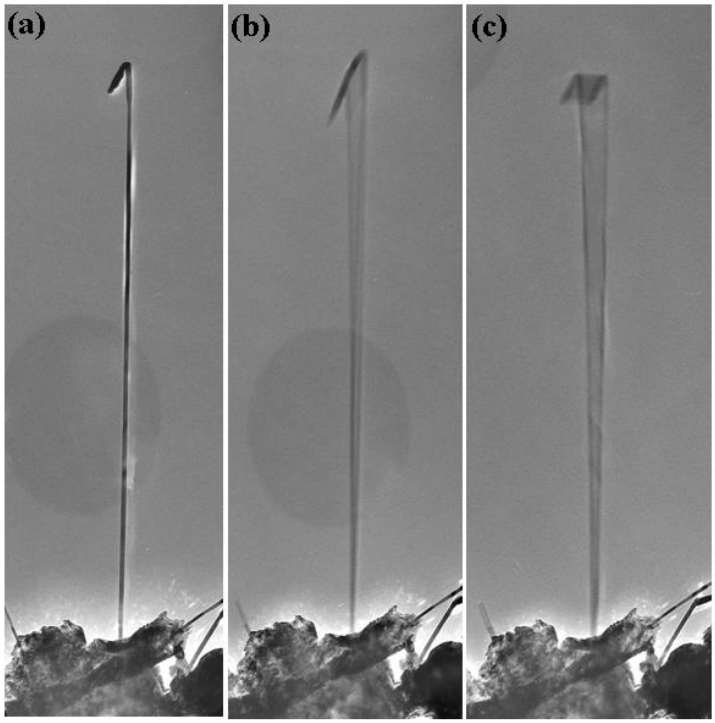

Figure 6.4 A selected ZnO nanobelt with a hooked end at (a) stationary, (b) resonance at 731 kHz, and (c) resonance at 474 kHz.

could be useful in nanoelectromechanical systems and highly functional nanodevices. Similar to carbon nanotubes, the nanobelts could also be used as functional tips for scanning probe microscopy.[231,232]. The bending modulus of the ZnO nanobelts is ~52

GPa and the damping time constant of nanobelt resonance in vacuum of 10^{-8} Torr is ~1.2 ms.

6.1.2 Work Function Measurement of ZnO Nanobelt

As mentioned previously, Zinc oxide (ZnO) is a semiconductor with a wide band gap of 3.37 eV and a large exciton binding energy of 60 meV, which is suitable for short-wavelength optoelectronic devices at room temperature. The field-emission property for well-aligned ZnO nanowire arrays has been reported, demonstrating a promising application of semiconductor nanowires as field emitters for flat panel display. From the Fowler-Nordheim (F-N) theory, it is known that surface work function is an important physic quantity for electron field emission. For the emitters such as ZnO nanowire arrays, most of the electrons are emitted from tips of the nanowires, and it is the local work function that matters to the properties of the field emission. However, the work function measured based on the F-N theory is an average over the large scale of emitting materials. So it is necessary to measure the local work function at the tip of individual emitter.

The work by Gao et. al. has successfully measured the work function at the tips of carbon nanotubes by an *in-situ* transmission electron microscopy (TEM) technique. The measurement relies on the mechanical resonance of the carbon nanotube induced by an externally applied oscillating voltage with tunable frequency. In this section, based on the mechanical resonance of the nanobelt induced by an externally alternative electric field, work function of ZnO nanobelts tips has been measured, around 5.2 eV, which shows little dependence on their dimension. This result provides an experimental basis for the

work function of ZnO nanostructures and is important for understanding their field emission characteristics.

The measurement of work function at the tip of a single ZnO nanobelt was carried out *in-situ* at 200 kV in a Hitachi HF-2000 FEG TEM. Similar to the resonance measurement in section 6.1.1, the specimen holder was built for applying a voltage across a nanobelt and its counter gold electrode. The nanobelts to be used for measurements are directly imaged under TEM.

Figure 6.5 is a setup for work function measurement. One end of the nanobelt was electrically attached to a gold wire, and the other end faces directly against the gold ball. Because of the difference in the surface work function between the ZnO nanobelt and the counter Au ball, a static charge Q_0 exists at the tip of the nanobelt to balance this potential difference.19 The magnitude of Q_0 is proportional to the difference between work function of the nanobelt tip (NBT) and the Au electrode, $Q_0 = \alpha (\phi_{Au} - \phi_{NBT})$, where α is related to the geometry and distance between the nanobelt and the electrode.

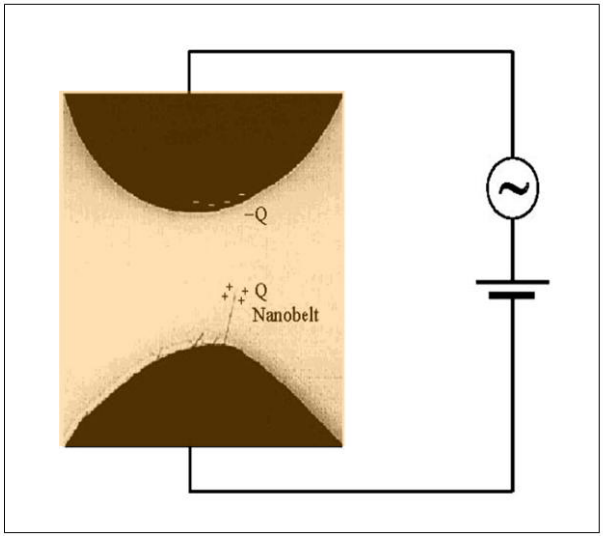

Figure 6.5 Experimental set up for measuring the work function at the tip of a ZnO nanobelt.

Figure 6.6a shows the attached ZnO nanobelt can be regarded as a vibration cantilever clamped at one end. Experimentally, a constant voltage V_{dc} and an oscillating voltage $V_{ac}\cos 2\pi ft$

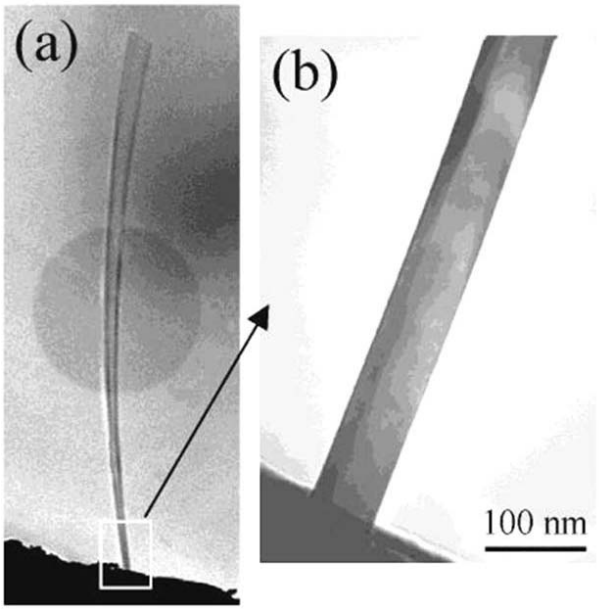

Figure 6.6 (a) TEM image of a fixed ZnO nanobelt at mechanical resonance as induced by an oscillating voltage at f = 0.576 MHz and Vac = 3.0 V. (b) TEM image recorded from the root of the nanobelt, showing the projected geometry of the nanobelt.

are applied to the nanobelt (Figure 6.5), where f is the frequency and V_{ac} is the amplitude. Thus, the total induced charge on the nanobelt is

$$Q=Q_0 + \alpha\, e\, (V_{dc}\cos 2\pi ft) \qquad \text{equation (4)}$$

The force acting on the nanobelt is proportional to the square of the total charge on the nanobelt.

$$F= \beta[Q_0 + \alpha e\, (V_{dc}\cos 2\pi ft)]^2$$

$$= \alpha^2 \beta\{[(\phi_{Au}-\phi_{NBT} + eV_{dc})2 + e^2V_{ac}{}^2/2]$$

$$+2eV_{ac}\,(\phi_{Au}-\phi_{NBT} + eV_{ac})\cos 2\pi ft + e^2V_{ac}{}^2/2\cos 4\pi ft]\} \qquad \text{equation (5)}$$

where α is a proportional constant. In eq 2, the first term is constant and it causes a static deflection of the ZnO nanobelt. The second term is a linear term, and the resonance occurs if the applied frequency f is tuned to the intrinsic mechanical resonance frequency f_0 of the ZnO nanobelt, as shown in Figure 6.6a. According to vibration theory and considering the rectangular cross-section of the nanobelt, and from eqations (1) and (2), mechanical resonance could be along the thickness or width direction at frequencies given by

$$f_T = \frac{1.875^2 T}{8\pi L^2}\sqrt{\frac{E_T}{3\rho}} \qquad \text{equation (6a)}$$

$$f_W = \frac{1.875^2 W}{8\pi L^2}\sqrt{\frac{E_W}{3\rho}} \qquad \text{equation (6b)}$$

respectively, where T is the thickness of the nanobelt, W its width, L its length, ρ the volume density, and E the bending modulus of the nanotube. The last term in eq 2 is the second harmonics. The most important result of eq 2 is that, for the linear term, the resonance amplitude A of the nanobelt is proportional to $V_{ac}(\phi_{Au} - \phi_{NBT} + eV_{dc})$.

The principle of the measurement is as follows. We first set V_{dc}=0 and tune the frequency f to get the mechanical resonance induced by the applied oscillating field. Second, under the resonance condition of keeping $f = f_0$ and V_{ac} constant, slowly change the magnitude of V_{dc} from zero to a value V_{dc0} that satisfies $\phi_{Au} - \phi_{NBT} + eV_{dc0} = 0$. At this moment, the resonance amplitude A becomes zero although the external AC voltage is still in effect. Therefore, the work function at the tip of ZnO nanobelt is $\phi_{NBT} = \phi_{Au} + eV_{dc0}$, while ϕ_{Au} = 5.1 eV.21 Figure 6.7 is a plot of the vibration amplitude A of the nanobelt as a function of the applied direct current voltage Vdc, from which the value for

V_{dc0} is determined. The dual-mode resonance of the nanobelts has been observed experimentally, as defined by eqs 3a and 3b.22 It is important to point out that it does not matter which resonance direction/frequency one chooses, either along the thickness or width direction, the measured V_{dc0} remains the same.

To investigate the dependence of the work function of ZnO nanobelts on the size of their cross-section, i.e., the width *W* and thickness *T* of the nanobelts, we measured the geometrical size of the nanobelts from which the work function was measured. Using the projected dimension

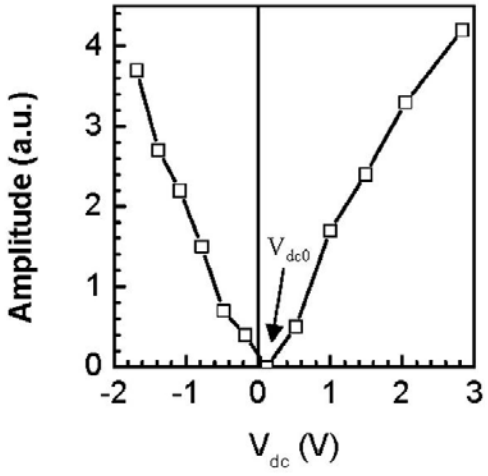

Figure 6.7 Plot of vibration amplitude of a ZnO nanobelt as a function of the applied direct current voltage, from which the offset voltage V_{dc0} = 0.12 V.

measured from the TEM image and the orientated angle determined from the corresponding electron diffraction pattern, the geometrical parameters of the nanobelts are obtained. The experimental results are summarized in Table 6.2. The work function at the tip of the ZnO nanobelt is around 5.2 eV and shows no significant dependence on the crosssection size of the ZnO nanobelts.

To ensure the accuracy of the measurements, the resonance stability and frequency drift of the ZnO nanobelts have been examined prior to and post measurement

Table 6.2 Work Functions of the ZnO nanobelts with different cross-secion size

nanobelt	width W (nm)	thickness T (nm)	work function ϕ (eV)
1	78	43	5.22
2	51	39	5.23
3	55	35	5.18
4	41	20	5.16
5	34	20	5.26

so that the change in vibration amplitude is solely attributed to the effect of V_{dc}. The sensitivity of this measurement is excellent because the full width at half-maximum for the resonance peak is $\Delta f/f_0$ =0.2%. Furthermore, the influence of surface condition on work function is important. In our experiments, the surfaces of the ZnO nanobelts are clean, atomically sharp, and without any sheathed amorphous phase. 1 This resonant method can also be applied to measure the work functions of other materials, such as the case shown in Figure 6.8. A carbon particle of diameter ~300 nm is attached at the tip of a nanobelt. Since the induced charges are accumulated mainly at the surface of the carbon particle, the measured work function should be for the surface of the particle. Using the

Figure 6.8 Measurement of the work function of an attached carbon particle on the tip of a ZnO nanobelt at f = 0.349 MHz and Vac =9.0 V.

same technique as demonstrated above, the mechanical resonance of the nanobelt gives a work function of 5.05 eV, which is consistent with that of carbon (ϕ_C = 5.0 eV). This demonstrates a technique for measuring the work function of a single nanoparticle.

In conclusion, the work functions at the tips of individual ZnO nanobelts have been measured by an electromechanical resonant method using *in-situ* TEM. The work function at the tip of a ZnO nanobelt is ~5.2 eV, which shows little dependence on the geometrical size. This quantity is important in the interpretation of the field emission properties of nanobelts. Using a ZnO nanobelt as a carrier beam, the work functions of a nanoparticle of a different material on the tip of the nanobelt has also been measured. The detected materials could be extended to variety of biological species like cells, virus particles, etc.

6.1.3 *In-situ* Optical Microscopy Measurement Technique

Using the electro-mechanical resonance phenomena in TEM, a nanobalance based on a single nanotube has been demonstrated for measuring the mass of a tiny particle in the order of ~ 22 fg, and as described in section 6.1.1, ZnO nanobelts have also been shown to behave as dual-mode nanoresonators. These experiments were conducted in a vacuum of ~ 10^{-5}–10^{-7} torr and the resonance was observed with the assistance of transmission electron microscopy. For biological species, the factors involving high vacuum and high electron-energy irradiation are of high damaging effects to the biological structures. Inevitably, these limitations have hindered the use of the above developed techniques in TEM for biological species detection.

Optical microscopy is one of the most important tools for characterization of biological samples such as cells, bacteria, etc. The nondestructive characteristics is the most important asset for its use in biomedical science research. It is worth noting that the development of *in-situ* optical microscopy has been attracting more and more researchers to work on it. The optical microscope is generally operated under ambient conditions, which will lead to the high viscosity of the environment greatly damping the resonance. Thus the performances of the balance and resonator will be greatly reduced.

Recently, J. Zhou et al. have used optical microscope to study the mechanical resonance behavior of a ZnO nanowire/nanorod at ambient condition by cutting its length using focused ion beam (FIB) microscopy. Nanobalance using a ZnO nanowire as the cantilever has been demonstrated for measuring the mass in the order of pico-grams in working atomosphere. The measurement limit of the balance is estimated to be ~ 1 pg, which is six orders of magnitude higher than that of a quartz balance.[233]

As shown in figure 6.9 is a demonstration of the ZnO nanowire as the picobalance for measuring the mass of small particle. Before placing a tiny mass at its tip, the resonance vibration behavior of a ZnO nanowire cantilever with length L of 103.0 μm and side width of 385 nm was carefully studied. Figures 6.9b and c shows the stationary and resonance vibration optical microscope images, respectively, of the cantilever at ambient condition. The corresponding frequency response plot was shown in Figure 6.9a, with the resonance frequency at ~ 46.3 kHz. Then, a tiny Pt short segment was built at the very end by depositing Pt using an FIB. As shown in Figure 6.9d, the Pt particle has a rod-shape of length 2.05 μm, width 373 nm and thickness 1.75 μm. Figures 6.9e and f

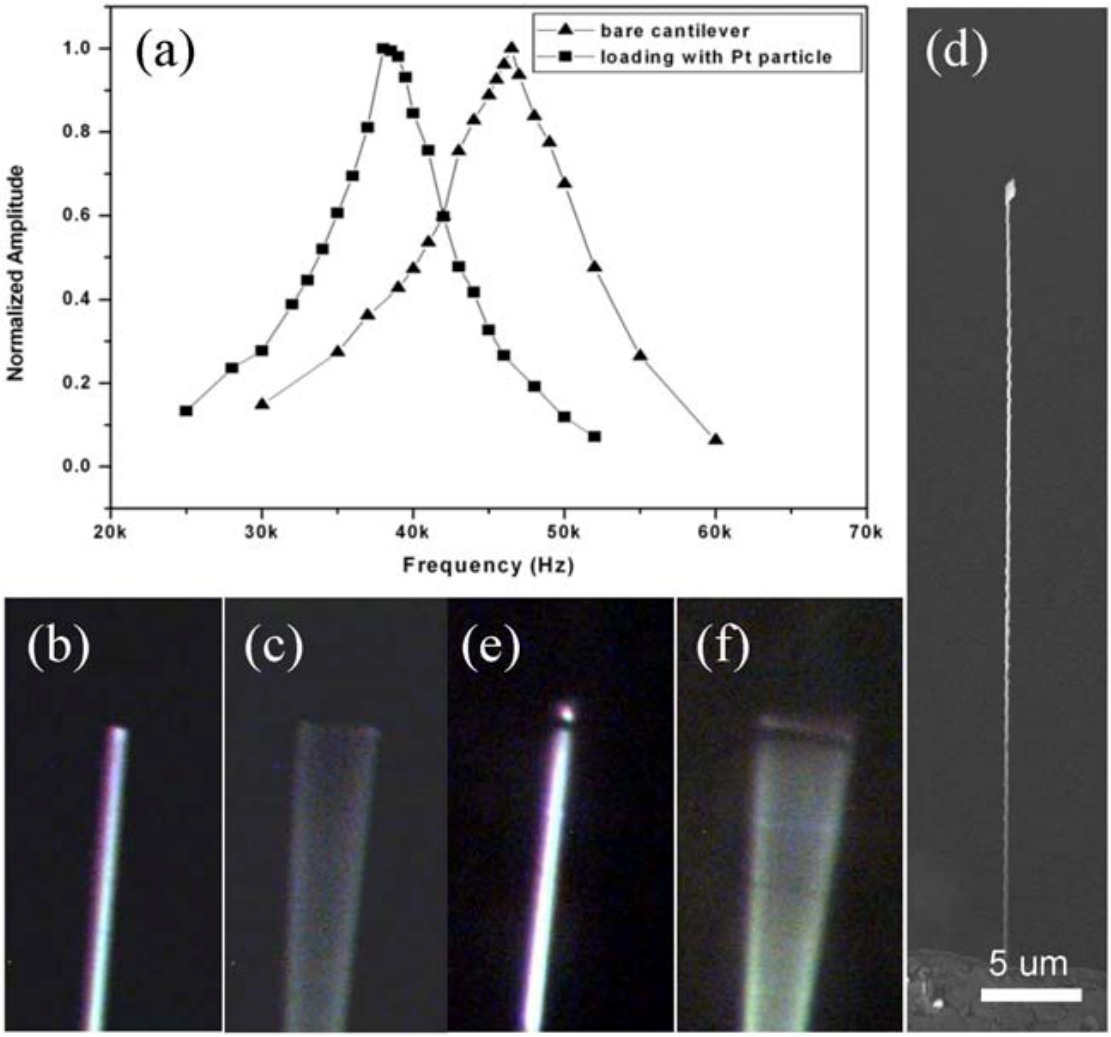

Figure 6.9 (a) Frequency response plots of a cantilever before and after attaching a Pt particle at its tip, respectively; Optical microscopy images of the native ZnO nanowire cantilever at (b) stationary (c) the first harmonic resonance; (d) SEM image of the cantilever with a Pt particle at its tip, and the corresponding optical microscopy images of the loaded cantilever at (e) stationary and (f) the first harmonic resonance.

particle at the tip, respectively. The frequency response curve shown in Figure 6.9a show the stationary and resonance vibration optical microscope images of the cantilever with the Pt indicated that the resonance frequency decreased to ~38.25 kHz. The shift in resonance frequency can be used to calculate the mass of the Pt particle.

For the harmonic resonance, the mass of the Pt particle is given by:[234]

$$M_{eff} = 3(M_0/\beta^4)[(f_0/f)^2 - 1] \quad \text{equation (7)}$$

Where $M_{eff} = M_p(x/l)$ is the effective mass of the loading material to the cantilever, M_p is the mass of the loading particle that is located at a distance x from the base of the cantilever, l is the length of the cantilever, the M_0 is the mass of the bare cantilever, and f_0 is the resonance frequency of the native cantilever, and f is the resonance of the cantilever with the particle. β is the first harmonic constant.

The mass of the Pt particle was found to be $M_p \sim 2.64 \times 10^{-11}$ g = 26.4 pg. This value is very close to that calculation from the shape of the Pt particle, which is $M_p \sim 28.7$ pg by using bulk density, showing the accuracy and reliability of the measurement.

We believe, the above successful demonstration of mass measurement of Pt particle on tip of ZnO nanowire suggested that the biological sensing and detection could be realized in ambient atmosphere using *in-situ* optical microscopy technique with enough sensitivity and selectivity. Right now, we have begun to use biological cell particles such as blood cells to test the validation of the *in-situ* optical microscopy technique in terms of biological detection. Behind this, the development of the manipulation technique of individual tiny biological species onto the nanowire or

nanobelt balance would be the bottle neck as critical as that of the manipulation technique of tiny nanowire or nanobelt.

6.2 Surface Modification and Functionalization of ZnO Nanostructures

Most of sensing applications require control of interfacial properties, e.g., the gas sensors need the surface of nanostructures to be highly sensitive to selective adsorption. For biomedical application, there are more requirements on the materials such as biocompatibility for specific application environment, bioinert ability that allows the materials to be survived in biofluid environment, etc. The interfacial properties can range from straightforward adhesion between different materials, to direct modification of surface functional group of one material by another at an interface. To control various properties including wettability (hydrophobic or hydrophilic, or amphiphilic), adhesion, etc. that are especially important for the stability, selectivity and sensitivity of the functional component surfaces for biosensing in terms of molecular recognition ability. For example, specific receptors have to be adhered onto the optical biosensor component surface so as to achieve the specificity (selectivity) for recognize certain types of targeted molecules.

As have been mentioned in chapter 2 (experimental methodologies), physical attachment and chemical adsorption are two basis mechanisms for surface functionalization. In this chapter, based on the physical adsorption in terms of electrostatic force and Van der Waals force, we investigated the possibility of polar surfaces of ZnO nanostructures to be selectively functionalized, the biocompatibility of

ZnO nanostructures in several biological buffers, and also protein attachment on ZnO nanostructures surface. In terms of chemical adsorption mechanism, the standard silanization was also used for surface modification of ZnO nanobelts, some initial experimental results using different silanes were presented.

6.2.1 Selective Functionalization Study on Polar Surfaces of ZnO

It has been known that the most common polar surface of ZnO is the basal plane. The oppositely charged ions produce positively charged Zn-(0001) and negatively charged O-$(000\bar{1})$ surfaces, resulting in a normal dipole moment and spontaneous polarization along the *c*-axis. Electrostatic force has been one of the most important asset for surface modification. Let the electrostatic force to be the dominant force involved in the modification process, then for polar surface dominated ZnO, selective surface modification of positive or negative charged organic functional groups could be achieved.

In this section, based on the polar surface dominated piezoelectric ZnO nanostructures, a great interest is to prove the selectivity of the two (0001) surfaces for different functional groups. Furthermore, if it is selective, then different functional groups modified on polar surface pair will give a tremendous space for further bio-organic group's functionalization.

In chapter 3 a successful synthesis of the free standing nanpropeller arrays of ZnO has been achieved through a two-step heating process. As shown in Figure 6.10, the dominated polar surfaces pair on nanopropeller blades is of a significant difference from the morphological points of view, which has a stepped surface +(0001) (figures 6.10a and c), while the negative charged surface is rather smooth (Figure 6.9b)

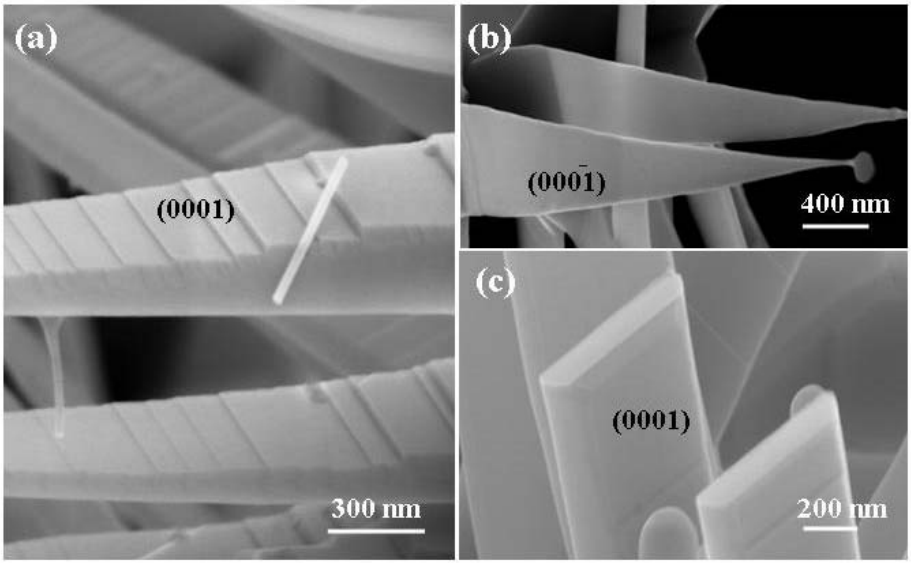

Figure 6.10 Polar surfaces of ZnO nanopropeller arrays with smooth –(0001) surface and stepped +(0001) surface.

In the methodology chapter (chapter 2), a cartoon schematic experiment has been designed and proposed in Figure 2. 4. The magnetite nanoparticles (NPs) with a size range about ~5 nm have been chosen as the intermediated materials to be modified with different functional groups, which later on will be used for the selective functionalization of ZnO nanopropeller arrays. The functional groups as we designed were of two types. One is the carboxyl acid group with a negative charge; the other is the amino group with a positive charge. Based on our electrostatic assumption, the expected experimental results as shown in the schematic Figure 2.4 should be:

a. NPs with NH_2-group prefer to absorption on negative charged polar surface of ZnO nanopropellers;

b. NPs with COOH-group prefer to being adhered on positive charged polar surface of ZnO.

*Th*e carboxyl acid group linked nanoparticles will try to be adsorbed on the positive charged Zn^{2+} surface, while the amino group modified nanoparticles will attach on the negative charged O^{2-} surface of nanopropeller blades.

The experimental procedure was carried out as following.

1. Disperse scratched nanopropellers by sonicaton in ethanol for 1 min;
2. Transfer same amount of nanopropeller ethanol solution into two identical containers, ready for use.
3. Dilute the Fe_3O_4 nanoparticles suspensions with NH_2-group and COOH-group respectively using ethanol and water.
4. Transfer same amount of Fe_3O_4 diluted suspensions with NH_2-group and COOH-group into two containers with same amount of ZnO nanopropellers.
5. Sonicating the mixed suspensions prepared by above procedure for 30 s, then keep for 1 hour.
6. Drops of dispersed solution onto SEM sample stub, after natural drying (overnight), SEM observation.

After SEM observation, it is found that the results were not as what we expected. As shown in Figure 6.11, a random distribution of NPs deposition on both polar surfaces is observed. Figs. 6.11a and b illustrated the case for carboxyl acid group linked NPs. From the SEM images, random and spotty clumps of nanoparticles are located on both polar surfaces +-(0001). For the amino negative group modified NPs, the adsorption is also

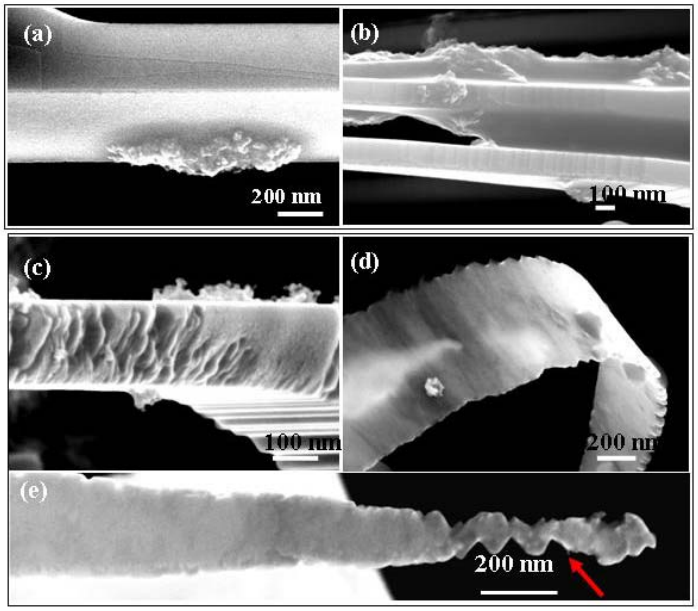

Figure 6.11 Random adsorption of magnetite with functional groups on ZnO nanopropeller blades. a) & b), COOH modified magnetite adsorption; c)-e) NH_2 group modified magnetite nanoparticles adsorption.

tending to be random in the experiment, as displayed in figs. 6.11 c-e. It is indicated from these SEM images that not only a non-selective adsorption is found, but the corrosion of the nanoblades also happened. As shown in Figure 6.11 d, originally stepped $\{01\bar{1}0\}$ side surfaces become rugged despite of still intact polar surfaces {0001}. It is also found that even though there is a possibility that the functionalized amino group tends to be a little bit basic, in Figure 6.11e the straight nanopropeller blade became corroded after adsorption. It is suggested that there need a precise control over PH value of the suspensions.

In summary, it is clear that there is no significant evidence for selective attachment of Fe_3O_4 NPs on ZnO polar surfaces in the course of observation; chemical reaction happened for deposition of NH_2-NPs onto ZnO Nanopropellers, leading to curved nanoblades and jagged edges of nanoblades. There might be two reasons resulting

in the above phenomenon: a. excess noise factors like gravity deposition, capillary forces and hydrogen bonding, etc. b. lack of purification and PH control during the experiments.

To further investigate the selective functionalization on polar surfaces, it is suggested that an elimination or reduction in the noise factors is necessary by adjusting and refining the parameters such as Time (t, min), PH value of suspensions and Temperature (T, ^{o}C), etc. And also the sample cleaning and purification might be of more importance in the sense of selectivity.

6.2.2 Biosurface Modification and Functionalization Study

Towards biosensing purpose, it is necessary to get the sensing element to be both biocompatible and bioinert based on the electrical signal detection mechanism in this study. Keeping this in mind, we have designed and carried out two specific types of interfacial modification and fucntionalization towards linking biological fucntional groups.

The first experiment on boronic acid compound modification is inspired and designed for the purpose for cancer detection in which the sugar [mono (poly)saccharides] types and amount in the cancer related cell surface are an important parameter to be monitored and detected. A specific boronic acid polymer-1 is chosen for surface modification. Its structural formula is shown in Figure 6.12. This type of boronic acid is a specific organic macromolecule which can be targeted to the sugar (monosaccharide or polysaccharide) with different specificities in a variety of sensing signal categories, such as fluorescence, UV/color change, electrochemical change, etc.[235] The essence inside is that there could be some specific binding events between the

boronic acid and the saccharides to be targeted, which would lead to the significant variation in terms of sensing signals.

The second experiment is that we directly attached certain types of protein or DNA onto the ZnO nanostructures surface to see the compatibility of the protein with ZnO nanostructures. To find the suitable biological buffer for ZnO nanostructures, several biological buffers' compatibility with ZnO nanobelt, have been tested. And also several types of silanes have been tested for modifying ZnO nanobelt surface with linker molecules which could further modified with functional proteins or DNAs. This type of surface functionalization is the first step towards utilizing the concept of antibody-based cancer detection, no matter what kind of detection mechanisms we use.

6.2.2.1 Polymeric Boronic Acid-based Surface Modification

First, we have done a series of experiment to test the surface chemistry between the boronic acid polymer-1 and ZnO nanobelt surface, by using SEM and TEM characterization; we can judge the intact ability after the polymer coating process.

6.2.2.1a Surface Modification Procedure

The experimental procedure is described as follows.

1. Boronic acid solution: 1.5 mg polymer-1 in 1.5 ml CH_2Cl_2 (solvent) with a concentration of 1 mg/ml;
2. The mixture of ZnO nanobelts (0.1 mg) and 1.5 ml polymer-1 CH_2Cl_2 solution was ultrasonicated for 30 min, and then shaked for 2 min, a uniform suspension of ZnO nanobelts in polymer solution was achieved;

3. A drop of solution of ZnO nanobelts was drawn using glass pipette and dispensed on Au electrodes and in copper grid coated with carbon film (400 mesh).
4. The coated copper grid dried for 24 hrs and then ready for TEM observation. The coated nanobelts on Au electrodes will be further processed for the electrical measurement purpose (see text in sections 6.3 and 6. 4).

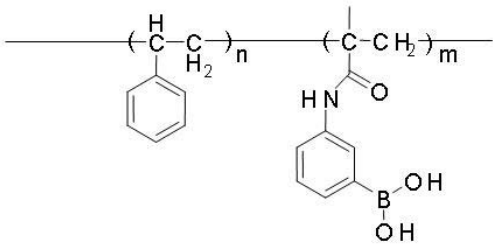

Figure 6.12 The structure of polymeric boronic acid: polymer 1.

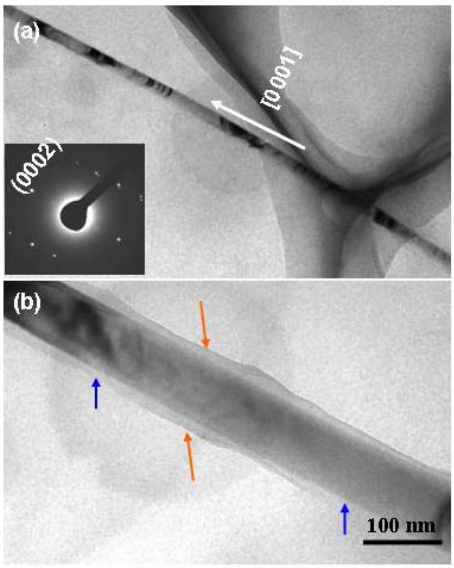

Figure 6.13 Polymer 1 coated ZnO nanobelts grown along [0001] direction. Orange arrow indicates the continuous coating on belt surface, while blue arrows point the non-continuous polymer layer section.

6.2.2.1b Surface Modification Results

As shown in Figure 6. 13 is a series of TEM images of boronic acid coated ZnO nanobelts. As shown in Figure 6.13a is a typical low magnification TEM image showing a ZnO nanobelt around 100 nm in diameter, which was covered by a layer of polymer-1 coating. From the inset diffraction pattern, a set of $[01\bar{1}0]$ spots is the only visible spot corresponding to the nanobelt core with growth direction along c-axis. This fact revealed that the coated polymer-1 is in a long range order or in amorphous structure. The magnified image in Figure 6.13b gave a clear illustration of the uniformity of the polymer coating. Roughly the polymer-1 coating is quite uniform with a layer thickness about 10-20 nm, however, as the blue arrows pointed there are some non-continuous coating areas despite of some other rather continuous polymer layers as the orange arrows indicated in Figure 6.12b. In addition, it is evident that the interface between the nanobelt and boronic acid coating seemed to be quite smooth as intact as before the coating processing despite of a 24 hours stay in the solution with an acidic PH value of ~6.8, which suggested that the polymeric boronic acid coating on ZnO nanobelts could function as a long life-time fluorescence probe for cell-surface saccharides such as fructose. It is worth noting that there could be chemical adsorption effect in addition to the physical adsorption for boronic acid modification on ZnO..

In Figure 6.14, the binding event between the boronic acid-based polymer-1 and the sugar is schemed. It is clear that due to this binding event, there have happened two types of changes. One is that a diol group within the carbonhydrate has been hydrolyzed with the boron acidic group in the polymer-1, a conformational change resulted from the

polymer-1-sugar complex. The other is origin of the fluorescence sensing property of the boronic acid,which is resulted from the internal charge transfer after the binding event.

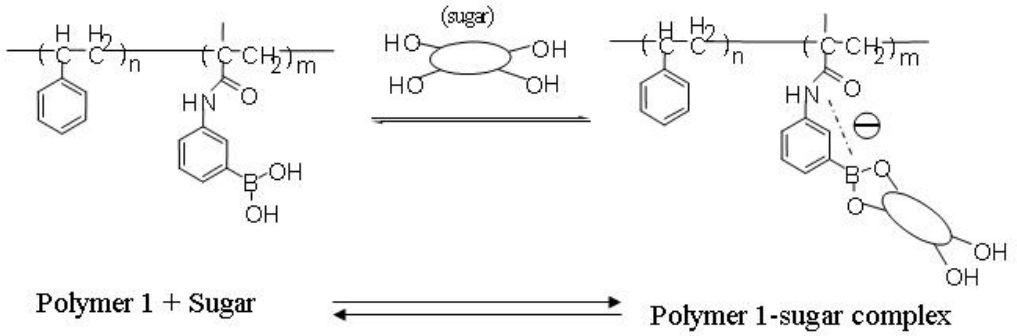

Figure 6.14 Binding between polymeric boronic acid 1 and the additional sugar on ZnO nanobelts surface: conformation change and internal charge transfer due to the binding event.

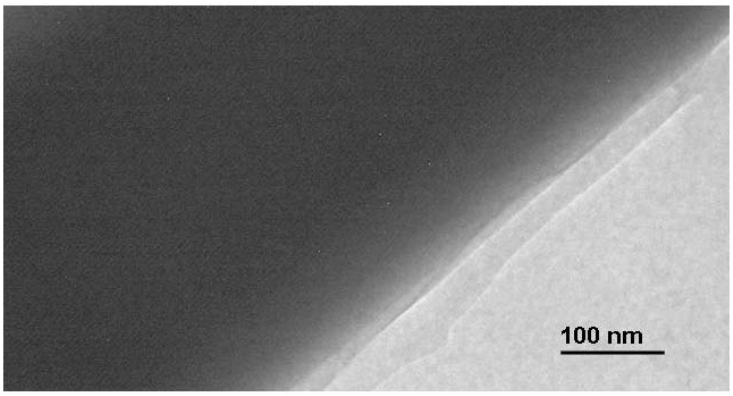

Figure 6.15 TEM image showing the coated ZnO nanobelt surface after further coating processing of a fructose based on the polymeric boronic acid coated ZnO nanobelts.

In Figure 6.15 is a TEM image showing the further coating of a fructose based on the polymeric boronic acid coated ZnO nanobelts in Figure 6.13. There is only one layer of coating on the nanobelt surface with no separated layers respectively corresponding to the polymer-1 and fructose. There needs a further confirmation of the presence of the fructose or the complex through optical measurement process to see if there is a UV

excited fluorescence property change from the boronic acid coated ZnO belts to sugar coated samples. It would be interesting to see if the internal charge transfer upon the second coating process could influence the surface chemistry of the polymer-1 coated nanobelts. In terms of electrical signal, we have built some nanobelts devices for investigating these binding events. If there is some significant electronic transport properties variation, then next it will be more interesting to find out if the electric signal could reflect the similar sensitivity to the fluorescence intensity variation due to different monosaccharide binding events.

6.2.2.2 Surface Functionalization of ZnO Nanobelt with Protein

In this section, our goal is to directly target the protein and DNA modification on the ZnO nanostructures surface, for which we considered the biological buffer compatibility of ZnO nanobelt, and also have tried some experiments on the surface modification. This type of surface functionalization is the first step towards utilizing the concept of antibody-based biosensing, no matter what kind of detection mechanisms we can use eventually. Three instant and complementary experiments have been designed and carried out in this study: a).Buffered saline solutions try-out for ZnO nanobelts; b). Silanization of nanobelts; c).Protein modification of ZnO nanobelts.

To find a biological environment that we can utilize ZnO nanostructures without damaging the structure morphology, i.e., to keep its own characteristics, two types of biological buffer solutions have been tried out on the ZnO nanobelts. One is the popular phosphate buffered saline (PBS), the other is carbonic acid buffered saline (CBS).

Silanization has been a standard procedure for modifying the inorganic surface to achieve a layer of stable linker molecules to be linked with biological organic species

such as protein and DNA. There has been a great deal of reports on silanization of bulk oxide surface, while not many literature on nanostructures oxide surface, especially on one dimensional nanostructure, which is because that the biosensing study on one-dimensional nanostructures is a brand-new research topic emerged recently.

Generally covalent bonded surface linker molecules layer is the idea case for the surface functionalization. On the bulk surface, typically there are two generic methods of silanization. One is directly use solution based method to bind the silane groups onto bulk surface via surface adsorption and hydrolyzation and condensation process. This method has been comprehensively made use of due to its low-cost and simplicity advantage. And also there could be a strong surface chemistry tuning ability by using different chemical processing in the solution. The other method needs to use plasma enhanced CVD process to help change the surface chemistry of ZnO nanobelts, to achieve a polymerized layer on the surface. In this study, an effort has been made on the chemical rout.

The third experiment is the protein modification. The protein we choose to bind ZnO nanobelts is the Enhanced Yellow Fluorescent Protein (EYFP). It is a modified version of Green Fluorescent Protein (GFP). The reason we chose this type of protein for surface modification is two-fold. The first reason is that due to the fluorescence property of the protein, we can directly visualize the existence of the protein on the nanobelts if the coating process is significant. Secondly, the EYFP can be conjugated with specifically modified DNA for specific molecular recognition, further modification on EYFP coated ZnO nanobelts might be of interest.

6.2.2.2a Experimental Procedures

For biological buffer compatibility test, the experimental procedure has been carried out: we directly soaked the nanobelts into prediluted 0.1% buffered saline using deionized water, and then periodically record the surface morphology of ZnO nanobelts at a certain interval using optical microscope. During this experiment, the nanobelts will be instantly kept soaked with the buffer in analogy to a surrounding aqueous biological environment.

Two kinds of silanes were used for surface silanization. One is with dicholoro-group; the other has trimethoxyl-group. Both groups will hydrolize and condense with surface hydroxyl. For this experiment, we first put the ZnO nanobelts into the chloroform to form a suspension, for which it is found that the suspended ZnO nanobelts kept intact for a long time period. And then we add the two types of silanes into two test glass tubes of ZnO-chloroform suspensions. A regular interval was set for recording the nanobelts morphological evolution in the suspension with silanes.

For protein attachment, we directly immersed the nanobelts into the EYFP protein solution for a certain time of period (CAN YOU SPECIFY THE AMOUNT OF TIME?). The nanobelts after a certain time period of incubation in EYFP solution were observed under conventional optical microscope and fluorescence microscope in comparision with the bare nanobelts. TEM imaging was used for characterizing the EYFP coating and interface between nanobelts and coatings.

6.2.2.2a Experimental Results

The buffer solutions try-out is very important for the late experiments in terms of finding suitable buffers. Experimental results showed that ZnO nanobelts could survive in carbonic acid buffer (CBS) for over 48 hours without visible morphology damage under

the optical microscope. The test with the PBS turned out to be the opposite result. As shown in Figure 6.16, only after 5 minutes of soaking in PBS, the surface of ZnO belt has been visibly spotty (Figure 6.16a); after 3-hour exposure with PBS, glassy and transparent stuff has been observed on the belt surface (Figure 6. 16b), which means there was a chemical reaction happened between ZnO and PBS. From literature, it has been reported that ZnO and phosphate could react and form a type of amorphous glass, zinc phosphate.

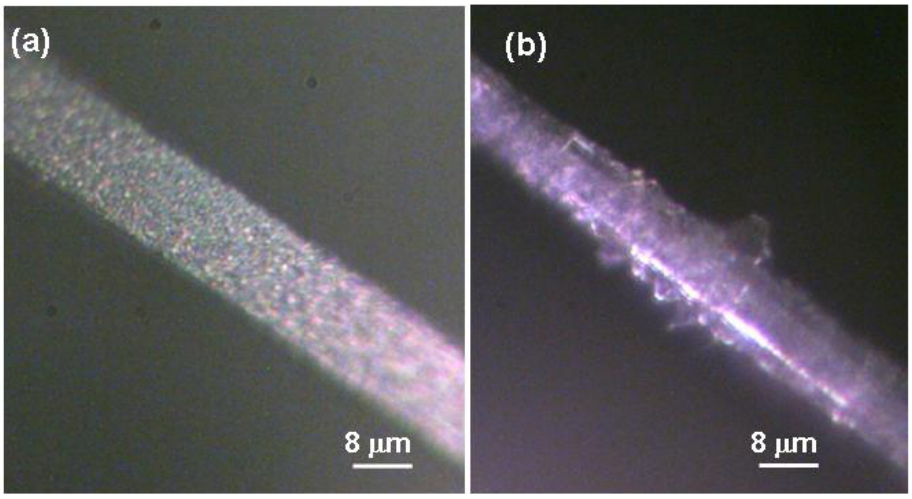

Figure 6.16 Optical microscopy of ZnO nanobelts soaked in phosphate buffered saline solution (PBS). a). dark field OM image at the beginning (5 min); b). dark field OM image at 3 hours exposure, $Zn_3(PO_4)_2$ related glass was produced on the surface of ZnO belt.

For bulky metal oxides surfaces, the two types of silanes we used have been reported to work well. However, it is not for the case of nanobelts. It was found that after adding the dichlorosilane, ZnO nanobelts dissolved quickly, in 1-2 minutes all nanobelts disappeared. After about 20 minutes, the solution became yellowish and then brown. The solution was transparent. It is suggested that there happened chemical reaction between ZnO and the dichlorosilane.

For trimethoxysilane case, the nanobelts did not dissolve after addition. To test if the surface coating with trimethoxysilane completely covered the nanbelts which possibly will block the interation between the outside buffer and ZnO surface, a further test was carried out. We transferred the coated nanobelts into PBS, which has been found to be reactive with ZnO bare belts. Unfortunately, these nanobelts still dissolved, indicating that this layer of silane formed could not protect the surface of ZnO.

To get a layer of linker molecules that not only functions for the further modification, but also protects the inner ZnO surface, plasma enhanced CVD might be an idea method for the surface polymerization of ZnO nanobelts, which will not be further discussed here.

As shown in Figure 6.17 is respectively a bright field (BF) (figure 6.17a) and fluorescent optical image (figure 6.17b). The top and bottom parts of figure 6.17a and b are respectively corresponding to the bare ZnO nanobelts and EYFP modified nanobelts. After incubating together, the coated ZnO nanobelts displayed stronger green fluorescence in the bottom part micrograph of figure 6.17b as compared to the top part fluorescence micrograph of the figure 6.17b corresponding to the bare belts, indicating the successful coating of EYFP on the nanobelts. Afte 10 days of stay in the EYFP solution, TEM characterization was carried out for the EYFP coated nanobelts. A series of TEM images was shown in Figure 6. 18. It is found that ~10 nm thick EYFP has been coated on ZnO nanobelt, about a monolayer of EYFP in Figure 6.18. And the zig-zag

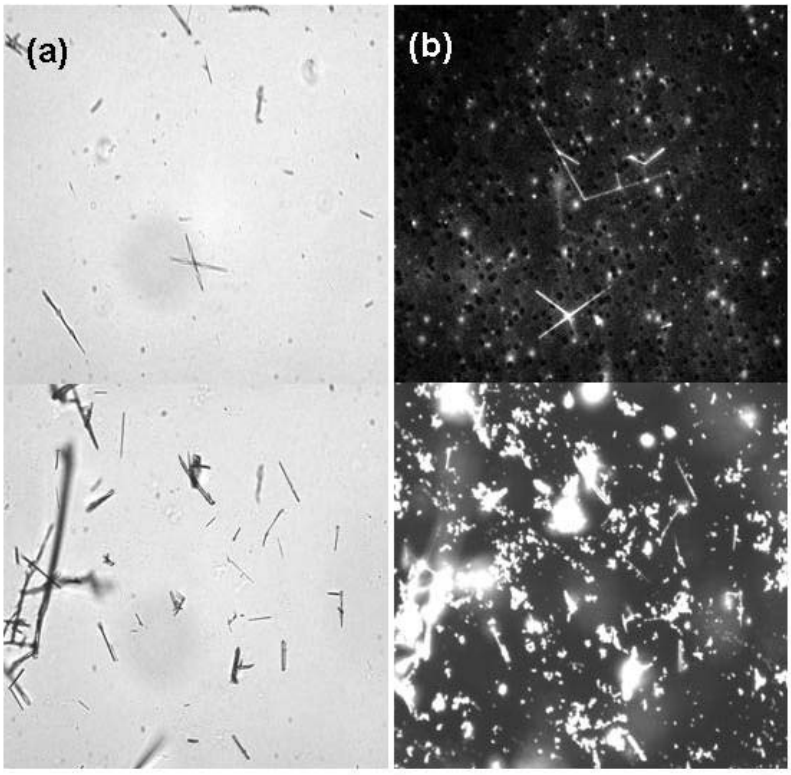

Figure 6.17 Optical microscopy of ZnO nanobelts binded with EYFP. a). Bright field optical image of bare nanobelts (top part) and coated nanobelt (bottom part); b). Fluorescence optical image with much stronger green emission of coated nanobelt (bottom part) than the bare nanobelts (top part).

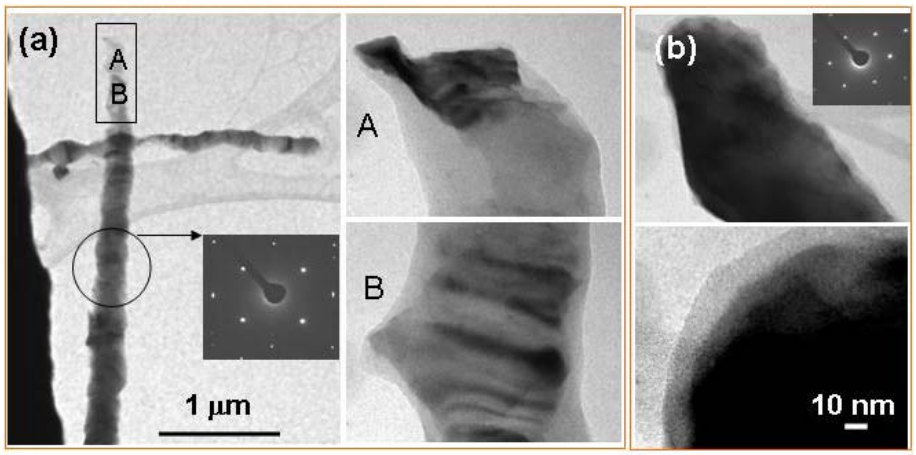

Figure 6.18 Enhanced yellow fluorescence protein coating on ZnO nanobelts. a). TEM images shows ~10 nm thick EYFP coating on ZnO nanobelt, about a monolayer of EYFP; b) partially stable ZnO nanobelt with non-uniform surface coating, a zig-zag feature suggested the existence of corrosion by EYFP.

feature of the interface between ZnO nanostructures and EYFP indicates that even though ZnO is rather stable upon the coating of EYFP, the surface is still tending to be unstable and corroded by the protein.

6.2.3 Conclusions

So far, we have explored the surface modification and functionalization of ZnO nanostructures. From the results, it has been shown that ZnO nanobelts could be modified by polymeric boronic acid, which could function as fluorescence probe of specific saccharides such as fructose in cell surface. ZnO nanobelts could survive in a specific biological environment such as carbonic acid buffered saline. The ZnO nanobelts may be modified with certain types of proteins such as EYFP, but there may be a corrosion problem between the ZnO and EYFP. A stable and uniform surface functionalization will be an important step for ZnO nanostructures to be useful in biosensing applications. Much future work on product development will be necessary before the sensors can be characterized in terms of sensitivity, selectivity and stability. More and further investigation on this topic would be necessary for the possible success of the biosensing application using ZnO nanostructures as the sensing building blocks.

6.3 Nanodevices Fabrication and Characterization

Optical lithography has been playing a key role in the success of CMOS technology as the microelectronics evolves. By using smaller and smaller wavelengths year upon year, the required performance on critical feature sizes has been achieved. In

addition, using variety of emerging techniques such as sophisticated mask technology including phase-shift masks and optical proximity corrections, has pushed the physical limits further down to nanoscale range (50-100 nm). These critical requirements imply more complex masks and processes and higher costs for this type of sophisticated equipment.

Now, the so-called "Next Generation Lithography'' (NGL) options proposed several years ago such as X-ray, projection electron-beam and projection ion-beam lithographies have been gradually used not only for creating small structures in the science and technology research, but also for helping semiconductor industry in terms of quality control and the technological innovation. In this section, we utilize the focused electron-beam and ion-beam to fabricate nanoscale devices which will incorporate the as-synthesized one dimensional nanostructures of ZnO for sensing purpose.

6.3.1 Electron Beam Nanolithography and Focused Ion Beam Nanolithography

Electron beam lithography (EBL) makes use of the fact that electrons can be deflected and modulated by electrostatic or magnetic fields to produce an image, which is specialized technique for creating small patterns. The fundamental resolution limit is given by the Heisenberg uncertainty ($\Delta x\ \Delta p \geq h/2\pi$) offering the possibility to achieve patterning below 10 nm. There are two ways to perform E-beam lithography, either by scanning the beam to generate patterns or to perform electron imaging through masks like conventional photolithgraphy. Upon scanning a electron beam across a surface covered with a resist film sensitive to those electrons, a desired pattern will form in the resist film, which could be later on lifted off or left as the stamp pattern.

Electron-beam lithography is the essential basis of nanostructure fabrication at present. Gaussian beam pattern generators or scanning electron microscopes are used with high-energy electrons (100 to 200 keV) and a small electron probe size (1 to 10 nm). Using high resolution and low sensitivity PMMA resist, dimensions down to 30 nm are routinely produced in many research laboratories with high reproducibility. Resolutions down to 4 nm have been demonstrated. The biggest disadvantage of this technology is the large writing time, causing a low throughput that makes electron beam lithography prohibitively expensive for the mass production of integrated circuits.

Focused Ion Beam Lithography (FIBL) uses a technology called "direct writing" for nanofabrication, which transfers patterns by direct impingement of a small spot of the FIB onto a substrate. Direct writing is comprised of several major approaches, including milling, implantation, ion-induced deposition, and ion-assisted etching, which respectively perform material removal from, property change on, material addition on, and material removal from the substrates with or without chemical assistance []. The FIBL could be controlled in a variety of parameters, such as the beam size, current density, and energy density to remove or add a required amount of material with or without chemical reactions from a predefined location. In this way, high-precision and complex three-dimensional (3D) nanostructures can be created.

FIBL has many advantages over other high-energy particle beams used in nanofabrication. For example, heavy ions with high energy has made FIBL capable of directly writing on hard materials with small penetration depth and small back (or forward) scattering effect in a short wavelength. And the lateral exposure in FIBL is rather low, therefore allowing writing very narrow lines in the strictly predefined area,

making it more capable to directly fabricate nanostructures. Consequently, FIBL has become a popular fabrication tool adopted by the semiconductor industry, for mask repairing, device modification, integrated circuit (IC) debugging, as well as a powerful tool in fabricating high-precision nanostructures with high-quality.

6.3.2 Electrodes and Microchannels Fabrication

As shown in Figure 5. 19 is a typical schematic of side view of nanobelts device structure to be fabricated using E-beam lithography. The nanobelt is designed to be sandwiched by the bottom electrodes pair and two top electrode pads to ensure the omic contact between the nanbelts and the electrodes.

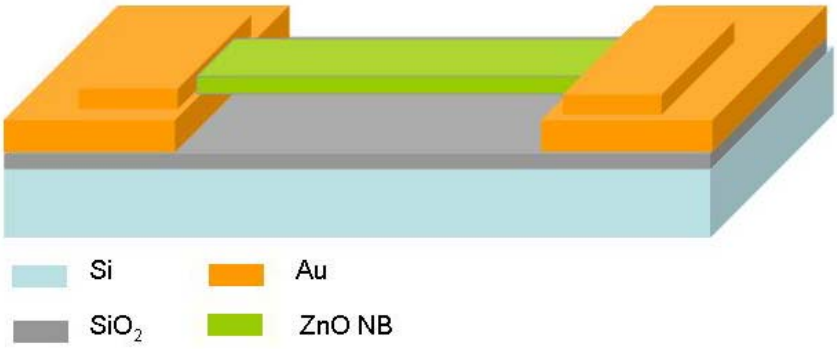

Figure 6.19 A schematic of the nanobelt device structure.

The nanobelt devices are typically fabricated using polished silicon wafer (100) with a native grown oxide layer about 3 nm thick, giving very high resistance insulation effects. Thermally grown oxide or SiN layer made by plasma enhanced CVD are also the choices for insulation purpose.

As shown in Figure 6.20 is the electrode fabrication flow process using EBL.

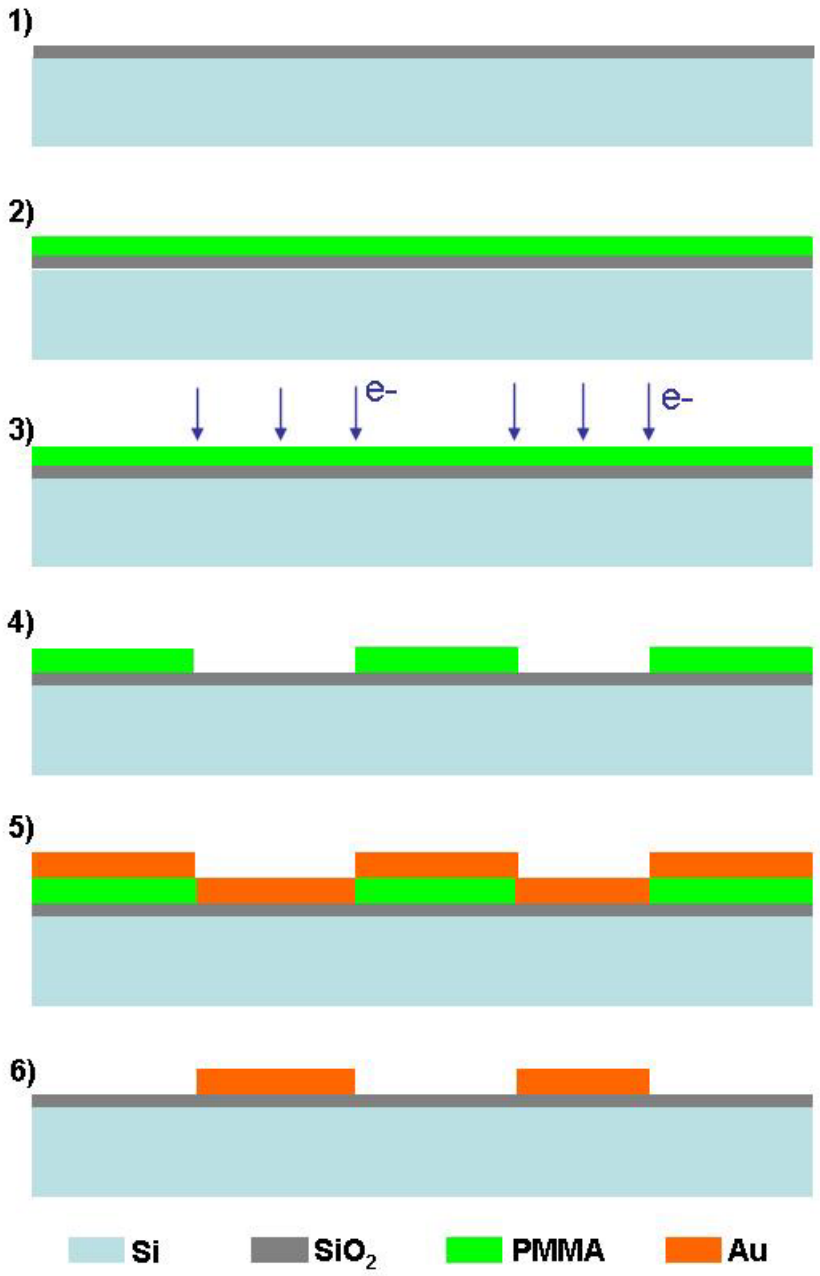

Figure 6.20 Au electrodes fabrication flow process using E-beam lithography.

The procedure for the fabrication is: a). Firstly ultrasonically clean the Si wafer in trichloroethylene (TCE) followed by acetone and isopropanol (IPA) for 15 minutes in each solution. b). Then the wafer is blown dry using compressed dry N_2. c). Electron-sensitive resist PMMA coating (step 1-2 in Figure 6.20); d). Eelectron beam scanning for generating desired pattern on PMMA(step 3); e). acetone development of exposed area (dissolution of e-beam exposed area) (step 4); e). Metal (Au) deposition (step 5); f) Lift off of PMMA area, a pattern transfer process (step 6). PMMA resists represent a popular used polymethyl methacrylate with a large molecule weight (950k) resins in 2% chlorobenzene for the top layer Thermal evaporation technique was used for metal (Au) deposition.

The electron-beam lithography equipment that is used is a Scanning Electron Microscope JSM 5910, which is controlled by Nanometer Pattern Generation System (NPGS) software during the writing of the patterns. Using NPGS, a variety of parameters such as beam current, center to center spacing, line spacing, dosage and magnification can be set to write properly on the samples.

To achieve good enough contact between the electrodes and the nanobelts, we have chosen to make both end of nanobelt to be sandwiched by Au pads. After above described processing, a whole Si wafer with many pairs of bare Au electrodes could be achieved depending on the writing process. Then we dispersed the nanobelts suspension onto the Si wafer, where ZnO nanobelts will randomly distributed on the patterned Si wafer. To achieve aligned nanobelts across the electrodes pair, an alternating electric field was applied on each electrodes pair to make at least several nanobelts aligned across the electrodes based on the electrostatic driving effect upon the alternating electric field.

Now the bottom surface of both ends of ZnO nanobelts will contact with the Au pad. While to make a sandwiched contact, a top layer of Au pads will be needed. Then this time another patterning process will be done based on the prepatterned electrodes and nanobelts to allow the overlapped pattern with the electrode pads. The procedure is the same as before, the only difference is that a precise alignment to the previous pattern is necessary to guarantee the formation of the sandwiched structured electrodes with nanobelts ends as the meat part.

As shown in Figure 6.21 is an as-fabricated nanobelts device with aligned nanobelts sandwiched by top Au pads and bottom Au electrodes. Figure 6.21b displays two nanobelts ~300 nm wide crossed the electrodes. On the right, the two nanobelts definitely are covered by another layer of Au, the top layer of the sandwiched structure.

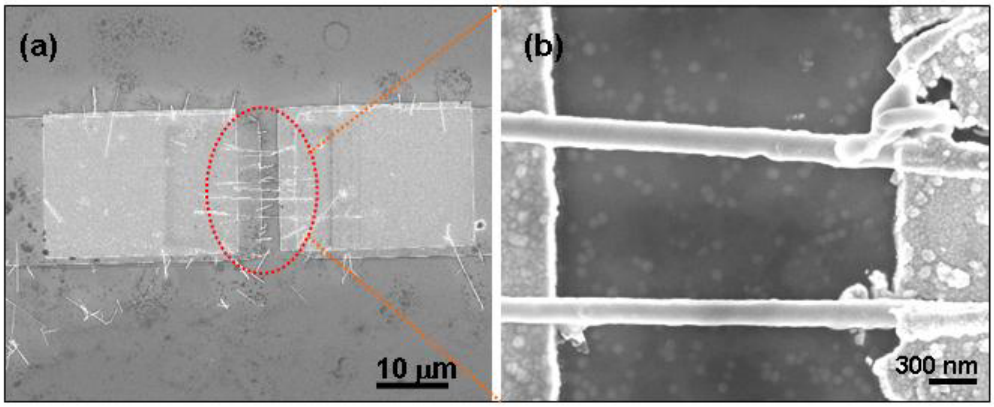

Figure 6.21 Bare nanobelts on Au electrodes made by E-beam lithography.

For the resonator and flow sensor fabrication, it is inevitable to introduce microtrenchs and microchannels fabrication. Typically, photolithography is the technique to be popularly used for creating the micron sized channels for microfluidics application. In this study, we are trying to avoid the complicated procedures involved in the clean room operation. Using focused ion beams, we can directly blow the materials in

specifically designed pattern with certain quantity to form a microtrench, and also we can deposite certain amount of metals in specifically defined pattern as electrodes or interconnect in the devices. And also since based on the nanohelix resonator and flow sensor design we have to arrange the nanostructures across the micro-channels, there is an advantage that can be utilize in FIBL technology. In the FIB microscope, there generally installs a micromanipulator for TEM sample preparation. It in fact also can be used for transferring the nanostructures onto the trench or microchannel if necessary before the sealing the channels. As for the resonator and flow sensor design, the device structure has to be modified as shown in Figure 6. 22 from the nanobelts device structure in Figure 6. 19. There needs a specifically large enough height in between the nanostructures and the bottom surface of the microtrenches (channels).

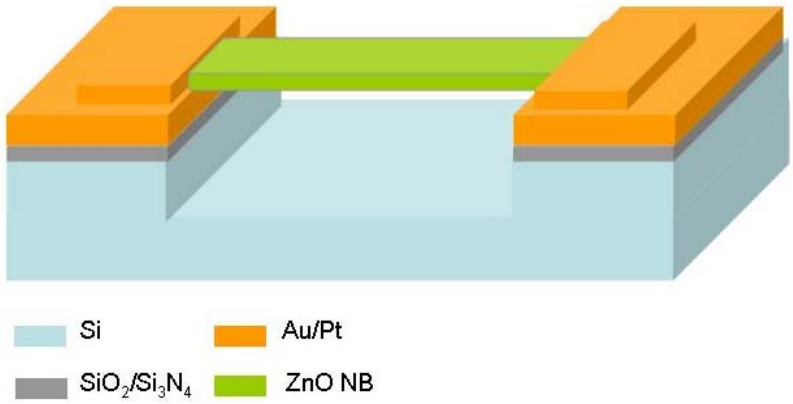

Figure 6.22 A schematic of nanobelt/nanohelix device structure for future resonance measurement or flow measurement (bottom part).

As shown in Figure 6.23 is a series of SEM images showing the fabricated microchannels array and Pt electrodes array on Si substrates using FIBL. The blue arrows in Figure 6.23a represent the microtrenches parallel to each other and these microtrenches have a uniform width ~3 μm, and depth ~5 μm. And the orange arrows point the FIB

deposited Pt interconnects with uniform width around 1 μm, and thickness of 300 nm. It is suggested that with reasonable processing parameters and device designs, prototype nanobelt/nanohelix devices could be fabricated using the focused ion beam lithography in conjuction with the micromanipulating capability.

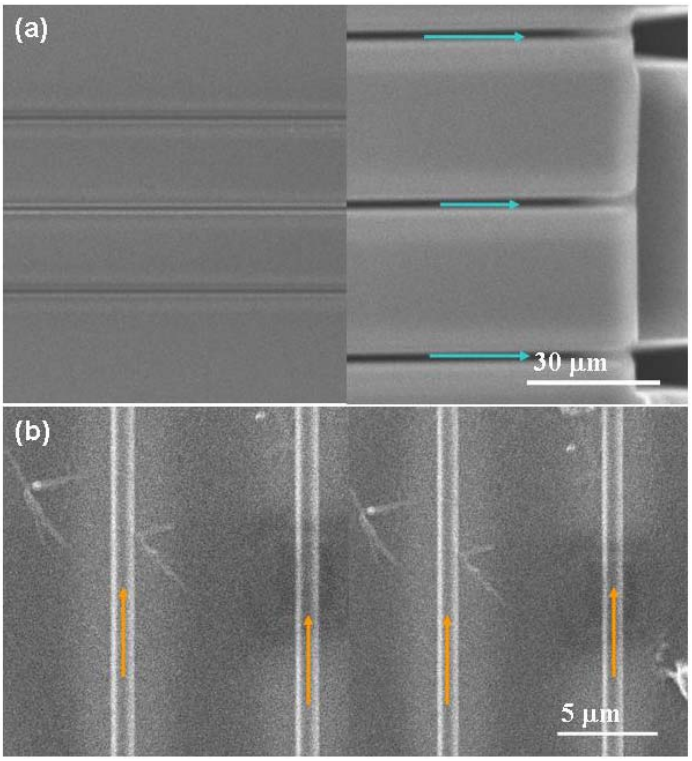

Figure 6.23 Microchannels and Pt electrodes fabricated on Si (100) substrate using FIBL.

6.3.3 Electrical Measurement on Nanohelices

Electrical transport properties study of nanobelts and nanowires is of great importance for nanobelts and nanowires characterization, electrical signal based device applications, and the investigation of unusual transport phenomena arising from one-dimensional quantum effects. Important factors that determine the transport properties of nanobelts include the belt thickness and width (which is important for both classical and quantum size effects), material composition, surface conditions, crystallinity, and the

crystallographic orientation in terms of anisotropic parameters, such as the effective piezo-coefficient, the band structure, etc.

Electronic transport phenomena in one-dimensional system can be classified into two categories: ballistic transport and diffusive transport.[236,237] Ballistic transport phenomena occur when the electrons can travel across the nanowire without any scattering. In this case, the conduction is mainly determined by the contacts between the nanowire and the external circuit, and the conductance is quantized into an integral number of universal conductance units $G_0 = 2e^2/h$. Ballistic transport phenomena are usually observed upon the electron mean free path is much longer than the wire length and the conduction is a pure quantum phenomenon. On the other hand, for nanowires with lengths much larger than the carrier mean free path, the electrons (or holes) undergo numerous scattering events when they travel along the wire. In this case, the transport is in the diffusive regime, and the conduction is dominated by carrier scattering within the wires, due to lattice vibrations, boundary scattering, lattice and other structural defects, and impurity atoms.

Electrical biosensing using the electronic transport phenomena in the solid sensing probe has been a challenge due to the aquous working environment requirement, where there might very possibly involve the electrochemical process which could complicate this process to a significant extent. Despite of this issue, recently there have emerged quite a lot successful examples of the electric signal detection for biosensing, but to a maximum degree suppressed the electrochemical phenomena. In this section, electrical measurement on the bare ZnO nanohelix devices will be conducted as the base

of the further biosensing properties measurement. The current-voltage characteristics will be elaborated.

As shown in figure 6.24a is an optical image of an as-fabricated ZnO nanohelix device. Platinum nanointerconnects with a width of ~200 nm and a thickness of 200 nm have been made by focused ion beam induced deposition to connect the as-deposited

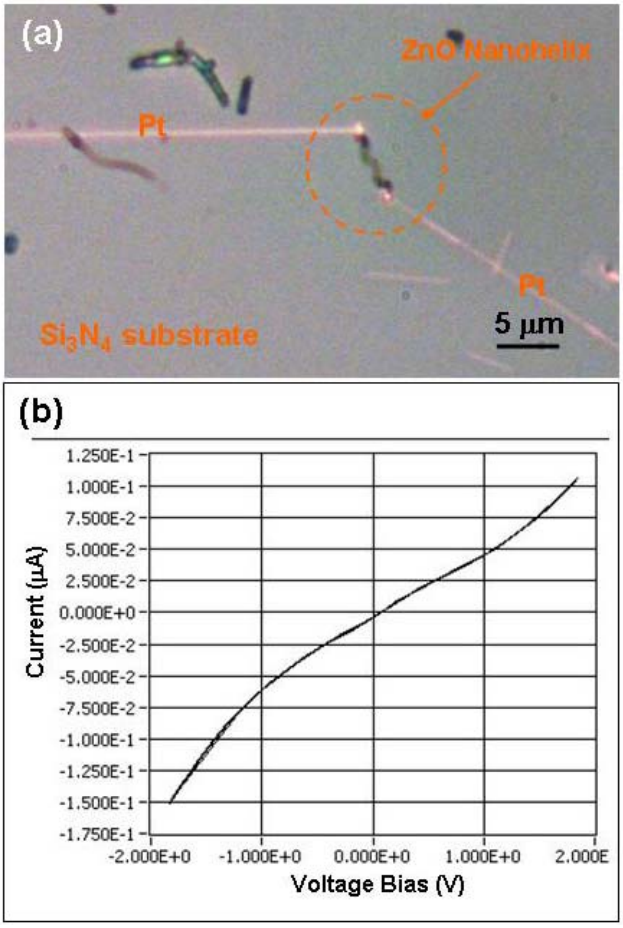

Figure 6.24 a). An optical image showing the fabricated ZnO nanohelix device; b). The current-voltage characteristics of ZnO nanohelix device.

ZnO nanohelix to blank two-terminal device electrodes for a two-probe electrical measurement. The measurement was conducted by applying a slowly varying voltage bias of $2V_{p-p}$ with a 0.01 Hz triangle waveform across the nanohelix. The insulating layer

of SiN ~1 μm thick has ensured a very large resistance of ~2 TΩ between the Si gate electrode and the two terminal Au electrodes. The current-voltage data was acquired by using Labview 7.0 after the nanohelix device circuit is loaded with bias for 30 s for electrically aging purpose. In figure 6.24b, a typical current-voltage characteristics of the nanohelix is shown, revealing that the nanohelix with a length of ~5.6 μm has a resistance of ~10MΩ upon voltage span of 1-2 V. The linear characteristics of IV curve in the lower voltage scanning range from -1 V to 1 V suggested that an ohmic contact has been achieved, the resistance of the nanohelix is ~16 MΩ. But in the voltage span of 1-2 V, the curve becomes non-linear with increasing conductivity with about half the resistance in the lower voltage span range. To explain the nonlinear characteristics, further investigation needs to be carried out. But there could have two types of possibilities responsible for this phenomenon. The first is that the non-linear characteristics might be due to the tunneling effect from the Pt interconnects, which has been reported recently; the second explanation might go to the intrinsic electronic transport property of the superlattice nanohelix, which probably has a quantum resonance property.

Further electrical characterization of the nanohelix devices is going on. The further investigation on these devices would be of great interest for probing and understanding the electronic transport properties in the fantastic one-dimensional piezoelectric nanostructures system.

6.5 Summary

Based upon a vision of the future of human health care, more and more research effort has been being input for the development of the in vivo sensing of signatures of pathologic cell types for early detection, diagnosis and therapy treatment. In this chapter, I have explored a broad view on the biosensing application study of several specific configurations of piezoelectric ZnO nanostructures such as nanobelts, nanopropellers and nanohelices in perspectives of mass sensing, surface functionalization, device fabrications and electrical measurement.

From mass sensing points of view, by using *in-situ* TEM measurement technique, a dual mode resonance mode of ZnO nanobelt has been observed, and the tip work function of ZnO nanobelt also measured, which could have potentials to find biosensing applications. However, the harsh environment such as high vacuum and electron irradiation in the TEM for biological species has hindered the development of this technique. The *in-situ* optical microscopy measurement has been successfully used for picogram level mass measurement, which suggested that a bio-friendly optical microscope might be a better choice in terms of biological mass sensing over electron microscopy.

For surface modification studies, carbonic acid buffer was shown to be compatible with ZnO, and polymeric boronic acid was successfully modified onto ZnO nanobelts, which might be used as a fluorescence probe for optical sensing of specific saccharides such as fructose. The ZnO nanobelt fluorescence probe in conjunction with

electrical sensing may be of great interest for development of an integrated biosensing probe for cell-surface saccharides.

From device fabrication and properties measurement perspectives, we have successfully fabricated several prototype devices based on nanobelts and nanohelices of ZnO, and achieved some preliminary electrical property data. For the future, further investigation of surface functionalization and sensing mechanism studies of the nanobelts and nanohelices might be very promising since these materials could be very good systems for biosensing applications.

CHAPTER 7

CONCLUSIONS

A systematic study has been conducted on the synthesis, characterization and devices application of piezoelectric ZnO nanstructures in this thesis work. The following goals have been achieved:

1. Rational design and growth contol over versatile nanostructures of ZnO;
2. Improved chemical and physical understanding of ZnO nanostructure growth;
3. Opening study on devices application, for which the biosensing is the main target.

Firstly, through a systematic investigation on the Sn-catalyzed ZnO nanostructure, an improved understanding of the chemical and physical process occurred in the growth of hierarchical nanostructures has been achieved:

1.a. Well-aligned ZnO nanorods with six identical facets of $\{2\bar{1}\bar{1}0\}$ and orientation ordering have been successfully synthesized. Reduced Sn from SnO_2 acts as catalysts that guide the aligned growth of ZnO nanorods.

1.b. One-step thermal evaporating a mixture of ZnO and SnO_2 has led to the formation of self-assembled nanowire-nanoribbon junction arrays of ZnO. And a two-step heating process would lead to formation of polar surface dominated ZnO nanopropeller arrays.

1.c. Using electron diffraction and high-resolution electron microscopy, it is found that tin catalyst not only can guide [0001] growth nanowires, but also can guide $[01\bar{1}0]$ and $[2\bar{1}\bar{1}0]$ growth nanobelts. Specific orientation relationship are kept between

ZnO nanowire/nanobelt and the single crystal β phase Sn particle. One tin particle can initiate the growth of two 1D nanostructures; the tin particle is single crystal post the growth and it preserves epitaxial relationships with the grown nanostructures.

1.d. The interfacial region of the tin particle with the ZnO nanowire/nanobelt could be crystalline or atomically ordered during the VLS growth, although the local growth temperature is much higher than the melting point of tin, and it may play a key role in initiating 1D nanostructure. The interface prefers to take the least lattice mismatch, thus, the crystalline orientation of the tin particle may determine the growth direction and the side surfaces of the nanowires/nanobelts.

1.e. Anisotropical Sn catalyzed ZnO nanowire/nanotrunk growth on a single crystal ZnO substrate has been experimentally proved to be attributed to the atomic-termination of the substrate, surface charges and interface adhesion. But the VLS process is dominant.

Secondly, using pure ZnO as the only source materials, by precisely tunning and controlling the growth kinetics, a variety of hierarchical polar surface dominated nanostructures have been achieved such as single crystal nanorings, nanobows, nanosprings. The most important results are concluded as following:

2.a. By controlling the growth kinetics through refining parameters such as temperature, pressure and duration time, especially the pre-growth pressure level, single crystal ZnO nanosprings were synthesized at high yield (> 50%). Our experiments indicate that doping is not necessary for forming the polar surface dominated nanosprings and nanoloops, but a pre-growth low pressure seems to be the key.

2.b. It has been experimentally observed that planar defects are usually present in the polar surface dominated nanobelts.

2.c. For wurzite ZnO, spontaneous polarization can lead to a few unusual growth features, such as nanorings, nanobows, nanohelixes and nanospirals, which are the results of minimizing the electrostatic energy due to the polarization. As a result of switching growth modes, combinated ZnO nanoarchitectures could form, which revealed that the fundamental growth features can co-exist during the growth, and their recombination produces a diversity group of nanoarchitectures including several types of nanorings, nanobows, platelet circular structures, Y-shape split ribbons, and crossed ribbons. The switching growth phenomena can be very popular upon controlling the right growth kinetics.

2.d. A distinctive helical structure of ZnO, made of a superlattice-structured nanobelt has been synthesized spontaneously. The superlattice nanobelt is a periodic, coherent, epitaxial and parallel growth of two alternating nanostripes of ZnO crystals oriented with their c-axes perpendicular to each other.

2.e. The formation of the nanohelix is a rigid structural alteration caused by the alternating stripes in the superlattice, and the formation of a superlattice is likely to be a polar charge induced structural transformation. The winding of the nanobelt is terminated after the nanobelt fully transforms from a partial-polar-surface-dominated and superlattice-structured nanoobject into a single-crystal nanoribbon dominated by nonpolar surface, which is likely to be caused by a change in growth kinetics.

2.f. The perfect helix shape we observed is of great interest not only for understanding the growth behavior of polar surface driven growth process in the wurtzite system, such as GaN, AlN and InN, but also for investigating fundamental physics and optical phenomena. The piezoelectric and semiconducting properties of ZnO suggest that the nanohelix could be a fundamental unit for investigating electromechanically coupled nanodevices by utilizing the superlattice piezoelectric domains. The nanohelix is likely to have important applications in sensors, transducers, resonators and photonics.

Thirdly, two new strategies have been successfully probed and developed for fabrications of a versatile group of nanostructures building blocks for nanoelectronics and optoelectronics.

3.a. A brand-new strategy involving electron-solid interaction is designed and demonstrated to successfully fabricate ultra-small quantum dots pattern on bulk materials.

3.b. By using the simple vapor-sold growth process, in conjunction with the physical and chemical understanding of ZnO crystal growth process, a strategy for growing various types of nanostructures from nanodiskettes to nanotubes has been developed, which could be extended to a potential strategy for the other II-VI class and III-V group wurtzite structured semiconductors nanostructures.

The fourth, a broad view has been brought up on the biosensing application study of several specific configurations of piezoelectric ZnO nanostructures such as nanobelts, nanopropellers and nanohelices in perspectives of mass sensing, surface functionalization, device fabrications and electrical measurement.

4.a. From mass sensing points of view, by using *in-situ* TEM measurement technique, a dual mode resonance mode of ZnO nanobelt has been observed, and the tip work function of ZnO nanobelt also measured, which could have potentials to find biosensing applications. However, the harsh environment such as high vacuum and electron irradiation in the TEM for biological species has hindered the development of this technique. The *in-situ* optical microscopy measurement has been successfully used for picogram level mass measurement, which suggested that a bio-friendly optical microscope might be a better choice in terms of biological mass sensing over electron microscopy.

4.b. For surface modification studies, carbonic acid buffer was shown to be compatible with ZnO, and polymeric boronic acid was successfully modified onto ZnO nanobelts, which might be used as a fluorescence probe for optical sensing of specific saccharides such as fructose. The ZnO nanobelt fluorescence probe in conjunction with electrical sensing may be of great interest for development of an integrated biosensing probe for cell-surface saccharides.

4.c. From device fabrication and properties measurement perspectives, we have successfully fabricated several prototype devices based on nanobelts and nanohelices of ZnO, and achieved some preliminary electrical property data. For the future, further investigation of surface functionalization and sensing mechanism studies of the nanobelts and nanohelices might be very promising since these materials could be very good systems for biosensing applications.

APPENDIX A

PUBLICATIONS AND PATENTS

[1] C.S. Lao, J. Liu, P.X. Gao, L.Y. Zhang, D. Davidovic, R. Tummala, Z.L. Wang, "ZnO nanobelt/nanowire Schottky diodes formed by dielectrophoresis alignment across Au electrodes", *Nano Letts.*, **2005**, submitted.

[2] J. Zhou, C. S. Lao, P. X. Gao, W. J. Mai, Z. L. Wang and N. S. Xu, "Nanowire as pico-gram balance at workplace atmosphere", *J. Appl. Phys.*, **2005**, submitted.

[3] P. X. Gao, C. S. Lao, Y. Ding and Z. L. Wang, "Metal-Semiconductor Core-Shell Nanodiskettes and Nanotubes", *Adv. Funct. Mater.*, **2005**, early view (November).

[4] C. S. Lao, P. X. Gao, R. S. Yang, Y. Zhang, Y. Dai and Z. L. Wang, "Formation of double-side teethed nanocombs of ZnO and self-catalysis of Zn-terminated polar surface ", *Chem. Phys. Letts.*, **2005**, 417, 359.

[5] P. X. Gao, Y. Ding, W. J. Mai, W. L. Hughes, C. S. Lao and Z. L. Wang, "Conversion of Zinc Oxide Nanobelts into Superlattice Structured Nanohelices", *Science*, 2005, 309, 1700.

[6] P. X. Gao and Z. L. Wang, "High-yield synthesis of single-crystal nanosprings of ZnO", *Small*, **2005**, 1, 945.

[7] P. X. Gao, C. S. Lao, W. L. Hughes and Z. L. Wang, "Three-dimensional interconnected nanowire networks of ZnO", *Chem. Phys. Letts.*, **2005**, 408, 174.

[8] P. X. Gao and Z. L. Wang, "Nanoarchitectures of Semiconducting and Piezoelectric Zinc Oxide", *J. Appl. Phys.*, **2005**, 97, 044304.

[9] W. G. Lu, P. X. Gao, W. B. Jian, Z. L. Wang and J. Y. Fang, "Perfect Orientation Ordered in-Situ One-Dimensional Self-Assembly of Mn-Doped PbSe Nanocrystals**"**, *J. Am. Chem. Soc.*, **2004**, 126, 14816.

[10] Z. L. Wang, X. Y. Kong, Y. Ding, P. X. Gao, W.L. Hughes, R. Yang and Y. Zhang," Semiconducting and Piezoelectric Oxide Nanostructures induced by Polar Surfaces", *Adv. Funct. Mater.*, **2004**, 14, 943.

[11] F. Li, Y. Ding, P. X. Gao, X. Q. Xin, and Z. L. Wang, "Single-Crystal Hexagonal Disks and Rings of ZnO: Low-Temperature, Large-Scale Synthesis and Growth Mechanism**",** *Angew. Chem. Int. Ed.*, **2004**, 116, 5350.

[12] P. X. Gao and Z.L. Wang, "Substrate atomic-termination induced anisotropic growth of ZnO nanowires/nanorods by VLS process", *J. Phys. Chem. B*, **2004**, *108*, 7534 + Cover.

[13] P. X. Gao and Z. L. Wang, "Nanopropeller Arrays of Zinc Oxide", *Appl. Phys. Letts.*, **2004**, *84*, 2883 + Cover.

[14] Y. Ding, P. X. Gao and Z. L. Wang, "Catalyst-nanostructure interfacial lattice mismatch in determining the shape of VLS grown nanowires and nanobelts: a case of Sn/ZnO", *J. Am. Chem. Soc.*, **2004**, *126*, 2066.

[15] C. Ronning, P.X. Gao, Y. Ding, and Z.L. Wang, D. Schwen, "Manganese doped ZnO nanobelts for spintronics", *Appl. Phys. Letts.*, **2004**, *84*, 783.

[16] P. X. Gao, Y. Ding and Z. L. Wang, "Crystallographic-Orientation Aligned ZnO Nanorods Grown by Tin Catalyst", *Nano Letters*, **2003**, *3*, 1315.

[17] X. D. Bai, E. G. Wang, P. X. Gao and Z. L. Wang, "Measuring the work function at a nanobelt tip and at a nanoparticle surface", *Nano Letters*, **2003**, 3, 1147.

[18] P. X. Gao and Z. L. Wang, "Mesoporous Polyhedral Cages and Shells formed by Textured Self-assembly of ZnO Nanocrystals", *J. Am. Chem. Soc.*, **2003**, *125*, 11299.

[19] X.D. Bai, P.X. Gao, Z.L. Wang and E.G. Wang, "Dual-mode mechanical resonance of individual ZnO nanobelts", *Appl. Phys. Letts.*, **2003**, *82*, 4806.

[20] P. X. Gao and Z.L. Wang, "Self-assembled Nanowire-Nanoribbon Junction Arrays of ZnO", *J. Phys. Chem. B*, **2002**, *106*, 12653 + Cover.

[21] X. D. Wang, P. X. Gao, J. Li, C. J. Summers and Z. L. Wang, "Rectangular porous ZnO-ZnS nanocables and ZnS nanotubes", *Adv. Mater.*, **2002**, *14*, 1732.

[22] Z.L. Wang and P.X. Gao, "Nanoscale junction arrays and methods for making same"**,** US patent No. 6,918,959, **2005**.

[23] Z.L. Wang, P.X. Gao and Y. Ding, "Superlattice structured nanohelix for electromechanical coupled piezoelectric sensor, actuator and resonator", provisional patent filed (**2005**).

REFERENCES

[1] S. Iijima, T. Ichihashi *Nature*, **1993**, 363, 603

[2] Z.L. Wang (ed.) Nanowires and Nanobelts – materials, properties and devices; Vol. I: Metal and Semiconductor Nanowires , Kluwer Academic Publisher, **2003**.

[3] C. R. Martin., *Chem. Mater.*, **1996**, 8, 1739

[4] Y.N. Xia, P.D. Yang, Y.G. Sun, Y.Y. Wu, B. Mayers, B. Gates, Y.D. Yin, F. Kim, Y.Q. Yan, *Adv. Mater.*, **2003**, *15*, 353.

[5] M. H. Huang, S. Mao, H. Feick, H. Yan, Y. Wu, H. Kind, E. Weber, R. Russo, P. Yang, *Science* **2001**, *292*, 1897.

[6] E. W. Wong, B. W. Maynor, L. D. Burns, C. M. Lieber , *Chem. Mater.*, **1996**, 8, 2041.

[7] P. D. Yang, C. M. Lieber , *Science* **1996**, *273*, 1836.

[8] L. Vayssieres, *Adv. Mater.*, **2003**, 15, 464.

[9] Z.L. Wang (ed.) *Nanowires and Nanobelts – materials, properties and devices; V*ol. II: *Nanowires and Nanobelts of Functional Materials*, Kluwer Academic Publisher, **2003**.

[10] Z. W. Pan, Z. R. Dai, Z. L. Wang, *Science* **2001**, *291*, 1947.

[11] X. Y. Kong, Y. Ding, R. Yang, Z. L. Wang, *Science* **2004**, *303*, 1348.

[12] Z. L. Wang, *Ann. Rev. Phys. Chem.* **2004**, 55, 159.

[13] Z. R. Dai, Z. W. Pan, Z. L. Wang, *Adv. Funct. Mater.* **2003**, 13, 9.

[14] P. Avouris, *Acc. Chem. Res*., **2002**, 35, 1026.

[15] S. J. Tans, A. R. M. Verschueren, C. Dekker, *Nature*, **1998,** 393, 49

[16] W. A. Deheer, A. Chatlain, D. Ugarte, *Science*, **1995**, 270, 1179.

[17] S. Frank, P. Poncharal, Z. L. Wang, W. H. De Heer, *Science*, **1998**, 280, 1744.

[18] J. Kong, N.R. Franklin, C. W. Zhou, M. G. Chapline, S. Peng, K. J. Cho, H. Dai, *Science*, **2000**, 287, 622.

[19] X. F. Duan, Y. Huang, Y. Cui, J. F. Wang, C. M. Lieber, *Nature*, **2001**, 409, 66.

[20] M. Arnold, P. Avouris, Z.L. Wang,. *J. Phys. Chem. B*, **2002**, *107*, 659.

[21] E. Comini, G. Faglia, G. Sberveglieri, Z.W. Pan, Z.L. Wang *App. Phys. Letts.*, **2002**, *81*, 1869.

[22] X. D. Bai, P. Gao, Z.L. Wang and E.G. Wang, *Appl. Phys. Letts*., **2003**, *82*, 4806.

[23] V. Sazonova, Y. Yaish, H. U. Stunel, D. Roundy, T. A. Arias & P. L. McEuen, *Nature*, **2004,** 431, 284.

[24] Z.L. Wang (ed.) *Nanowires and Nanobelts – materials, properties and devices; V*ol. II: *Nanowires and Nanobelts of Functional Materials*, Kluwer Academic Publisher, **2003**.

[25] J. Singh, D. E. Wolfe, *J. Mater. Sci.*, **2005**, 40, 1.

[26] T. Karabacak, A. Mallikarjunan, J. P. Singh, D. Ye, G.-C. Wang, T.-M. Lu, *Appl. Phys. Letts*., **2003**, 83, 3096.

[27] B. Marson, K. Sattler, *Phys. Rev. B* **1999**, 60, 11593.

[28] L. M. Cao, Z. Zhang, L L Sun, C X Gao, M. He, Y. Q. Wang, Y. C. Li, Y. Zhang, G. Li, J. Zhang and W. K. Wang, *Adv. Mater.* **2001**, 13**,** 1701.

[29] L. M. Cao, K. Hahn, C. Scheu, and M. Rühle Y. Q. Wang and Z. Zhang , C. Gao, Y. C. Li, Y. Zhang, M. He, L. L. Sun, and W. K. Wang, *Appl. Phys. Letts*., **2002**, 80, 4226.

[30] K. Suenaga, M. P. Johansson, N. Hellgren, E. Broitman, L. R. Wallenberg, C. Colliex, J. E. Sundgren, L. Hultman, *Chem. Phys. Letts.*, **1999**, 300, 695.

[31] D.S. Bethune, C.H. Klang, M.S. de Vries, G. Gorman, R. Savoy, J. Vazquez and R. Beyers. *Nature* **1993,** 363, 605.

[32] P. R. Willmott, *Prog. Surf. Sci.*, **2004**, 76, 163.

[33] D. Dijkkamp, T. Venkatesan, D. Wu, S. A. Shaheen, N. Jisrawi, Y. H. Minlee, W. L. Mclean, M. Croft, *Appl. Phys. Letts.*, **1987**, 51, 619.

[34] A. Thess, R. Lee, P. Nikolaev, H. Dai, P. Petit, J. Robert, C. Xu, Y.H. Lee, S.G. Kim, A.G. Rinzler, D.T. Colbert, G. Scuseria, D. Tomanek, J.E. Fisher and R.E. Smalley. *Science* **1996**, 273, 483.

[35] A. M. Morales, C. M. Lieber, *Science*, **1998**, 279, 208.

[36] C. Lauhon, L. J. Gudiksen, M. S.; Wang, D.; Lieber, C. M. *Nature* **2002**, *420*, 57.

[37] S. Han, C. Li, Z. Liu, B. Lei, D. Zhang, W. Jin, Liu, T. Tang, and C. W. Zhou, *Nano Lett.* **2004,** *4*, 1241.

[38] C.J. Lee and J. Park. *Appl. Phys. Lett.* **2000, 77**, 3397.

[39] J. C. Wang, S. Q. Feng, D. P. Yu, *Appl. Phys. A*, **2002**, 75, 691.

[40] Z. Zhong, F. Qian, D. Wang, C. M. Lieber, *Nano Lett.*, **2003,** *3*, 343.

[41] B. Zheng, C. Lu, G. Gu, A. Makarovski, G. Finkelstein and J. Liu, *Nano Letts.*, **2002,** 2, 895.

[42] C. M. Hsu, C. H. Lin, H. J. Lai, C. T. Kuo, *Thin Solid Films*, **2005**, 471, 140.

[43] X. F. Duan, C. M. Lieber, *Adv. Mater.* **2000,** 12, 298.

[44] Y. Cui, L. J. Lauhon, M. S. Gudiksen, J. Wang, C. M. Lieber, *Appl. Phys. Lett.* **2001**, 78, 2214.

[45] X. F. Duan, C. M. Niu, V. Sahi, J. Chen, J. W. Parce, S. Empedocles and J. L. Goldman, *Nature*, **2003**, 425, 274.

[46] M. S. Gudiksen, L. J. Lauhon, J. F. Wang, D. C. Smith and C. M. Lieber, *Nature*, **2002**, 415, 617.

[47] L.J. Lauhon, M.S. Gudiksen, D. Wang, and C.M. Lieber , *Nature* **2002,** 420, 57.

[48] Y. H. Kim, J. Y. Lee, S. H. Lee, J. E. Oh, H. S. Lee, *Appl. Phys. A* **2005**, 80,1635.

[49] H. Hasegawa, S. Kasai,*Phys. E***, 2001**, 11, 149.

[50] Z. H. Wu, M. Sun, Y. Mei, H. E. Ruda, *Appl. Phys. Lett.*, **2004**, 85, 657.

[51] Y. S. Min, E. J. Bae, K. S. Jeong, Y. J. Cho, J. H. Lee, W. B. Choi, G. S. Park, *Adv. Mater.*, **2003**, 15, 1019.

[52] M. S. Sander, M. J. Cote, W. Gu, B. M. Kile, C. P. Tripp, *Adv. Mater.*, **2004**, 16, 2052.

[53] H. Shin, D. K. Jeong, J. Lee, M. M. Sung, J. Kim, *Adv. Mater.*, **2004**, 16, 1197.

[54] X. D. Wang, E. Graugnard, J. S. King, Z. L. Wang, and C. J. Summers, *Nano Lett.*, **2004**, 4, 2223.

[55] J.J. Urban, W.S. Yun, Q. Gu, H. Park, *J. Am. Chem. Soc.*, **2002**, 124, 1186.

[56] J.J. Urban, J. E. Spanier, O. Y. Lian, W.S. Yun, H. Park, *Adv. Mater.* **2003**, 15, 423.

[57] W. B. Bu, Z. L. Hua, L. Zhang, H. R. Chen, W. M. Huang, J. L. Shi, *J. Mater. Res.* **2004**, 19, 2807.

[58] W. B. Bu, Z. L. Hua, H. R. Chen, L. Zhang, J. L. Shi, *Chem. Letts.*, **2004**, 33, 612.

[59] Q. W. Chen, T. Zhu, *Chem. Phys. Letts.* **2003**, 375, 167.

[60] K. Kempa, B. Kimball, J. Rybczynski, Z. P. Huang, P. F. Wu, D. Steeves, M. Sennett, M. Giersig, D. V. G. L. N. Rao, D. L. Carnahan, D. Z. Wang, J. Y. Lao, W. Z. Li, and Z. F. Ren, *Nano Lett.*, **2003**, 3, 13.

[61] Z. Zhong, D.Wang, Y. Cui, M. W. Bockrath, C. M. Lieber, *Science* **2003**, 302, 1377.

[62] S. J. Tans, R. M. Verschueren, C.Dekker, *Nature* **1998,** 393, 49.

[63] P. L. McEuen, M. Bockrath, D. H. Cobden, Y.-G. Yoon, S. G. Louie, *Phys. Rev. Lett.* **1999**, *83*, 5098.

[64] A. Bachtold, P. Hadley, T. Nakanishi, C. Dekker, *Science* **2001**, *294*, 1317.

[65] Y. Cui, Z. Zhong, D. Wang, W. Wang, C. M. Lieber., *Nano Lett.* **2003, 3**, 149.

[66] J. Kong, H. T. Soh, A. Cassell, C. F. Quate, H. Dai, *Nature* **1998**, *395*, 878.

[67] J. Kong, N. R. Franklin, C. Zhou, M. G. Chapline, S. Peng, K. Cho, H. Dai, *Science* **2000**, *287*, 622.

[68] Y. Cui, Q. Wei, H. Park, C. M. Lieber, *Science* **2001**, *293*, 1289.

[69] F. Patolsky, G. F. Zheng, O. Hayden, M. Lakadamyali, W. Zhuang, C. M. Lieber, *Proc. Nat. Aca. Sci. USA*, **2004**, 101, 14017.

[70] M. C. Mcalpine, R. S. Friedman, C. M. Lieber, *Proc. IEEE* **2005**, 93, 1357.

[71] R.S. Friedman, M.C. McAlpine, D.S. Ricketts, D. Ham and C.M. Lieber, *Nature*, **2005**, 434, 1085.

[72] M. J. Zheng, L. D. Zhang, G. H. Li, Y. Zhang, F. Wang, *Appl. Phys. Letts.* **2001**, 79, 839.

[73] Z. R. Dai, J. L. Gole, J. D. Stout, Z. L. Wang, *J. Phys. Chem. B* **2002**, 106, 1274.

[74] Z. W. Pan, Z. R. Dai, L. Xu, S. T. Lee, and Z. L. Wang, *J. Phys. Chem. B*, **2001**, 105, 2507.

[75] C. A. Huber, T. E. Huber, M. Sadoqui, J. A. Lubin, S. Manalis, C. B. Prater, *Science* **1994**, 263, 800.

[76] K. Kempa, B. Kimball, J. Rybczynski, Z. P. Huang, P. F. Wu, D. Steeves, M. Sennett, M. Giersig, D. V. G. L. N. Rao, D. L. Carnahan, D. Z. Wang, J. Y. Lao, W. Z. Li, and Z. F. Ren, *Nano Lett.*, **2003**, 3, 13.

[77] X. D. Wang, C. J. Summers, and Z. L. Wang, *Nano Lett.*, **2004**, 4, 423.

[78] Y. Li, X. L. Ma, *Phys. Stat. Sol. A*, **2005**, 202, 435.

[79] S. Y. Bae, J. Lee, H. Jung, J. Park, J.-P. Ahn, *J. Am. Chem. Soc.*, **2005**, 127, 10802.

[80] R. Tenne, L. Margulis and M. Genut. *Nature* **1992**, 360, 444.

[81] Y. Feldman, E. Wasserman, D.J. Srolovitz and R. Tenne. *Science* **1995**, 267, 222.

[82] E.J.M. Hamilton, S.E. Dolan, C.E. Mann and H.O. Colliex, *Science* **1993**, 260, 649.

[83] X. Y. Kong, Z. L. Wang, J. S. Wu, *Adv. Mater.* **2003,** 15, 1445.

[84] J. Goldberger, R. R. He, Y. F. Zhang, S. W. Lee, H. Q. Yan, H. J. Choi, P. D. Yang, *Nature* **2003**, 422, 599.

[85] Y. Liu, J. Dong, M. Liu, *Adv. Mater.* **2004**, 16, 353.

[86] L. Vayssieres, K. Keis, A. Hagfeldt and S.E. Lindquist. *Chem. Mater.* **2001,** 13, 4386.

[87] J. P. Cheng, R. Y. Guo, Q. M. Wang , *Appl.. Phys. Letts*. **2004**, 85, 5140.

[88] J. J. Wu, S. C. Liu, C. T. Wu, K. H. Chen and L. C. Chen, *Appl. Phys. Letts*. **2002**, 81, 1312.

[89] J. Zhang , L. D. Sun , C. S. Liao and C. H. Yan , *Chem. Commun.* **2002**, 3, 262.

[90] Y. J. Xing, Z. H. Xi, Z. Q. Xue, D. Zhang, and J. H. Song, R. M. Wang, J. Xu, Y. Song, S. L. Zhang and D. P. Yu, *Appl. Phys. Letts*. **2004**, 83, 1689.

[91] B. P. Zhang, N. T. Binh, K. Wakatsuki, Y. Segawa, Y. Yamada, N. Usami, M. Kawasaki and H. Koinuma, *Appl. Phys. Letts*. **2004**, 84, 4098.

[92] R. V. Parish, *The metallic Elements*, **1977**, Longman Inc., New York.

[93] P. X. Gao, C. S. Lao, Y. Ding, Z. L. Wang, *Adv. Fun. Mater.* **2005,** in press.

[94] M.H. Zhao, Z.L. Wang and S.X. Mao, *Nano Letts.*, **2004**, 4, 587.

[95] E. Comini, G. Faglia, G. Sberveglieri, Zhengwei Pan, Zhong L. Wang, *Appl. Phys. Lett.*, **2002**, 81, 1869.

[96] W. Hughes and Z.L. Wang, *Appl. Phys. Letts.*, **2003**, 82, 2886.

[97] Y. Cui, Q. Wei, H. Park, and C.M. Lieber, *Science* **2001**, 293, 1289.

[98] G. Zheng, F. Patolsky, Y. Cui, W.U. Wang and C.M. Lieber, Nat. Biotechnol. **2005,** 23, 1294.

[99] C. Li, M. Curreli, H. Lin, F. N. Ishikawa, R. Datta, R. Cote, M. E. Thompson, and C. Zhou, *J. Am. Chem. Soc.*, **2005,** 127(36), 12484.

[100] F. Patolsky, G. Zheng, O. Hayden, M. Lakadamyali, X. Zhuang and C.M. Lieber, *Proc. Natl. Acad. Sci. USA* **2004**, 101, 14017.

[101] Y. C. Tai & R. S. Muller, *Sensors Actuator*, **1988**, 15, 63.

[102] J. G. Santiago et al., *Exp. Fluidics*, **1998**, 25, 316.

[103] P. H. Paul et al., *Anal. Chem.*, **1998**, 70, 2459.

[104] J. B. Knight et al., *Phys. Rev. Letts.* **1998**, *80*, 3863.

[105] P. X. Gao, Y. Ding and Z. L. Wang, *Nano Lett.*, **2003,** 3(9), 1315.

[106] M. H. Huang, S. Mao, H. Feick, H. Q. Yan, Y. Y. Wu, H. Kind, E. Weber, R. Russo, and P. D. Yang, *Science* **2001**, 292, 1897.

[107] H. T. Ng, J. Li, M. K. Smith, P. Nguyen, A. Cassell, J. Han, M. Meyyanppan, *Science*, **2003,** 300, 1249.

[108] C. J. Lee, T. J. Lee, S. C. Lyu, Y. Zhang, H. Ruh, H. J. Lee, *Appl. Phys. Lett.*, **2002**, 19, 3648.

[109] S. C. Lyu, Y. Zhang, H. Ruh, H. J. Lee, H. W. Shim, E. K. Suh, C. J. Lee, *Chem. Phys. Lett.*, **2002**, 363, 134.

[110] J. –J. Wu, and S. –C. Liu, , *Adv. Mater.*, **2002**, 14, 215.

[111] W. I. Park, G. C. Yi, J. W. Kim, S. M. Park, *Appl. Phys. Lett*., **2003**, 82, 4358.

[112] W. I. Park, G. Yi, M. Kim, S. L. Pennycook, Adv. Mater. **2002**, 14, 1841.

[113] K. Ogata, K. Maejima, Sz.k Fujita, Sg. Fujita, *J. Crys. Grow.*, **2003**, 248, 25.

[114] P.X. Gao, Z.L. Wang, *J. Phys. Chem. B,* **2002**, *106*, 12653.

[115] J. Y. Lao, J. G. Wen, Z. F. Ren, *Nano Lett.*, **2002**, 2, 1287.

[116] S. Hassani, A. Tromson-Carli, A. Lusson, G. Didier, and R. Triboulet, *Phys. Stat. Sol. (b),* **2002**, 229, 835.

[117] Y. Q. Zhu, W. K. Hsu, W. Z. Zhou, M. Terrones, H. W. Kroto, D. R. M. Walton, *Chem. Phys. Lett.*, **2001**, 347, 337.

[118] A. K. Abduev, A. K. Akhmedov, V. G. Baryshnikov, S.O. Shakhshaev, *Tech. Phys. Lett.*, **2000**, 4, 37.

[119] K. Ogata, T. Kawanishi, K. Maejima, Sz. Fujita, and Sg. Fujita, *J. Crys. Growth*, **2002**, 237-239, 553.

[120] R. S. Wagner, and W. C. Ellis, *Appl. Phys. Lett*., **1964**, 4, 89.

[121] Z.R. Dai, Z.W. Pan, and Z.L. Wang, *J. Am. Chem. Soc.*, **2002**, *124*, 8673.

[122] P. X. Gao & Z. L. Wang, *J. Am. Chem. Soc*., **2003**, 125, 11299.

[123] Y. Ding, P.X. Gao and Z.L. Wang, *J. Am. Chem. Soc*., **2004**, *126*, 2066.

[124] Y. Y. Wu, P. D. Yang, *J. Am. Chem. Soc*., **2001**, *123 (13)*, 3165.

[125] A. M. Morales, C. M. Lieber, *Science*, **1998**, *279*, 208.

[126] Y. Cui, L. J. Lauhon, M. S. Gudiksen, J. F. Wang, C. M. Lieber, *Appl. Phys. Lett*. **2001**, *78*, 2214.

[127] M.H. Huang, Y.Y. Wu, H. N. Feick, T. E. Weber, P.D. Yang, *Adv. Mater.* **2001**, *13*, 113.

[128] C.H. Liang, L.D. Zhang, G.W. Meng, Y.W. Wang, Z.Q. Chu, *J. Non-Crystalline Solids* **2000,** *277*, 63.

[129] Y.Q. Zhu, W.K. Hsu, M. Terrones, N. Grobert, H. Terrones, J.P. Hare, H.W. Kroto, D.R.M. Walton, *J. Mater. Chem.* **1998**, *8*, 1859.

[130] Y.C. Choi, W.S. Kim, Y.S. Park, S.M. Lee, D.J. Bae, Y.H. Lee, G.S. Park, W.B. Choi, N.S. Lee, J.M. Kim, *Adv. Mater.* **2000**, *12*, 746.

[131] Z.W. Pan, Z.R. Dai, C. Ma, Z.L. Wang, *J. Am. Chem. Soc.*, **2002**, *124 (8)*, 1817.

[132] 1997 JCPDS-International center for diffraction data, 04-0673.

[133] F. Gallaso, *Structure and Properties of Inorganic Solids* (Pergamon Press, New York, **1970**).

[134] Z.W. Pan, Z. R. Dai, Z. L. Wang, *Science*, **2001**, *291*, 1947-1949.

[135] R. V. Parish, *The metallic Elements*, (Longman Inc., New York, **1977**).

[136] L. Zhang, Z. H. Jin, L. H. Zhang, M. L. Sui, K. Lu, *Phys. Rev. Lett.*, **2000**, *85*, 1484.

[137] P. X. Gao and Z. L. Wang, *Appl. Phys. Lett.*, **2004**, 84, 2803.

[138] Z. R. Dai, J. L. Gole, J. D. Stout, Z. L. Wang, *J. Phys. Chem. B* **2002**, 106, 1274.

[139] F. Krumeich, H. J. Muhr, M. Niederberger, F. Bieri, B. Schnyder and R. Nesper, *J. Am.Chem. Soc.*, **1999**, 121, 8324.

[140] Y. C. Choi, W. S. Kim, Y. S. Park, S. M. Lee, D. J. Bae, Y. H. Lee, G. S. Park, W. B. Choi, N. S. Lee and J. M. Kim, *Adv. Mater.*, **2000**, 12, 746.

[141] Y. H. Tang, Y. F. Zheng, N. Wang, I. Bello, C. S. Lee and S. T. Lee, *Appl. Phys. Lett.*, **1999**, 74, 3824.

[142] B. C. Satishkumar, A. Govindaraj, E. M. Vogel, L. Basumallick and C. N. R. Rao, *J. Mater. Res.*, **1997**, 12, 64.

[143] J. –J. Wu, and S. –C. Liu, *Adv. Mater*., **2002**, 14, 215.

[144] Z. W. Pan, Z. R. Dai, L. Xu, S. T. Lee, and Z. L. Wang, *J. Phys. Chem. B*, **2001**, 105, 2507.

[145] C. L. Hoenig, A. W. Searcy, *J. Am. Ceram. Soc.*, **1966**, 49, 128.

[146] K. K. Kelly, *U. S. Bur. Mines Bull*., **1949**, 476, 187.

[147] Z. L. Wang, Z. W. Pan, *Adv. Mater*., **2002**, 14, 1029.

[148] Z. L. Wang, Z. C. Kang, *Functional and Smart Materials—Structure Evolution and Structure Ananlysis*, Plenum Press, New York, **1998.**

[149] Z. L. Wang, X. Y. Kong, and J. M. Zuo, *Phys. Rev. Lett.*, **2003,** 91, 185502.

[150] P. X. Gao and Z. L. Wang, *J. Phys. Chem B.,* **2004,**108, 7534.

[151] X. Y. Kong, Z. L. Wang, *Nano Lett*. **2003**, 3, 1625.

[152] X. Y. Kong, Z. L. Wang, *Appl. Phys. Letts.*, **2004**, 84, 975.

[153] W. Hughes, Z. L. Wang, *J. Am. Chem. Soc.* **2004,** 126, 6703.

[154] P. X. Gao, Z. L. Wang, *J. Appl. Phys.* **2005**, *97*, 044304.

[155] X. Y. Kong, Y. Ding, R. Yang, Z. L. Wang, *Science* **2004**, *303*, 1348.

[156] Y. Ding, X. Y. Kong, Z. L. Wang, *Phys. Rev. B*, **2004**, 70, 235408.

[157] P. X. Gao, Z. L. Wang, *Small*, **2005**, 1, 945.

[158] T. Murata, I. Yamato, Y. Kakinuma, A. G. W. Leslie, J. E. Walker, *Science*, **2005**, 308, 654.

[159] S. Amelinckx, B. Zhang, D. Bernaerts, F. Zhang, V. Ivanov, J.B. Nagy, *Science* **1994**, 265, 635.

[160] R.P. Gao, Z.L. Wang and S.S. Fan, *J. Phys. Chem.* B, **2000**, 104, 1227.

[161] H.F. Zhang, C.M. Wang, E.C. Buck and L.S. Wang, *Nano Lett.* **2003,** 3, 577.

[162] H.F. Zhang, C.M. Wang and L.S. Wang, *Nano Lett.* **2002**, 2, 941.

[163] O.G. Schmidt and K. Eberl, *Nature*, **2001,** 410, 168.

[164] X.Y. Kong and Z.L. Wang, *Appl. Phys. Letts.* **2004**, 84, 975.

[165] P. X. Gao and Z. L. Wang, *J. Appl. Phys.*, **2005**, 97, 044304.

[166] P. X. Gao, Y. Ding, W. J. Mai, W. L. Hughes, C. S. Lao and Z. L. Wang, *Science*, **2005**, 309, 1700.

[167] H Yang, N. Coombs, and G. A. Ozin, *Nature*, **1997**, *386*, 692.

[168] D. Zhao, J. Sun, Q. Li, and G. D. Stucky, *Chem. Mater,* **2000**, *12*, 275.

[169] Z.R.R. Tian, J. Liu, J.A. Voigt, B. McKenzie, H.F. Xu, *Angew. Chem. Inter. Ed.*, **2003**, *42*, 414.

[170] Z.R.R. Tian, J. Liu, H.F. Xu, J.A. Voigt, B. McKenzie, C.M. Matzke, *Nano Letters*, **2003**, *3*, 179.

[171] H. Y. Fan, S. Reed, T. Baer, R. Schunk, G. P. Lopez, C. J. Brinker, *Micorporous and Mesoporous Materials*, **2001**, *44*, 625.

[172] R.L. Whetten, J.T. Khoury, M.M. Alvarez, S. Murthy, I. Vezmar, Z.L. Wang, P.W. Stephens, C.L. Cleveland, W.D. Luedtke, and U. Landman, *Adv. Mater.*, **1996**, *8*, 428.

[173] C.P. Collier, R.J. Saykally, J.J. Shiang, S.E. Henrichs, and J.R. Heath, *Science*, **1997**, *277*, 1978.

[174] M.P. Pileni, *Appl Surf Sci.*, **2001**, *171*, 1.

[175] M.P. Pileni, *J Phys Chem B*, **2001**, 105, 3358.

[176] S.H. Sun, C.B. Murray, D. Weller, L. Folks, and A. Moser, *Science*, **2000**, *287*, 1989.

[177] C.J. Kiely, J. Fink, M. Brust, D. Bethell, and D.J. Schiffrin, *Nature*, **1998**, *396*, 444.

[178] C.B. Murray, C.R. Kagan, and M.G. Bawendi, *Science*, **1995**, *270*, 1335.

[179] X.G. Peng, L. Manna, W.D. Yang, J. Wickham, E. Scher, A. Kadavanich, and A.P. Alivisatos, *Nature*, **2000**, *404*, 59.

[180] P.V. Braun, P. Osenar, and S.I. Stupp, *Nature*, **1996**, *380*, 325.

[181] M.D. Bentzon, J. V. Wonterghem, S. Mø rup, A. Thölen, and C.J.W. Koch, *Phil. Mag. B*, **1989**, *60*, 169.

[182] J.S. Yin, and Z.L. Wang, *Phys. Rev. Lett*, **1997**, *79*, 2570.

[183] L. Esaki, and R. Tsu, *IBM J. Rese. Devel.* **1970**, 14, 61.

[184] S.C. Minne, S.R. Manalis, and C.F. Quate, *Appl. Phys. Letts*, **1995**, 67, 3918.

[185] K. Keis, L. Vayssieres, S. Lindquist, and A. Hagfeldt, *Nanostr. Mater.*, **1999**, 12(1-4), 487.

[186] C.R. Gorla, N.W. Emanetoglu, S. Liang, W.E. Mayo, Y. Lu, M. Wraback, and H. Shen, *J. Appl. Phys.*, **1999**, *85*, 2595.

[187] F. Bernardini, V. Fiorentini, and D. Vanderbilt, *Phys. Rev. B*, **1997**, *56*, 10024-10027. The theoretically calculated piezoelectric coefficients for ZnO are: e_{33} = 0.89, e_{31} = -0.51 C/m^2. The experimentally measured e33 = 1.0-1.2 C/m2.

[188] Z. W. Pan, Z. R. Dai, and Z. L. Wang, *Science*, **2001**, *291*, 1947.

[189] Gallaso, F., *Structure and Properties of Inorganic Solids* (Pergamon Press, New York, **1970**).

[190] R. Uyeda, *J. Crystal Growth*, **1974**, *24/25*, 69.

[191] A. K. Petford-Long, and D. J. Smith, *J. Crystal Growth*, **1987**, *80*, 218.

[192] P. X. Gao, Z. L.Wang, *J. Phys. Chem. B*, **2002**, *106*, 12653.

[193] Y. Ding, X. Y. Kong and Z. L. Wang, *J. Appl. Phys.* **2004**, 95, 306.

[194] R. Tenne, L. Margulis and M. Genut. *Nature* **1992**, 360, 444.

[195] Y. Feldman, E. Wasserman, D.J. Srolovitz and R. Tenne. *Science* **1995**, 267, 222.

[196] E.J.M. Hamilton, S.E. Dolan, C.E. Mann and H.O. Colliex, *Science* **1993**, 260, 649.

[197] X. Y. Kong, Z. L. Wang, J. S. Wu, *Adv. Mater.* **2003,** 15, 1445.

[198] J. Goldberger, R. R. He, Y. F. Zhang, S. W. Lee, H. Q. Yan, H. J. Choi, P. D. Yang, *Nature* **2003**, 422, 599.

[199] Y. Liu, J. Dong, M. Liu, *Adv. Mater.* **2004**, 16, 353.

[200] L. Vayssieres, K. Keis, A. Hagfeldt and S.E. Lindquist. *Chem. Mater.* **2001,** 13, 4386.

[201] J. P. Cheng, R. Y. Guo, Q. M. Wang , *Appl.. Phys. Letts*. **2004**, 85, 5140.

[202] J. J. Wu, S. C. Liu, C. T. Wu, K. H. Chen and L. C. Chen, *Appl. Phys. Letts*. **2002**, 81, 1312.

[203] J. Zhang , L. D. Sun , C. S. Liao and C. H. Yan , *Chem. Commun.* **2002**, 3, 262.

[204] Y. J. Xing, Z. H. Xi, Z. Q. Xue, D. Zhang, and J. H. Song, R. M. Wang, J. Xu, Y. Song, S. L. Zhang and D. P. Yu, *Appl. Phys. Letts*. **2004**, 83, 1689.

[205] B. P. Zhang, N. T. Binh, K. Wakatsuki, Y. Segawa, Y. Yamada, N. Usami, M. Kawasaki and H. Koinuma, *Appl. Phys. Letts*. **2004**, 84, 4098.

[206] R. V. Parish, *The metallic Elements*, **1977**, Longman Inc., New York.

[207] P. X. Gao, C. S. Lao, Y. Ding, Z. L. Wang, *Adv. Fun. Mater.* **2005,** in press.

[208] P. X. Gao, Z. L. Wang, *J. Am. Chem. Soc.,* **2003,** 125, 11299.

[209] R. Berger, C. Gerber, H. P. Lang, and J. K. Gimzewshi, *Microelectron. Eng*. **1997,** 35, 373.

[210] G. H. Wu, R. H. Datar, K. M. Hansen, T. Thundat, R. J. Cote, and A. Majumdar, *Nature Biotechnology* **2001,** 19, 856.

[211] K.A. Stevenson, A. Mehta, P. Sachenko, K.M. Hansen, and T. Thundat, *Langmuir* **2002,** 18, 8732.

[212] X.D. Bai, P.X. Gao, Z.L. Wang and E.G. Wang, *Appl. Phys. Letts.*, **2003**, *82*, 4806.

[213] X. D. Bai, E. G. Wang, P. X. Gao and Z. L. Wang, *Nano Letters*, **2003**, 3, 1147.

[214] G. Abadal, Z. J. Davis, B. Helbo, X. Borrise, R. Ruiz, A. Boisen, F. Campabadal, J. Esteve,, E. Figueras, F. Perez-Murano, and F. Barniol, *Nanotechnology* **2001,** 12, 100.

[215] Z.J. Davis, G. Abadal, O. Khn, O. Hansen, F. Grey, and A. Boisen, *J. Vac. Sci. Technol. B* **2000,** 18, 612.

[216] Z. W. Pan, Z. R. Dai, and Z. L. Wang, *Science* **2001,** 291, 1947.

[217] M.H. Huang, S. Mao, H. Feick, H. Yan, Y. Wu, H. Kind, E. Weber, R. Russo, and P. Yang, *Science* **2001,** 292, 1897.

[218] M.S. Arnold, P. Avouris, Z.W. Pan, and Z.L. Wang, *J. Phys. Chem*. B **2003**, 107, 659.

[219] E. Comini, G. Faglia, G. Sberveglieri, Z.W. Pan, and Z.L. Wang, *Appl. Phys. Lett*. **2002,** 81, 1869.

[220] Y. Cui, Q. Wei, H. Park, and C. M. Lieber, *Science* **2001,** 293, 1289.

[221] M.K. Gudiksen, L.J. Lauhon, J. Wang, D.C. Smith, and C.M. Lieber, *Nature* **2002,** 415, 617.

[222] H. G. Craighead, *Science* **2000,** 290, 1532.

[223] W. Hughes, and Z.L. Wang, *Appl. Phys. Letts*. **2003**, 82, 2886.

[224] P. Poncharal, Z.L. Wang, D. Ugarte, and W.A. de Heer, *Science* **1999,** 283, 1513.

[225] Z. L. Wang, P. Poncharal, and W. A. de Heer, *Pure Appl. Chem.* **2000,** 72, 209.

[226] R.P. Gao, , Z.L Wang, Z.G. Bai, W.A. de Heer, L.M. Dai, and M. Gao, *Phys. Rev. Lett.* **2000,** 85, 622.

[227] Z.L. Wang, *Adv. Mater.* **2000,** 12, 1295.

[228] Z.L. Wang, Z.R. Dai, Z.G. Bai, R.P. Gao, and J. Gole, , *Appl. Phys. Lett.* **2000,** 77, 3349.

[229] Meirovich, L. *Elements of Vibration Analysis*, (McGraw-Hill, New York, 2nd edition, **1986**).

[230] S.X. Mao, M.H. Zhao, and Z.L. Wang, *Appl. Phys. Letts.*, **2003,** 83, 993.

[231] H.J. Dai, J.H. Hafner, A.G. Rinzler, D.T. Colbert, and R.E. Smalley, *Nature*, **1996,** 384, 147.

[232] S.S. Wong, E. Joselevich, A.T. Woolley, C.L. Cheung, and C.M. Lieber, *Nature*, **1998,** 394, 52.

[233] J. Zhou, C. S. Lao, P. X. Gao, W. J. Mai, Z. L. Wang and N. S. Xu, *J. Appl. Phys.*, **2005**, submitted.

[234] W. Wang, X. Gao, B. Wang, *Current Organic Chemistry*, **2002**, 6, 1285.

[235] D. A. Wharam, T. J. Thornton, R.Newbury, M. Pepper, H. Ahmed, J. E. F. Frost, D. G. Hasko, D. C. Peacock, D. A. Ritchie, and G. A. C. Jones, *J. Phys. C: Solid State Phys*, **1988**, 21, L209.

[236] B. J. Van Wees, H. van Houten, C. W. J. Beenakker, J. G. Williamson, L. P. Kouvenhoven, D. van der Marel, and C. T. Foxon, *Phys. Rev. Lett.* **1988**, 60, 848.